creative commons
COMMONS DEED

저작자표시 2.0 대한민국

이용자는 아래의 조건을 따르는 경우에 한하여 자유롭게

- 이 저작물을 복제, 배포, 전송, 전시, 공연 및 방송할 수 있습니다.
- 이차적 저작물을 작성할 수 있습니다.
- 이 저작물을 영리 목적으로 이용할 수 있습니다.

다음과 같은 조건을 따라야 합니다:

저작자표시. 귀하는 원저작자를 표시하여야 합니다.

- 귀하는, 이 저작물의 재이용이나 배포의 경우, 이 저작물에 적용된 이용허락조건을 명확하게 나타내어야 합니다.
- 저작권자로부터 별도의 허가를 받으면 이러한 조건들은 적용되지 않습니다.

저작권법에 따른 이용자의 권리는 위의 내용에 의하여 영향을 받지 않습니다.

이것은 이용허락규약(Legal Code)을 이해하기 쉽게 요약한 것입니다.

Disclaimer

dCollection

이학박사 학위논문

Development of the TRAO control system for the multi-beam receiver and Observational study of water and methanol masers in massive star-forming regions

대덕전파천문대 다중빔 수신기용 제어시스템 구축과 고질량성 생성 영역에 대한 물과 메탄올메이저 관측연구

2014년 8월

서울대학교 대학원

물리·천문학부 천문학전공

강 현 우

Development of the TRAO control system for the multi-beam receiver and Observational study of water and methanol masers in massive star-forming regions

지도교수 박 용 선

이 논문을 이학박사 학위논문으로 제출함

2014년 4월

서울대학교 대학원

물리·천문학부 천문학전공

강 현 우

강 현 우의 이학박사 학위논문을 인준함

2014년 6월

위 원 장 _____

부 위 원 장 _____

위 원 _____

위 원 _____

위 원 _____

Development of the TRAO control system for the multi-beam receiver and Observational study of water and methanol masers in massive star-forming regions

by

Hyunwoo Kang
(orionkhw@kasi.re.kr)

A dissertation submitted in partial fulfillment of the requirements for the degree of

Doctor of Philosophy

in

Astronomy

in

Astronomy Program
Department of Physics and Astronomy
Seoul National University

Committee:

Professor	Bon-Chul Koo
Professor	Yong-Sun Park
Professor	Hyung Mok Lee
Professor	Do-Young Byun
Professor	Kee-Tae Kim

To my daughters, Jian & Nayun

ABSTRACT

Multi-beam receiver can greatly increase the observation efficiency by allowing observations of wide-field of sky in a short time. World-wide observatories have made efforts to develop such multi-feed receivers. The TRAO imported a multi-beam receiver called QUARRY from the FCRAO, USA, instead of developing it by himself, to swiftly follow the trend. We developed control system for the multi-beam receiver to be compatible with the remaining system. We made a new program and an interface to control spectrometers that acquire data from the receiver, improved a front-end system that manages the receiver, and installed a new data acquisition storage that saves data from Modcomp. In software part, we applied an asynchronous timer and a non-blocking method to the back-end system, used several communication methods to carry command and data directly, and edited the front-end system program with the non-blocking method to minimize a time of tuning process. In hardware part, we revised a DIO board, connected new DIO lines and serial lines, and adopted DMA method to transfer data quickly.

By using the radio telescope equipped with the multi-feed receiver and the KVN telescope, we carried out survey observations toward star forming regions in H_2O, CH_3OH masers and in HCO^+, $H^{13}CO^+$, and ^{13}CO thermal lines to understand their association with star formation activities. The targets are taken from Arecibo methanol maser Galactic plane survey and from Methanol Multibeam catalog identified with 6.7 GHz CH_3OH class II methanol maser. The detection rates of 22 GHz, 44 GHz, and 95 GHz toward 271 6.7 GHz class II methanol maser sources are 49 %, 51 %, and 44 %, respectively. Water maser is detected mostly with other masers, but does not show any correlation with them in terms of the flux density and the velocity. 12 sources out of the 66 sources in which water maser are detected have high-velocity ($> 30\,\mathrm{km\,s^{-1}}$) features, and the 7 sources out of the 12 sources may

be related with pole-on jets. 95 GHz class I methanol maser always comes with 44 GHz class I methanol maser. They are related with each other in the flux density and the velocity. Almost 44 GHz sources (87 %) come with 95 GHz maser. The distribution of velocity offset from the systemic velocity of 6.7 GHz peak flux density appears as a double peak shape and differs from others.

Keywords: radio telescope, control system, masers, star: formation

Student Number: 2004-30138

Contents

Abstract **i**

1 Introduction **1**

Reference 5

2 Development of the TRAO control system for the multi-beam receiver **7**

2.1 Introduction 8

2.2 Hardware structure 10

2.2.1 Modcomp 10

2.2.2 Platform PC (PPC) 12

2.2.3 Backend management PC (BPC) 14

2.2.4 correlator PC (CPC) 16

2.2.5 Data Acquisition Server (DAS) 18

2.2.6 Correlator 19

2.2.7 Time generator (TG) 20

2.2.8 digital input / output (DIO) divider 21

2.3 Details on the control system 23

2.3.1 Concepts of system programming 23

2.3.2 Communication between the control programs 33

2.3.3 Realization of the DMA method 42
2.4 Conclusion 44
Reference 49

3 Simultaneous observation of water and class I methanol masers toward class II methanol maser sources 51
3.1 Introduction 52
3.2 Source Selection and Observations 55
3.2.1 Source Selection 55
3.2.2 Observations 55
3.3 Results 57
3.3.1 Detection Rates 57
3.3.2 New Maser Sources 58
3.3.3 Notes on Selected Sources 60
3.4 Analyses 63
3.4.1 Velocity Characteristics 63
3.4.2 Flux Densities and Luminosities 67
3.4.3 Associated BGPS Clumps 71
3.4.4 Methanol Column Densities and Abundances 72
3.5 Conclusions 76
Reference 79

4 Observational study of water and class I methanol masers toward class II methanol maser sources 107
4.1 Introduction 108
4.2 Source Selection and Observations 111
4.2.1 Source Selection 111
4.2.2 Observations 111

4.3 Results 113
4.3.1 Detection Rates 113
4.3.2 Notes on Selected Sources 114
4.3.3 High velocity Features of Water Maser 117
4.4 Analyses 117
4.4.1 Velocity Characteristics 117
4.4.2 Analysis of detection rates 128
4.4.3 Flux Densities 131
4.4.4 BGPS counterparts 134
4.5 Conclusions 134
Reference 137

5 Conclusions **169**

List of Figures

2.1 The TRAO hardware organization 11
2.2 A block-diagram of the TRAO system 12
2.3 BIGMAP mode 13
2.4 Noisy signals on the old Modcomp DIO board 14
2.5 Clean signals on the new Modcomp DIO board 15
2.6 A interface diagram of the PPC 16
2.7 A capture of the PPC program 17
2.8 A BPC program 18
2.9 IF box control of the BPC 19
2.10 A CPC program 20
2.11 A spectrum window of the CPC 21
2.12 A schematic of the DIO divider. 22
2.13 Comparison of run-time OS and RTOS 24
2.14 Normal timer 27
2.15 Asynchronous timer 28
2.16 programming diagram 30
2.17 A flowchart of tuning process on the PPC 34
2.18 A flowchart of the integration communication 36
2.19 spaserv.sh 42
2.20 Timeupdate.sh 43

2.21 A02 terminal 44
2.22 A38 terminal 45
2.23 NTP synchronization 45
2.24 DMA method 46
2.25 Short circuits of the Modcomp 47

3.1 Venn diagram result of AMGPS 58
3.2 Detection rates as function of the 6.7 GHz peak flux and luminosity . 59
3.3 High velocity figures 64
3.4 Velocity offset distribution 65
3.5 Velocity offset of class I and class II 66
3.6 Histogram of velocity overlap 68
3.7 Peak flux density of 44 GHz and 95 GHz 69
3.8 Luminosity of 44 GHz and 95 GHz 71
3.9 Chen's criteria 73
3.10 BGPS mass and Luminosities 74
3.11 22 GHz detected sources 96
3.12 only 44GHz detected sources 100
3.13 All maser detected sources 101
3.14 44 GHz and 95 GHz detected sources 104
3.15 22 GHz and 44 GHz detected sources 105

4.1 Venn diagram of MMB 113
4.2 High velocity offset at 6.7 GHz 116
4.3 Two systemic velocity sources 118
4.4 High velocity sources at 22 GHz 119
4.5 Low possibility sources of high velocity feature 123
4.6 Velocity offsets of all sources 125

4.7 velocity offsets of class I and class II 126
4.8 Histogram of velocity overlap 127
4.9 Venn diagram of AMGPS and MMB sources 128
4.10 Galactic position of the sources 130
4.11 Detection rates at Galactic region 131
4.12 Detection rates as 6.7 GHz peak flux density 132
4.13 Peak flux density of 44 GHz and 95 GHz 133
4.14 BGPS plots with Chen's criteria 135

5.1 A first light by the QUARRY 170
5.2 A continuum observation of the Jupiter 171

List of Tables

2.1 Specification of Bandwidths of Correlator 22
2.2 A result of two timers on several conditions 27
2.3 Command bit list between BPC and CPC 37
2.4 Bit assignments between the Modcomp and the BPC 38
2.5 Command list between Modcomp and BPC 39

3.1 KVN Antenna Parameters 57
3.2 Column Densities and Fractional Abundances of Methanol 76
3.3 Source Summary with Detection Results 84
3.4 Line Parameters of Detected Masers 86
3.5 Maser Luminosities and associated BGPS Sources 93

4.1 Line Parameters of Detected Masers 140
4.2 Observation lists and results 159
4.3 BGPS counterparts list 166

Abbreviations

ACK acknowledgement

AMGPS Arecibo methanol maser Galactic plane survey

BPC back-end PC

BPF band pass filter

CPC correlator PC

CRC cyclic redundancy check

DAS data acquisition storage

DIO digital input / output

DMA direct memory access

FCRAO Five College Radio Astronomy Observatory

IF intermediate frequency

LO local oscillator

MMB Methanol multi-beam survey

NI National Instruments

NTP network time protocol

PPC front-end / platform PC

QUARRY Quabbin Array

REQ request

RTOS real time operating system

TG time generator

TRAO Taeduk Radio Astronomy Observatory

UCHII ultra compact HII

Chapter 1

Introduction

Taeduk Radio Astronomy Observatory (TRAO) 14 m telescope is the first mm-wave telescope in Korea. A dual-channel receiver which enables observation in 100 GHz and 150 GHz band simultaneously, has been used since 1998. Main research field with the use of the TRAO 14 m telescope includes circumstellar environment of late-type stars, physical properties of molecular clouds and star forming regions (Cho et al. 1998; Kim et al. 2000; Kang & Lee 2005).

Around 2000, world class observatories started the development of multi-feed receivers. Mm wave technology allowed production of mm wave components with rather uniform performance. When equipped with such multi-feed receivers, telescope can make images of sky very fast, which may be a quantum leap like a transition from photo-multiplier to CCD in optical community. Such efforts include QUARRY and SEQUOIA of Five College Radio Astronomy Observatory (FCRAO) (Erickson et al. 1992, 1999), BEARS of Nobeyama Radio Observatory (Sunada et al. 2000), and recent 3X3 multi-beam receiver of Purple Mountain Observatory (Chen et al. 2012).

The TRAO also has considered the adoption of such a multi-feed system to keep up with the international trend. Final conclusion was to import a multi-beam array

receiver, QUARY from the FCRAO (Erickson et al. 1992; Lee et al. 2007). It has of 5X3 feeds with which multiple positions in the sky can be observed simultaneously.

The Quabbin Array (QUARRY) has been imported in 1999 and 15 autocorrelation spectrometer has been installed in 2004. However, the multi-beam system had to be inactive for a long time till around 2007. Hardware and software environment were not revised accordingly to be compatible with the receiver. Moreover old main control computer system was getting out of order.

This study describes efforts that have been made to put life on the TRAO telescope with the QUARRY, which consist of the installation of new devices, the replacement of obsolete broken components, and the revision of control software.

The most crucial point in the revision of control programs is how to share time among processors based on the priorities of the processors using real-time process (Kang et al. 2005) or effective time control (Kang & Kang 2013) when one wants to develop complicated control system like the QUARRY. We adopt the ideas to programs in the computers communicating the QUARRY and spectrometer. We also use a direct memory access (DMA) method to transfer data fast and safely.

To make the QUARRY and spectrometer fully operational, we made four important developments as follows. Firstly, we developed a control program of the new spectrometer system. Secondly, program was improved to automatically tune the receiver stably and promptly. Thirdly, we manufactured a new DAS to take observation data from the Modcomp, which allows user to access the data easily. And lastly, we apply a DMA method to carry data fast among the systems. In Chapter 2, we discuss these development of the control system for the multi-beam system in detail.

With the refurbished TRAO telescope together with Korean VLBI Network telescopes (Kim et al. 2011; Lee et al. 2011), we initiated observational study of massive star forming regions in H_2O and CH_3OH maser transitions and in HCO^+ and CO

thermal lines. We do not conduct VLBI observation with KVN telescopes, but use them in single dish mode.

Masers are signposts of star formation activities, and particularly an important probe to understand an evolution of the massive star forming region. Among others, CH_3OH masers have identified relatively recently (Menten 1991) and their properties and relation with star formation activities remain uncertain. There are two types of methanol masers, class I and II (Menten 1991; Cragg et al. 1992). Class I is known to be pumped by collision while class II is by radiation. Codella et al. (2004) searched for 6.7 GHz methanol maser and water maser in 136 ultra compact HII (UCHII) regions, and found water and methanol masers are related with the outflow. Codella & Moscadelli (2000) claimed that the 6.7 GHz methanol maser disappears as UCHII region grows. Ellingsen (2006) found that GLIMPSE point sources that are related with class I and class II methanol maser are redder than other point sources that are only related with class II. He argues that class I methanol maser appears earlier than class II. The 6.7 GHz methanol maser is class II type, and is known to be related with massive star formation regions (Minier et al. 2003). H_2O maser has been found with the 6.7 GHz methanol maser (Beuther et al. 2002) though any correlation could not be found. The relation between class I and class II masers are controversy (Slysh et al. 1994; Ellingsen 2005).

In the mean while, several catalogs of 6.7 GHz methanol maser survey has been published including Arecibo methanol maser Galactic plane survey (AMGPS) and Methanol multi-beam survey (MMB) catalogs (Pandian et al. 2007; Caswell et al. 2010; Green et al. 2010). The surveys are unbiased ones sweeping Galactic plane blindly. We used the KVN telescopes as a single dish instrument to observe massive star forming regions identified by these 6.7 GHz maser surveys in the three maser lines, H_2O at 22 GHz and class I methanol masers at 44 GHz and 95 GHz. We observed 232 sources and added 39 sources that are observed by Kim et al. (in prep)

when analyzing data. The added sources are members of the MMB catalogs. In total, we have studied the 271 massive star forming regions. Observations with the KVN and TRAO telescopes in thermal lines of HCO^+ and CO are followed to find the systemic velocity of the sources and to verify high velocity features at 22 GHz. In Chapter 3 and 4, we describe in greater detail the simultaneous observational study of water and methanol masers together with HCO^+ and CO thermal lines toward massive star-forming regions.

References

Beuther, H., Walsh, A., Schilike, P., Sridharan, T.K., Menten, K.M., & Wyrowski, F. 2002, A&A, 390, 289

Caswell, J.K., Fuller, G.A., Green, J.A., et al. 2010, MNRAS, 404, 1029

Chen, X., Ellingsen, S.P., He, J.-H., et al. 2012, ApJS, 200, 5

Cho,S.-H., Chung, H.-S., Kim, H.-R. Oh, B.-Y., Lee, C.-H., & Han, S.-T. 1998, ApJS, 115, 277

Codella, C. & Moscadelli, L. 2000, A&A, 362, 723

Codella, C., Lorenzani, A., Gallego, A.T., Cesaroni, R., & Moscadelli, L. 2004, A&A, 417, 615

Cragg, D.M., Johns, K.P., Godfrey, P.D., & Brown, R.D. 1992, MNRAS, 259,203

Ellingsen, S.P. 2005, MNRAS, 359, 1498

Ellingsen, S.P. 2006, ApJ, 638, 241

Erickson, N.R., Goldsmith, P.F., Novak, G., Grosslein, R.M., Viscuso, P.J., Erickson, R.B., & Predmore, C.R. 1992, IEEE Trans. Microwave Theory Tech, 40, 1

Erickson, N. R., Grosslein, R. M., Erickson, R. B., & Weinreb, S. 1999, IEEE Trans. Microwave Theory Tech, 47, 2212

Green, J.A., Caswell, J.L., Fuller, G.A., et al. 2010, MNRAS, 409, 913

Kang, M. & Lee, Y. 2005, J. Korean Astron. Soc., 38, 33

Kang, H.W., Byun, D.-Y., & Park, Y.-S. 2005, P. Korean Astron. Soc., 20, 73

Kang, H. & Kang, H. 2013, J. Korea Industrial Information System Soc., 18, 37

Kim, H.-D., Cho, S.-H., Chung, H.-S., et al. 2000, ApJS, 131, 483

Kim, C.-H., Kim, K.-T., & Park, Y.-S., in prep

Kim, K.-T., Byun, D.-Y., Je, D.-H., et al. 2011, J. Korean Astron. Soc., 44, 81

Lee, Y., Kim, B.G., Jung, J.H., et al. 2007, J. Korean Astron. Soc., 40, 133

Lee, S.-S., Byun, D.-Y., Oh, C.S., et al. 2011, PASP, 123, 1398

Menten, K.M. 1991, in ASP Conf. Ser. 16, Atoms, Ions and Molecules: New Results in Spectral Line Astrophysics, ed. A.D. Haschick & P.T.P. Ho (San Francisco, CA: ASP), 119

Minier, V., Ellingsen, S.P., Norris, R.P., & Booth, R.S. 2003, A&A, 403, 1095

Pandian, J.D., Goldsmith, P.F., & Deshpande, A.A. 2007a, ApJ, 656, 255

Slysh, V.I., Kalenskii, S.V., Val'tts, I.E., & Otrupcek, R. 1994, MNRAS, 268, 464

Sunada, K., Yamaguchi, C., Kuno, N., Okumura, S., Nakai, N., & Ukita, N. 2000, ASPC, 217, 19s

Chapter 2

Development of the TRAO control system for the multi-beam receiver

Abstract TRAO has been used to study molecular cloud and late-type stars. In 1999, the TRAO imported a fifteen multi-beam receiver called QUARRY that had been used by FCRAO. Since the TRAO has grown under environment different from that of the FCRAO, we needed to develop new control programs for the QUARRY. In order to replace an obsolete control PC for the QUARRY, we prepared a new receiver control PC and revised its control software with a non-blocking programming method to manage several peripherals promptly. We bought multi-channel spectrometer from Spaceborne Inc. in USA for back-end system of the QUARRY. The back-end system, especially, has slow transfer speed of 32 bytes per 1 ms by the USB 1.1. To endure the low speed, we use asynchronous timer and non-blocking programming method. We adopt several communication technics and a Direct Memory Access method to transfer commands among a main control computer Modcomp

and the new peripherals, the front-end and the back-end control systems. Data from one correlator can be transferred at 4 ms to the Modcomp by the DMA method. In addition, Data Acquisition Server enabled easy data transfer to outside from the Modcomp. Consequently, the front-end system stably controls the QUARRY by commands of the Modcomp, and the back-end system runs every 50 ms adding time loss of 7 ms. In 2009, the QUARRY system has opened and have been operating successfully.

2.1 Introduction

TRAO 14 m telescope has imported a multi-beam receiver called QUARRY to improve the imaging capability in 1999, that had been developed and used by Five College Radio Astronomy Observatory (FCRAO). The QUARRY had been developed and utilized by Five College Radio Astronomy Observatory (FCRAO). The QUARRY has 15 feeds consisting of two bundles of 3X3 and 3X2 feeds (Erickson et al. 1992). Quasi-optical wave guides and mirrors are used to make the beams of two arrays interleaved, resulting in 5 x 3 beams with 50″spacing in the five beam direction and 100″spacing in the three beam direction on the sky. The signals from 15 feed horns are down-converted to 1.4 GHz intermediate frequency by cryogenic shorttkey diode mixers and amplified by HEMT amplifier at 20 K stage. The system temperates range from 400 $\sim$ 500 K at 100 GHz and 600 K $\sim$ 800 K at 115 GHz. An intermediate frequency (IF) box again down-converts the 1.4 GHz IF to 600 MHz before feeding the signals to the back-end.

There are adjustable components by a front-end PC, a de-rotator, a chopper, mixer bias suppliers, local oscillator (LO) filters, a SSB, a synthesizer, a tripler, a YIG oscillator, and YIG control unit. We bought auto-correlation type spectrometers as a back-end to support the multi-beam system. We need to adapt the QUARRY to TRAO observation environment and to a new spectrometer set. During the adapta-

tion process, we have encountered several problems as follow, that should be resolved eventually.

The QUARRY has several adjustable components to operate properly, a derotator, a chopper, mixer bias suppliers, LO filters, a SSB filter, a synthesizer, a tripler, a YIG oscillator, and YIG control unit. An old DOS-based PC to tune the receiver was replaced with a new Window-based one, which we will call front-end PC (PPC) hereafter. We have to develop control programs working on the new PPC to automatically tune the receiver and communicate with Modcomp, the observation control computer of the TRAO system.

Second one is the communication capability of a new spectrometer. In 2004, A new back-end system has been brought from Spacebonne Inc. in USA that consists of 15 correlators and a time generator. The correlator is designed to be managed by a PC on windows XP OS. The peripheral works on USB 1.1. It takes 0.6 seconds for gathering data from 15 correlators. The peripheral should be able to hold data acquisition when the receiver is out of lock or pointing is out of range. However since this function was not supported, the correlator backend could not be used until 2007.

Third problem was that a main control system (Modcomp) has worked over twenty years and has been worse. External peripherals such as magnetic tape driver and unix machine had exhausted. There are only 32 ports of 16 bits DIO board and serial ports on the Modcomp.

Therefore, in order to make full use of the QUARRY, we need to develop (1) the front-end system and (2) the back-end system, and (3) communication methods between the systems and the Modcomp.

In designing such control programs on different OS dealing with devices with different interface, it is crucial how to share time among processors with appropriate priorities. Solutions will be to use real time operating system (RTOS) or OS with similar function. A RTOS like MAX IV that works on the Modcomp is adequate

for controlling and managing hardwares with following precise time exactly (Brewer 1995). Run-time OSs like Windows and linux OS also support time-based environments to control any system. The run-time OS applies kinds of asynchronous timer or manages the system by experimentally measured period (Kang et al. 2005; Kang & Kang 2013).

In section 2.2, we first introduces the hardware structure of the QUARRY systems. Then we describe the development of programs that control the back-end system and the correlators and that transfer data among Modcomp and other devices in section 2.3.

2.2 Hardware structure

There are several computers (Figure 2.1), the Modcomp, a Platform PC (PPC), one back-end PC (BPC), fifteen correlator control PCs (CPC), and data acquisition server (DAS). PPC is replaced with new one and its software is revised to control peripherals at front-end system. BPC, 15 CPCs, 15 correlators, and a TG have been installed for the QUARRY. A DIO divider interlink the BPC with 15 CPCs simultaneously. Fig 2.2 shows a block-diagram of communication connections of the TRAO control system. We introduce the hardwares with newly installed interfaces as follow.

2.2.1 Modcomp

The Modcomp is made by Modcomp Inc., and its model name is Class II/95. Its OS is an RTOS called Max IV. The OS provides pre-emptive priority on processes. It consists of several boards, a CPU, a 2 MB memory, a DIO management, and a serial support board. There are 32 pairs of input and output ports of 16 bits at the end of DIO part.

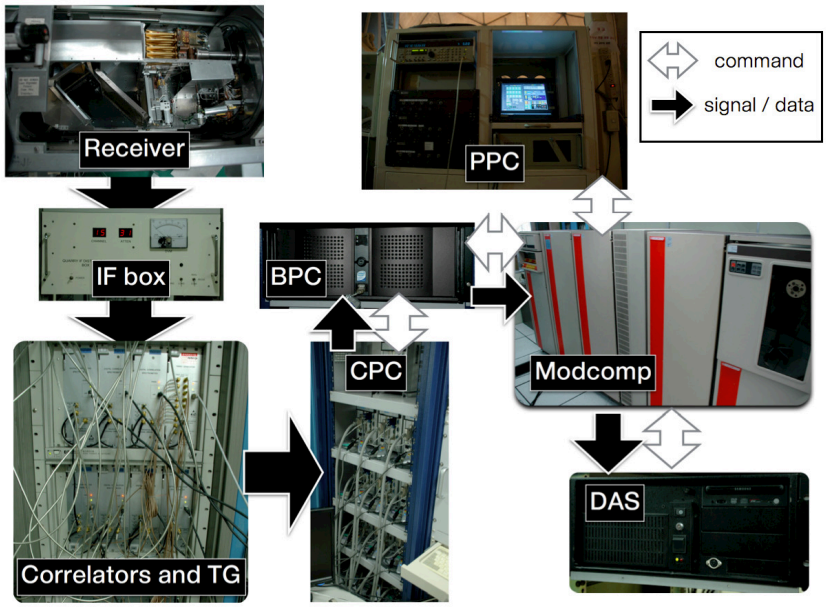

Figure 2.1: A picture of the TRAO hardware organization. White arrows indicate command flows, and black arrows describe how the signal and data flow.

We make several connections to/from other hardwares with the Modcomp. The PPC is connected with a pair of DIO port and a serial port. The pair of DIO port is used for responding current PPC status to the Modcomp, and the serial port is applied to send commands from the Modcomp. The BPC is connected with the Modcomp via 2 input ports and one output port. The pair of DIO port is utilized to transfer commands, and the other input port is attached to carry data by a Direct Memory Access (DMA) method. The DAS is linked with the Modcomp via four serial ports and three DIO ports. The DMA method is also adopted to export observed data to others.

Since in the course of developing the system, several mixers are broken, we rearranged 3X5 array to 3X3 array with a spacing of 2 arcmins. A BIGMAP code, one of the observation program, was edited to manage the new 3X3 array (Fig 2.3).

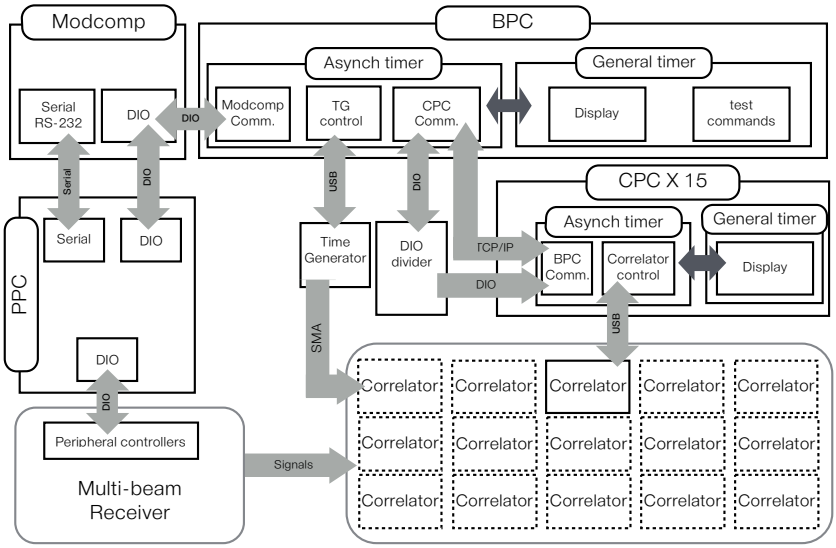

Figure 2.2: A block-diagram of communication connections of the TRAO control system

Also, the Modcomp DIO board was timeworn with serious noise (Figure 2.4). New one is substituted to improve the signal (Choi & Kang 2009) (Figure 2.5).

2.2.2 Platform PC (PPC)

An industrial PC substitutes an obsolete DOS PC. A Single Board Computer of PCI Industrial Computer Manufacturers Group 1.0 is adopted to support current several ISA cards. The PPC is located at the receiver platform and a main role of the PPC is to control and monitor frond-end system. It communicates with a digital interface box to control a YIG and its controller, Mixer bias suppliers, a synthesizer, a tripler, a dewar de-rotater, and a chopper. The PPC orders LO filters and a SSB via three Digital Motor Control (DMC) cards. A synthesizer is connected with the PPC via General Purpose Interface Bus (Figure 2.6).

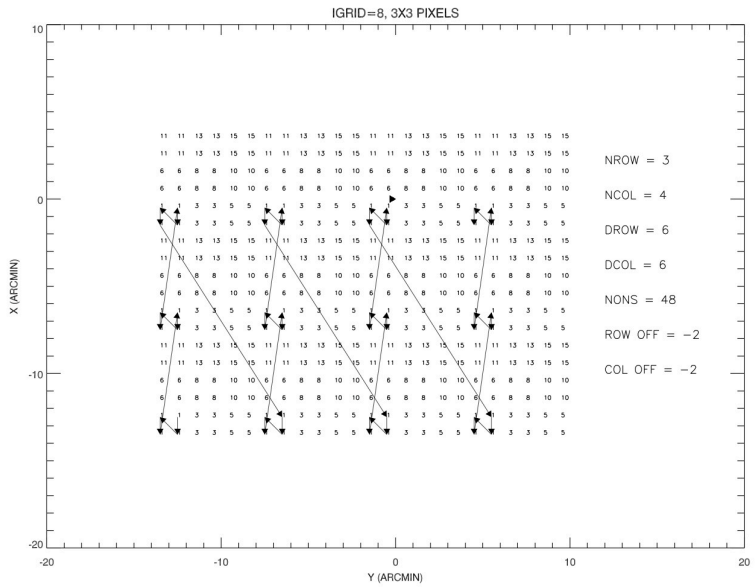

Figure 2.3: A simulation result of the new BIGMAP mode

A PPC program was developed with the National Instruments (NI) Labwindows ™/CVI from National Instruments Inc. on Windows XP OS already. Partial functions of moving individual instruments worked, but managing a YIG and a YIG controller, and tuning frequency were failed (Figure 2.7). We revise the programs with non-blocking programming (see Section 2.3.1).

The front-end system needs to be stand-by before any observation, and changes situations sometimes. There are one serial port for commands of the Modcomp and one DIO port for the PPC status notification. As a tuning command of frequency, a SSB filter position, and a dewar rotation angle are carried on the serial port to the PPC. The response of the lock and dewar status are answered by the DIO port. The Modcomp waits until the bit turn on again.

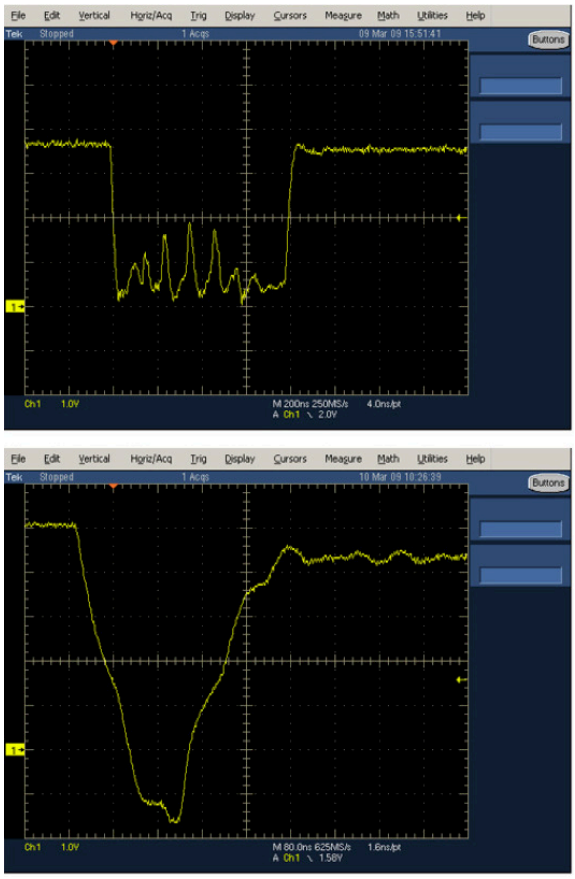

Figure 2.4: Noisy signals on the old Modcomp DIO board

2.2.3 Backend management PC (BPC)

A BPC controls back-end system. It sets observation interval and command integration to the TG. It collects each data from CPCs, and give them to the Modcomp. The BPC of industrial type runs Windows XP OS. Back-end control program on the BPC is coded with the NI Labwindows^{TM}/CVI also (Figure 2.8). It is connected with the Modcomp, the TG, the IF box, and the CPCs. The TG can be managed via the USB 1.1 mode. The BPC communicates with CPCs via DIO and ethernet. Between the BPC and CPCs, there is a DIO divider (see section 2.2.8). SCSI cable

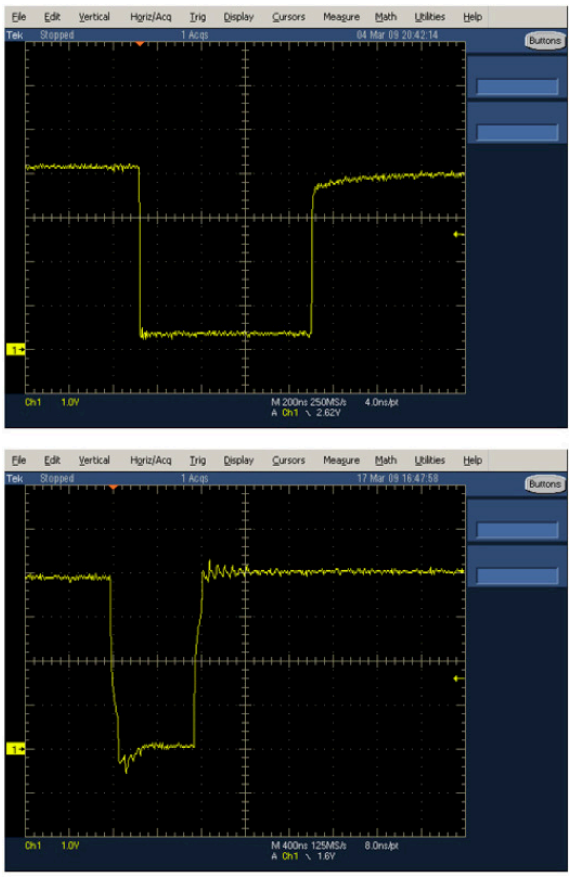

Figure 2.5: Clean signals on the new Modcomp DIO board

that is customized to transfer signals at differential mode connects the BPC with the Modcomp to carry stable data and command fast. The IF box that converts center frequency of the IF and attenuates its power is linked with the BPC via other DIO cable. A control window on the BPC program is supported for user to manage the IF box (Figure 2.9).

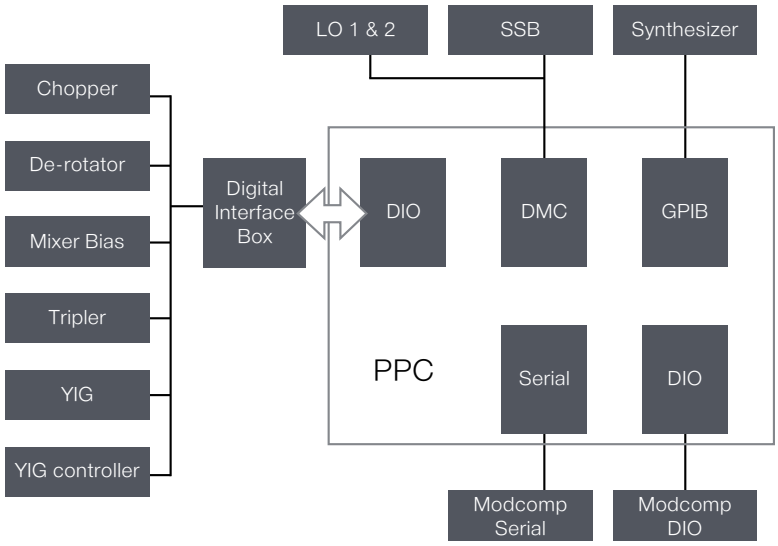

Figure 2.6: A interface diagram of the PPC

2.2.4 CPC

There are 15 CPCs. It was a hard problem to acquire data from 15 correlators via USB 1.1. A firmware inside the correlator supports 64 Bytes per 1 ms. It takes 32 ms to get a data from a correlator, and 480 ms to receive data from all correlators. By the way, integration process can not be hold at bad condition of pointing error, lock status or and so on. It was necessary to minimize the acquisition period to decrease time loss. Moreover, previous CPC program used general timer and blocking programming. It could not guarantee even the speed of 64 Bytes per 1 ms. We reconstruct a PPC program with asynchronous timer and non-blocking programming (see section 2.3.2)

The CPCs run on Windows XP, and they were purchased from Advantech Technologies Inc. The model is fan-less type and supports up to 3 slots (2 PCI slots and 1 PCIe slot). Each CPCs are linked with fifteen correlators via USB 1.1 mode,

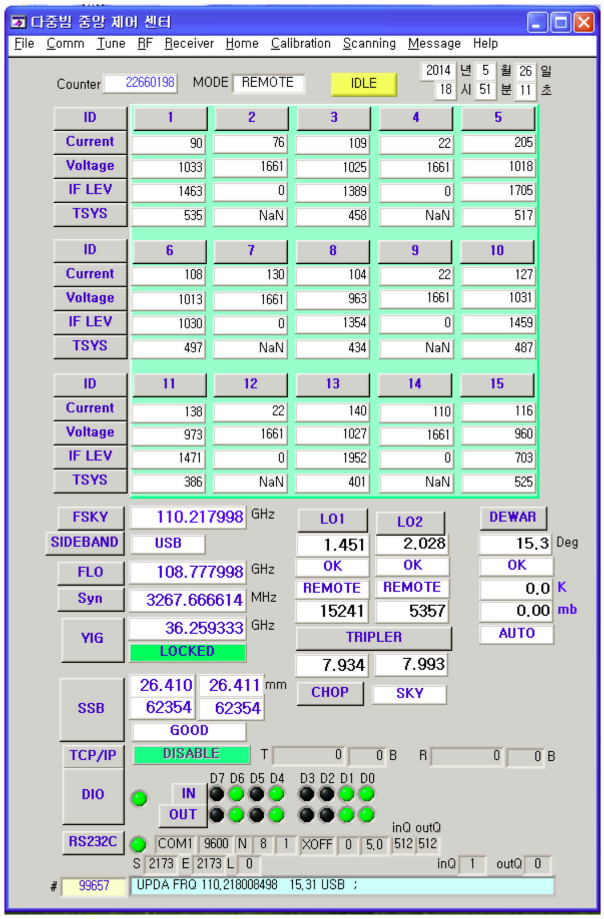

Figure 2.7: A capture of the PPC program

individually. A USB hub is adopted to minimize a USB communication latency. The hub conducts some parts of USB protocols that is proceeded by software when the hub is not connected. It can secure the 32 ms time on the Windows XP. When it is not attached, it takes more than 60 ms to get a data (Kang et al. 2007). One

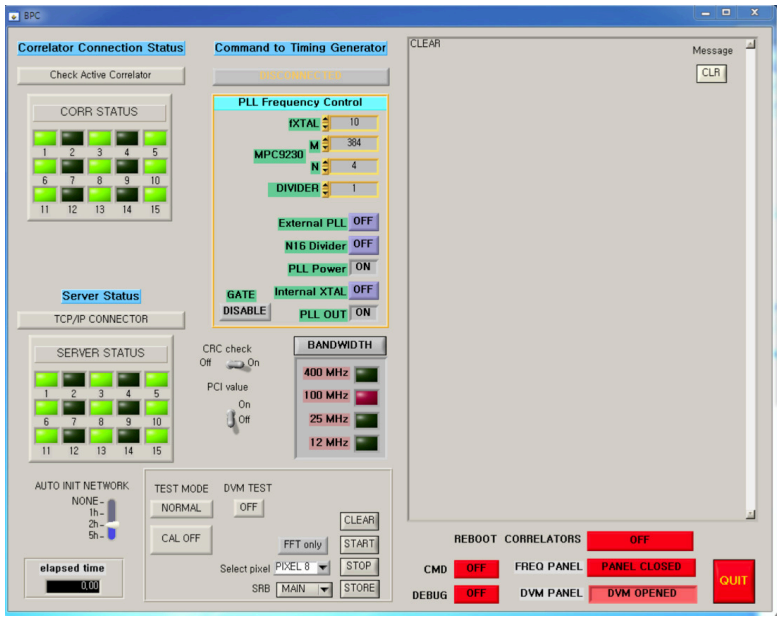

Figure 2.8: A BPC program

DIO card connects with the BPC. Input and output peripherals that consist of a monitor, a keyboard, and a mouse, are attached with KVM switch that connects the keyboard, the video and the mouse with several PCs. A CPC program is made with the NI Labwindows^{TM}/CVI using an asynchronous timer of 1 ms period (Figure 2.10). Reduced spectrum can be seen at a additional window (Figure 2.11).

2.2.5 Data Acquisition Server (DAS)

We install a new industrial PC running linux. It receives observation data from the Modcomp and store them on its local hard disk. There are four serial ports, two digital output ports, and one digital input port for connection with the Modcomp. Three serial ports handle terminals for managements, and the other is used for time synchronization with the network time protocol (NTP). The digital input port is used to receive the observation data from the Modcomp using the DMA method and

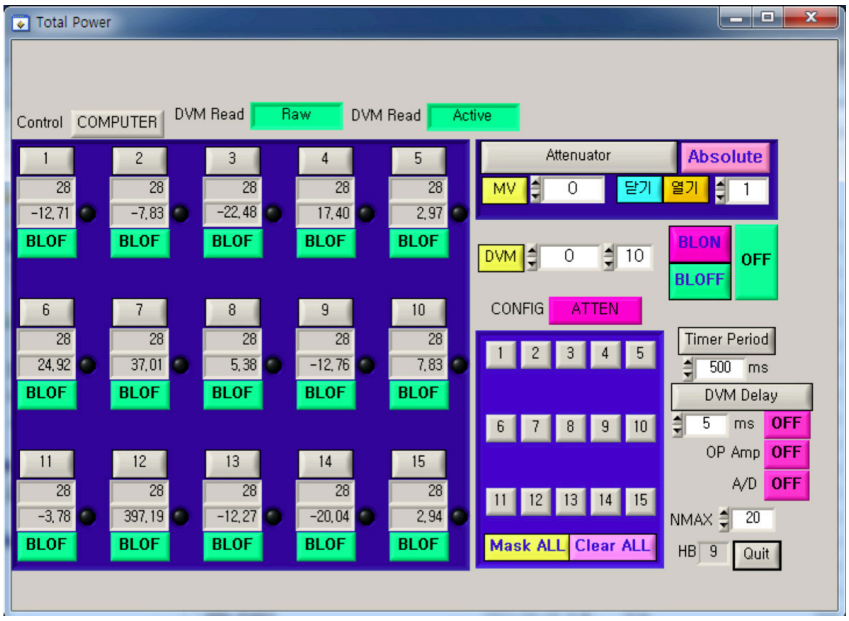

Figure 2.9: A IF box control window. It opens when DVM button is pushed on the BPC program.

the one pair of the DIO ports is used to transfer commands between the Modcomp and the DAS.

The DAS serves various advanced observation environments. Formerly the Modcomp had been accessed just by a console terminal and exported data via a magnetic tape and a unix machine that were obsolete. The DAS runs instead of the instruments. A user can access the Modcomp via the DAS. More details are introduced in section 2.3.2.

2.2.6 Correlator

Model name is SP500S512VXI, a digital autocorrelation spectrometer instrument. It computes the auto-correlation function of an analog input signal. The lag data is carried on the CPC. The CPC performs a fast-Fourier transform function. It includes

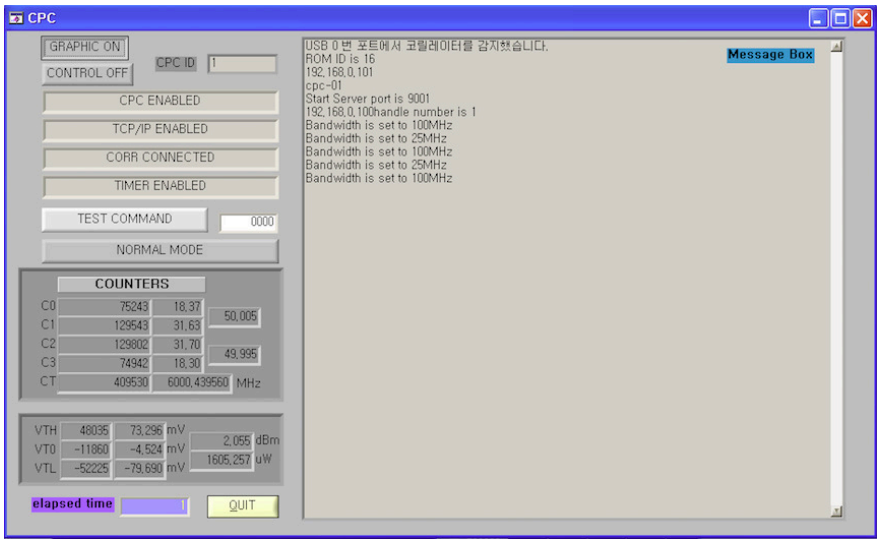

Figure 2.10: A CPC program

4 band pass filter (BPF), 12 MHz, 25 MHz, 100 MHz, and 400 MHz. The BPF can be selectable by command via USB. Descriptions of the BPF is in table 2.1. The power of the analog input should be between -10 dBm to 0 dBm. The central frequency of the IF is customized at 660 MHz.

2.2.7 Time generator (TG)

Spectrometer system consists of a TG and fifteen correlators. The TG provides synchronous integration times and clock signal for correlators. A 32-bit timer is implemented to provide precise integration times. An included clock generator can provide signals with frequency ranging from 50 MHz to 800 MHz, and the signal can be modified from 3.125 MHz to 800 MHz using a dividing circuit. It has on the front panel 15 timing outputs for correlators. External reference clock can be connected. It is installed on VXI slot with the correlators.

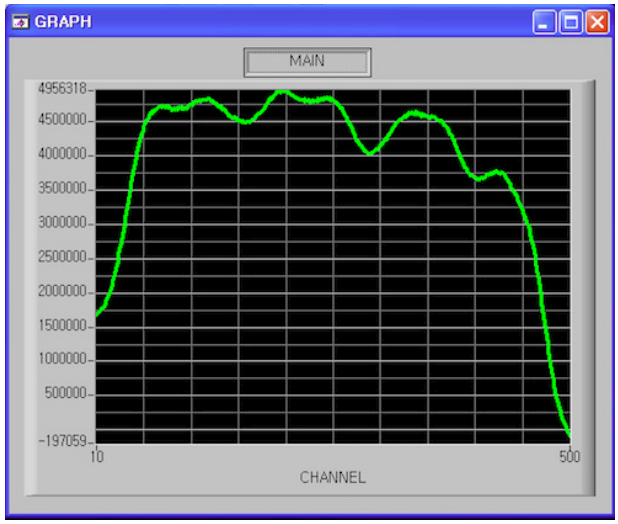

Figure 2.11: A spectrum window. It opens when a GRAPHIC button is pushed on the CPC program.

The integration time sets via USB connection. Only a start command is supported. The BPC sets the time and orders to start. The TG responds a dump signal when the integration ends. More detail things are described at section 2.3.2.

2.2.8 DIO divider

The BPC has to send a command to several CPCs at once, and receive responses from them, promptly. The DIO divider casts a command to fifteen CPCs, and collecting

Table 2.1: Specification of Bandwidths of Correlator

Band (MHz)	Sample Freq. (MHz)	Resolution (KHz)	Effective Band. (CHs)	Center Freq. (MHz)
12	15.9036	31.062	386	659.9994
25	32.195	62.9	396	659.9975
100	120	234.4	427	660
400	440	859.4	465	660

each one bits of the CPC responses (Kang et al. 2007). There are 4 input and 1 output ports of 16 bits. The output port transfers BPC commands, and the others input ports carry CPC responses. Maximum 4 bits of response from one CPC is possible. (Figure 2.12)

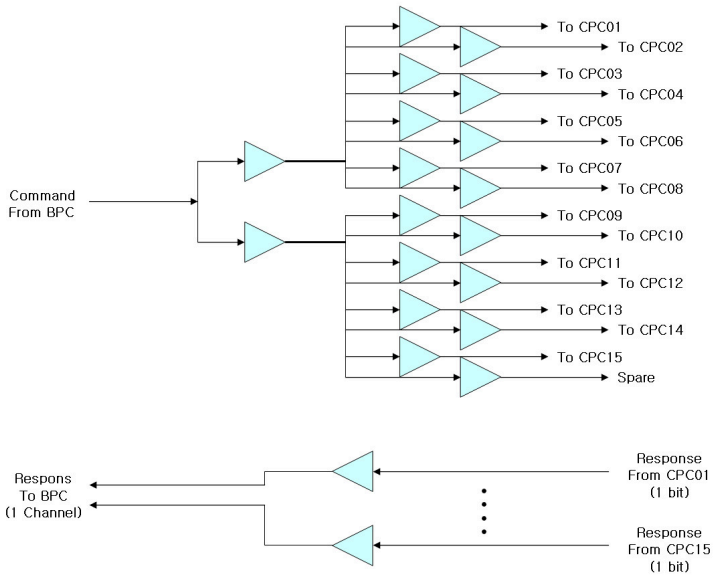

Figure 2.12: A schematic of the DIO divider.

2.3 Details on the control system

In this section, we describe a basics of programming for the hardwares but not for the Modcomp to control effectively (section 2.3.1), and introduce the connection details among the systems (section 2.3.2). For this we had hardwares the QUARRY and the spectrometer ready. For external connections, the Modcomp uses the DMA method to transfer data. Serial communications between the Modcomp and the DAS are adopted to get a time and date and to utilize the observation system easily.

2.3.1 Concepts of system programming

System programming needs to perform accessing external peripherals and internal calculations simultaneously. A blocking programming is general method for normal calculation by writing commands in order. However it is difficult with this method to communicate with complex peripherals. This section explains how to make system programming of front-end and back-end system on Windows OS mainly.

Run-time vs Real-time

Widely used operating systems such as windows, linux and unix are run-time operating systems which are adequate to support multiple users. Priorities for general input peripherals, such as a keyboard and a mouse, are reserved by interrupts and have high priority. Displaying process has also high priority. A kernel inside the OS makes and manages several virtual memories that are volatile and independent. The kernel consumes some times on attaching a memory and accompanying peripherals on running process. The currently running process has an high priority. For example, when a web browser opens, the kernel secures a virtual memory for the web browser and arranges accompanying modules, java, active-X, and so on. The kernel yields the authority when the process is ended or stopped by itself.

In RTOS, We assign priorities to all tasks and then CPU time is assigned to the tasks with higher priority. If there is an higher priority task to be run, the RTOS kernel runs it by holding the lower priority task. RTOS does not support a virtual memory and independent memory areas for scheduled tasks. This allow the kernel to switch to memory for new task with very low latency. Therefore, RTOS can guarantee precise real-time operation for tasks of high priority.

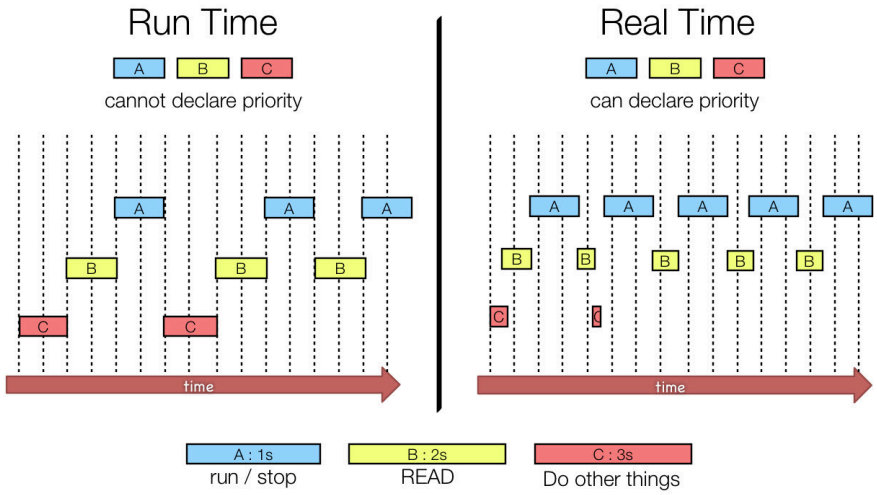

Figure 2.13: A flowchart of three programs on run-time OS (left) and real-time OS (right)

Fig 2.13 is an example of a comparison between the OSs. A, B, and C represent three independent processes with different priorities in order. And they runs every 1, 2, and 3 s, individually. For example, the A is a process of highest priority that controls antenna motors, the B process of middle priority plays on reading the positions, and the lowest priority process C is related with user access of putting parameters. On the run-time OS, user can get an authority when the A and the B

are hold. The authority is passed to the B for reading current values. Again, user checks and puts some parameters after the A process is ended. The A process may not run within 1 s. As the C process calls the B process, the A process have to wait for long time, sometimes. This kind of unexpected delay in operation can result in large tracking error. To avoid this undesired error, programmer have to make a code with an estimate holding time.

On the other hand, the RTOS can manages the A process to run every 1 s exactly. The B process can be executed next to the A. If the A process and the B process take much times, the C process does not have a time to run. The RTOS preserves the movement of the antenna in this way.

Here is another example. On the run-time OS, control functions are written as follows, normally.

```
out_command(board id, output port, value);  //send a value to output port
delay or sleep;                             //wait for the command is accomplished
in_command(board id, input port, value);    //read a value from input port
delay or sleep;                             //wait for the command is accomplished
```

Because the upper code has the authority itself, the functions of out_command and in_command are delayed. Therefore the delay command makes the authority shift to the command functions. But on the RTOS, the code is more simple as below.

```
out_command(board id, output port, value);  //send a value to output port
in_command(board id, input port, value);    //read a value from input port
```

The out_command and in_command have higher priorities on the OS. Therefore,

the command functions run immediately. This system provides programmers with favorable environments for designing control programs.

General timer vs asynchronous timer on Windows

Windows OS can imitate the RTOS. As the RTOS runs on a precise timer, the windows OS also supports similar timers. By the way, the windows OS offers multi-processing methods with a general timer, basically. The multi-processing technique is effective to a normal operation, but not to a system programming. It is not guaranteed for the process to run exactly with the general timer. Therefore a thread function of Windows XP is adopted. On the Windows XP, the thread can run with a minimum interval of 1 ms. It is also called an asynchronous timer on the NI Labwindows^{TM}/CVI.

We have compared accuracy of the general timer and the synchronous timer. A test system consists of an intel core2 6400 (2.13 GHz) CPU and 2 GB memory. The NI Labwindows^{TM}/CVI is utilized to make an example. It draws a sign curve at every 10 ms by the two timer. Fig 2.14 represents results of the general timer, and fig 2.15 displays results of the asynchronous timer. Table 2.2 summarizes the results. With the general timer, other conditions or interrupt give a critical effect on the work of drawing the sign curve. On the other hand, the asynchronous timer offers more stable authority.

Concepts of programming on the run-time OS

There are two types of programming methods, blocking and non-blocking (Figure 2.16). The blocking method keeps the authority and holds other process. It can be a good solution when managing just one instrument. If a system just handle a simple device, the blocking programming method makes a program react synchronously. By the way, the non-blocking method checks a status and returns the authority to

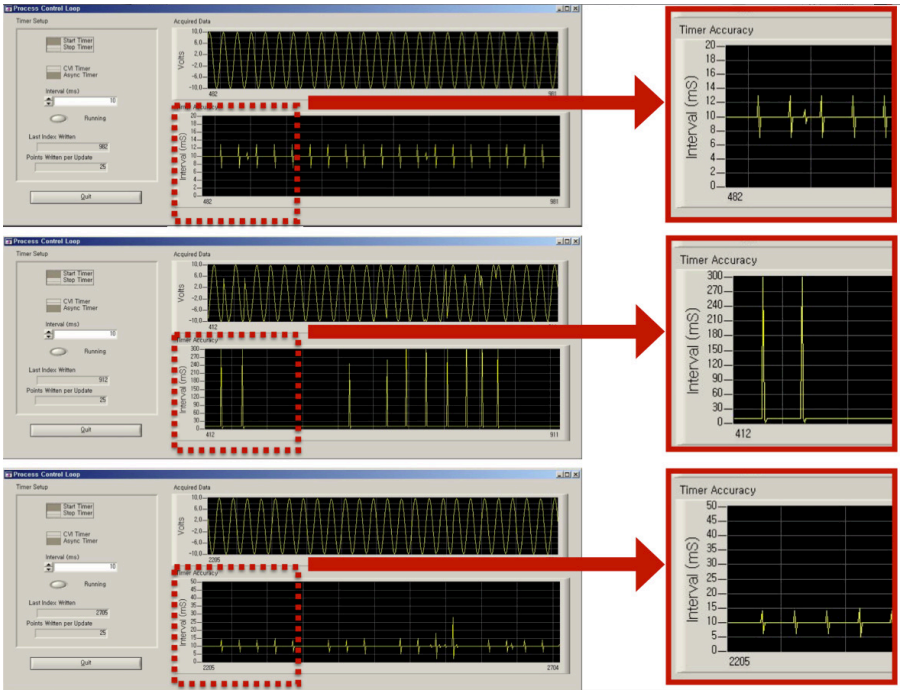

Figure 2.14: A drawing sign curve test at 10 ms by general timer : conditions of (Upper) normal, (middle) dragging a mouse, (bottom) searching a folder

Table 2.2: A result of two timers on several conditions

Timer	Condition	Max. error (ms)
General	Normal	13
	dragging a mouse	300
	searching a folder	28
Asynchronous	Normal	1
	dragging a mouse	1
	searching a folder	1

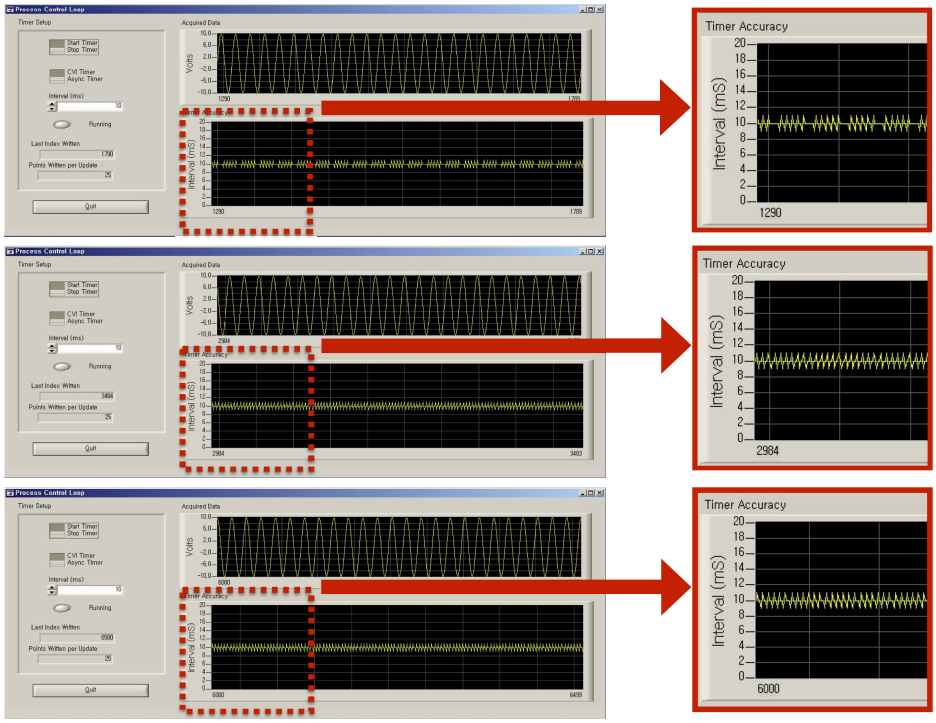

Figure 2.15: A drawing sign curve test at 10 ms by asynchronous timer : conditions of (Upper) normal, (middle) dragging a mouse, (bottom) searching a folder

other process. It allows multiple process to run fairly and stably. Non-blocking programming can not give synchronous response. It is up to a fine timer that manage a instrument rapidly. Run-time OS supports multiple process environment. Unexpectedly, the blocking programming method on Run-time OS can not give authority to holding process. It is shown in previous section of 2.3.1 that even a general timer can not be assured to execute regularly.

To adopt the non-blocking method, the PPC, BPC, CPC, and DAS run their own timer functions. The DAS on linux OS uses a general timer of the sleep function with loops. The PPC applies a general timer of a 100 ms interval. The BPC and CPC run asynchronous timer at every 1 ms. On the BPC and CPC, global structures are used in common, but local structures are locked in asynchronous timer function. The local values in the asynchronous timer function can be transferred by thread commands to the global structures. The usages of the asynchronous timer and the transmission via thread commands are as follows.

- Example : The usage of asynchronous timer

```
#define MS_DELAY 0.001        //s unit
int StartAsyncReadMODCOMPTimer(void)
{
SetTimeOfLastCall(0);
g_timerId = NewAsyncTimer(MS_DELAY, -1, 1, MODCOMPTimerCallback,
NULL);
if(g_timerId< 0)
{
MessagePopup("MODCOMP Async Timer","Error creating Asynchronous
Timer!!");
```

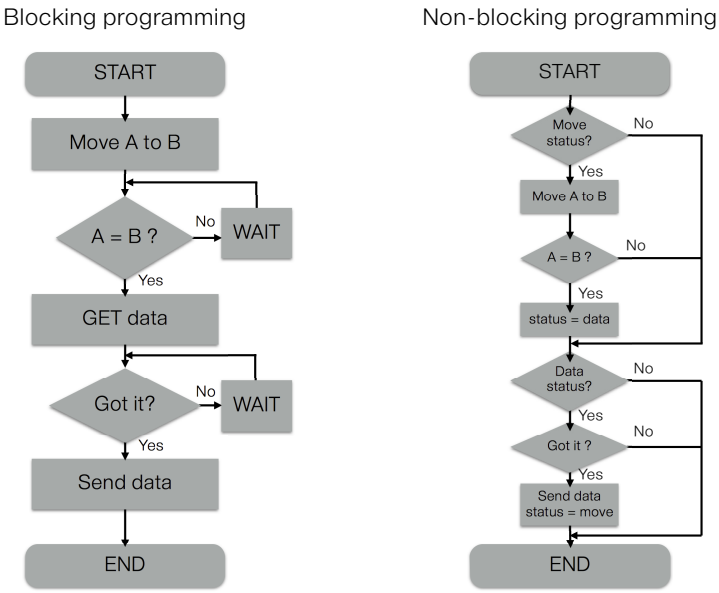

Figure 2.16: Two flowcharts of blocking (left) and non-blocking (right) programming.

```
return -1;
}
return g_timerId;
}

int CVICALLBACK MODCOMPTimerCallback (int reserved, int theTimerId,
int event, void *callbackData, int eventData1, int eventData2)
{
double currentTime = 0.0;
double deltaTime = 0.0;

int err=0;
```

```
if ((double*)eventData1)
currentTime = *((double*)eventData1);
if ((double*)eventData2)
deltaTime = *((double*)eventData2);
if (event == EVENT_TIMER_TICK)
err = DoWorkForMODCOMP ((int)(currentTime * 1000));
if(err) {
CloseThreads();
return err;
}

if (event == EVENT_DISCARD)
g_timerId = 0;
return 0;
}
```

• Example : Transmission of command by thread functions

```
int CreateThreads(void)
{
/* Create Thread-Safe Queues to transfer data between threads */
if (CmtNewTSQ ( MODCOMP_QUEUE_SIZE, sizeof(int),
OPT_TSQ_AUTO_FLUSH_ALL, &g_MODCOMPQueueHdl) < 0)
return ERR_INIT;

InitializeTimeOfLastCall();
```

```
return 0;
}

/* A function to call on general timer environment */
int BridgeOfWriteWithCommandOfMANUAL(unsigned int cmd)
{
WriteWithCommandOfMANUAL(cmd);

return 0;
}

/* Write on asynchronous timer environment */
static int WriteWithCommandOfMANUAL (unsigned int cmd)
{
unsigned int cmd_bpc[1];

cmd_bpc[0]=cmd;

while(CmtWriteTSQData (g_MODCOMPQueueHdl, cmd_bpc, 1,
TSQ_INFINITE_TIMEOUT,NULL)<0)
{
Delay(0.001);
}
return 0;
}
```

Tuning process on the PPC

In observing mode, the PPC only controls a YIG controller, a SSB filter, and a dewar rotator. But when one want to tune the QUARRY receiver for the observation, the PPC has to manage all of the instruments. The tuning process is displayed at Figure 2.17. The process has an order of YIG control, optimization of filters, and setting best position of mixer bias. A non-blocking method makes the tuning process run stably and quickly.

The YIG control process sets the YIG and the synthesizer on requested values. The YIG controller manages the YIG automatically. It returns a result of the process. When the result gives error, the PPC adjust the YIG again.

The LO filters, SSB, and tripler are controlled after the YIG process. The LO filters and SSB do not have any encoder to notify a current position. After returning home position, number of step pulses are counted according to the requested positions. The LO filters and tripler have to search their best positions for tuning frequency. The PPC controls the instruments and reads mixer currents simultaneously. The position of LO filters and tripler are set at a maximum value of the mixer current.

Finally, mixer bias values are searched by measuring T_{RX}. A chopper changes its on and off status. There is not a sensor to notify the chopper status. Several hundred milliseconds are needed to secure the on and off positions. Mixer bias values are adjusted till the lowest values of the T_{RX} are obtained for each mixers.

We succeed in developing the process to search optimal tuning positions for the instruments rapidly without infinite loops or errors.

2.3.2 Communication between the control programs

We utilize several methods to communicate among the hardwares, general DIO bits, an handshaking method, a RS-232 communication, a TCP/IP socket, and a DMA

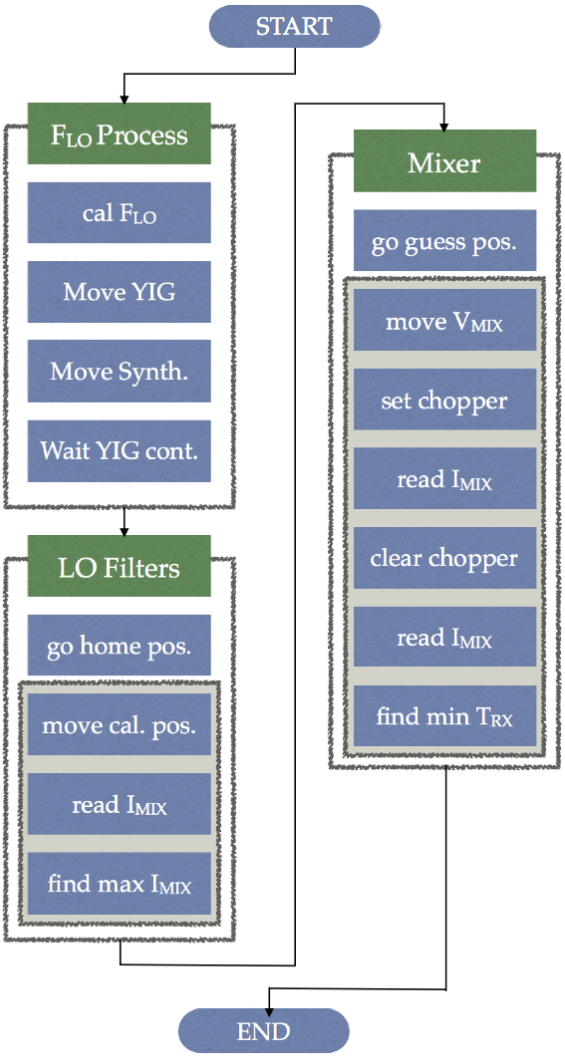

Figure 2.17: A flowchart of tuning process on the PPC

method. Process of data acquisition at back-end system, especially, is described here. the DMA method will be talked at a separated session.

Process of data acquisition

The data acquisition process mainly work on the BPC and CPC. Programs in the BPC and CPC utilize asynchronous timer to manage correlators and a TG. In case of the BPC, asynchronous timer is utilized to control the TG and to talk with the Modcomp and the CPCs. The CPC uses the asynchronous timer to communicate with the correlator and the BPC. Commands are carried via the DIO lines quickly, and data are transferred by the TCP/IP socket. On the DIO line, there is a multiple handshake method. The BPC sends commands continuously - clear buffer, shift buffer, and send data, in order. All CPCs respond to the commands by each one output bit. Each value of the output bit represents the identify of CPC. The DIO divider collects the bits from the 15 CPCs and carries to the BPC. After confirming the value, the BPC sends next commands. Masquerading method is used to support many commands, and command bit list is on table 2.3.

The BPC send a 50 ms integration time to the TG via the USB line at first, and makes the TG start the integration. Because the BPC can not make the TG pause or stop, it monitors the TG at every 1 ms. When the TG notifies an end of the integration via the USB line with a dump signal, the BPC sends an acquisition command to specified CPCs via a DIO divider. Data from the correlator has 512 channels of 32-bits (2 KB). A firmware in the correlator has a transfer speed of 64 Bytes per 1 ms (a maximum payload on USB 1.1). Totally, it takes 32 ms from one correlator to the CPC. Normally, the transferred quantity can be increased as data buffer increase. But a current firmware in the CPC does not set sufficient data buffer. There is a time loss at the ideal integration period of 50 ms. As the USB permits minimum access interval of 1 ms, communications between the BPC and TG creates

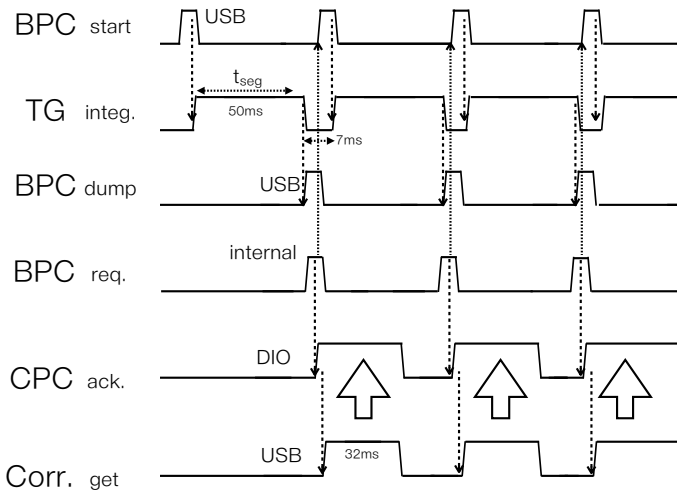

Figure 2.18: A flowchart of the integration communication

several milliseconds delay. A dump command from the TG has to be transferred to the CPC before another integration starts via the BPC. Consequently, we obtain the integration period of 57 ms. Fig 2.18 displays a flowchart of the acquisition sequence.

The Modcomp to the BPC

There are two timers, an asynchronous timer and a general timer on the BPC. The former communicates with the Modcomp, TG and CPCs, and the latter updates current status and permits input commands from a manager. The asynchronous timer operates at every 1 ms. Modcomp utilizes two input ports and one output port to link with the BPC. One pair of the DIO port is adopted to transfer commands between them. The bit assignments are listed on table 2.4.

For a semi-handshaking mode, 0X8000 is used as a request signal. The Modcomp sends signals at every 50 ms (Brewer 1995), and the BPC checks the signals at every

Table 2.3. Command bit list between BPC and CPC

Command	Bit	ETC.
BIT_DUMP	0X0001	
BIT_BAD	0X0002	
BIT_SRC1	0X0004	01B :MAIN, 10B : REF, 11B : BLANK
BIT_SRC2	0X0008	
BIT_CLR_MAIN	0X0010	
BIT_CLR_REF	0X0020	
BIT_CLR_BUF1	0X0040	Temp. of MAIN BUF and Clear COUNTER
BIT_CLR_BUF2	0X0080	Temp. of REF BUF
BIT_ADD_MAIN	0X0100	
BIT_ADD_REF	0X0200	
BIT_ADD_BLANK	0X0400	
BIT_CONTINUUM	0X0800	
BIT_DUMP_CNT	0X1000	
BIT_THRESHOLD	0X2000	
BIT_SET_CORR	0X4000	
BIT_REQ	0X8000	

1 ms. The BPC just transfers error messages and does not respond an acknowledge signal to activate fast. A command list for the BPC is on table 2.5

The Modcomp runs at internal clock of 50 ms, and orders for BPC to send data. The BPC collects all data, and carries to the Modcomp. The BPC uses the DMA method with Cyclic Redundancy Check (CRC) to send data. When a CRC error occurs, the Modcomp reorders the data.

Table 2.4: Bit assignments between the Modcomp and the BPC

The Modcomp to the BPC		
BITS	0 - 12	Commands*
BIT	14	Integration Hold
BIT	15	Command Request
BPC to Modcomp		
BITS	0 -3	Error Code
BITS	4 - 7	Error Location
BITS	8 - 11	Correlator Number
BIT	13	Correlator Driver Busy
BIT	15	Transfer Initiate

*Refer the commands to table 2.5

Table 2.5. Command list between Modcomp and BPC

BIT	Descriptions	activated PC
0100	CLEAR CORRELATOR	CPC
	CLEAR BUFFERS 1 AND 2	CPC
	CLEAR MAINBUF AND REFBUF	CPC
0100 + NMAINS	CLEAR MAIN DISK BUFFERS 1 TO NMAINS	BPC
	REMEMBER NMAINS	BPC
	FLAGS ON BUF CLEAR, NOW WRITE IT!	BPC
	IF WRITE AT FIRST, PLEASE TURN OFF FLAGS	BPC
	SO, IF THE ADDRESS CALLED AGAIN,ADD DATA NOT WRITE	BPC
0180 + NREFS	CLEAR REFERENCE DISK REGISTERS	BPC
	REMEMBER NREFS	BPC
0200	CLEAR REFBUF	CPC
0200 + NREG	ADD BUFFER 1 TO MAINBUF	CPC
	SEND MAIN BUFFER TO BPC'S HOLD MAIN BUFFER	CPC
	CLEAR BUFFER 1	CPC
	STORE HOLD MAIN BUFFER TO POINTED TO	
	MAIN DISK BUFFER (OLD_NREG)	BPC
	(IF DISK BUFFER'S FLAG ON, WRITE IT AND FLAG OFF,	BPC
	ELSE IF THAT'S FLAG OFF, ADD IT)	BPC
	SET MAIN DISK BUFFER POINTER, OLD_NREG = NREG	BPC
0300	ACCUMULATE DATA IN BLANKING MODE	CPC
0301	ACCUMULATE DATA IN BUFFER 2	CPC
0302	ACCUMULATE DATA IN BUFFER 1	CPC
0303	STOP ACCUMULATING DATA	CPC
	IF(CONT)	BPC
	IF BLANK STOP, SAVE DVMPWR INTO PWRBLANK	BPC
	ELSE IF REF, SAVE DVMPWR INTO PWRREF	BPC
	ELSE IF MAIN, SAVE DVMPWR INTO PWRMAIN	BPC
0304	SEND CURRENT ACCUMULATOR CLOCK SUM	BPC
	(JUST SEND ZERO)	BPC
0401	ADD BUFFER 1 TO MAINBUF	CPC
	ADD BUFFER 2 TO REFBUF	CPC
	CLEAR BUFFERS 1 AND 2	CPC
	SAVE PWRS INTO CONT DISK BUFFER	BPC
	CONT(I) HAS PWRBLK, PWRREF AND PWRMAIN	BPC
	INCREMENT CONTINUUM DATA POINTER	BPC
0402	END BLANKING MEASUREMENT	CPC
	STORE BLANKING OFFSET, PWRBLANK	BPC
0410 + NREFS	ADD BUFFER 2 TO REFBUF	CPC
	SEND REFBUF TO BPC'S HOLD REF BUFFER	CPC
	CLEAR BUFFER 2	CPC
	STORE HOLD REF BUFFER TO POINTED	
	REF DISK BUFFER (OLD_NREFS)	BPC
	(IF DISK BUFFER'S FLAG ON, WRITE IT AND FLAG OFF,	BPC
	ELSE IF THAT'S FLAG OFF, ADD IT)	BPC

Table 2.5 (cont'd)

BIT	Descriptions	activated PC
	SET REF DISK BUFFER POINTER, OLD_NREFS = NREFS	BPC
0500 + JCOR - 1	END SCAN	BPC
	IF(500) THEN	BPC
	ADD BUFFER 1 TO MAIN BUFFER	CPC
	CLEAR BUFFER 1	CPC
	ADD BUFFER 2 TO REF BUFFER 1	CPC
	CLEAR BUFFER 2	CPC
	ENDIF	
	ELSE NEGLECT THEM, JCOR - 1	BPC
	(BPC CONTROLS CPC WHOLE AT ONCE)	
0510 + JCOR - 1	END SCAN	BPC
	IF(510)THEN	BPC
	ADD BUFFER 1 TO MAIN BUFFER	CPC
	CLEAR BUFFER 1	CPC
	ENDIF	
	ELSE NEGLECT THEM, JCOR - 1	BPC
	(BPC CONTROLS CPC WHOLE AT ONCE)	
0520 + JCOR - 1	END SCAN	
	IF(520)THEN	BPC
	ADD BUFFER 2 TO REF BUFFER 1	CPC
	CLEAR BUFFER 2	CPC
	ENDIF	
	ELSE NEGELECT THEM, JCOR - 1	BPC
	(BPC CONTROLS CPC WHOLE AT ONCE)	
0530	END SCAN	BPC
	SEND MAIN BUFFER TO BPC'S HOLD MAIN BUFFER	CPC
	IF REF BUFFER REMAINED, SEND REF BUFFER TO	
	BPC'S HOLD REF BUFFER	CPC
	STORE HOLD MAIN BUFFER IN POINTED TO	
	MAIN DISK BUFFER (OLD_NREG)	BPC
	(IF DISK BUFFER'S FLAG ON, WRITE IT AND FLAG OFF,	BPC
	ELSE IF THAT'S FLAG OFF, ADD IT)	BPC
	STORE HOLD REF BUFFER IN POINTED TO	
	REF DISK BUFFER (OLD_NREFS)	BPC
	(SAME AS MAIN DISK BUFFER, WATCH FLAG ON OR OFF)	BPC
0600 + VAL	SET POWER LEVEL TO VAL	BPC
	RANGE 1 - 127, BUT BPC CONTROLS 0 - 31dB FOR DVM	BPC
0680	SET MAIN THRESHOLDS	CPC
0688 + MODE	SET OBSERVING MODE: 0 = SPECTRAL LINE	BPC
	1 = CONTINUUM	BPC
	2 = CHOPPED CONTINUUM	BPC
	3 = FREQUENCY SWITCHED	BPC
0690 + VAL	SET BANDWIDTH TO VAL, RANGE = 0 - 7	BPC
	0 : 400, 1 : 100, 2 : 25, 3: 12MHZ	BPC

Table 2.5 (cont'd)

BIT	Descriptions	activated PC
	COMMAND SET BW TO CPC	BPC
0800 + JCOR - 1	SEND MAINBUF TO BPC'S HOLD MAIN BUFFER	CPC
	SEND REQUESTED JCOR'S HOLD MAIN BUFFER	BPC
0810 + JCOR - 1	SEND REFBUF TO BPC'S HOLD REF BUFFER	CPC
	SEND REQUESTED JCOR'S HOLD REF BUFFER	BPC
0820 + JCOR - 1	DIVIDE REQUESTED PIXEL IN HOLD MAIN BUFFER	BPC
	BY PIXEL IN HOLD REF BUFFER, SUBTRACT 1	
	SEND REQUESTED PIXEL FROM HOLD MAIN BUFFER	BPC
	TO MODCOMP	
1000 + 16 * (NREG - 1) + JCOR - 1		
	COPY MAIN DISK BUFFER OF NREG TO HOLD MAIN BUFFER	BPC
	CLEAR MAIN DISK BUFFER OF NREG	BPC
	(SET FLAG ON)	BPC
	COPY REF DIS BUFFER NEAR NREG TO HOLD REF BUFFER	BPC

The Modcomp to the DAS

There are two programs on the DAS for talking with the Modcomp. The one is 'spaserv.sh', and the other is 'Timeupdate.sh' (Figure 2.19 & 2.20). The two programs are based on the GNU C and shell codes. The 'spaserv.sh' brings data with the SPA format from the Modcomp. The SPA data file is regenerated at every 1000 scan numbers with other name.

The DAS uses a NTP client. The date and time are transferred to the Modcomp by the serial port. Fig 2.23 shows a synchronized moment between the Modcomp and the NTP timer program of the DAS. We make the Modcomp get the data within 1 ms.

Operators can control the observation program from the DAS via network. We connect three serial ports with three terminals, A02, A38, and A40. A kermit utility of serial communication program is adopted. The A02 is assigned to the observation console (Figure 2.21) and the A38 and the A40 is management terminals (Figure 2.22).

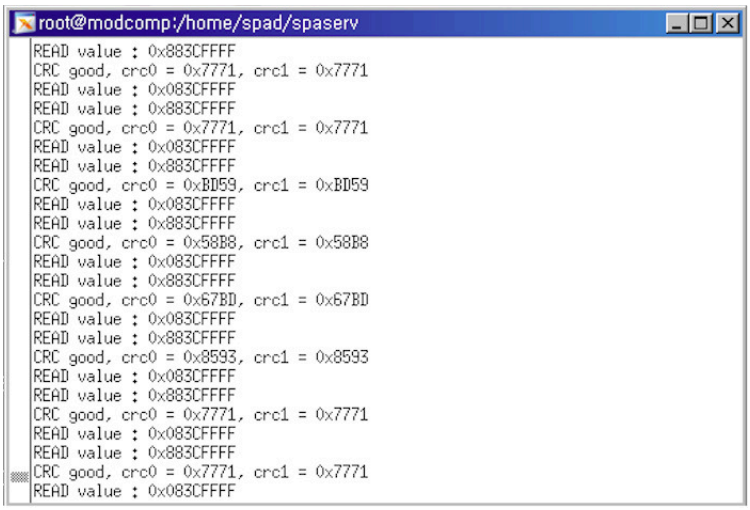

Figure 2.19: A capture of running spaserv.sh. It prints CRC check result after receiving data.

2.3.3 Realization of the DMA method

The QUARRY system makes 15 spectral data at once. It was a difficult problem to carry the data among the systems. A size of a piece of data is 16,384 bits. The Modcomp supports 16 bits input port with a 50 ms period. Normally, the data can be transferred within 51.2 seconds via the one input port. The general DIO method can not give reliable time. We found that the PCI-7200 DIO card can perform the DMA method, and the Modcomp originally uses the DMA method to access the DIO board.

There are two signals of a request (REQ) and a acknowledgement (ACK). A receiver gives a REQ to a sender for getting a data. The sender responds a ACK to notify that the data is ready. The data is carried after the receiver checks the ACK. At this time, the REQ goes down. The DIO board of the Modcomp uses 22 pins,

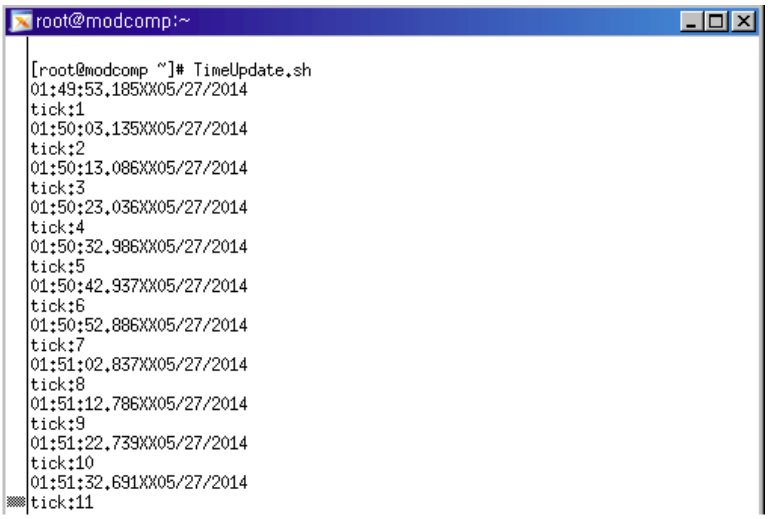

Figure 2.20: A capture of running Timeupdate.sh. It prints transferred time and date.

the 16 pins are used to carry a data, other 5 pins are adopted to select a address, and the other one pin plays a strobe signal. Normally, the strobe is the same with a REQ on the output board and a ACK on the input board. Figure 2.24 is an example of transmission of the DMA method. The blue line is the ACK of the BPC, and the yellow is the REQ of the Modcomp. At first stage, the BPC has uploaded a data on transfer line. A high status of ACK means that a piece of data is ready. At second stage, the Modcomp make the REQ low and take the data. At the end of the second stage, the REQ returns high. The REQ flip makes the BPC understand that the Modcomp has already taken the data. The BPC makes the ACK flop and loads next data to the line. After loading the data, the ACK returns high.

One signal takes 4 us per 16 bits. A time to transfer a piece of data is about 4 ms. Because the Modcomp runs at 50 ms, the process can run in normal condition. But sometimes, the data can be broken for the fast transmission. The CRC-16 is adopted

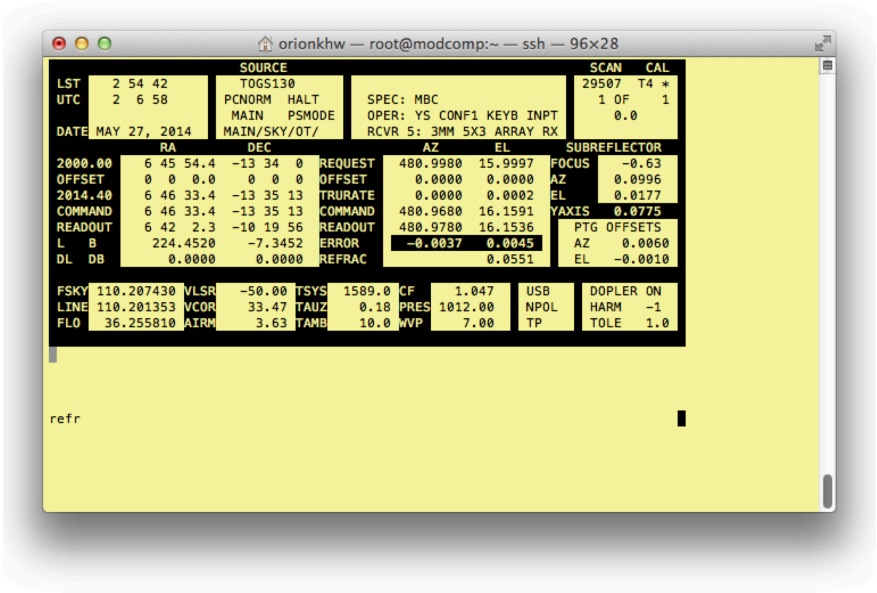

Figure 2.21: A capture of A02 terminal. Users can control the observation program via network.

to verify the data. To do so, 513 channels of 32 bits are sent, and the last channel is a CRC-16 value. The CRC-16 uses a CRC table. A CRC-16 value is matched from the table with sum of 512 channel values. A sender calculates a CRC-16 value and send it to a receiver with a 512 channel data. The receiver calculates a CRC-16 value with sum of the channel values. It verifys the value with received CRC-16 value of 513th channel. The DMA method is used for communications between the BPC and Modcomp and between the Modcomp and DAS.

2.4 Conclusion

We summarize the result of the development of the TRAO control system for the QUARRY.

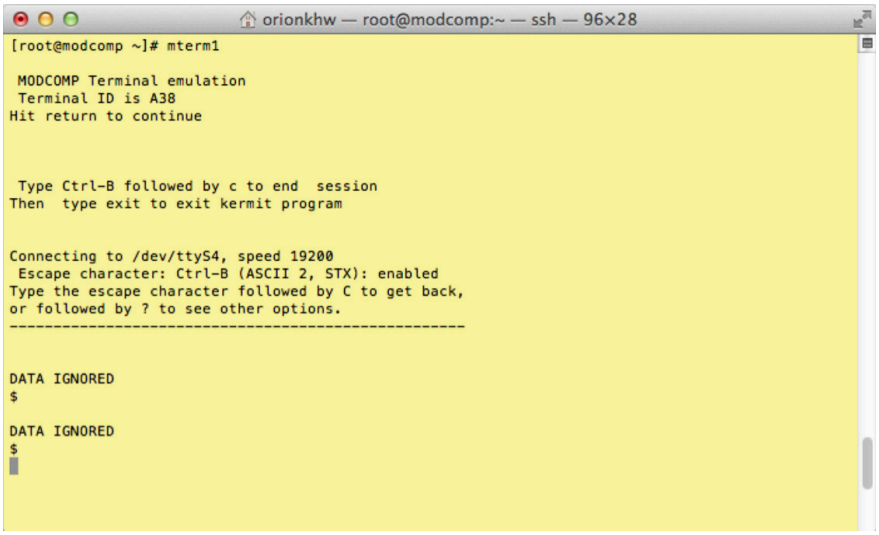

Figure 2.22: A capture of A38 terminal. A manager can handles the Modcomp programs via network.

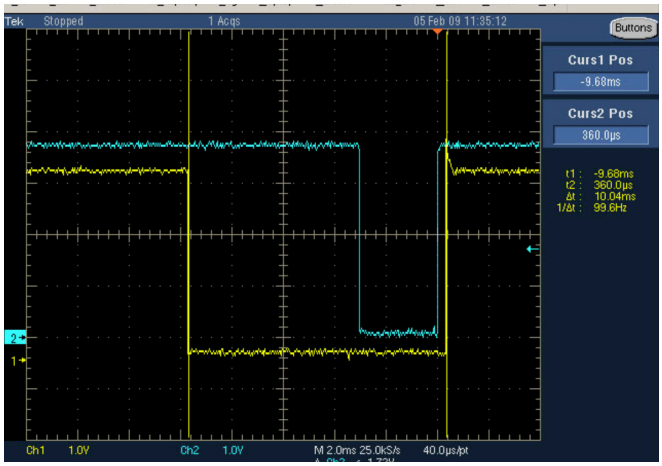

Figure 2.23: A capture of two time values syncing a signal of the Modcomp (yellow) and the DAS (blue)

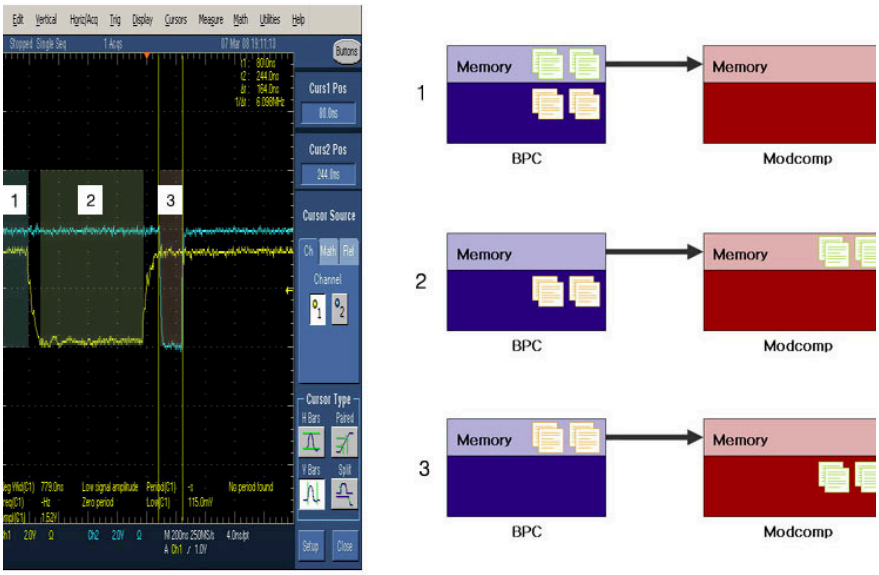

Figure 2.24: A picture of how to carry a data on the DMA method

(1) The PPC can manage instruments to tune the QUARRY in a specified frequency.

(2) The back-end system can control spectrometers with 1 ms asynchronous timer.

(3) The DAS supports advanced observation environment.

(4) The DMA method enables the fast transmissions of the data among the systems.

We successfully have developed the QUARRY system. There were many trials to make interfaces effective and stable on the front-end and back-end systems. An ordeal of short circuits almost close the QUARRY development (Figure 2.25). The Modcomp could be revived by developing the front-end and the back-end systems, and attaching the DAS. The QUARRY has opened in October 2009.

Figure 2.25: A picture of short circuits of the Modcomp system. In 2008, water was overflowed from an troubled air conditioner. The air conditioner was on upper floor from the Modcomp directly. The short circuits made the unix machine and the Modcomp boards breakdown.

References

Brewer, M.K. 1995, Multi-feed Systems for Radio Telescopes ASP Conference Series, 75, 285

Choi, J.-H. & Kang, H. 2009, a local technical memo at the TRAO

Erickson, N.R., Goldsmith, P.F., Novak, G., Grosslein, R.M., Viscuso, P.J., Erickson, R.B., & Predmore, C.R. 1992, IEEE Trans. Microwave Theory Tech, 40, 1

Kang, H., Jung, J.-H., Choi, J.-H., et al. 2007, Technical report of KASI, 07-002-067

Kang, H. & Kang, H. 2013, J. Korea Industrial Information System Soc., 18, 37

Kang, H.W., Byun, D.-Y., & Park, Y.-S. 2005, P. Korean Astron. Soc., 20, 73

Chapter 3

Simultaneous observation of water and class I methanol masers toward class II methanol maser sources

Abstract We present a simultaneous single-dish survey of 22 GHz water maser and 44 GHz and 95 GHz class I methanol masers toward 77 6.7 GHz class II methanol maser sources, which were selected from the Arecibo methanol maser Galactic plane survey (AMGPS) catalog. Water maser emission is detected in 39 (51 %) sources, of which 15 are new detections. Methanol maser emission at 44 GHz and 95 GHz is found in 25 (32 %) and 19 (25 %) sources, of which 21 and 13 sources are newly detected, respectively. We find 4 high-velocity (>30 $\mathrm{km\,s^{-1}}$) water maser sources, including 3 dominant blue- or redshifted outflows. The 95 GHz masers always appear with the 44 GHz maser emission. They are strongly correlated with 44 GHz masers in velocity, flux density, and luminosity, while they are not correlated with either

water or 6.7 GHz class II methanol masers. The average peak flux density ratio of 95 GHz to 44 GHz masers is close to unity, which is two times higher than previous estimates. The flux densities of class I methanol masers are more closely correlated with the associated BGPS core mass than those of water or class II methanol masers. Using the large velocity gradient (LVG) model, we derive the fractional abundance of methanol in the 4.2×10^{-8} to 2.3×10^{-6} range with a median value of $3.3 \pm 2.7\times10^{-7}$, assuming unsaturated class I methanol maser emissions.

3.1 Introduction

Masers are widely recognized as indirect tools for understanding the early stages of massive star formation. H_2O masers are frequently detected in star-forming regions. They are pumped by collisions with neutral particles and appear within accretion disks or outflows (Elitzur et al. 1989; Torrelles et al. 1997; Moscadelli et al. 2006). Furthermore, H_2O masers are detected near young stellar objects (YSOs) regardless of mass, and more massive YSOs tend to have stronger maser emission (Genzel & Downes 1977; Furuya et al. 2003; Bae et al. 2011). Water masers often exhibit variable flux densities and line velocities (Rodriguez et al. 1980; Bae et al. 2011; Choi et al. 2012). Moreover, the maser presents high-velocity features near outflows (Gwinn et al. 1992; Gwinn 1994). Beuther et al. (2002) tried to find a spatial relationship between the water and 6.7 GHz methanol masers. Both maser species are closely associated with the early stages of massive star formation, but no spatial correlations were observed.

CH_3OH maser appears various transition lines. Methanol maser transitions are empirically divided into two groups: class I and class II (Menten 1991). Class I methanol masers such as the $4_{-1}-3_0$ E, 7_0-6_1 A^+, $5_{-1}-4_0$ E, and 8_0-7_1 A^+ lines at 36, 44, 84, and 95 GHz, respectively, are normally detected with the offset from HII regions, infrared sources, OH, and H_2O masers (Plambeck & Menten 1990; Kurtz

et al. 2004). However, class II methanol masers such as the $5_1 - 6_0$ A^+, $2_0 - 3_{-1}$ E, $9_2 - 10_1$ A^+, and $J_0 - J_{-1}$ E lines at 6.7, 12, 23, and 157 GHz, respectively, are found close to other star formation indicators (Walsh et al. 1998). Using a theoretical model, Cragg et al. (1992) inferred that class I methanol masers are pumped by collisions, while class II masers are excited by radiative pumping.

Methanol masers are related with star formation regions. Weak class I methanol masers can be detected in low- and intermediate-mass star forming regions (Kalenskii et al. 2010; Bae et al. 2011). But 6.7 GHz class II methanol maser is only found at massive star formation regions (Breen et al. 2013). Class I methanol masers appear in the interface region of surrounding cloud with outflows or shocks (Plambeck & Wright 1988; Plambeck & Menten 1990; Kurtz et al. 2004; Voronkov et al. 2006, 2014). Val'tts et al. (2000) reported that the peak flux density of 44 GHz maser is about three times higher than that of 95 GHz class I methanol maser. Class II methanol masers, on the other hand, are detected at the early evolutionary phase of massive star formation. Though water and class II maser have different pumping mechanisms, both maser species are associated with the earliest stages of massive star-forming regions (Beuther et al. 2002; Codella et al. 2004). Contrary to water maser, it is ambiguous whether class II masers trace disks or outflows (Norris et al. 1993; Pestalozzi et al. 2004; Walsh et al. 1998; Minier et al. 2000; Dodson et al. 2004).

Slysh et al. (1994) searched for 44 GHz class I methanol maser with 5 to 10 Jy detection limits toward about 250 HII regions and water and 6.7 GHz class II methanol maser sources. Of the 55 detected 44 GHz maser sources, 64 % are related to 6.7 GHz masers. They suggested that class I and class II have anti correlations of velocity and flux density; however, their observations were based on single dish data with no accurate positions and made towards source sample with significant biases. Subsequent more comprehensive studies, such as those by Ellingsen (2005) do not

support the suggestions of Slysh et al.

In this study we report a simultaneous survey of 22 GHz water and 44 GHz and 95 GHz class I methanol masers toward 6.7 GHz class II methanol masers, which were selected from the Arecibo methanol maser Galactic plane survey (AMGPS) catalog (Pandian et al. 2007). The AMGPS covered the inner Galactic region of $35.2^\circ \lesssim l \lesssim 53.7^\circ$ and $|b| \lesssim 0.41^\circ$ with a detection limit of 0.27 Jy (3σ). The properties of the AMGPS sources such as distance, luminosity, and kinetic temperature have been subsequently studied by Pandian et al. (2009, 2011, 2012). The AMGPS sources may represent various status of massive star formation region related with class II, because they were identified by an unbiased survey with low detection limits. We statistically investigate the detection rates of the observed masers and correlations between them. We are particularly interested in the relationship between class I and II methanol masers. Since water and class I methanol masers are both pumped by collision mechanisms, one may expect a significant correlation between them. Chen et al. (2012) recently suggested selection criteria for the Bolocam Galactic Plane Survey (BGPS) clumps with 95 GHz class I methanol maser. We also investigate the validity of these criteria using our data sets.

Section 2 gives the source selection and observation methodology. Section 3 presents the detection statistics, new detections, and short descriptions of some interesting sources. Section 4 describes velocity characteristics, flux densities and luminosities, comparison with the BGPS clump parameters, and methanol column densities and abundances. Section 5 summarizes the main results.

3.2 Source Selection and Observations

3.2.1 Source Selection

We selected 77 sources from the AMGPS catalog of 88 6.7 GHz methanol maser sources. The catalog originally consisted of 86 sources (Pandian et al. 2007), and later 2 new sources (G37.04-0.04 and G49.42+0.32) were added via MERLIN observations (Pandian et al. 2011). Considering the beam size of the telescope at 95 GHz, 33″ (see § 2.2), we excluded 9 sources in two very crowded regions: W49N (G43.15+0.02, G43.16+0.02, G43.17+0.01, G43.17-0.00, and G43.18-0.01) and W51 (G49.47-0.37, G49.48-0.40, G49.49-0.37, and G49.49-0.39). We also rejected G49.42+0.32 due to its proximity to G49.41+0.33 (Pandian et al. 2011), and G41.87-0.10 due to its uncertain coordinates (Pandian et al. 2007). The systemic velocities of the individual sources were taken from the previous molecular line observations (Pandian et al. 2009, 2012). Table 3.3 lists the 77 sources in our sample together with their equatorial coordinates and systemic velocities.

3.2.2 Observations

Using the Korean VLBI Network (KVN) 21 m telescopes, we performed simultaneous surveys of the H_2O $6_{16} - 5_{23}$ (22.23508 GHz), CH_3OH $7_0 - 6_1 A^+$ (44.06943 GHz), and CH_3OH $8_0 - 7_1 A^+$ (95.169463 GHz) masers toward the 77 class II methanol maser sources. The KVN consists of three 21 m telescopes (Kim et al. 2011; Lee et al. 2011). Each telescope is equipped with a multi-frequency receiving system with 22 GHz, 44 GHz, 86 GHz, and 129 GHz bands (Han et al. 2008). We used the telescopes as single dish instruments at the Yonsei and Ulsan sites[1]. Table 3.1 presents the aperture efficiencies, half-power beam widths (HPBWs), and conversion factors of the telescopes. We used the position switching method, and the detection limit

[1]See http://kvn.kasi.re.kr/index.html

was about 1.2 Jy with a three-sigma noise level on the basis of 95 GHz. For calibration, we adopted the standard chopper-wheel method. The pointing and focus were checked every 2−3 hours. The system temperature (T_{sys}) ranges were 70−90 K at 22 GHz, 100−150 K at 44 GHz, and 150−250 K at 95 GHz. The bandwidths were set to 32 MHz for all receivers. The KVN receivers support dual-polarization mode, and the computational backend can process up to four inputs simultaneously (Lee et al. 2011). To approximately equalize the noise levels, we used the single-polarization mode for the 22 GHz and 44 GHz bands and the dual-polarization mode for the 95 GHz band. We conducted grid mapping to assess if the detected maser emission is contaminated by any nearby strong source, because the KVN telescopes are shaped Cassegrain and hence have fairly high first sidelobe levels of about 5 % (Kim et al. 2011; Lee et al. 2011). We avoided cloudy and rainy days. For elevations over 20°, the elevation dependence of the aperture efficiencies is quite flat (Lee et al. 2011). The site averaged pointing accuracies at Q and W bands are 4.9″and 4.2″(Lee et al. 2011; Kim et al. 2011). We also checked the pointing accuracy every 2 or 3 hours during the observations. The complete observation took 18 days during 2011 Nov – 2012 Mar; 15 days were used for maser observations, and the side lobe effects were verified during the last three days. To distinguish side lobe effects, all detected sources were mapped again with 7×7 grid by a half of each FWHMs.

We also observed 4 sources in the ^{13}CO (J=1−0) (110.201353 GHz) line and one of them in the HCO^+ (J=1−0) (89.188523 GHz) line using the Taeduk Radio Astronomy Telescope (TRAO) 14 m telescope in 2014 March 17. These observations aimed to investigate the origin of the water maser features with large velocity offsets (see § 3.3.3). The system temperatures were 560 K at 89 GHz and 760 K at 110 GHz. The main-beam efficiencies of the telescope are 50% and 49% at 89 GHz and 110 GHz, respectively. All the data were reduced and analyzed with the GILDAS/CLASS package and IDL. The bisector method was adopted for the linear regression calcu-

Table 3.1. KVN Antenna Parameters

Site	Frequency (GHz)	Aperture efficiency (%)	HPBW ($''$)	Conversion factor (Jy K^{-1})
Yonsei	22	65	119	12.3
	44	63	62	12.7
	95	48	32	16.6
Ulsan	22	62	120	12.9
	44	62	62	12.9
	95	49	33	16.3

lations (Isobe et al. 1990).

3.3 Results

3.3.1 Detection Rates

We detected maser lines 46 of the 77 sources with a detection limit of 1.2 Jy at 95 GHz. At 22 GHz, 44 GHz, and 95 GHz maser observations, 39 (51 %), 25 (32 %), 19 (25 %) are found, respectively (Table 3.3). Number of sources overlapped at the different transitions are displayed at Figure 3.1. 95 GHz maser always accompanies 44 GHz maser and often (84 %) appears with water maser. Figure number of each spectrum is listed in Table 3.3.

Since the 6.7 GHz maser sources in our sample have a wide range of peak flux densities, 0.13–55.56 Jy and luminosities, $10^{-9} - 10^{-5}\,L_{\odot}$, we investigate the detection rates of the three observed masers along with the flux density and luminosity (Figure 3.2). All three rates tend to increase with the 6.7 GHz maser flux density and luminosity, although the trend is not strong. Ellingsen (2005) also searched

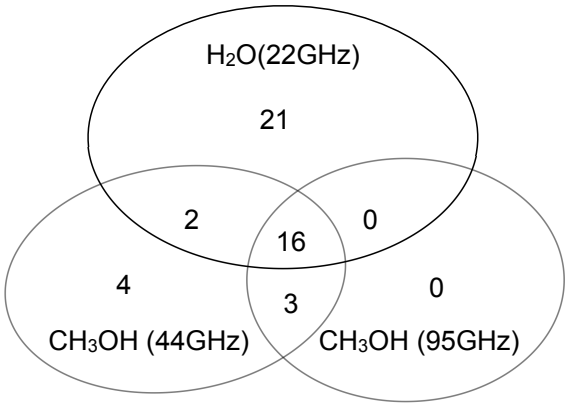

Figure 3.1: Venn diagram displaying the number of sources detected in the three observed maser transitions.

for the 95 GHz maser emission with a flux limit of ∼4 Jy (3σ) toward 66 6.7 GHz methanol maser sources found by previous blind surveys, and detected the emission in 25 sources. The detection rate (38%) is significantly higher than our value (25 %) in spite of considerably poorer sensitivity. This is presumably because their sample contains more bright sources than our sample. The fractions of sources with flux densities ≥10 Jy are about 60% for their sample and about 20% for our sample.

3.3.2 New Maser Sources

Through comparison of our results with those of Palagi et al. (1993); Codella et al. (1994); Han et al. (1998); Forster & Caswell (1999); Valdettaro et al. (2001); Codella et al. (2004); Szymczak et al. (2005); Urquhart et al. (2011), we identify that 15 of our water maser detections are new discoveries using the VizieR service[2] (Ochsenbein et al. 2000). Szymczak et al. (2005) searched for water maser emission

[2]See http://vizier.u-strasbg.fr/viz-bin/VizieR

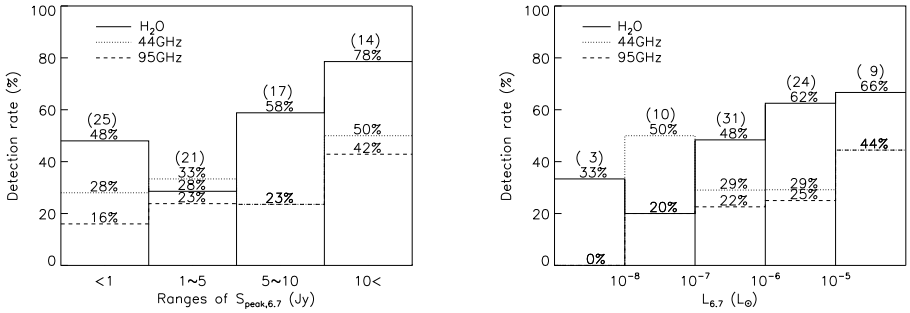

Figure 3.2: Detection rates of 22 GHz water (solid line), 44 GHz (dotted line), and 95 GHz (dashed line) methanol masers as a function of the peak flux of 6.7 GHz class II methanol maser (left) and the luminosity of 6.7 GHz (right). The numbers of 6.7 GHz maser sources are presented in parentheses.

in four sources (G36.70+0.09, G37.02-0.03, G37.04-0.04, G38.03-0.30), but did not detect. This may be due to the different beam size and positions observed. They used the Effelsberg 100 m telescope with an HPBW of 40″ at a root-mean-square (rms) noise level of 0.45 Jy. We observed same positions that 6.7 GHz were detected, and positions of Szymczak et al. (2005) are offset from ours by 27″–87″. It is possible that our detection is from other site for larger beam size of 120″. We may apply the same explanation for the other two sources (G40.28-0.22 and G42.03+0.19) in which no water maser emission was detected by Urquhart et al. (2011) using the GBT 100 m telescope with an rms noise of 0.12 Jy.

To date, there have been few surveys of class I methanol masers. We find that 21 of the 25 detected 44 GHz methanol maser sources are new detections (Kurtz et al. 2004; Cyganowski et al. 2009; Bayandina et al. 2012).

Thirteen of the 19 detected 95 GHz methanol maser sources are new detections from comparison with those of Chen et al. (2011, 2012). Chen et al. (2011, 2012) also used single dish observation with no accurate position of class I maser. Among

the new sources, positions near G37.55+0.19 and G45.49+0.13 have been observed by Chen et al. (2011) using the Mopra 22 m telescope with a 36″ beam size at a detection limit of 1.6 Jy (3σ). Their positions are different from ours by 40″.5 and 33″.3, respectively. Because the KVN beam size at 95 GHz is 33″, the sources are not overlapped.

3.3.3 Notes on Selected Sources

G35.03+0.35, G43.04-0.46, and G45.07+0.13

These source are already known sources at water and 44 GHz class I methanol maser lines. They show variations at water maser line between previous observations and our results. But class I methanol maser seems to have similar velocity position of peak flux density. G35.03+0.35 has peak flux density velocity at 68.45 km s^{-1} with 18.5 Jy in previous result (Forster & Caswell 1999). But our result has the peak velocity at 44.66 km s^{-1} with 63.87 Jy. Cyganowski et al. (2009) reported that 44 GHz class I methanol maser is detected at 52.4 km s^{-1} toward G35.03+0.35 with K unit. The line velocity is similar with our result of 52.75 km s^{-1}. G43.04-0.46 also has different results of peak flux density velocity positions at 22 GHz. Valdettaro et al. (2001) announced a peak velocity position at 57.55 km s^{-1} with 5.1 Jy of peak flux density. But we found peak flux density of 5.68 Jy at 45.73 km s^{-1}. Kurtz et al. (2004) showed 44 GHz peak velocity position at 58.0 km s^{-1} with 3.84 Jy, it is agree with our result of 58.0 km s^{-1} with 8.72±1.07 Jy though peak flux density is different. G45.07+0.13 has several reports of 22 GHz maser detection. Velocity positions of peak flux density are recorded at 60.1 km s^{-1}, 60.64 km s^{-1}, 60.10 km s^{-1}, and 60.06 km s^{-1} by Palagi et al. (1993), Forster & Caswell (1999), Valdettaro et al. (2001), and our result, individually. Peak flux densities are 50.7 Jy, 21.50 Jy, 41 Jy, and 23.65 Jy, respectively. Kurtz et al. (2004) found 44 GHz peak velocity position at 59.3 km s^{-1} with 1.08 Jy, and we also detected at 59.20 km s^{-1} with 1.71±0.47 Jy.

G36.92+0.48, G38.26-0.08, G41.58+0.04, G43.80-0.13, G44.64-0.52, and G45.07+0.13

The systemic velocities of these sources were not determined by the NH_3 lines (Pandian et al. 2012) but by the ^{13}CO ($J = 2-1$) or CS ($J = 5-4$) lines (Pandian et al. 2009). G43.80-0.13 and G45.07+0.13 show strong NH_3 lines, but the line profiles are complicated (Pandian et al. 2012). These two sources show all maser emissions, and G43.80-0.13 is the strongest water maser source in our sample (Table 3.4). The other four sources have no detectable NH_3 line. Only G38.26-0.08 among them shows water maser emission.

G37.02-0.03 and G37.04-0.04

Two sources are separated by $47''.7$ and overlap in the 22 GHz and 44 GHz beam size of the KVN. They exhibit two common 22 GHz lines at 80.65 and 81.75 km s^{-1}. Therefore, we count them as one detection. A more detailed investigation using interferometric observations is required to clarify the origin of water maser emission in this area. The BGPS counterpart, G037.042-00.034, is closer to G37.04-0.04 than G37.02-0.03.

G38.66+0.08, G39.39-0.14, and G42.43-0.26

These sources are associated with ultracompact (UC) HII regions (Pandian et al. 2010). G42.43-0.26 has all three maser species, while G39.39-0.14 shows both class I methanol masers, and G38.66+0.08 displays no maser emission.

G40.28-0.22 and G48.99-0.30

These two sources show the strongest maser emissions at 44 GHz and 95 GHz in our sample (Table 3.4). G40.28-0.22 has peak flux density of 89.21±1.41 Jy and 72.66±0.98 Jy at 44 GHz and 95 GHz, respectively. The two peak flux densities lies

at 72.7 km s^{-1} and 72.8 km s^{-1}, individually. G48.99-0.30 has 44 GHz peak flux density of 93.17±1.24 Jy at 66.4 km s^{-1}. and 95 GHz peak flux density of 54.19±0.89 Jy at 66.5 km s^{-1}. G40.28-0.22 is associated with a luminous ($L_{\rm bol} \simeq 2.1 \times 10^5\ L_{\odot}$) YSO, which might be a hypercompact HII region (Pandian et al. 2010). In this source, 44 GHz methanol and water maser emissions were newly detected, while 95 GHz methanol maser emission has been detected by Chen et al. (2011) with 53.21 Jy at 72.77 km s^{-1}. Urquhart et al. (2011) searched for water maser emission at the site, but they could not observe. In G48.99-0.30, both class I methanol maser emissions were newly found, whereas the water maser emission has been detected by multiple previous surveys (see Table 3.3). Codella et al. (1994) and Valdettaro et al. (2001) observed similar water maser emission of peak flux density of 7 Jy at 71.0 km s^{-1} and 8 Jy at 70.94 km s^{-1}. Urquhart et al. (2011) detected peak flux density of 58.89 Jy at 65.3 km s^{-1}. Our result of 62.40 Jy at 66.0 km s^{-1} is similar with the latter.

High velocity Features of Water Maser

We found 4 water maser sources showing very different (>30 km s^{-1}) velocity components from the systemic velocities. G35.59+0.06, G37.60+0.42, G41.08-0.13, and G41.34-0.14 have maser lines with velocity offsets of −60.5, +48.0, −77.6, and +47.5 km s^{-1} respectively. Breen et al. (2010) found several blue- or red-shifted high velocity features of water maser emissions. These features can be produced by high-velocity jets/outflows from the massive YSOs associated with 6.7 GHz methanol masers (Gwinn et al. 1992; Gwinn 1994) or associated with other YSOs at different distances in the same lines of sight. In order to distinguish between the two possibilities, we observed ^{13}CO (J=1−0) line emission toward these sources, and found no ^{13}CO line emission related to the large velocity-offset features in any of them except G41.34-0.14 (Figure 3.3). We also observed G41.34-0.14 in the HCO$^+$ (J=1−0)

line, which is a very reliable tracer of massive star-forming cores (e.g., Purcell et al. 2006), and detected the line emission only at the systemic velocity. Therefore, the large velocity-offset features are likely to be high-velocity components caused by jets/outflows, even though we cannot exclude the possibility that the feature of G41.34-0.14 may be associated with a low-mass YSO at a different distance in the same line of sight.

G37.60+0.42 has a maser emission near the systemic velocity as well, while the others do not. G35.59+0.06 and G41.08-0.13 are so-called dominant blue-shifted water maser outflows. Caswell & Phillips (2008) reported 3 such water maser sources and suggested that they can be generated from pole-on jets. G41.34-0.14 may be the red-shifted counterpart of the dominant blue-shifted water maser sources. Further various high-resolution observations are required to understand the origin of these objects.

3.4 Analyses

3.4.1 Velocity Characteristics

Figure 3.4 exbihits the distribution of the peak velocity offsets from the systemic velocities for each maser. The bin size is 2 $\mathrm{km\,s^{-1}}$. The averaged offsets of 6.7 GHz, 22 GHz, 44 GHz, and 95 GHz masers are -0.0 ± 5.0, -0.6 ± 4.8, 0.2 ± 1.1, and $0.4 \pm 1.1\,\mathrm{km\,s^{-1}}$, respectively. Here the 4 high-velocity water maser sources are excluded. The velocity offsets of 44 GHz and 95 GHz masers are always within ± 4 $\mathrm{km\,s^{-1}}$. This matches with the previous studies (e.g., Fonatani et al. 2010; Bae et al. 2011). Plambeck & Menten (1990); Kurtz et al. (2004) reported that methanol maser is associated with ambient molecular cloud that is heated by outflows and is not accelerated by the outflow. our result may support the hypothesis. The offsets of 6.7 GHz class II methanol masers are much more widely distributed, but are still

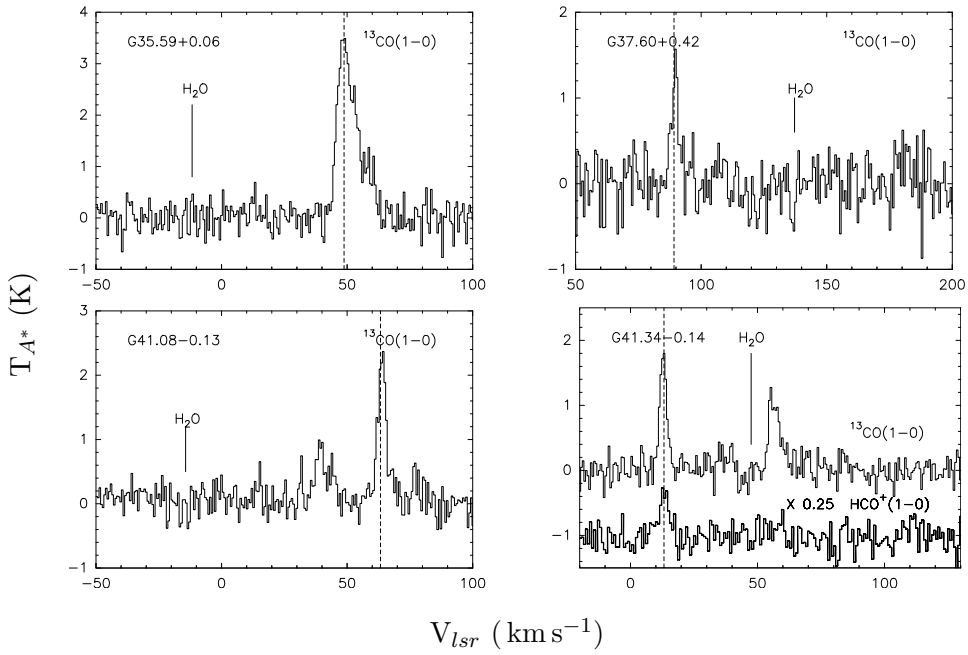

Figure 3.3: ^{13}CO (J=1−0) and HCO$^+$ (J=1−0) line spectra of the four water maser sources with large (>30 km s^{-1}) velocity offsets. The vertical dashed lines show the systemic velocities, and solid lines show the positions of high velocity figures of water maser. The HCO$^+$ spectrum of G41.34−0.14 is magnified by a factor of 4.

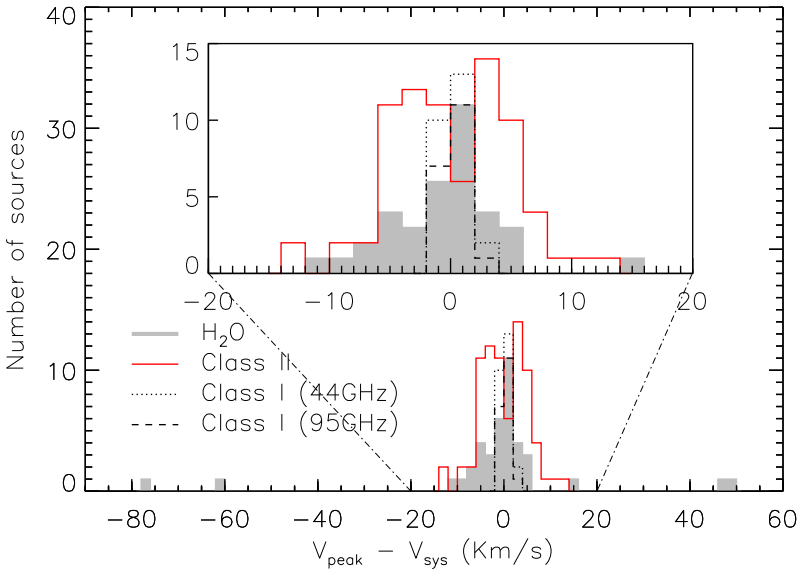

Figure 3.4: Velocity offset distributions of the four maser transitions.

within ± 10 km s^{-1} for 95% of the sources. The distribution is double peaked with a dip around zero. This is consistent with the finding of Byun et al. (2012) that a large sample of 284 6.7 GHz masers shows a double-peaked distribution of velocity offsets. On the contrary, the distributions are single peaked around zero for the other masers. The offset dispersion of water maser lines appears to lie between those of class I and class II methanol masers. Half of the sources are within ± 2.3 km s^{-1} and ± 3.7 km s^{-1} for water and 6.7 GHz masers, respectively. For comparison, Fontani et al. (2010) surveyed 6.7 GHz, 44 GHz, and 95 GHz methanol masers toward 296 massive YSO candidates, which had been observed in water maser emission. They found that water and class II methanol masers have very similar single-peaked distributions of velocity offsets. The bin size in their histograms was 6 km s^{-1}. This large bin might hinder them from the double-peaked distribution of 6.7 GHz masers. The class I masers in their sample almost all showed velocity offsets within ± 6 km s^{-1}.

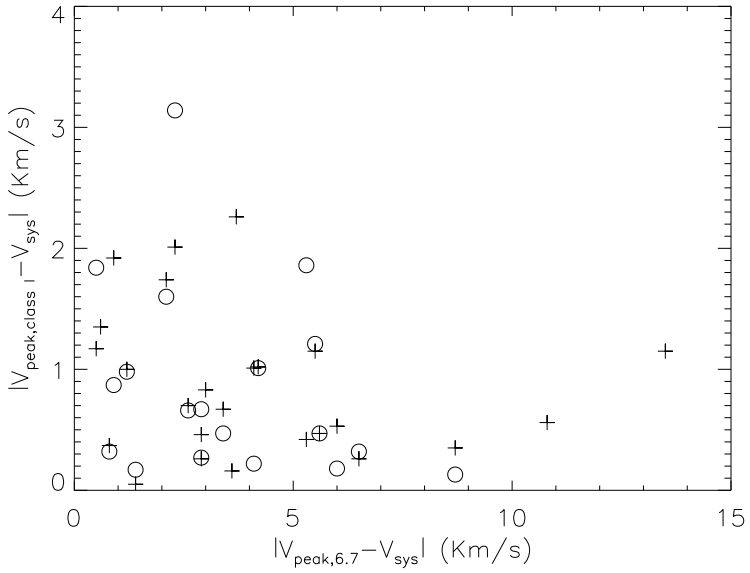

Figure 3.5: Plot of the absolute value of velocity offset of class I methanol maser against that of 6.7 GHz maser. Plus signs and open circles are the data points of 44 GHz and 95 GHz masers, respectively.

Figure 3.5 compares the velocity offsets of class I and class II masers. Large velocity offsets of both masers appear to be avoided. Slysh et al. (1994) reported that class I and class II have anti-correlation at radial velocities where class I and class II do not co-exist. Some of our data shows the anti-correlation, but almost do not follows the trend.

We derive the velocity overlap of class I and class II methanol maser spectra to examine the relationship between the two classes. The velocity overlap is defined by the difference between the lowest velocity of the class with higher mean velocity and the highest velocity of the other class with lower mean velocity (Ellingsen 2005). Negative values of velocity overlap hence imply that the velocity ranges of the two classes overlap. Figure 3.6 displays a histogram of the velocity overlap. Nineteen (76%) of 25 44 GHz maser sources and 14 (74%) of 19 95 GHz maser sources show negative values. This portion is slightly higher than that of Ellingsen (2005) for 95 GHz maser sources, 62% (23/37).

3.4.2 Flux Densities and Luminosities

Tables 3.4 and 3.5 present the peak flux densities and the isotropic luminosities of the detected masers, respectively. Figure 3.7 compares the flux densities of 44 GHz and 95 GHz methanol masers. A strong correlation exists between the two parameters, as shown below:

$$\mathrm{S_{peak}}(95) = (0.71 \pm 0.08)\ \mathrm{S_{peak}}(44) - (0.28 \pm 0.52), \quad \mathrm{r} = 0.98, \tag{3.1}$$

$$\log(\mathrm{S_{peak}}(95)) = (0.95 \pm 0.05)\ \log(\mathrm{S_{peak}}(44)) - (0.13 \pm 0.06), \quad \mathrm{r} = 0.95, \tag{3.2}$$

where r is the correlation coefficient.

Val'tts et al. (2000) also reported a quite good correlation between the two with a correlation coefficient of 0.73: $\mathrm{S_{peak}}(95) = (0.32 \pm 0.08)\,\mathrm{S_{peak}}(95) - (8.1 \pm 2.7)$. Our estimate of $\mathrm{S_{peak}}(95)$/Speak(44) is two times higher than theirs. It should be

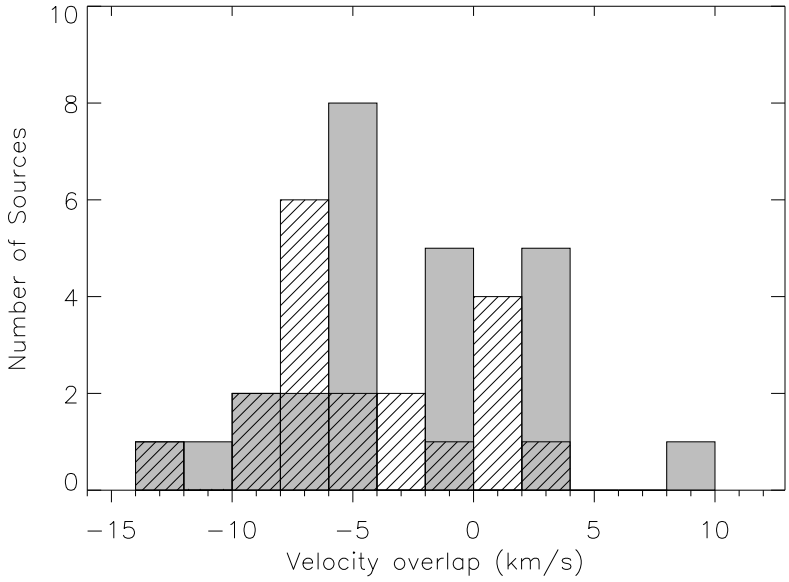

Figure 3.6: Histogram of the velocity overlap between class I and 6.7 GHz class II methanol masers. Filled and slant bars indicate 44 GHz and 95 GHz masers, respectively. A negative value means that the velocity ranges of the two masers overlap (See the text for details).

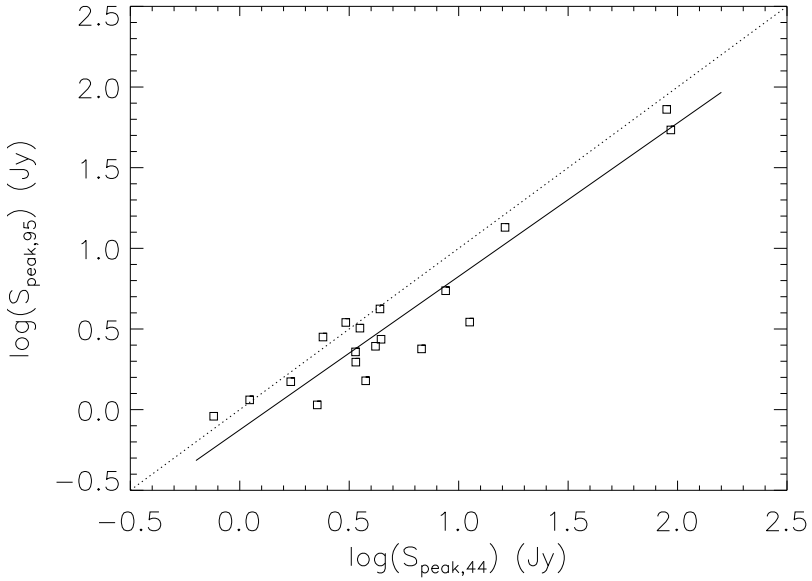

Figure 3.7: Comparison between the peak flux densities of 44 GHz and 95 GHz class I methanol masers. A strong correlation exists between the two parameters. The solid line is the least-squares fitting result with a correlation coefficient of 0.95.

noted that they used data sets obtained with different telescopes at different epochs. Additionally, the sources in their sample were generally strong, with a 3σ limit of $\sim$5 Jy. In contrast, our data sets were simultaneously taken with the same telescopes simultaneously and are more sensitive down to 1.5 Jy. Our value thus seems to be more reliable.

We look for any relationships between the peak flux density of 6.7 GHz maser and those of the observed 3 masers, but there appears to be little correlation between them:

$$\log(S_{\rm peak}(22)) = (0.96 \pm 0.05)\ \log(S_{\rm peak}(6.7)) + (0.42 \pm 0.12), \quad r = 0.18, \tag{3.3}$$

$$\log(S_{\rm peak}(44)) = (-0.85 \pm 0.18)\ \log(S_{\rm peak}(6.7)) + (1.10 \pm 0.19), \quad r = -0.19, \tag{3.4}$$

$$\log(S_{\rm peak}(95)) = (-0.90 \pm 0.15)\ \log(S_{\rm peak}(6.7)) + (1.12 \pm 0.22), \quad r = -0.20. \tag{3.5}$$

Beuther et al. (2002) could not find any correlation between 22 GHz water and 6.7 GHz class II methanol masers. Slysh et al. (1994) reported anti-correlation between 44 GHz class I and 6.7 GHz class II methanol masers in velocity and flux density. However, Ellingsen (2005) found no anti-correlation between 95 GHz and 6.7 GHz masers. Our results are consisted with the suggestions of Ellingsen (2005) and Beuther et al. (2002). We also investigate the relationship between water and class I methanol masers, but there seem to be no correlation between them. The correlation coefficients of water maser with the 44 GHz and 95 GHz masers are -0.05 and -0.05, respectively.

Using the distance estimated by Pandian et al. (2009), we calculate the isotropic luminsoties from the integrated flux densities in Table 3.4 (see, e.g., Bae et al. 2011), and investigate relationships between them. As in the cases of flux densities, there is a strong correlation between the luminosities of the two class I masers (Figure 3.8).

$$\log(L_{95}/L_{\odot}) = (0.89 \pm 0.08)\ \log(L_{44}/L_{\odot}) - (0.14 \pm 0.34), \quad r = 0.89, \tag{3.6}$$

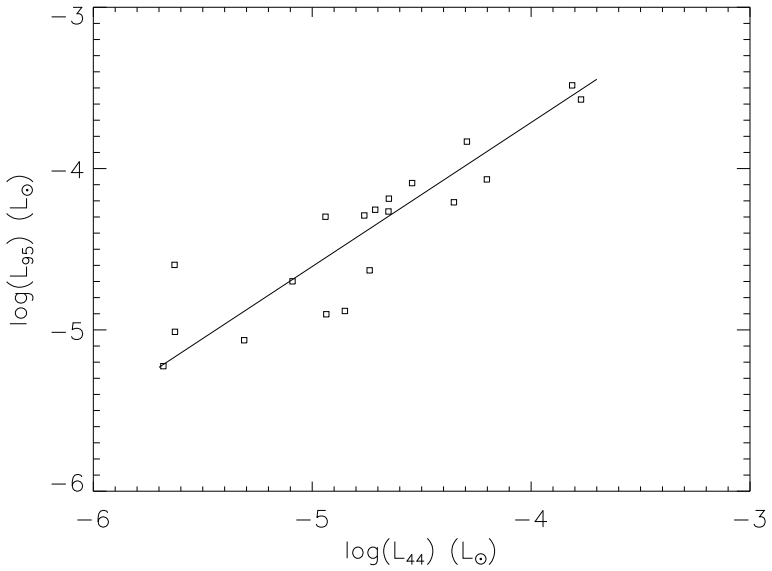

Figure 3.8: Comparison between the isotropic luminosities of 44 GHz and 95 GHz class I methanol masers. The solid line is the result of a least-squares fit with a correlation coefficient of 0.89.

$$\mathrm{L_{95}/L_{\odot}} = (1.84 \pm 0.19)\ \mathrm{L_{44}/L_{\odot}} + (7.47\mathrm{e}^{-6} \pm 5.46\mathrm{e}^{-6}), \quad \mathrm{r} = 0.96. \tag{3.7}$$

We could not find any significant correlation between the luminosities of the water and methanol masers.

3.4.3 Associated BGPS Clumps

For targeted searches of 95 GHz class I methanol maser, Chen et al. (2012) proposed criteria of the integrated flux density and beam-averaged H_2 column density of the BGPS clumps: $\log(\mathrm{S_{int}}) \lesssim -38.0{+}1.72\log(\mathrm{N_{H_2}^{beam}})$ and $\log(\mathrm{N_{H_2}^{beam}}) \gtrsim 22.1$. The BGPS is a 1.1 mm continuum survey of the inner Galaxy region of $-10^{\circ} < l < 90^{\circ}$ and $|b| \lesssim 0.5^{\circ}$ (Rosolowsky et al. 2010). The survey was undertaken using the Caltech

Submillimeter Observatory (CSO) with an HPBW of 33″. We test the validity of the Chen et al.'s criteria with 44 BGPS clumps associated with the sources in our survey (Pandian et al. 2012). For simplicity, we used the same parameters as in Chen et al. (2012) in deriving the beam-averaged H_2 column density: mean mass per particle of μ=2.37, kinetic temperature of 20 K, and beam solid angle of 2×10^{-8} Sr. Figure 3.9 shows that all the 14 BGPS clumps with 95 GHz maser meet the criteria. It is worth noting that they are just 39% of the 36 BGPS clumps fitting the criteria. This detection rate is considerably lower than the prediction of Chen et al. (2012), $> 60\%$.

We estimate the BGPS clump mass in a similar manner to Chen et al. (2012) except with the kinetic temperature measured by the NH_3 line observation (Pandian et al. 2012). The relationship between the BGPS mass and the four maser luminosities are derived below and are displayed in Figure 3.10:

$$\log(L_{6.7}/L_\odot) = (1.46 \pm 0.22)\ \log(M_{BGPS}/M_\odot) - (10.41 \pm 0.68), \quad r = 0.29, \quad (3.8)$$

$$\log(L_{22}/L_\odot) = (1.50 \pm 0.25)\ \log(M_{BGPS}/M_\odot) - (9.50 \pm 0.82), \quad r = 0.50, \quad (3.9)$$

$$\log(L_{44}/L_\odot) = (1.01 \pm 0.18)\ \log(M_{BGPS}/M_\odot) - (7.80 \pm 0.50), \quad r = 0.67, \quad (3.10)$$

$$\log(L_{95}/L_\odot) = (1.21 \pm 0.18)\ \log(M_{BGPS}/M_\odot) - (8.15 \pm 0.51), \quad r = 0.59. \quad (3.11)$$

Our results suggest that the luminosities of class I methanol masers are more closely related to the BGPS clump mass than those of water and 6.7 GHz class II methanol masers.

3.4.4 Methanol Column Densities and Abundances

Val'tts et al. (2000) investigated the physical condition of class I maser emitting region using a large velocity gradient (LVG) code with the observed flux densities of 44 GHz and 95 GHz methanol masers. Under the assumption of a methanol density

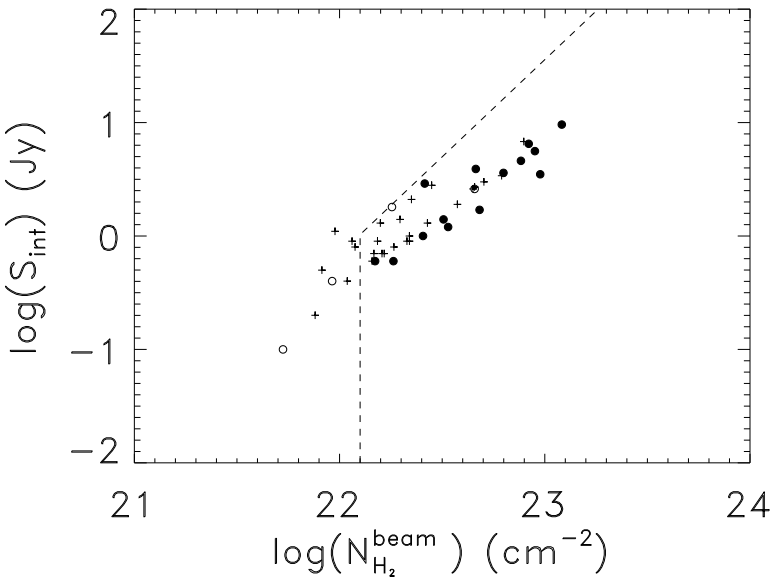

Figure 3.9: Distribution of the associated BGPS sources in a plane of the beam-averaged H_2 column density and the 1.1 mm integrated continuum flux density. Filled circles, open circles, and plus signs represent the sources with both 44 GHz and 95 GHz masers, the ones with only 44 GHz maser, and the ones without any of the two, respectively. The dashed lines show the criteria of Chen et al. (2012).

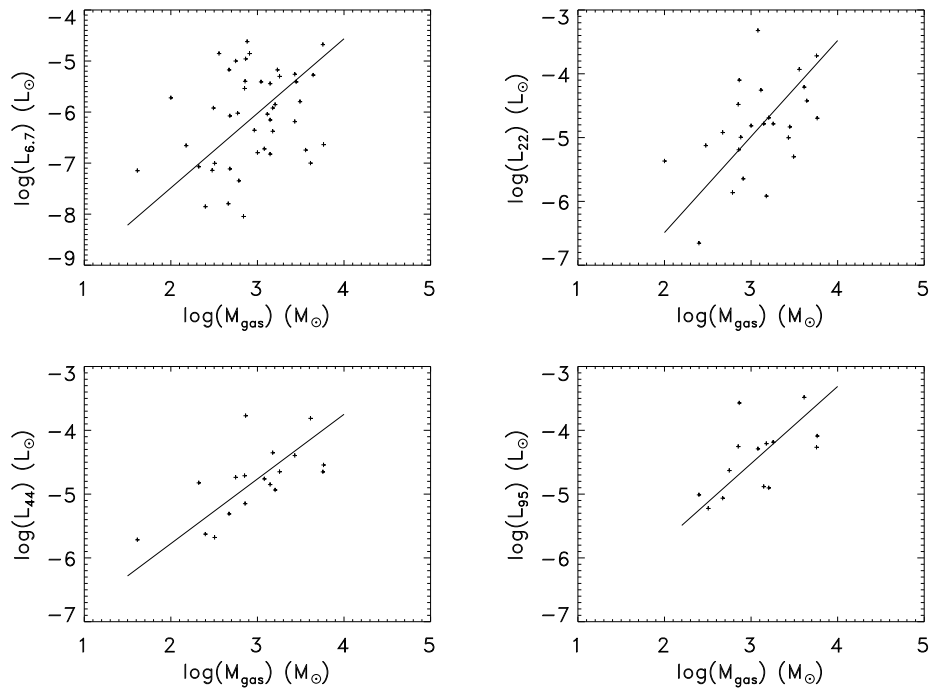

Figure 3.10: Relationship between the isotropic maser luminosity and the associated BGPS source mass for 6.7 GHz (upper left), 22 GHz (upper right), 44 GHz (bottom left), and 95 GHz (bottom right) masers. The solid lines represent the least-sqaures fitting results. The correlation coefficients are 0.29, 0.50, 0.67, and 0.59 for the 6.7 GHz, 22 GHz, 44 GHz, and 95 GHz transitions, respectively.

divided by velocity gradient of $0.67 \times 10^{-2}\,\mathrm{cm}^{-3}$ $(\,\mathrm{km\,s}^{-1}\ pc^{-1})^{-1}$, they obtained a gas temperature of about 20 K and an H_2 number density of less than $10^6\,\mathrm{cm}^{-3}$. Using the LVG model, we estimate the methanol column density with the measured flux density ratio of 44 GHz and 95 GHz masers. We utilize the A-CH_3OH molecular data from the LAMDA database[3] (Schöier et al. 2005), and the model code modified using RADEX[4] (van der Tak et al. 2007). van der Tak et al. (2007) suggested that the calculated values may be inaccurate at $-1 \lesssim \tau \lesssim -0.1$ and meaningless at $\tau \lesssim -1$. The H_2 number density is calculated from the BGPS clump mass estimated in the last section, assuming that the clump is a sphere with uniform density. It should be reminded that the H_2 number density from the BGPS data is minimum value, because the flux density of the BGPS is beam-averaged value and maser revelation position will reside in. The kinetic temperature is taken from ammonia observation result ofPandian et al. (2012). The line width is adopted from the mean value between the FWHMs of the 44 GHz and 95 GHz maser spectra in Table 3.4. We consider only the cosmic microwave background at 2.73 K, and assume that the 44 GHz and 95 GHz maser emissions emanate from the same region.

As mentioned above, 14 of the 19 sources with both 44 GHz and 95 GHz class I methanol masers have associated BGPS clumps. The methanol column densities are derived to be between 1.3×10^{15} and 3.5×10^{16} cm^{-2} with one exception. Table 3.2 lists the values together with the calculated optical depths. We estimate the methanol abundance relative to H_2 by comparing the calculated methanol column density with the H_2 column density by the BGPS data of Pandian et al. (2012). The fractional methanol abundances range from 4.2×10^{-8} to 2.3×10^{-6} with a median value of $3.3 \pm 2.7 \times 10^{-7}$. These values are close to the typical abundance in the interaction regions between the outflows and molecular cloud gas (Plambeck & Menten 1990; Menten et al. 1988).

[3]See http://home.strw.leidenuniv.nl/∼moldata/

[4]See http://www.sron.rug.nl/∼vdtak/radex/radex.php

Table 3.2. Column Densities and Fractional Abundances of Methanol

Source	$S_{p,95}/S_{p,44}$	n(H_2) ($10^3 cm^{-3}$)	N(H_2)* ($10^{21} cm^{-2}$)	τ_{44} (10^{-2})	τ_{95} (10^{-3})	N(CH_3OH) ($10^{15} cm^{-2}$)	$\chi(CH_3OH)$ (10^{-7})
G35.03+0.35	0.96	0.3	11.6	-1.8	-3.2	3.8	3.3
G37.55+0.19	0.23	2.4	24.5	-26.3	-11.9	11.0	4.4
G37.60+0.42	0.59	19.9	17.0	-6.7	-7.4	1.3	0.8
G37.77-0.22	0.49	2.0	35.7	-5.0	-4.6	5.4	1.5
G39.39-0.14	1.18	3.2	13.2	-1.2	-2.6	1.7	1.3
G40.28-0.22	0.81	5.2	25.1	-9.5	-1.5	1.3	0.5
G42.43-0.26	0.31	0.3	6.5	-10.7	-6.6	6.7	10.0
G43.04-0.46	0.63	5.4	26.8	-5.0	-5.8	1.6	0.6
G44.31+0.04	0.62	0.2	15.1	-1.5	-1.7	35.0	23.0
G45.81-0.36	0.90	4.3	11.9	-5.0	-6.8	4.2	3.6
G48.99-0.30	0.58	3.0	27.6	-11.4	-12.8	1.6	0.6
G49.27+0.31	0.47	1.3	10.2	-3.5	-3.0	16.0	15.0
G53.04+0.11	0.58	2.3	14.6	-4.5	-4.8	13.0	9.2
G53.14+0.07	0.83	6.7	30.4	-5.3	-8.1	1.3	0.4

*The H_2 column density from Pandian et al. (2012)

3.5 Conclusions

We conducted simultaneous observation of 22 GHz water and 44 GHz and 95 GHz class I methanol masers toward 77 6.7 GHz class II methanol maser sources. Our main results are as follows.

(1) The water maser was most frequently detected with a rate of 51 %, while the class I methanol masers were detected with lower rates of 32 % at 44 GHz and 25 % at 95 GHz. There are 15, 21, and 13 new detections at the 22 GHz, 44 GHz, and 95 GHz bands, respectively. We identified 4 high-velocity (>30 $km\,s^{-1}$) water maser sources, of which two are dominant blue-shifted outflows and one is dominant redshifted outflow. 95 GHz class I maser accompanies always with 44 GHz maser and frequently with water maser.

(2) The peak velocities of class I methanol masers are always within ± 4 $km\,s^{-1}$ of the systemic velocities, while those of 6.7 GHz class II methanol masers are signif-

icantly offset. The velocity offset dispersion of water masers appear to lie between those of class I and II masers. Interestingly, class II masers show a double-peaked distribution of velocity offsets while water and class I masersshow single-peaked distributions.

(3) 44 GHz and 95 GHz masers exhibit strong correlations in velocity and flux density. The flux density of 95 GHz maser is usually as strong as that of 44 GHz maser. We could not find any anti-correlations between class I and class II methanol masers in velocity and flux density.

(4) The isotropic luminosities of class I masers are correlated with the BGPS clump mass. All the 14 BGPS clumps with both 44 GHz and 95 GHz masers satisfy the criteria of Chen et al. (2012).

(5) Assuming an unsaturated system, we applied the LVG model to derive the column densities and the fractional abundances of methanol for the 14 BGPS clumps except one. The calculated colunn densities range from 1.3×10^{15} to 3.5×10^{16} cm^{-2}. The estimated abundances are between 4.2×10^{-8} to 2.3×10^{-6}, which are comparable to the typical value in the interface of outflows with the surrounding region.

References

Bae, J.-H., Kim, K.-T., Youn, S.-Y., Kim, W.-J., Byun, D.-Y., Kang, H., & Oh, C.S. 2011, ApJS, 196, 21

Bayandina, O.S., Val'tts, I.E., & Larionov, G.M. 2012, AZh, 89, 611

Beuther, H., Walsh, A., Schilike, P., Sridharan, T.K., Menten, K.M., & Wyrowski, F. 2002, A&A, 390, 289

Breen, S.L., Caswell, J.L., Ellingsen, S.P., & Phillips, C.J. 2010, MNRAS, 406, 1487

Breen, S.L., Ellingsen, S.P., Contreras, Y., Green, J.A., Caswell, J.L., Stevens, J.B., Dawson, J.R., & Voronkov, M.A. 2013, MNRAS, 435, 524

Caswell, J.L., & Phillips, C.J. 2008, MNRAS, 386, 1521

Chen, X., Ellingsen, S.P., Shen, Z.-Q., Titmarsh, A., & Gan, C.-G. 2011, ApJS, 196, 9

Chen, X., Ellingsen, S.P., He, J.-H., et al. 2012, ApJS, 200, 5

Choi, M., Kang. M., Byun, D.-Y., & Lee, J.-E. 2012, ApJ, 759, 136

Codella, C., Felli, M., Natale, V., Palagi, F., & Palla, F. 1994, A&A, 291, 261

Codella, C., Lorenzani, A., Gallego, A.T., Cesaroni, R., & Moscadelli, L. 2004, A&A, 417, 615

Cragg, D.M., Johns, K.P., Godfrey, P.D., & Brown, R.D. 1992, MNRAS, 259,203

Cyganowski, C.J., Brogan, C.L., Hunter, T.R., & Churchwell, E. 2009, ApJ, 702, 1615

Dodson, R., Ohja, R., & Ellingsen, S.P. 2004, MNRAS, 351, 779

Ellingsen, S.P. 2005, MNRAS, 359, 1498

Elitzur, M., Hollenbach, D.J., & McKee, C.F. 1989, ApJ, 346, 983

Fontani, F., Cesaroni, R., & Furuya, R.S. 2010, A&A, 517, A56

Forster, J.R., & Caswell, J.L. 1999, A&AS, 137, 43

Furuya, R.S., Kitamura, Y., Wootten, H.A., Claussen, M.J., & Kawabe, R. 2003, ApJS, 144, 71

Genzel, R. & Downes, D. 1977, A&AS, 30, 145

Gwinn, C.R., Moran, J.M., & Reid, M.J. 1992, ApJ, 393, 149

Gwinn, C.R. 1994, ApJ, 429, 253

Han, F., Mao, R.Q., Lu, J., Wu, Y.F., Sun, J., Wang, J.S., Pei, C.C., Fan, Y., Tang, G.S., & Ji, H.R., 1998, A&AS, 127, 181

Han, S.-T., Lee, J.-W., Kang, J., et al. 2008, Int. J. Infrared Millim. Waves, 29, 69

Isobe, T., Feigelson, E.D., Akritas, M.G., & Babu, G.J. 1990, ApJ, 364, 104

Kalenskii, S.V., Johansson, L.E.B., Bergman, P., et al. 2010, MNRAS, 405, 613

Kim, K.-T., Byun, D.-Y., Je, D.-H., et al. 2011, J. Korean Astron. Soc., 44, 81

Kurtz, S., Hofner, P., & Álvarez, C.V. 2004, ApJS, 155, 149

Lee, S.-S., Byun, D.-Y., Oh, C.S., et al. 2011, PASP, 123, 1398

Menten, K.M., Walmsley, C.M., Henkel, C., & Wilson, T.L. 1988, A&A, 198, 253

Menten, K.M. 1991, in ASP Conf. Ser. 16, Atoms, Ions and Molecules: New Results in Spectral Line Astrophysics, ed. A.D. Haschick & P.T.P. Ho (San Francisco, CA: ASP), 119

Minier, V., Booth, R.S., & Conway, J.E. 2000, A&A, 362, 1093

Moscadelli, L., Testi, L, Furuya, R.S., Goddi, C., Claussen, M., Kitamura, Y., & Wootten, A. 2006, A&A, 446, 985

Norris R.P., Whiteoak J.B., Caswell J.L., Wieringa M.H., & Gough R.G. 1993, ApJ, 412, 222

Ochsenbein, F., Bauer, P., & Marcout, J. 2000, A&AS, 132, 23

Palagi, F., Cesaroni, R., Comoretto, G., Felli, M., & Natale, V. 1993, A&AS, 101, 153P

Pandian, J.D., Goldsmith, P.F., & Deshpande, A.A. 2007a, ApJ, 656, 255

Pandian, J.D., Menten, K.M., & Goldsmith, P.F. 2009, ApJ, 706, 1609

Pandian, J.D., Momjian, E., Xu, Y., Menten, K.M., & Goldsmith, P.F. 2010, A&A, 522, A8

Pandian, J.D., Momjian, E., Xu, Y., Menten, K.M., & Goldsmith, P.F. 2011, ApJ, 730, 55

Pandian, J.D., Wyrowski, F., & Menten, K.M. 2012, ApJ, 753, 50

Pestalozzi M.R., Elitzur M., Conway J.E., & Booth R.S. 2004, ApJ, 603, L113

Plambeck, P.L. & Wright, M.C.H. 1988, ApJ, 330, 61

Plambeck, P.L. & Menten, K.H. 1990, ApJ, 364, 555

Purcell, C.R., Balasubramanyam, R., Burton, M.G., et al. 2006, MNRAS, 367, 553

Rodriguez, L.F., Moran, J.M., Ho, P.T.P., & Gottlieb, E.W. 1980, ApJ, 235, 845

Rosolowsky, E., et al. 2010, ApJS, 188, 123

Schöier, F.L., van der Tak, F.F.S., van Dishoeck E.F., & Black, J.H. 2005, A&A, 432, 369

Slysh, V.I., Kalenskii, S.V., Val'tts, I.E., & Otrupcek, R. 1994, MNRAS, 268, 464

Szymczak, M., Pillai, T., & Menten, K.M. 2005, A&A, 434, 613

Torrelles, J.M., Gómez, J.F., Rodríguez, L.F., Ho, P.T.P., Curiel S., & Vázquez R. 1997, ApJ, 489, 752

Urquhart, J.S., Morgan, L.K., Figura, C.C., Moore, T.J.T., Lumsden, S.L., Hoare, M.G., Oudmaijer, R.D., Mottram, J.C., Davies, B., & Dunham, M.K. 2011, MNRAS, 418, 1689

Valdettaro, R., Palla, F., Brand, J., Cesaroni, R., et al. 2001, A&A, 368, 845

Val'tts, I.E., Ellingsen, S.P., Slysh, V.I., Otrupcek, R., & Larionov, G.M. 2000, MNRAS, 317, 315

Van der Tak, F.F.S., Black, J.H., Schöier, F.L., Jansen, D.J., & van Dishoeck, E.F., 2007, A&A, 468, 627

Voronkov, M.A., Brooks, K.J., Sobolev, A.M., Ellingsen, S.P., Ostrovskii, A.B., & Caswell, J.L. 2006, MNRAS, 373, 411

Voronkov, M.A., Caswell, J.L., Ellingsen, S.P., & Green, J.A. 2014, MNRAS, 439, 2584

Walsh A.J., Burton M.G., Hyland A.R., & Robinson G. 1998, MNRAS, 301, 640

Table 3.3. Source Summary with Detection Results

Source† (l, b)	R.A. (J2000)† (h m s)	Decl. (J2000)† (°′″)	V_{sys}[a] ($km\,s^{-1}$)	Date (yyyymmdd)	22 GHz water	44 GHz class I	95 GHz class I	Fig. No.
G34.82+0.35	18 53 37.4‡	01 50 32‡	56.6	20111216				
G35.03+0.35	18 54 00.658	02 01 19.23	53.1	20111216	(4)	(9)	New	3.13
G35.25-0.24	18 56 30.388	01 57 08.88	61.6	20111216		New		3.12
G35.39+0.02*	18 55 51.2‡	02 11 37‡	93.9	20111216		New		3.12
G35.40+0.03*	18 55 50.799	02 12 19.08	94.6	20111216				
G35.59+0.06	18 56 04.219	02 23 28.34	48.8	20111216	(10)	New	New	3.13
G35.79-0.17	18 57 16.892	02 27 58.05	61.3	20111217	New	New		3.15
G36.02-0.20	18 57 45.868	02 39 05.67	86.8	20111217				
G36.64-0.21	18 58 55.236	03 12 04.72	74.8	20111217	New			3.11
G36.70+0.09	18 57 59.123	03 24 06.12	59.4	20120127	New(8)			3.11
G36.84-0.02	18 58 39.214	03 28 00.89	59.0[c]	20111217				
G36.90-0.41	19 00 08.6‡	03 20 35‡	79.6	20111218	New			3.11
G36.92+0.48	18 56 59.786	03 46 03.60	-30.7[b]	20111218				
G37.02-0.03*	18 59 03.642	03 37 45.08	80.1	20120227	New(8)			3.11
G37.04-0.04*	18 59 04.406	03 38 32.77	80.8	20120227	New(8)			3.11
G37.38-0.09	18 59 51.586	03 55 18.02	57.1	20111217		New		3.12
G37.47-0.11	19 00 07.144	03 59 53.08	58.4	20111120	(8)			3.11
G37.53-0.11	19 00 16.056	04 03 16.09	51.7	20120227				
G37.55+0.19	18 59 09.985	04 12 15.54	84.6	20111120	(8)(10)	New	New(11)	3.13
G37.60+0.42	18 58 26.799	04 20 45.47	89.2	20111217	(8)	New	New	3.13
G37.74-0.12	19 00 36.841	04 13 19.98	45.5	20111218	(2)(5)			3.11
G37.76-0.19	19 00 55.421	04 12 12.56	59.6	20111218	(2)(5)			3.11
G37.77-0.22	19 01 02.268	04 12 16.55	64.1	20111218	(2)(5)	New	(13)	3.13
G38.03-0.30	19 01 50.470	04 24 18.94	61.6	20111120	New(8)			3.11
G38.08-0.27	19 01 47.317	04 27 20.90	64.7	20120128				
G38.12-0.24	19 01 44.152	04 30 37.42	82.7	20120128				
G38.20-0.08	19 01 18.730	04 39 34.32	82.9	20120128				
G38.26-0.08	19 01 26.233	04 42 17.26	11.6[b]	20120128	(10)			3.11
G38.26-0.20	19 01 52.956	04 38 39.47	65.4	20120128				
G38.56+0.15	19 01 08.345	05 04 36.71	28.2	20120128	(10)			3.11
G38.60-0.21	19 02 33.461	04 56 36.37	66.1	20120128	New			3.11
G38.66+0.08	19 01 35.244	05 07 47.36	-39.1	20120227				
G38.92-0.36	19 03 38.659	05 09 42.49	37.9	20120128	(3)(5)	New	New	3.13
G39.39-0.14	19 03 45.312	05 40 42.68	66.0	20120129		New	(11)	3.14
G39.54-0.38	19 04 53.5‡	05 41 59‡	60.4	20120130				
G40.28-0.22	19 05 41.215	06 26 12.69	73.1	20120129	New(10)	New	(11)	3.13
G40.62-0.14	19 06 01.630	06 46 36.18	32.5	20120129	(4)(10)			3.11
G40.94-0.04	19 06 15.378	07 05 54.49	39.3	20111226				
G41.08-0.13	19 06 49.047	07 11 06.57	63.3	20111226	New			3.11
G41.12-0.11	19 06 50.248	07 14 01.49	37.8	20111226				
G41.12-0.22	19 07 14.856	07 11 00.69	59.7	20111226		New		3.12
G41.16-0.20	19 07 14.369	07 13 18.08	60.4	20111226				

Table 3.3 (cont'd)

Source† (l, b)	R.A. (J2000)† (h m s)	Decl. (J2000)† (°′″)	V_{sys}[a] ($km\,s^{-1}$)	Date (yyyymmdd)	22 GHz water	44 GHz class I	95 GHz class I	Fig. No.
G41.23-0.20	19 07 21.378	07 17 08.17	58.9	20111230				
G41.27+0.37	19 05 23.606	07 35 05.25	14.9	20111230				
G41.34-0.14	19 07 21.842	07 25 17.27	13.2	20111120	New			3.11
G41.58+0.04	19 07 09.178	07 42 25.24	12.4[b]	20111230				
G42.03+0.19	19 07 28.185	08 10 53.47	17.7	20111230	New(10)			3.11
G42.30-0.30	19 09 43.592	08 11 41.41	27.8	20111230	New			3.11
G42.43-0.26	19 09 49.858	08 19 45.40	64.7	20111230	(10)	New	New	3.13
G42.70-0.15	19 09 55.069	08 36 53.45	-44.4	20111230				
G43.04-0.46	19 11 38.984	08 46 30.71	57.4	20120130	(5)	(7)(12)	(13)	3.13
G43.08-0.08	19 10 22.050	08 58 51.49	12.6	20120130				
G43.80-0.13	19 11 53.990	09 35 50.61	43.7	20120130	(1)(4)(5)(10)	New	New	3.13
G44.31+0.04	19 12 15.816	10 07 53.52	56.2	20111218	(10)	New	New	3.13
G44.64-0.52	19 14 53.766	10 10 07.69	46.0[b]	20120129				
G45.07+0.13	19 13 22.129	10 50 53.11	59.2[b]	20120129	(1)(4)(5)(10)	(7)(12)	New	3.13
G45.44+0.07	19 14 18.291	11 08 58.97	59.0[c]	20120129	(2)(4)(6)(10)			3.11
G45.47+0.05	19 14 24.147	11 09 43.43	57.1	20120130	(2)(4)(6)(10)			3.11
G45.47+0.13	19 14 07.362	11 12 15.98	61.6[c]	20120130	(4)(6)			3.11
G45.49+0.13	19 14 11.357	11 13 06.41	59.5[c]	20120130	(4)(6)	New	New(11)	3.13
G45.57-0.12	19 15 13.152	11 10 16.54	4.5	20120130	New			3.11
G45.81-0.36	19 16 31.081	11 16 12.01	58.7	20120130	New	New	(11)	3.13
G46.07+0.22	19 14 56.077	11 46 12.98	18.8	20111216				
G46.12+0.38	19 14 25.520	11 53 25.99	55.0	20111225	New			3.11
G48.89-0.17	19 21 47.5‡	14 04 58‡	55.7	20111225				
G48.90-0.27	19 22 10.330	14 02 43.51	68.4	20120130	(2)(5)	New		3.15
G48.99-0.30	19 22 26.134	14 06 39.78	67.4	20111225	(2)(5)(10)	New	New	3.13
G49.27+0.31	19 20 44.859	14 38 26.91	3.3	20111225		New	New	3.14
G49.35+0.41	19 20 32.449	14 45 45.44	66.2	20111225				
G49.41+0.33	19 20 59.211	14 46 49.66	-21.3	20111225				
G49.60-0.25	19 23 26.611	14 40 16.99	56.7	20111225				
G49.62-0.36	19 23 52.805	14 38 03.25	54.5	20120128				
G50.78+0.15	19 24 17.411	15 54 01.60	42.1	20120130				
G52.92+0.41	19 27 34.960	17 54 38.14	44.7	20111120				
G53.04+0.11	19 28 55.494	17 52 03.11	4.8	20111218		(7)(12)	New	3.14
G53.14+0.07	19 29 17.581	17 56 23.21	21.7	20120129	(10)	New	(13)	3.13
G53.62+0.04	19 30 23.016	18 20 26.68	22.8	20111217				

†The position and name from the accurate astrometry (Pandian et al. 2011)

‡The position from the AMGPS catalog (Pandian et al. 2007)

[a]The systemic velocity from the NH_3 observation (Pandian et al. 2012)

[b]The systemic velocity from the ^{13}CO ($J = 2-1$) or CS ($J = 5-4$) lines (Pandian et al. 2009)

[c]The systemic velocity from the NH_3 observation (Pandian et al. 2012) that is near the previous result(Pandian et al. 2009)

*Overlapped sources at 22 and 44 GHz

References. — (1) Palagi et al. 1993; (2) Codella et al. 1994; (3) Han et al. 1998; (4) Forster & Caswell 1999; (5) Valdettaro et al. 2001; (6) Codella et al. 2004; (7) Kurtz et al. 2004; (8) Szymczak et al. 2005; (9) Cyganowski et al. 2009; (10) Urquhart et al. 2011; (11) Chen et al. 2011; (12) Bayandina et al. 2012; (13) Chen et al. 2012.

Table 3.4. Line Parameters of Detected Masers

Source	Frequency (GHz)	Gaussian Fit				Integrated Fit				
		S_{int} (Jy km s^{-1})	V_{peak} (km s^{-1})	FWHM (km s^{-1})	S_{peak} (Jy)	S_{int} (Jy km s^{-1})	v_{min} (km s^{-1})	v_{max} (km s^{-1})	S_{peak} (Jy)	V_{peak} (km s^{-1})
G35.03+0.35	22	6.54 ± 0.79	40.6 ± 0.0	0.7 ± 0.1	9.18 ± 0.87	7.24	39.3	41.1	9.02	40.7
	22	7.46 ± 0.82	41.7 ± 0.1	0.9 ± 0.1	7.86 ± 0.87	7.36	41.1	42.7	7.48	41.7
	22	47.74 ± 0.52	44.7 ± 0.0	0.7 ± 0.0	62.52 ± 0.87	49.69	43.3	46.4	64.07	44.7
	22	3.14 ± 4.65	55.0 ± 0.6	0.9 ± 1.6	3.20 ± 4.85	3.52	53.7	55.6	3.66	55.0
	22	4.55 ± 5.45	56.6 ± 0.7	1.5 ± 2.3	2.89 ± 4.85	4.77	55.6	58.2	2.99	56.7
	22	3.91 ± 3.04	59.2 ± 0.3	0.7 ± 0.7	5.14 ± 4.85	4.08	58.2	59.9	5.76	59.2
	44	0.70 ± 0.40	50.7 ± 0.1	0.4 ± 0.2	1.53 ± 0.59	0.95	50.1	51.0	1.55	50.6
	44	1.84 ± 0.54	51.5 ± 0.1	0.8 ± 0.3	2.06 ± 0.59	1.71	51.0	52.1	2.10	51.5
	44	1.72 ± 0.24	52.8 ± 0.0	0.4 ± 0.1	4.37 ± 0.59	1.84	52.1	53.3	4.31	52.7
	95	2.66 ± 0.54	51.7 ± 0.1	1.0 ± 0.2	2.39 ± 0.73	2.87	50.7	52.4	3.08	51.4
	95	2.29 ± 0.41	52.9 ± 0.0	0.5 ± 0.1	4.21 ± 0.73	2.20	52.4	53.6	3.93	53.0
G35.25-0.24	44	1.57 ± 0.27	62.2 ± 0.0	0.5 ± 0.1	3.02 ± 0.55	1.49	61.5	62.8	2.82	62.2
	44	1.45 ± 0.37	80.9 ± 0.1	0.7 ± 0.3	1.91 ± 0.55	1.41	80.2	81.8	1.90	80.9
G35.39+0.02	44	1.00 ± 0.23	93.7 ± 0.0	0.4 ± 0.1	2.33 ± 0.50	1.30	93.2	94.1	2.43	93.7
	44	1.13 ± 0.21	94.7 ± 0.0	0.3 ± 0.1	3.43 ± 0.50	1.14	94.1	95.6	3.51	94.7
G35.59+0.06	22	7.99 ± 0.43	-11.5 ± 0.0	1.6 ± 0.1	4.84 ± 0.51	8.01	-13.5	-9.0	4.89	-11.7
	22	7.88 ± 0.48	-3.4 ± 0.1	1.9 ± 0.1	3.91 ± 0.51	7.92	-5.9	-1.2	4.42	-3.5
	44	4.80 ± 0.47	47.9 ± 0.1	1.2 ± 0.1	3.70 ± 0.54	5.47	45.8	48.8	4.35	47.8
	44	6.11 ± 0.43	49.4 ± 0.0	0.8 ± 0.1	6.77 ± 0.54	7.00	48.8	51.4	8.44	49.3
	95	7.72 ± 0.89	49.2 ± 0.2	3.0 ± 0.5	2.38 ± 0.71	7.87	45.7	51.6	3.31	49.5
G35.79-0.17	22	12.48 ± 0.58	59.3 ± 0.0	2.0 ± 0.1	5.93 ± 0.62	11.10	56.9	61.2	5.73	59.9
	22	7.82 ± 0.50	62.9 ± 0.0	1.4 ± 0.1	5.27 ± 0.62	7.24	61.2	64.7	4.91	63.1
	44	2.26 ± 0.48	59.9 ± 0.1	0.7 ± 0.2	3.05 ± 0.71	3.01	59.0	60.7	4.16	59.9
	44	7.67 ± 0.72	61.9 ± 0.1	1.9 ± 0.2	3.72 ± 0.71	7.17	60.7	64.4	3.88	62.1
G36.64-0.21	22	12.29 ± 0.31	77.5 ± 0.0	0.8 ± 0.0	14.51 ± 0.49	13.12	75.9	79.1	14.98	77.4
G36.70+0.09	22	4.15 ± 0.52	52.9 ± 0.1	1.2 ± 0.2	3.17 ± 0.67	4.58	51.4	54.8	3.75	52.6
G36.90-0.41	22	2.92 ± 0.40	84.9 ± 0.0	0.6 ± 0.1	4.68 ± 0.74	2.38	84.1	86.1	4.46	85.1
G37.02-0.03	22	1.86 ± 0.29	80.7 ± 0.1	0.9 ± 0.2	2.05 ± 0.42	2.39	79.7	81.4	2.15	80.7

Table 3.4 (cont'd)

Source	Frequency (GHz)	Gaussian Fit S_{int} (Jy km s^{-1})	Gaussian Fit V_{peak} (km s^{-1})	Gaussian Fit FWHM (km s^{-1})	Gaussian Fit S_{peak} (Jy)	Integrated Fit S_{int} (Jy km s^{-1})	Integrated Fit v_{min} (km s^{-1})	Integrated Fit v_{max} (km s^{-1})	Integrated Fit S_{peak} (Jy)	Integrated Fit V_{peak} (km s^{-1})
	22	0.70 ± 0.24	81.6 ± 0.1	0.4 ± 0.2	1.56 ± 0.42	0.84	81.4	82.3	1.70	81.5
G37.04-0.04	22	1.14 ± 0.27	80.8 ± 0.1	0.9 ± 0.3	1.18 ± 0.35	1.15	79.7	81.2	1.52	80.7
	22	0.70 ± 0.16	81.8 ± 0.0	0.3 ± 0.1	2.12 ± 0.35	0.87	81.2	82.4	2.14	81.8
G37.38-0.09	44	2.82 ± 0.36	56.0 ± 0.1	0.8 ± 0.1	3.21 ± 0.57	3.48	54.7	57.6	3.33	55.9
G37.47-0.11	22	1.48 ± 0.19	56.8 ± 0.0	0.5 ± 0.1	3.10 ± 0.36	1.06	55.4	58.0	3.16	56.8
G37.55+0.19	22	7.49 ± 0.21	83.7 ± 0.0	0.7 ± 0.0	10.61 ± 0.36	7.82	82.5	84.4	10.28	83.7
	22	16.88 ± 0.26	85.7 ± 0.0	1.1 ± 0.0	14.61 ± 0.36	17.15	84.4	87.7	14.53	85.6
	22	3.16 ± 0.30	94.5 ± 0.1	1.4 ± 0.2	2.10 ± 0.36	3.22	93.1	96.0	2.30	94.5
	44	1.09 ± 0.28	84.0 ± 0.1	0.5 ± 0.2	1.87 ± 0.47	1.34	83.3	84.6	1.83	84.0
	44	1.59 ± 0.37	85.1 ± 0.1	0.8 ± 0.2	1.76 ± 0.47	2.03	84.6	85.8	1.82	85.5
	44	4.72 ± 0.43	86.6 ± 0.0	1.2 ± 0.1	3.76 ± 0.47	4.75	85.8	88.6	4.35	86.5
	95	0.88 ± 0.29	84.0 ± 0.1	0.5 ± 0.2	1.51 ± 0.36	1.17	83.0	84.5	1.65	84.1
	95	1.31 ± 0.56	85.2 ± 0.2	1.3 ± 0.5	0.96 ± 0.36	1.53	84.5	86.3	1.68	85.5
	95	1.70 ± 0.59	87.0 ± 0.3	1.9 ± 0.7	0.85 ± 0.36	1.32	86.3	88.6	1.29	86.7
G37.60+0.42	22	2.13 ± 0.72	97.4 ± 0.1	0.6 ± 0.1	3.49 ± 0.54	3.52	96.0	98.1	3.91	97.4
	22	2.90 ± 0.99	98.5 ± 0.2	1.3 ± 0.6	2.03 ± 0.54	2.54	98.1	100.0	2.77	98.7
	22	7.38 ± 0.42	137.0 ± 0.0	1.3 ± 0.1	5.26 ± 0.54	7.43	135.3	139.1	5.17	137.2
	44	3.03 ± 0.30	89.8 ± 0.0	0.7 ± 0.1	4.17 ± 0.50	2.78	87.4	90.5	4.51	89.9
	95	1.71 ± 0.42	89.8 ± 0.1	0.7 ± 0.2	2.47 ± 0.63	2.27	88.1	91.6	2.84	89.7
G37.74-0.12	22	7.52 ± 0.46	42.0 ± 0.2	1.0 ± 0.2	7.17 ± 0.73	11.10	40.3	43.1	7.65	42.2
	22	18.68 ± 0.46	43.8 ± 0.2	1.0 ± 0.2	17.20 ± 0.73	20.52	43.1	45.2	18.35	43.7
	22	10.16 ± 0.46	46.0 ± 0.2	1.8 ± 0.2	5.35 ± 0.73	8.31	45.2	47.2	6.66	46.0
	22	7.76 ± 0.46	52.7 ± 0.2	1.4 ± 0.2	5.34 ± 0.73	7.74	51.4	54.2	6.25	52.8
G37.76-0.19	22	1.93 ± 0.39	54.6 ± 0.1	0.5 ± 0.1	3.84 ± 0.77	2.06	53.3	55.2	3.48	54.7
	22	23.84 ± 0.58	60.1 ± 0.0	1.1 ± 0.0	19.93 ± 0.77	24.49	58.0	62.1	19.99	60.1
G37.77-0.22	22	2.44 ± 0.44	58.1 ± 0.1	1.6 ± 0.3	1.48 ± 0.44	2.09	56.6	59.0	1.43	57.8
	22	3.31 ± 0.41	60.2 ± 0.1	1.3 ± 0.2	2.44 ± 0.44	3.18	59.0	61.8	2.53	60.1
	22	1.06 ± 0.27	64.5 ± 0.1	0.6 ± 0.2	1.60 ± 0.44	0.88	63.7	65.7	1.66	64.5

Table 3.4 (cont'd)

Source	Frequency (GHz)	Gaussian Fit S_{int} (Jy km s^{-1})	Gaussian Fit V_{peak} (km s^{-1})	Gaussian Fit FWHM (km s^{-1})	Gaussian Fit S_{peak} (Jy)	Integrated Fit S_{int} (Jy km s^{-1})	Integrated Fit v_{min} (km s^{-1})	Integrated Fit v_{max} (km s^{-1})	Integrated Fit S_{peak} (Jy)	Integrated Fit V_{peak} (km s^{-1})
	22	1.63 ± 0.34	66.7 ± 0.1	0.8 ± 0.2	2.03 ± 0.44	1.65	65.7	67.1	1.91	66.9
	22	2.43 ± 0.36	67.8 ± 0.1	1.0 ± 0.2	2.39 ± 0.44	2.07	67.1	68.8	2.47	67.7
	44	4.18 ± 0.58	63.5 ± 0.1	1.8 ± 0.3	2.20 ± 0.45	3.60	62.6	64.5	2.48	64.0
	44	3.09 ± 0.40	65.3 ± 0.0	0.9 ± 0.1	3.38 ± 0.45	3.48	64.5	66.3	3.88	65.2
	95	3.10 ± 0.67	63.5 ± 0.1	1.3 ± 0.2	2.28 ± 0.56	4.13	61.8	64.9	2.75	63.7
	95	3.96 ± 0.87	65.6 ± 0.2	2.2 ± 0.6	1.67 ± 0.56	5.19	64.9	68.8	3.07	65.3
G38.03-0.30	22	9.30 ± 1.20	63.6 ± 0.1	2.0 ± 0.3	4.26 ± 0.47	8.31	60.6	64.4	4.61	63.4
	22	1.70 ± 0.89	65.1 ± 0.1	0.7 ± 0.2	2.24 ± 0.47	3.90	64.4	66.3	3.44	64.6
G38.26-0.08	22	49.54 ± 0.68	9.8 ± 0.0	1.2 ± 0.0	39.71 ± 0.90	47.43	7.8	12.1	38.68	9.8
G38.56+0.15	22	4.32 ± 0.57	29.8 ± 0.1	1.5 ± 0.2	2.75 ± 0.64	4.39	28.2	31.5	4.25	29.8
G38.60-0.21	22	2.34 ± 0.43	62.9 ± 0.1	1.0 ± 0.2	2.28 ± 0.64	3.06	62.1	64.2	2.70	63.1
	22	6.91 ± 0.57	65.3 ± 0.1	1.5 ± 0.1	4.39 ± 0.64	6.43	64.2	66.2	5.31	65.7
	22	8.46 ± 0.46	67.3 ± 0.0	1.0 ± 0.1	8.01 ± 0.64	8.92	66.2	69.1	7.63	67.1
G38.92-0.36	22	47.44 ± 0.39	33.2 ± 0.0	0.8 ± 0.0	54.89 ± 0.64	48.91	32.1	35.5	58.65	33.1
	22	2.11 ± 0.29	37.6 ± 0.0	0.6 ± 0.1	3.45 ± 0.64	2.14	36.8	38.1	3.53	37.5
	22	2.12 ± 0.31	38.7 ± 0.0	0.5 ± 0.1	3.77 ± 0.64	2.15	38.1	39.2	3.54	38.6
	44	12.61 ± 1.71	37.7 ± 0.2	3.9 ± 0.7	3.05 ± 1.08	10.10	35.7	41.9	5.50	37.4
	95	14.01 ± 1.03	37.9 ± 0.1	3.8 ± 0.4	3.47 ± 0.75	13.47	34.1	41.3	4.90	38.1
G39.39-0.14	44	2.58 ± 0.56	66.3 ± 0.1	1.0 ± 0.3	2.40 ± 0.62	2.48	64.6	67.6	2.50	66.5
	95	3.45 ± 0.35	66.3 ± 0.1	1.2 ± 0.1	2.82 ± 0.47	3.27	65.0	67.6	3.04	66.5
G40.28-0.22	22	41.47 ± 0.63	71.6 ± 0.0	1.0 ± 0.0	40.32 ± 0.89	46.52	70.4	72.5	41.07	71.4
	22	90.67 ± 0.69	73.7 ± 0.0	1.2 ± 0.0	71.29 ± 0.89	89.49	72.5	75.2	76.18	73.7
	22	7.45 ± 0.85	84.2 ± 0.1	1.5 ± 0.2	4.61 ± 0.89	7.49	83.2	85.7	6.62	84.1
	44	58.12 ± 2.17	72.7 ± 0.2	0.6 ± 0.2	89.21 ± 1.41	88.72	71.6	73.3	101.78	72.7
	44	67.83 ± 2.17	73.6 ± 0.2	1.2 ± 0.2	53.62 ± 1.41	49.43	73.3	74.5	53.64	73.4
	44	14.35 ± 2.17	75.2 ± 0.2	0.6 ± 0.2	21.83 ± 1.41	15.63	74.5	75.7	21.21	75.1
	95	59.11 ± 1.67	72.8 ± 0.2	0.8 ± 0.2	72.66 ± 0.98	78.40	71.6	73.6	78.36	72.8
	95	34.69 ± 1.67	73.8 ± 0.2	1.1 ± 0.2	30.73 ± 0.98	23.82	73.6	74.9	28.95	73.8

Table 3.4 (cont'd)

Source	Frequency (GHz)	Gaussian Fit				Integrated Fit				
		S_{int} (Jy km s^{-1})	V_{peak} (km s^{-1})	FWHM (km s^{-1})	S_{peak} (Jy)	S_{int} (Jy km s^{-1})	v_{min} (km s^{-1})	v_{max} (km s^{-1})	S_{peak} (Jy)	V_{peak} (km s^{-1})
	95	11.94 ± 1.67	75.3 ± 0.2	0.8 ± 0.2	14.62 ± 0.98	10.95	74.9	75.8	15.08	75.1
G40.62-0.14	22	13.65 ± 0.71	33.9 ± 0.0	1.2 ± 0.1	10.33 ± 0.84	14.78	32.1	36.8	10.56	34.1
G41.08-0.13	22	0.80 ± 0.11	-16.9 ± 0.2	0.9 ± 0.2	0.82 ± 0.34	1.18	-18.2	-16.6	1.17	-16.8
	22	1.33 ± 0.11	-15.8 ± 0.2	1.0 ± 0.2	1.27 ± 0.34	1.87	-16.6	-15.5	1.78	-15.3
	22	1.42 ± 0.11	-15.0 ± 0.2	0.7 ± 0.2	1.89 ± 0.34	2.80	-15.5	-14.4	3.02	-14.3
	22	2.67 ± 0.11	-14.1 ± 0.2	0.9 ± 0.2	2.77 ± 0.34	2.70	-14.4	-13.2	3.02	-14.3
	22	1.04 ± 0.11	-13.0 ± 0.2	0.8 ± 0.2	1.26 ± 0.34	0.85	-13.2	-11.9	1.50	-13.0
G41.12-0.22	44	2.23 ± 0.54	59.0 ± 0.1	0.9 ± 0.3	2.39 ± 0.72	2.42	57.9	59.8	3.25	59.0
	44	4.13 ± 0.67	60.5 ± 0.1	0.8 ± 0.1	5.01 ± 0.72	4.36	59.8	60.9	4.78	60.5
	44	4.37 ± 0.74	61.7 ± 0.1	0.9 ± 0.2	4.43 ± 0.72	4.84	60.9	63.3	5.26	62.0
G41.34-0.14	22	2.54 ± 0.41	60.8 ± 0.1	1.9 ± 0.4	1.28 ± 0.38	3.25	58.6	63.8	1.65	60.7
G42.03+0.19	22	2.69 ± 0.27	13.7 ± 0.0	0.7 ± 0.1	3.80 ± 0.48	2.90	12.3	14.5	3.55	13.7
G42.30-0.30	22	3.36 ± 0.57	21.8 ± 0.1	0.8 ± 0.1	3.83 ± 0.40	3.70	20.7	22.5	3.87	21.9
	22	2.19 ± 0.78	23.1 ± 0.1	1.2 ± 0.6	1.76 ± 0.40	2.07	22.5	24.2	1.93	23.0
G42.43-0.26	22	4.66 ± 0.56	63.4 ± 0.1	2.3 ± 0.3	1.93 ± 0.51	4.68	61.0	64.9	2.95	64.0
	22	1.69 ± 0.36	65.7 ± 0.1	0.9 ± 0.2	1.86 ± 0.51	2.05	64.9	66.8	2.06	65.4
	22	3.37 ± 0.34	68.7 ± 0.0	0.8 ± 0.1	3.83 ± 0.51	4.67	66.8	70.0	3.87	68.6
	44	5.13 ± 0.34	63.0 ± 0.0	0.4 ± 0.0	11.23 ± 0.73	4.96	62.1	63.7	9.65	63.0
	95	2.22 ± 0.30	63.1 ± 0.0	0.6 ± 0.1	3.49 ± 0.56	2.12	62.3	64.3	4.09	63.1
G43.04-0.46	22	4.56 ± 0.39	45.7 ± 0.0	0.8 ± 0.1	5.57 ± 0.66	5.45	43.8	46.6	5.41	45.8
	22	2.96 ± 0.55	51.4 ± 0.1	1.3 ± 0.3	2.10 ± 0.66	3.66	49.2	52.6	2.64	51.3
	22	1.46 ± 0.34	58.0 ± 0.1	0.7 ± 0.1	2.05 ± 0.66	1.23	57.1	58.7	2.00	57.8
	44	4.49 ± 0.65	58.0 ± 0.0	0.5 ± 0.1	8.72 ± 1.07	7.12	56.5	59.2	8.33	58.1
	95	4.24 ± 1.00	58.1 ± 0.0	0.7 ± 0.3	5.46 ± 0.81	9.56	55.7	61.5	7.07	58.1
G43.80-0.13	22	29.98 ± 13.18	35.4 ± 0.2	1.3 ± 0.2	22.02 ± 4.07	32.21	33.7	36.1	23.55	35.4
	22	88.35 ± 13.18	37.4 ± 0.2	1.2 ± 0.2	70.24 ± 4.07	88.69	36.1	38.3	71.72	37.3
	22	306.03 ± 13.18	39.9 ± 0.2	1.5 ± 0.2	194.49 ± 4.07	265.65	38.3	40.4	199.17	40.0
	22	493.93 ± 13.18	41.2 ± 0.2	0.6 ± 0.2	716.87 ± 4.07	607.75	40.4	42.0	714.22	41.1

Table 3.4 (cont'd)

Source	Frequency (GHz)	Gaussian Fit S_{int} (Jy km s^{-1})	Gaussian Fit V_{peak} (km s^{-1})	Gaussian Fit FWHM (km s^{-1})	Gaussian Fit S_{peak} (Jy)	Integrated Fit S_{int} (Jy km s^{-1})	Integrated Fit v_{min} (km s^{-1})	Integrated Fit v_{max} (km s^{-1})	Integrated Fit S_{peak} (Jy)	Integrated Fit V_{peak} (km s^{-1})
	22	69.63 ± 13.18	42.2 ± 0.2	0.9 ± 0.2	73.94 ± 4.07	51.93	42.0	42.9	80.30	42.1
	22	34.86 ± 0.99	43.6 ± 0.2	1.4 ± 0.2	23.95 ± 0.81	47.67	42.9	44.6	35.00	44.0
	22	32.44 ± 0.99	44.6 ± 0.2	2.3 ± 0.2	13.36 ± 0.81	17.77	44.6	46.9	15.30	45.1
	22	23.52 ± 0.99	49.2 ± 0.2	2.5 ± 0.2	8.71 ± 0.81	21.95	46.9	51.1	9.71	49.3
	44	4.34 ± 0.71	44.4 ± 0.4	5.4 ± 1.2	0.76 ± 0.39	3.04	42.1	47.6	1.28	44.7
	95	6.52 ± 0.75	43.5 ± 0.4	6.8 ± 0.9	0.91 ± 0.44	6.15	38.3	49.2	2.10	43.5
G44.31+0.04	22	45.50 ± 2.70	52.5 ± 0.2	0.5 ± 0.2	83.42 ± 0.78	80.80	50.9	52.9	100.88	53.1
	22	92.04 ± 2.70	53.3 ± 0.2	0.6 ± 0.2	138.23 ± 0.78	83.15	52.9	54.1	139.26	53.3
	22	59.74 ± 2.70	55.2 ± 0.2	1.3 ± 0.2	43.40 ± 0.78	107.12	53.4	65.0	96.82	53.5
	22	6.94 ± 2.70	64.2 ± 0.2	0.6 ± 0.2	11.07 ± 0.78	59.79	54.1	56.8	44.65	55.2
	44	4.56 ± 0.59	57.4 ± 0.1	1.0 ± 0.2	4.42 ± 0.72	6.07	55.0	58.9	5.95	57.4
	95	10.00 ± 1.22	57.7 ± 0.2	3.4 ± 0.6	2.73 ± 0.84	8.31	54.9	59.5	4.92	58.0
G45.07+0.13	22	2.94 ± 0.58	54.7 ± 0.2	0.7 ± 0.2	3.89 ± 0.59	3.56	53.6	55.3	4.34	54.7
	22	3.75 ± 0.58	56.7 ± 0.2	2.0 ± 0.2	1.79 ± 0.59	3.50	55.3	57.6	2.62	56.4
	22	8.16 ± 0.58	58.6 ± 0.2	0.8 ± 0.2	9.70 ± 0.59	10.58	57.6	59.2	10.08	58.7
	22	24.22 ± 0.58	60.1 ± 0.2	1.0 ± 0.2	23.15 ± 0.59	24.92	59.2	61.2	23.67	59.9
	22	5.17 ± 0.58	62.0 ± 0.2	1.5 ± 0.2	3.34 ± 0.59	5.60	61.2	62.9	4.12	62.0
	22	2.74 ± 0.50	63.4 ± 0.1	1.2 ± 0.3	2.18 ± 0.59	2.47	62.9	64.6	2.41	63.1
	22	5.06 ± 0.40	68.0 ± 0.0	0.9 ± 0.1	5.43 ± 0.59	5.93	66.6	69.0	6.09	67.9
	44	0.93 ± 0.33	59.2 ± 0.1	0.5 ± 0.3	1.71 ± 0.47	0.94	58.3	60.0	1.55	59.1
	95	5.49 ± 0.59	58.6 ± 0.2	3.5 ± 0.5	1.49 ± 0.46	4.68	55.7	60.6	2.33	59.4
G45.44+0.07	22	1.19 ± 0.30	38.8 ± 0.1	0.5 ± 0.1	2.28 ± 0.61	1.27	38.1	39.4	2.24	38.8
	22	5.28 ± 0.40	41.0 ± 0.0	1.0 ± 0.1	4.94 ± 0.61	5.09	40.0	42.0	4.77	41.1
	22	0.85 ± 0.22	49.5 ± 0.0	0.2 ± 1.1	3.79 ± 0.61	0.97	48.9	49.9	2.52	49.5
	22	14.04 ± 0.39	51.4 ± 0.0	0.9 ± 0.0	14.00 ± 0.61	13.88	49.9	52.6	14.16	51.2
	22	2.80 ± 0.38	56.0 ± 0.1	0.8 ± 0.1	3.19 ± 0.61	2.68	55.0	56.9	3.30	56.1
G45.47+0.05	22	3.12 ± 0.50	49.4 ± 0.1	1.5 ± 0.3	1.95 ± 0.55	2.67	48.2	50.0	2.19	49.5
	22	12.87 ± 0.40	51.4 ± 0.0	0.9 ± 0.0	13.29 ± 0.55	13.59	50.0	52.5	12.99	51.4

Table 3.4 (cont'd)

Source	Frequency (GHz)	Gaussian Fit				Integrated Fit				
		S_{int} (Jy km s^{-1})	V_{peak} (km s^{-1})	FWHM (km s^{-1})	S_{peak} (Jy)	S_{int} (Jy km s^{-1})	v_{min} (km s^{-1})	v_{max} (km s^{-1})	S_{peak} (Jy)	V_{peak} (km s^{-1})
G45.47+0.13	22	4.91 ± 0.48	67.1 ± 0.0	0.9 ± 0.1	5.23 ± 0.75	4.55	66.3	68.1	5.15	67.3
G45.49+0.13	22	2.66 ± 0.39	67.0 ± 0.1	1.2 ± 0.2	2.09 ± 0.48	2.85	65.1	68.2	2.49	66.9
	22	5.03 ± 0.64	74.4 ± 0.2	2.7 ± 0.5	1.73 ± 0.48	5.06	71.9	76.0	2.63	74.7
	22	1.17 ± 0.28	77.0 ± 0.1	0.6 ± 0.1	1.73 ± 0.48	1.42	76.0	77.9	1.86	77.0
	44	4.13 ± 0.64	62.4 ± 0.3	3.5 ± 0.6	1.11 ± 0.50	3.53	60.5	64.5	2.20	61.5
	95	3.94 ± 0.55	63.0 ± 0.2	3.2 ± 0.5	1.15 ± 0.45	4.02	59.8	66.2	1.69	62.6
G45.57-0.12	22	2.75 ± 0.41	7.4 ± 0.1	0.7 ± 0.1	3.79 ± 0.76	2.40	6.5	7.9	3.47	7.6
G45.81-0.36	22	3.25 ± 0.50	59.0 ± 0.1	1.1 ± 0.2	2.77 ± 0.68	3.74	57.6	60.2	3.04	58.9
	22	25.10 ± 0.40	63.0 ± 0.0	0.7 ± 0.0	32.66 ± 0.68	25.53	61.8	64.2	34.34	62.9
	44	6.82 ± 0.76	57.7 ± 0.1	1.8 ± 0.3	3.54 ± 0.66	6.97	55.8	59.5	4.60	57.7
	44	2.11 ± 0.54	60.7 ± 0.1	1.0 ± 0.4	1.99 ± 0.66	1.67	59.5	62.2	2.46	60.9
	95	8.31 ± 0.86	57.8 ± 0.1	2.4 ± 0.3	3.20 ± 0.68	8.39	55.6	59.7	4.82	57.7
	95	2.52 ± 0.70	60.6 ± 0.2	1.5 ± 0.4	1.63 ± 0.68	3.10	59.7	62.3	2.31	60.1
G46.12+0.38	22	1.94 ± 0.29	56.1 ± 0.1	0.9 ± 0.1	2.07 ± 0.46	1.43	55.2	57.0	1.75	55.9
G48.90-0.27	22	5.92 ± 0.46	66.4 ± 0.0	1.1 ± 0.1	5.12 ± 0.64	5.79	65.0	67.8	5.55	66.6
	44	2.63 ± 0.34	68.5 ± 0.0	0.5 ± 0.1	4.70 ± 0.62	1.98	67.7	69.7	4.37	68.6
G48.99-0.30	22	86.53 ± 0.95	66.0 ± 0.0	1.3 ± 0.0	62.40 ± 0.75	87.86	64.2	66.9	62.42	65.9
	22	11.85 ± 0.86	67.3 ± 0.0	0.8 ± 0.1	13.41 ± 0.75	14.88	66.9	68.3	21.88	67.0
	44	10.00 ± 1.71	65.5 ± 0.2	0.8 ± 0.2	12.39 ± 1.24	8.76	64.7	65.7	11.88	65.3
	44	50.78 ± 1.71	66.4 ± 0.2	0.5 ± 0.2	93.17 ± 1.24	56.03	65.7	66.8	96.31	66.4
	44	34.94 ± 1.71	67.5 ± 0.2	0.8 ± 0.2	39.07 ± 1.24	47.67	66.8	68.1	43.20	67.7
	44	24.49 ± 1.71	68.6 ± 0.2	2.0 ± 0.2	11.44 ± 1.24	16.67	68.1	70.3	14.76	68.3
	95	17.19 ± 1.44	65.9 ± 0.2	1.5 ± 0.2	10.59 ± 0.89	18.50	64.1	66.0	34.28	66.2
	95	29.48 ± 1.44	66.5 ± 0.2	0.5 ± 0.2	54.19 ± 0.89	39.66	66.0	66.9	60.83	66.4
	95	43.83 ± 1.44	67.6 ± 0.2	1.1 ± 0.2	38.82 ± 0.89	46.60	66.9	68.3	40.79	67.6
	95	21.67 ± 1.44	69.0 ± 0.2	1.7 ± 0.2	12.25 ± 0.89	22.76	68.3	70.9	17.92	68.4
G49.27+0.31	44	5.13 ± 0.50	3.2 ± 0.1	2.1 ± 0.3	2.26 ± 0.47	3.64	1.5	5.3	2.36	3.6
	95	2.80 ± 0.41	3.2 ± 0.2	2.5 ± 0.5	1.07 ± 0.37	2.15	0.9	5.6	1.27	3.0

Table 3.4 (cont'd)

Source	Frequency (GHz)	Gaussian Fit				Integrated Fit				
		S_{int} (Jy km s^{-1})	V_{peak} (km s^{-1})	FWHM (km s^{-1})	S_{peak} (Jy)	S_{int} (Jy km s^{-1})	v_{min} (km s^{-1})	v_{max} (km s^{-1})	S_{peak} (Jy)	V_{peak} (km s^{-1})
G53.04+0.11	44	11.30 ± 0.69	5.1 ± 0.1	3.1 ± 0.2	3.39 ± 0.60	11.00	2.2	7.6	4.42	4.4
	95	6.81 ± 0.86	5.6 ± 0.2	3.2 ± 0.5	1.97 ± 0.67	7.08	1.5	7.9	2.96	6.7
G53.14+0.07	22	2.30 ± 0.46	24.1 ± 0.1	0.7 ± 0.2	3.33 ± 0.73	2.66	23.1	25.5	3.72	24.0
	44	11.59 ± 0.79	21.9 ± 0.0	0.7 ± 0.1	16.29 ± 1.32	14.30	20.6	23.8	17.09	22.0
	95	10.88 ± 0.81	22.0 ± 0.0	0.8 ± 0.1	13.49 ± 1.15	27.30	15.6	26.1	14.73	22.0

Table 3.5. Maser Luminosities and associated BGPS Sources

Source	$L_{6.7}$* ($L_\odot$)	L_{22} ($L_\odot$)	L_{44} ($L_\odot$)	L_{95} ($L_\odot$)	T_{kin}** (K)	BGPS Source Name	S_{int} (Jy km s^{-1})	$N_{H_2}^{beam}$(T=20K) (10^{22}cm^{-2})	$M_{gas}(T_{kin})$ ($M_\odot$)
G34.82+0.35	9.0E-09				23.4	G034.820+00.350	3.4	6.2	6.9E+02
G35.03+0.35	2.1E-05	1.9E-04	2.2E-05	5.4E-05	40.0	G035.026+00.350	6.5	8.4	5.7E+03
G35.25-0.24	7.1E-08		1.9E-06		17.8	G035.247-00.238	0.1	0.5	4.1E+01
G35.39+0.02	2.8E-08		4.1E-06		16.7				
G35.40+0.03	7.7E-08				24.5	G035.398+00.026	0.9	1.2	4.8E+02
G35.59+0.06	7.3E-07	4.1E-05	6.3E-05	8.6E-05	23.5				
G35.79-0.17	4.0E-06	6.4E-06	7.1E-06		21.0	G035.794-00.176	2.6	4.5	7.2E+02
G36.02-0.20	1.6E-08				17.6	G036.012-00.198	0.7	1.5	4.6E+02
G36.64-0.21	2.9E-07	2.4E-05							
G36.70+0.09	5.5E-06	9.9E-06			16.2	G036.704+00.094	1.1	0.9	2.7E+03
G36.84-0.02	4.4E-07				14.3	G036.840-00.022	2.1	2.2	9.2E+02
G36.90-0.41	4.5E-08	1.4E-06			20.4	G036.899-00.410	1.3	1.6	6.1E+02
G36.92+0.48	8.8E-07								
G37.02-0.03	8.6E-07	1.9E-06			17.9				
G37.04-0.04	1.2E-06	1.2E-06			18.9	G037.042-00.034	2.8	2.8	1.5E+03
G37.38-0.09	8.5E-08		1.5E-05		48.4	G037.381-00.078	0.4	0.9	2.1E+02
G37.47-0.11	1.4E-05	2.3E-06			32.2	G037.475-00.102	0.8	1.8	8.1E+02
G37.53-0.11	3.9E-06				67.3	G037.547-00.112	2.6	4.5	1.1E+03
G37.55+0.19	1.4E-06	2.0E-05	1.2E-05	1.3E-05	25.4	G037.555+00.200	3.6	6.3	1.6E+03
G37.60+0.42	6.7E-06	1.2E-05	4.9E-06	8.6E-06	18.7	G037.599+00.426	0.6	1.8	4.7E+02
G37.74-0.12	1.8E-07	1.2E-04			28.2	G037.737-00.112	2.7	4.5	3.6E+03
G37.76-0.19	9.1E-07	5.5E-05			22.6	G037.753-00.192	0.9	2.1	1.3E+03
G37.77-0.22	2.3E-07	2.0E-05	2.9E-05	8.1E-05	25.1	G037.765-00.216	4.6	7.7	5.8E+03
G38.03-0.30	1.9E-06	4.3E-06			23.7	G038.041-00.300	0.4	1.1	1.0E+02
G38.08-0.27	2.1E-08								
G38.12-0.24	1.2E-06				24.5	G038.119-00.232	0.7	1.6	3.1E+02
G38.20-0.08	6.7E-06				18.6	G038.203-00.068	1.3	2.7	1.7E+03
G38.26-0.08	5.6E-06	1.6E-04							

Table 3.5 (cont'd)

Source	$L_{6.7}$* ($L_\odot$)	L_{22} ($L_\odot$)	L_{44} ($L_\odot$)	L_{95} ($L_\odot$)	T_{kin}** (K)	BGPS Source Name	S_{int} (Jy km s^{-1})	$N_{H_2}^{beam}$(T=20K) (10^{22}cm^{-2})	$M_{gas}(T_{kin})$ ($M_\odot$)
G38.26-0.20	7.2E-07				22.4				
G38.56+0.15	4.0E-09	4.5E-07							
G38.60-0.21	7.2E-08	7.5E-06			19.1	G038.599-00.214	0.8	1.2	3.0E+02
G38.66+0.08	1.3E-06								
G38.92-0.36	9.9E-07	1.4E-04	5.1E-05	1.5E-04	24.8				
G39.39-0.14	9.9E-08		2.1E-06	6.0E-06	27.7	G039.389-00.143	1.4	3.2	3.2E+02
G39.54-0.38	1.3E-07				25.4				
G40.28-0.22	1.1E-05	8.0E-05	1.7E-04	2.7E-04	37.7	G040.283-00.221	3.5	9.5	7.3E+02
G40.62-0.14	5.3E-06	3.8E-05			26.4	G040.622-00.139	3.0	5.1	4.4E+03
G40.94-0.04	1.0E-06								
G41.08-0.13	1.6E-07	1.5E-05			22.8	G041.076-00.125	0.9	1.5	1.0E+03
G41.12-0.11	4.4E-07								
G41.12-0.22	6.5E-07		4.0E-05		19.7	G041.122-00.223	1.8	1.8	2.7E+03
G41.16-0.20	1.0E-07				22.0				
G41.23-0.20	4.0E-06				26.2				
G41.27+0.37	1.5E-07				18.4	G041.268+00.373	0.5	0.8	1.4E+03
G41.34-0.14	2.4E-05	1.0E-05			16.6	G041.347-00.139	0.2	0.8	7.6E+02
G41.58+0.04	2.0E-07								
G42.03+0.19	2.6E-05	8.3E-06							
G42.30-0.30	3.9E-06	1.5E-05			20.3	G042.305-00.301	1.4	2.0	2.8E+03
G42.43-0.26	7.0E-07	1.6E-05	1.4E-05	1.3E-05	42.5	G042.435-00.263	2.9	2.6	1.4E+03
G42.70-0.15	7.1E-06								
G43.04-0.46	5.0E-06	1.6E-05	2.2E-05	6.5E-05	23.5	G043.039-00.455	1.7	4.8	1.8E+03
G43.08-0.08	3.6E-06				20.6	G043.073-00.079	0.6	1.4	1.4E+03
G43.80-0.13	2.5E-05	2.2E-03	1.2E-05	5.0E-05	28.3				
G44.31+0.04	1.9E-07	4.8E-04	1.7E-05	5.1E-05	61.3	G044.307+00.041	3.9	4.6	1.2E+03
G44.64-0.52	1.5E-07								
G45.07+0.13	8.4E-06	7.2E-05	2.4E-06	2.5E-05					

Table 3.5 (cont'd)

Source	$L_{6.7}$* ($L_\odot$)	L_{22} ($L_\odot$)	L_{44} ($L_\odot$)	L_{95} ($L_\odot$)	T_{kin}** (K)	BGPS Source Name	S_{int} (Jy km s^{-1})	$N_{H_2}^{beam}$(T=20K) (10^{22}cm^{-2})	$M_{gas}(T_{kin})$ ($M_\odot$)
G45.44+0.07	2.7E-07	3.0E-05			25.7				
G45.47+0.05	3.4E-06	1.9E-05			37.5				
G45.47+0.13	1.6E-06	5.0E-06			34.6	G045.477+00.135	6.8	7.9	3.1E+03
G45.49+0.13	1.7E-06	1.1E-05	8.1E-06	2.0E-05	16.2				
G45.57-0.12	2.6E-07	6.9E-06							
G45.81-0.36	2.9E-06	3.3E-05	1.9E-05	5.6E-05	24.3	G045.805-00.355	1.0	2.6	7.1E+02
G46.07+0.22	8.5E-07								
G46.12+0.38	4.1E-07	1.9E-06			30.5				
G48.89-0.17	3.6E-09								
G48.90-0.27	1.0E-07	3.5E-06	2.4E-06		17.0				
G48.99-0.30	1.0E-07	6.2E-05	1.5E-04	3.3E-04	22.9	G048.989-00.300	9.6	12.1	4.1E+03
G49.27+0.31	1.0E-05		1.8E-05	2.3E-05	35.8	G049.264+00.312	0.6	1.5	5.6E+02
G49.35+0.41	1.2E-06								
G49.41+0.33	2.4E-05								
G49.60-0.25	1.4E-05				23.3	G049.599-00.250	0.9	2.2	3.6E+02
G49.62-0.36	2.0E-07				23.3				
G50.78+0.15	9.5E-07				21.4	G050.774+00.151	0.7	1.6	5.9E+02
G52.92+0.41	8.4E-07				20.3	G052.922+00.412	1.0	2.2	4.8E+02
G53.04+0.11	4.2E-07		4.4E-05	6.2E-05	25.8	G053.036+00.112	1.2	3.4	1.5E+03
G53.14+0.07	1.4E-08	2.2E-07	2.4E-06	9.7E-06	27.9	G053.142+00.068	5.6	9.0	2.5E+02
G53.62+0.04	2.2E-07				20.8	G053.616+00.036	1.9	3.7	1.5E+02

*The luminosity is from Pandian et al. (2009).

**The kinetic temperature is from Pandian et al. (2012).

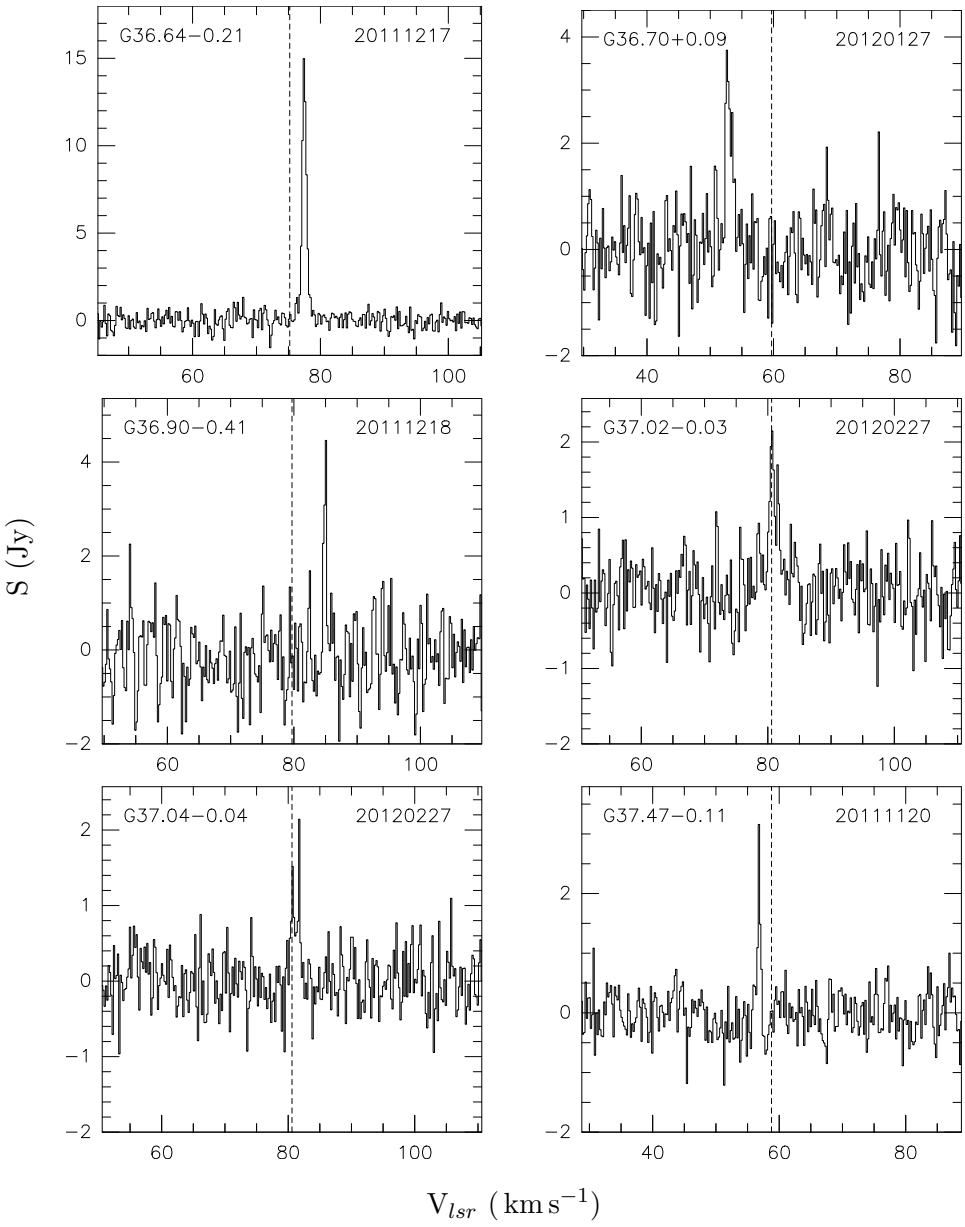

Figure 3.11: Sources detected only in the 22 GHz water maser. In each panel, the source name is presented at the top right corner and the dashed line shows the systemic velocity (Table 3.3).

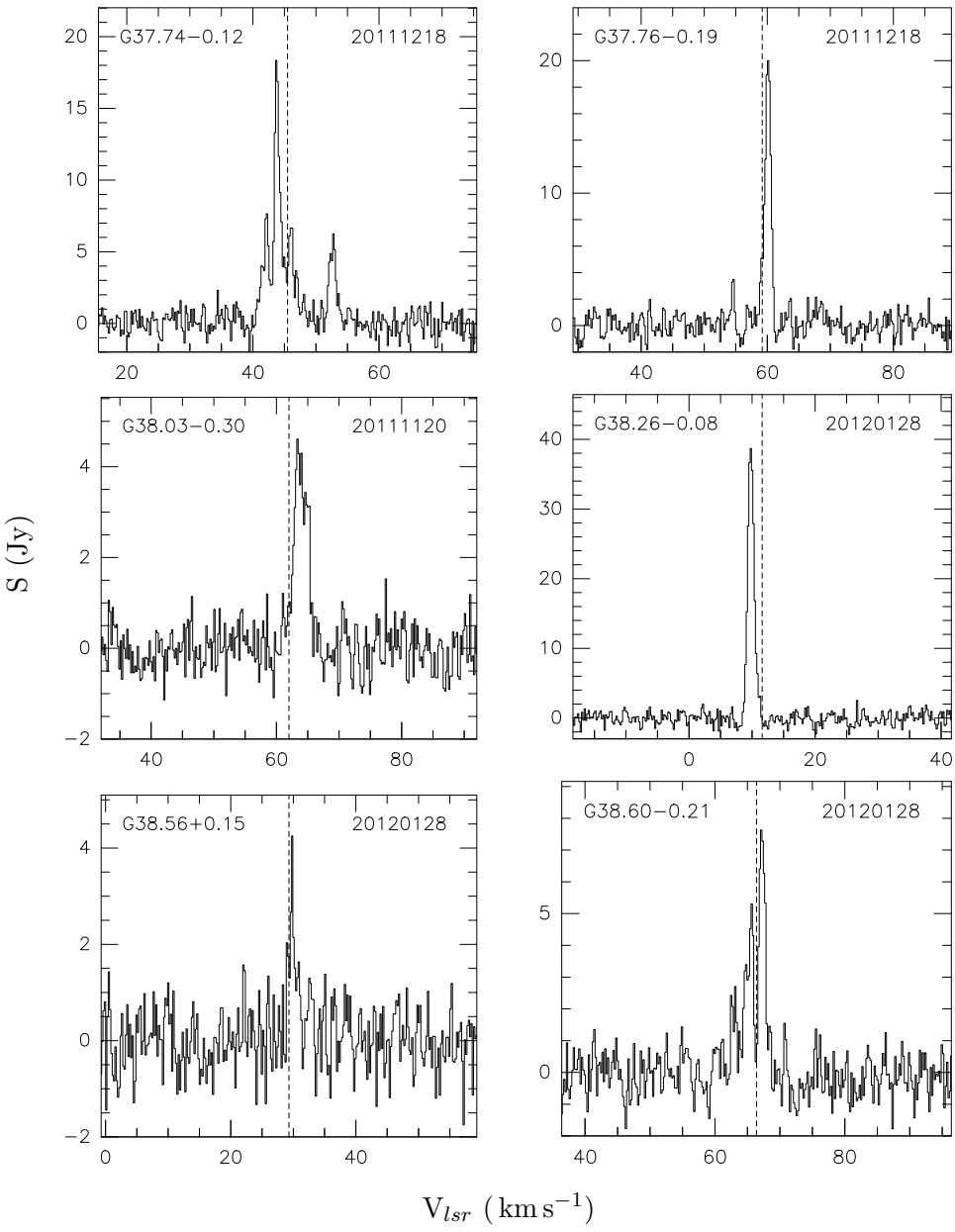

Figure 3.11: continued

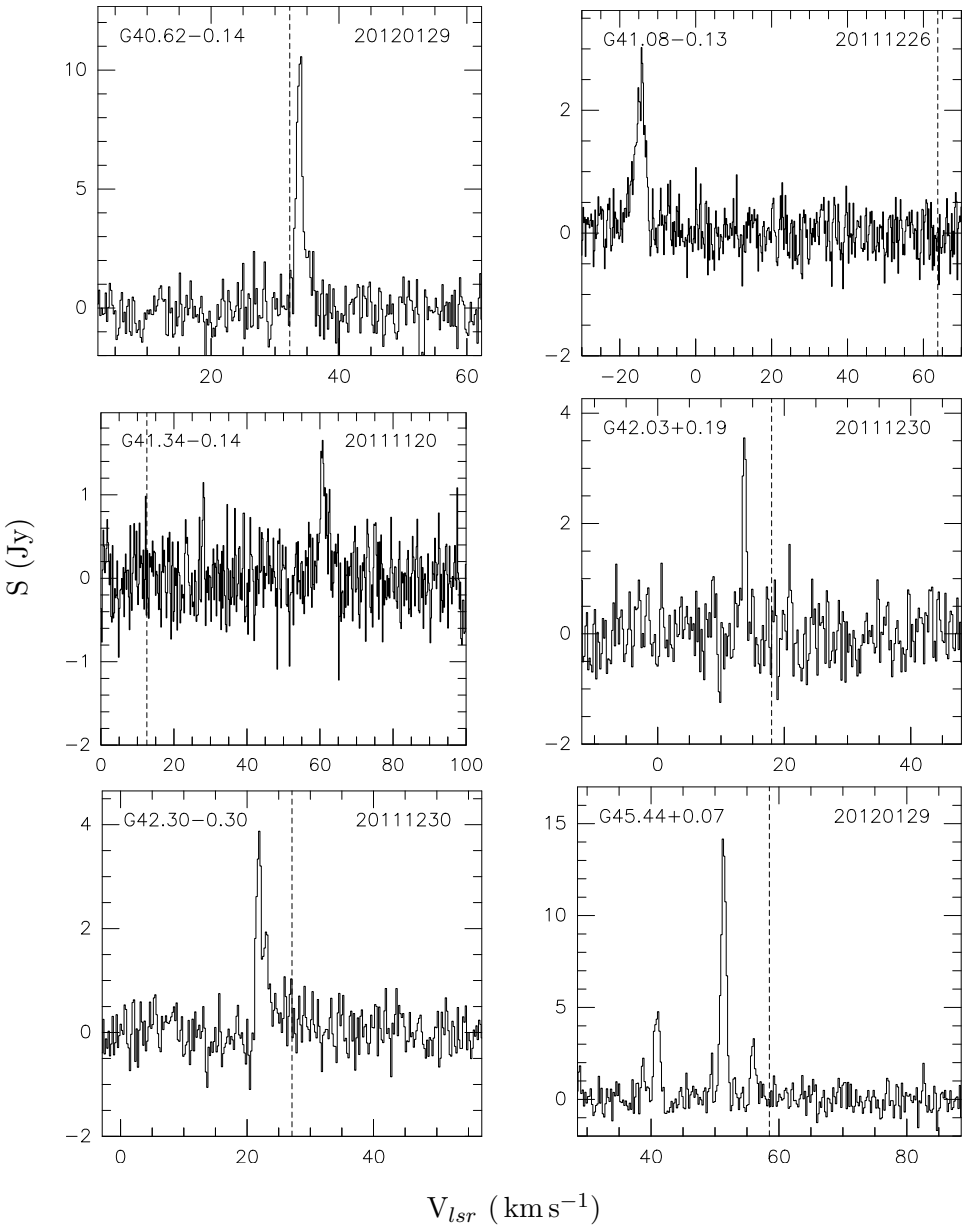

Figure 3.11: continued

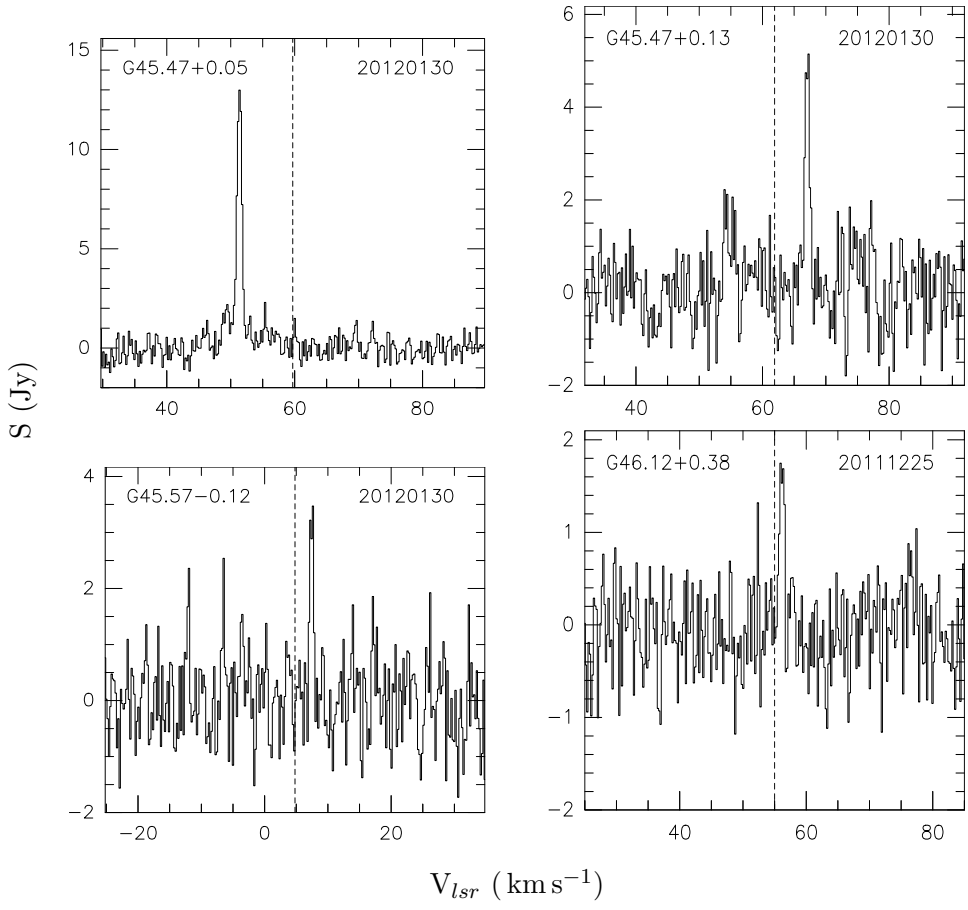

Figure 3.11: continued

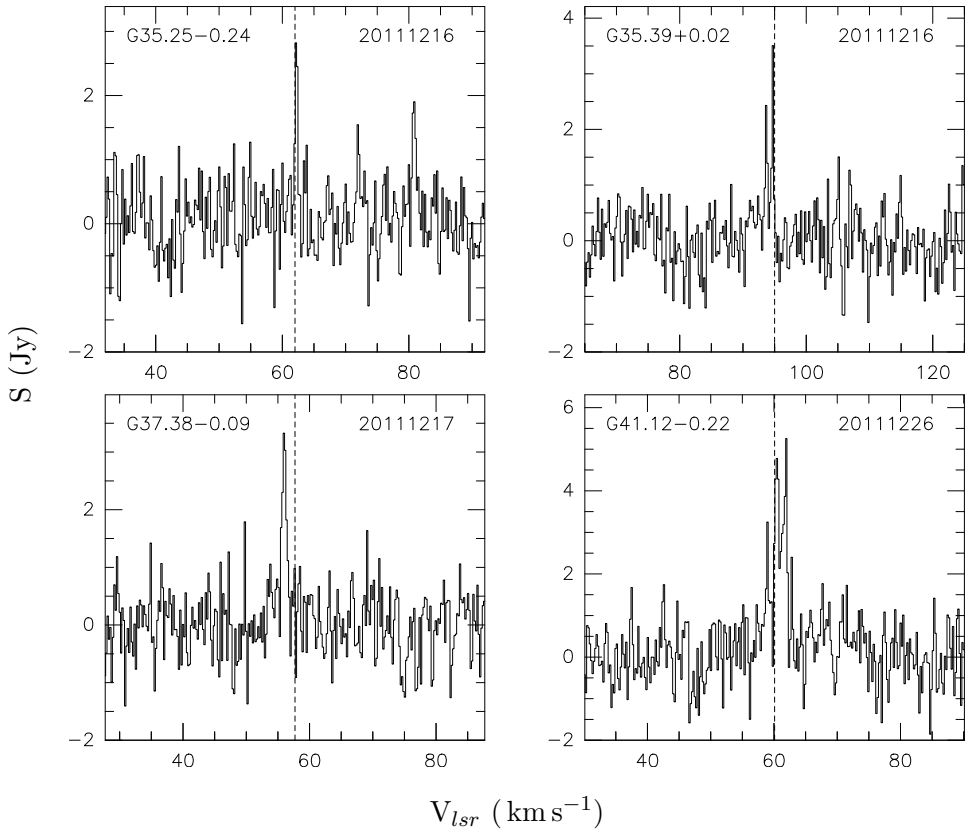

Figure 3.12: Sources detected only in the 44 GHz class I methanol maser.

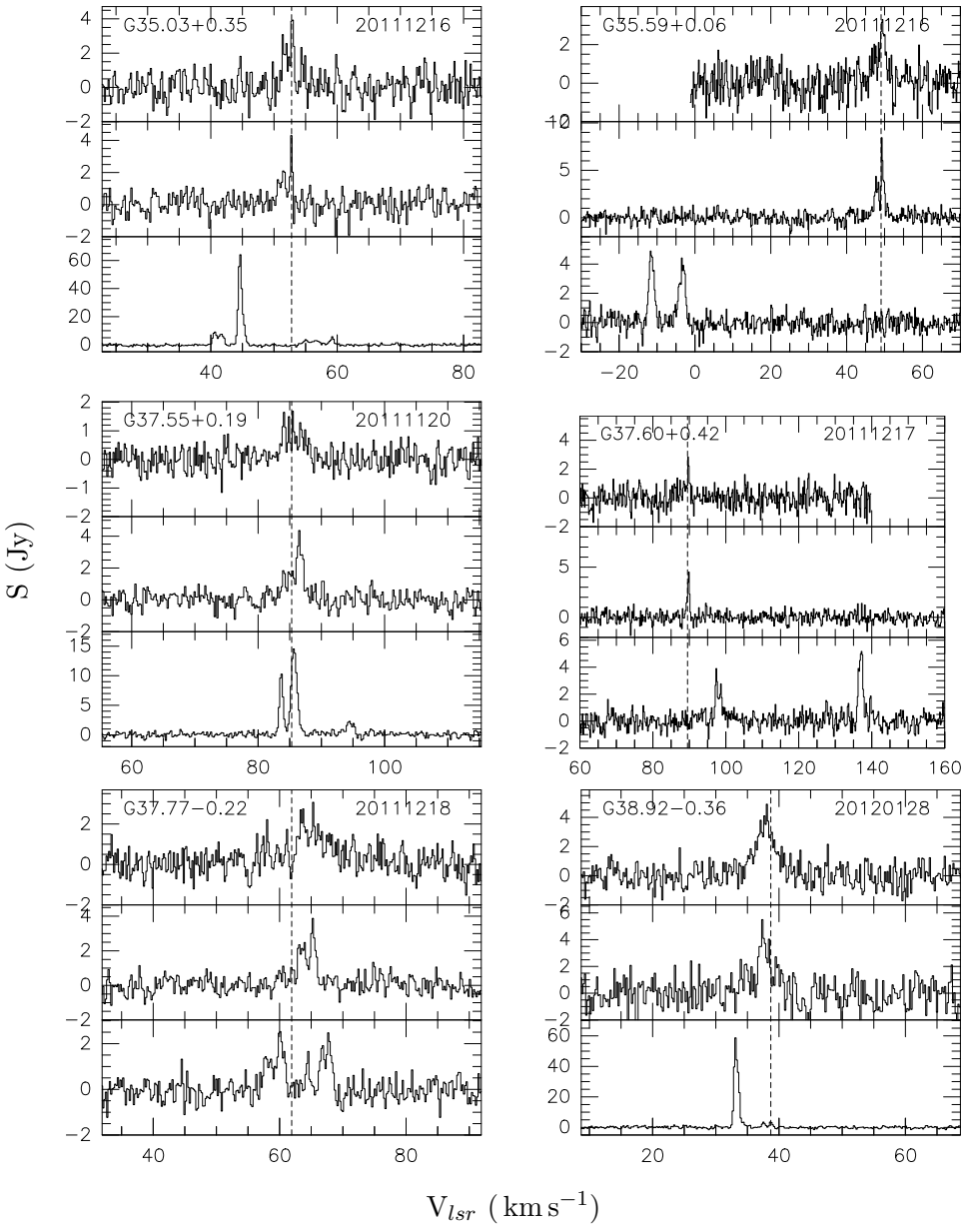

Figure 3.13: Sources detected in all the three maser transitions: 22 GHz (bottom), 44 GHz (middle), and 95 GHz (top).

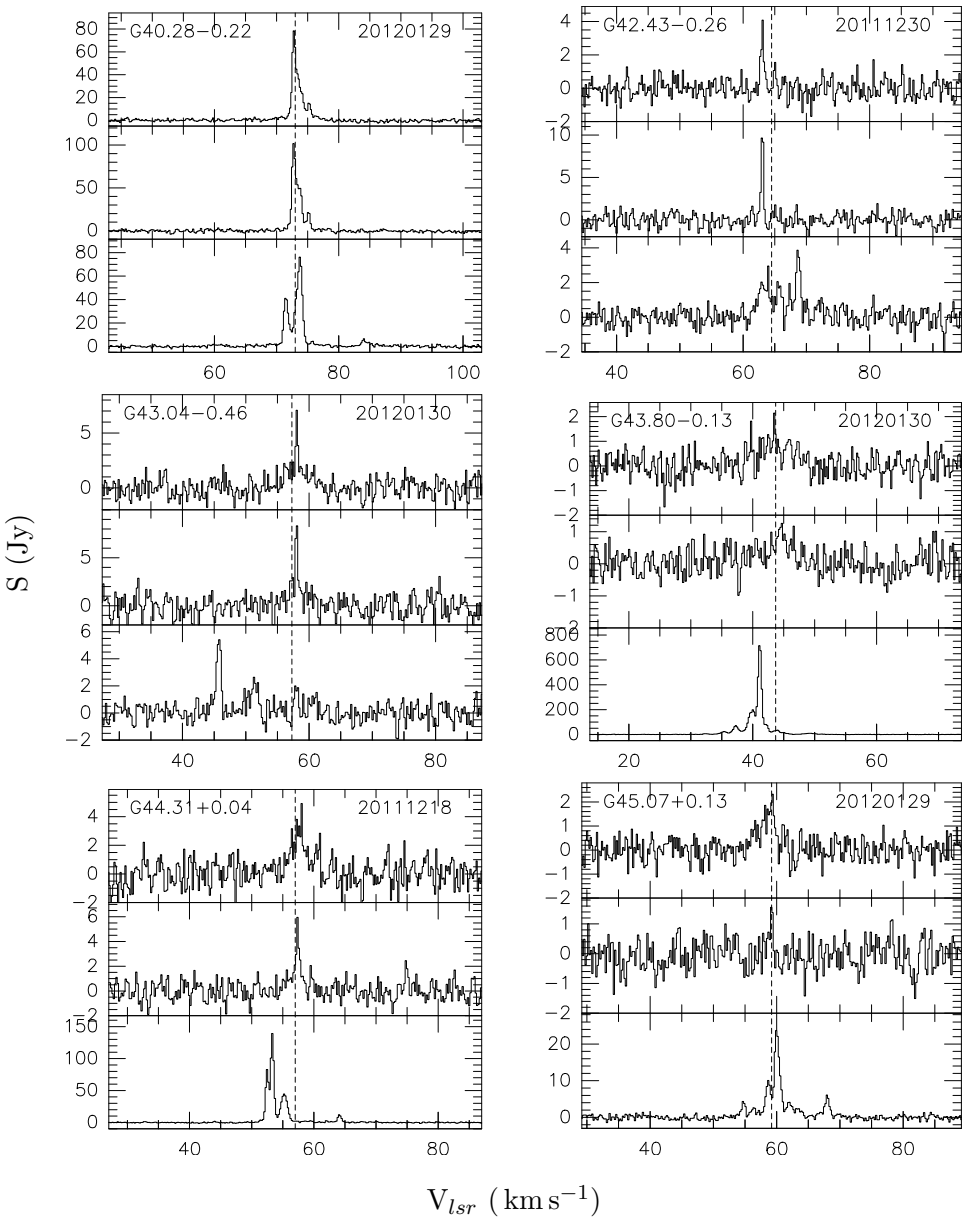

Figure 3.13: continued

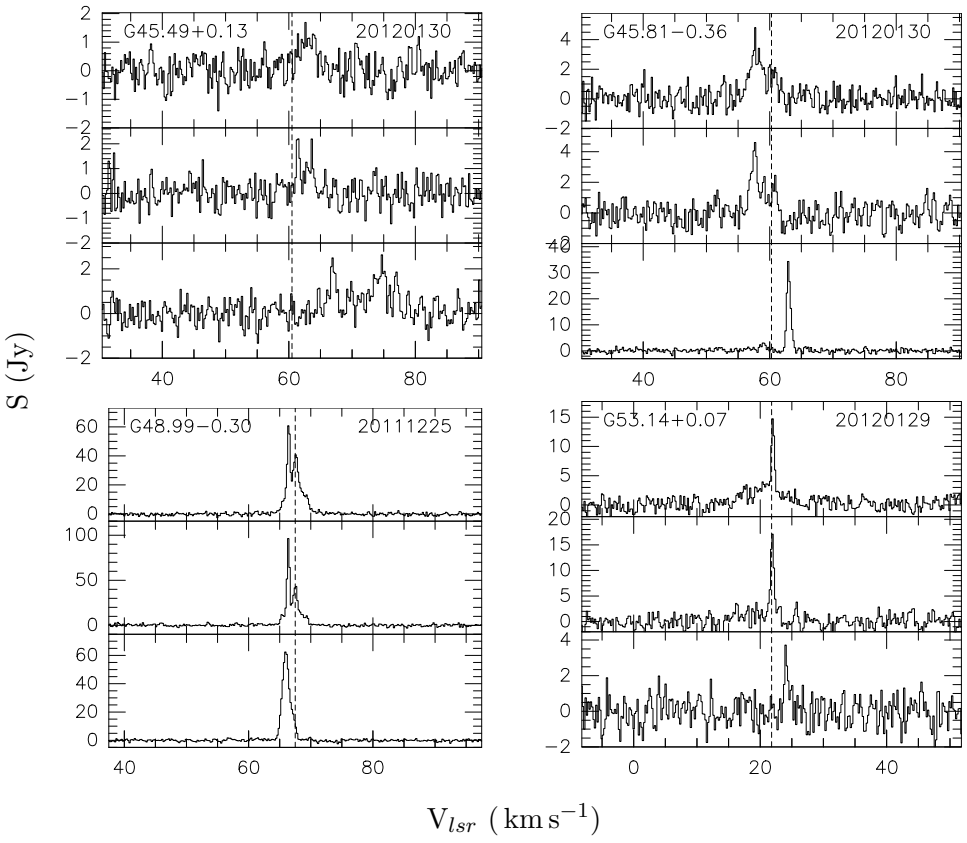

Figure 3.13: continued

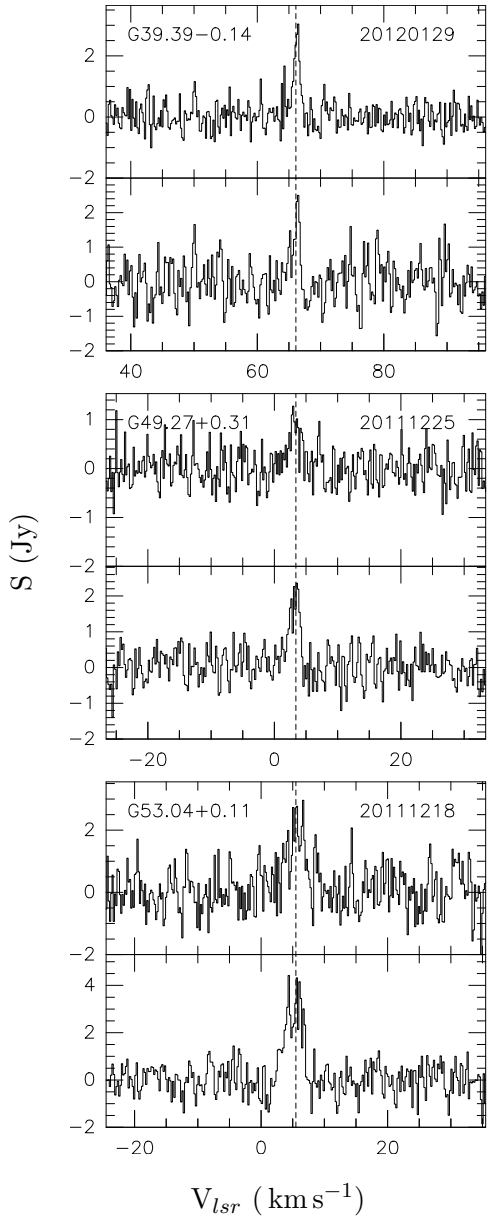

Figure 3.14: Sources detected both in the 44 GHz (lower) and 95 GHz (upper) class I methanol masers.

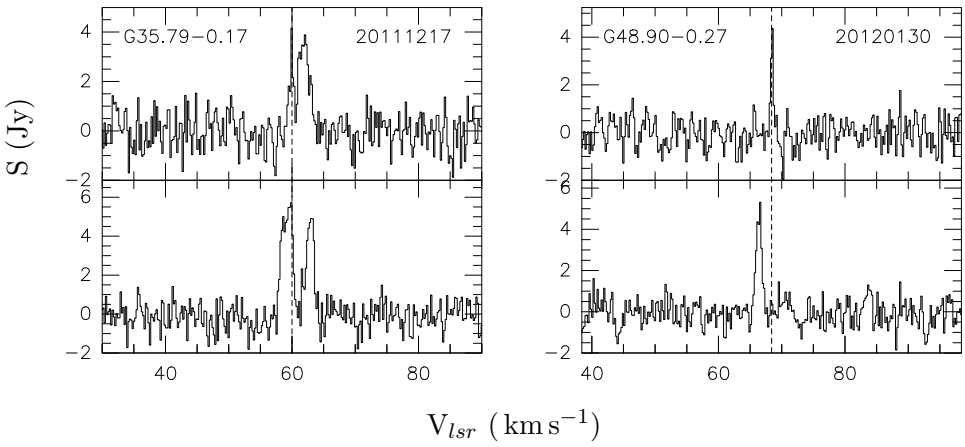

Figure 3.15: Sources detected both in the 22 GHz water (lower) and the 44 GHz class I methanol maser (upper).

Chapter 4

Observational study of water and class I methanol masers toward class II methanol maser sources

Abstract We selected one-hundred fifty-five 6.7 GHz class II methanol maser sources from Methanol Multibeam (MMB) catalogs, and conducted observations of 22 GHz water maser and 44 GHz and 95 GHz class I methanol masers, simultaneously. We also verified systemic velocities of the sources from molecular line observations of HCO^+ (1-0), $H^{13}CO$ (1-0), and ^{13}CO (1-0) using the Korean VLBI Network (KVN) and the Taeduk Radio Astronomy Observatory (TRAO). We investigate an observational study with the blind survey catalog sources including the rest of MMB catalog sources and Arecibo methanol maser galactic plane survey (AMGPS) catalog sources. The detection rates of 22 GHz, 44 GHz, and 95 GHz toward 271 6.7 GHz class II methanol maser sources are 49 %, 51 %, and 44 %, respectively. Wa-

ter maser is detected mostly with other masers, but does not show any correlation with them at the flux density and the velocity. 12 sources out of the 66 sources that water maser are detected have high-velocity ($> 30\,\mathrm{km\,s^{-1}}$) features, and the 7 sources out of the 12 sources may be related with pole-on jets. 95 GHz class I methanol maser always come with 44 GHz class I methanol maser. They have high connections at the flux density and the velocity. Almost 44 GHz sources (87 %) come with 95 GHz maser. The velocity offset from the systemic velocity of 6.7 GHz peak flux density appears a double peak shape and differs from others. In galactic regions, inner part has more class I methanol maser sources and less water maser sources than outer region at positions that 6.7 GHz class II methanol masers were detected. Water and class I methanol masers can be detected easily as flux density of 6.7 GHz goes high.

4.1 Introduction

Methanol masers are known to be important probes to investigate basic star formation processes, such as infall motions, accretion disks, and bipolar outflows. These masers are divided into two groups, class I (typically, 44 GHz ($7_0 - 6_1\ A^+$) and 95 GHz ($8_0 - 7_1\ A^+$) lines) and class II (including 6.7 GHz ($5_1 - 6_0\ A^+$)) according to their association with other star formation indicators (Menten 1991). Cragg et al. (1992, 2005) suggested through theoretical modelings that class I masers are pumped by collisions while class II masers are excited by radiative pumping. Class I masers are found both in low- and high-mass star-forming regions (Kalenskii et al. 2010; Bae et al. 2011). On the contrary, class II masers are detected exclusively in high-mass star-forming regions (Minier et al. 2003; Breen et al. 2013).

Water masers are related with biploar outflows in star-forming regions (Furuya et al. 2003; Bae et al. 2011). They are often detected with class I and/or class II methanol masers (Beuther et al. 2002; Kang et al. 2014). However, any significant

correlation is not found among the maser species. Theoretically, water masers can be excited at gas temperature of $\sim$400 K and density of 10^8 cm^{-3}, whereas methanol masers can be excited at lower temperature and density, $\sim$100 K and 10^5 cm^{-3} (Elitzur et al. 1989; Cragg et al. 1992, 2005).

Interferometric observations of methanol maser sources give a hint of their origins. Class II methanol masers are observed at the interface between discs/tori and outflows (Minier et al. 2000; Bartkiewicz et al. 2009; Sugiyama et al. 2014). They usually appear in an earlier evolutionary phase than ultracompact HII regions (UCHIIs), and disappear as UCHIIs devlop (e.g., Walsh et al. 1998). Class I methanol masers are detected in the interaction regions of outflows with the surrounding dense regions (Plambeck & Wright 1988; Plambeck & Menten 1990; Kurtz et al. 2004; Voronkov et al. 2006).

There are several previous single-dish surveys of class I methanol masers toward 6.7 GHz class II methanol maser sources (Slysh et al. 1994; Ellingsen 2005; Fontani et al. 2010; Kang et al. 2014). Slysh et al. (1994) found 55 44 GHz sources from about 250 HII regions, water maser sources, and 6.7 GHz maser sources. They reported a 44 GHz maser detection rate of 64 % for 6.7 GHz maser sources. Ellingsen (2005) acquired a 95 GHz maser detection rate of 38 % toward 66 6.7 GHz maser sources. Fontani et al. (2010) surveyed 6.7 GHz maser emission toward 296 high-mass protostellar objects (HMPOs) and 44 GHz maser emission in 88 of them. The target sources are classified into two groups named *high* and *low* on the basis of their IRAS colors of [25-12] and [60-12]. Fontani et al. obtained a 44 GHz maser detection rate of 61 % toward 6.7 GHz sources. Kang et al. (2014) searched for 22 GHz water maser, and 44 GHz and 95 GHz class I methanol masers toward 77 6.7 GHz class II methanol maser sources from the Arecibo methanol maser galactic plane survey (AMGPS) (Pandian et al. 2007, 2011). The sources in their sample are mostly weaker than the sources of other surveys. They acquired 44 GHz and 95 GHz detection rates

of 32 % and 25 %, respectively, for 6.7 GHz maser sources. Interestingly, Slysh et al. (1994) argued that there are anti-correlations in flux density and velocity between class I and II masers. However, Ellingsen (2005); Kang et al. (2014) could not find any anti-correlation between the two classes.

Chen et al. (2012) presented criteria for finding 95 GHz class I methanol maser sources with high probability (75 %) in the plane of H_2 column density versus 1.1 mm flux density. The sources in their sample were selected from the 1.1 mm Bolocam Galactic plane survey (BGPS) point source catalog (Rosolowsky et al. 2010). The survey covers the Galactic midplane of $-10^\circ < l < 90^\circ$ and $|b| \lesssim 0.5^\circ$. Kang et al. (2014) found that their detected 95 GHz maser sources are satisfied with the criteria, and that the isotropic luminosity of class I methanol maser correlates with the BGPS clump mass.

In this study, we present a simultaneous survey of 22 GHz water and 44 GHz and 95 GHz class I methanol masers toward 6.7 GHz class II methanol maser sources. The sources in our sample were chosen from the Methanol Multi-Beam (MMB) survey, which covers the inner Galactic region of $-15^\circ < l < 20^\circ$ and $|b| \lesssim 2.0^\circ$ with a rms noise level of 0.17 Jy using the Parkes 64 m telescope (Caswell et al. 2010; Green et al. 2010). The sources of Kang et al. (2014) were also adopted to increase effective samples. Section 4.2 describes the source selection and observation method. Section 4.3 gives the detection rates of masers, and Section 4.4 presents analysis results of velocity characteristics and flux densities among different maser species. Section 4.5 summarizes the main results.

4.2 Source Selection and Observations

4.2.1 Source Selection

The sources in our sample were selected from two MMB catalogs, which consist of 302 sources: 183 sources from 345° to 6° in the galactic longitude range (Caswell et al. 2010) and 119 sources from 6° to 20° (Green et al. 2010). The MMB survey was conducted with the seven-beam receiver installed at the Parks 64 m radio telescope. The beam size was 3.2′, and the typical rms noise level was 0.17 Jy. Subsequently, the Australia Telescope Compact Array (ATCA) was utilized to obtain accurate positions of the detected maser sources. The re-positioned sources were observed by the 'MX' mode with a rms noise level of 0.07 Jy.

Of the 302 sources, 86 are not observable from any KVN station. We excluded 22 sources located in crowded regions, considering the beam size of the KVN telescopes at 95 GHz, 32″. In addition, we did not observe 39 sources because they were already observed by Kim C.-H. et al. (2014) with the same telescopes. We will used their observational results of the 39 sources for statistical analyses. Consequently, 155 sources were chosen to observe maser lines.

4.2.2 Observations

We carried out simultaneous surveys of the H_2O $6_{16} - 5_{23}$ (22.23508 GHz), CH_3OH $7_0 - 6_1 A^+$ (44.06943 GHz), and CH_3OH $8_0 - 7_1 A^+$ (95.169463 GHz) masers toward the 155 6.7 GHz class II methanol maser sources with the KVN telescopes. The KVN consists of three 21 m telescopes loacted at the Yonsei, Ulsan, and Tamna stations. The telescopes are equipped with multi-frequency receiving systems with 22 GHz, 43 GHz, 86 GHz, and 129 GHz bands (Han et al. 2008). The receivers support dual-polarization mode, and up to 4 preparations can be set to acquire data simultaneously. The telescopes are shaped Cassegrain and have quite high first side-

lobe levels, $\sim$ -14dB (Kim et al. 2011; Lee et al. 2011).

The KVN 21 m telescope at the Tamna site was mainly utilized to observe sources with low declinations. The other telescopes were also used for high declination sources. The observations were performed in the position switching mode for 30 days between 2012 March and 2013 April. The detection limit was about 1.2 Jy with a three-sigma noise level. Bandwidths were set to 32 MHz. The system temperatures of 22 GHz, 44 GHz, and 95 GHz were about 100 K, 150 K, and 200 K, respectively.

We observed 108 sources in the HCO^+ (1-0) (89.188526 GHz), $H^{13}CO^+$ (1-0) (86.754288 GHz) and ^{13}CO (1-0) (110.201353 GHz) lines, as well, using the KVN 21 m and the Taeduk Radio Astronomy Observatory (TRAO) 14 m telescopes. The observations aimed at determining the systemic velocities of individual sources. The TRAO 14 m telescope has established multi-beam receiver (QUARRY), and covers a frequency range from 86 GHz to 115 GHz. The main beam efficiencies of the TRAO 14 m are 50 % and 49 % at 89 GHz and 110 GHz, respectively. We obtained the systemic velocities of 62 sources from Kim J.-S. et al. (2014) and those of 24 sources from the literature (Churchwell et al. 1990; Molinari et al. 1996; Sridharan et al. 2002; Chen et al. 2010; Sanhueza et al. 2012). Kim J.-S. et al. (2014) observed the 62 sources in the HCO^+ (1-0) and $H^{13}CO^+$ (1-0) lines using the KVN telescopes.

Additional ^{13}CO and HCO^+ line observations of 12 water maser sources with large velocity-offset features were made with the TRAO 14 m. It took 6 days between 2014 April and 2014 May. The system temperature of ^{13}CO ranged from 800 K to 1500 K, and the system temperature of HCO^+ from 600 K to 800 K.

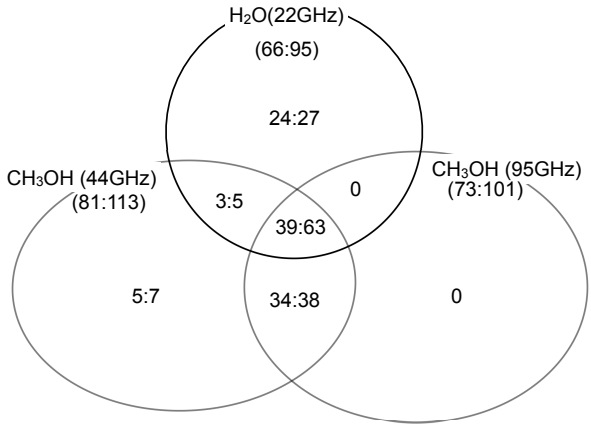

Figure 4.1: Venn diagram displaying the number of sources detected in the three observed maser species toward 194 sources. t numbers of A:B, A is our observation result, and B is expanded result that includes Kim C.-H. et al. (2014) data.

4.3 Results

4.3.1 Detection Rates

We detected at least one maser in 104 of the 155 sources in our sample (Table 4.1). The detection rates of 22 GHz water, 44 GHz methanol, and 95 GHz methanol masers are 43 % (66), 53 % (81), and, 46 % (73), respectively (Figure 4.1). All maser species were detected in 38 sources. 95 GHz class I methanol maser is always detected with 44 GHz maser. Twenty-four sources have only 22 GHz water maser, and five sources show 44 GHz maser alone. About half of the detected 44 GHz (52 %) and 95 GHz (53 %) class I methanol maser sources show water maser.

If the overlapped 39 of Kim C.-H. et al. (2014) are included, 22 GHz, 44 GHz, and 95 GHz masers were detected in 49 % (95), 58 % (113), and 52 % (101) of the

194 6.7 GHz mathanol maser sources, respectively (Figure 4.1). Fontani et al. (2010) reported that the detection rate of 22 GHz water maser is 53 %, and Kang et al. (2014) presented a detection rate of 51 %. These values are similar to our results. Slysh et al. (1994), Fontani et al. (2010), and Kang et al. (2014) obtained 44 GHz detection rates of 64 %, 61 %, and 32 %, respectively. The result of Kang et al. (2014) is significantly different with ours. Our 95 GHz detection rate of 53 % is also higher than 38 % of Ellingsen (2005) and 25 % of Kang et al. (2014). We will investigate details of the detection rates at section 4.4.2.

4.3.2 Notes on Selected Sources

358.931-0.030

22 GHz and 44 GHz appear at two velocity positions on this source, and 95 GHz is detected at one position (Figure 4.3). 6.7 GHz was shown at -15.9 $km\,s^{-1}$with other three masers. systemic velocity observation at HCO^+ and $H^{13}CO^+$ lines presents two position values of -62 $km\,s^{-1}$and -19.7/kms. It seems that two positions are overlapped on line of sight. This source is also announced at high velocity feature section (sec 4.3.3) even though it will not be.

1.719-0.088

1.719-0.088 does not appear any maser of 22 GHz, 44 GHz, nor 95 GHz. 6.7 GHz was detected at -8.1 $km\,s^{-1}$. We find various lines at ^{13}CO. But HCO^+ line shows only strong broad line at 50.6 $km\,s^{-1}$(Fig 4.2). The latter seems another dense molecular cloud. For complex lines at ^{13}CO and no line at HCO^+, we can not define exact systemic velocity. Velocity of the table HCO^+ is listed at Tabel 4.2.

3.502-0.200

This source has two lines at HCO^+ on -21 $km\,s^{-1}$and 44 $km\,s^{-1}$that data is reduced from Kim J.-S. et al. (2014). We detect 44 GHz at -21 $km\,s^{-1}$(Fig 4.2). But 6.7 GHz was found at 43.9 $km\,s^{-1}$. One HCO^+ line at -21 $km\,s^{-1}$is stronger and narrower than the other. 44 GHz and 6.7 GHz seems to be born at different clouds that are overlapped on line of sight.

5.677-0.027

6.7 GHz was detected at -11.7 $km\,s^{-1}$on this source. But our additional observations of ^{13}CO, HCO^+, and $H^{13}CO^+$ lines represent that systemic velocity is 14.0 $km\,s^{-1}$. But weak HCO^+ line is near at the velocity of 6.7 GHz. the 6.7 GHz line may be from other source on line of sight. Because offset between V_{sys} and $V_{6.7\,GHz}$ is high, it disappear at Fig 4.6. It does not affect other investigation for absence of other masers.

18.834-0.300

The source does not appear any other masers. Systemic velocity of 63.1 $km\,s^{-1}$is determined from Sanhueza et al. (2012). 6,7 GHz appeared at 41.3 $km\,s^{-1}$. The systemic velocity was observed with N_2H^+ line toward a IRDC that overlaps with our source within 3″. By the way, there are several IRDCs near the position within 25″. Other IRDCs have 41.7 $km\,s^{-1}$and 44.8 $km\,s^{-1}$of systemic velocities that are near from the velocity of 6.7 GHz. The MMB catalog has 0.4″pointing accuracy with ATCA observation, and Sanhueza et al. (2012) represents 11″pointing accuracy of their sources. Whether which is more accurate or not, the 6.7 GHz seems to be relate with the latter IRDCs.

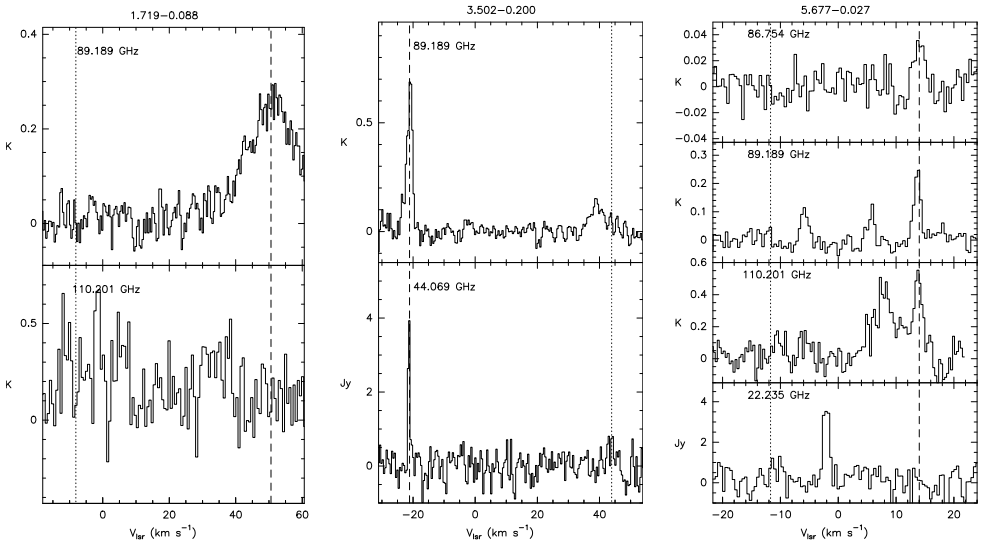

Figure 4.2: Sources that systemic velocity is different with the velocity of 6.7 GHz. Dashed line presents measured systemic velocity. Dot line indicates velocity of 6.7 GHz.

4.3.3 High velocity Features of Water Maser

As mentioned above, we made molecular line surveys of 108 sources in order to measure the systemic velocities of the natal dense cores (Table 4.2). We found in 12 of them that 22 GHz water maser lines are shifted from the systemic velocities by more than 30 km s^{-1}. These sources are commented with 'HV' in Table 4.2.

Two of them, 358.931-0.030 and 10.356-0.148, show HCO^+ lines near the large velocity-offset features (Figure 4.3). Thus they could be associated with different objects from the targeted sources in the same lines of sight. Seven of the 12 sources, 353.273+0.641, 353.363-0.166, 353.378+0.438, 357.965-0.164, 12.181-0.123, 16.112-0.303, and 16.855+0.641, do not have any associated ^{13}CO lines (Figure 4.4). The remaining three sources, 18.661+0.034, 18.667+0.025, and 18.999-0.239, show weak ^{13}CO lines near the large velocity-offset features, but no HCO^+ lines (Figure 4.5). Caswell & Phillips (2008) detected three of this kind of water maser sources and suggested that these blue-shifted high-velocity features can be produced by pole-on jets in massive star-forming regions. It should be noted that all the large velocity-offset features are blueshifted. Thus all the 12 sources but the first two may be high-velocity features generated by pole-on jets, although we cannot exclude the possibility that the last three can be related to low-mass young stellar objects (Gwinn et al. 1992; Gwinn 1994; Furuya et al. 2003).

4.4 Analyses

4.4.1 Velocity Characteristics

We investigate velocity offsets of the peak velocities of 4 maser species with respect to the systemic velocity for each source. Fig (4.6) exhibits the velocity offset distributions of 6.7 GHz, 22 GHz, 44 GHz, and 95 GHz masers. Almost all velocity offsets are distributed within ± 20 km s^{-1}. 6.7 GHz masers have a double-peaked distribu-

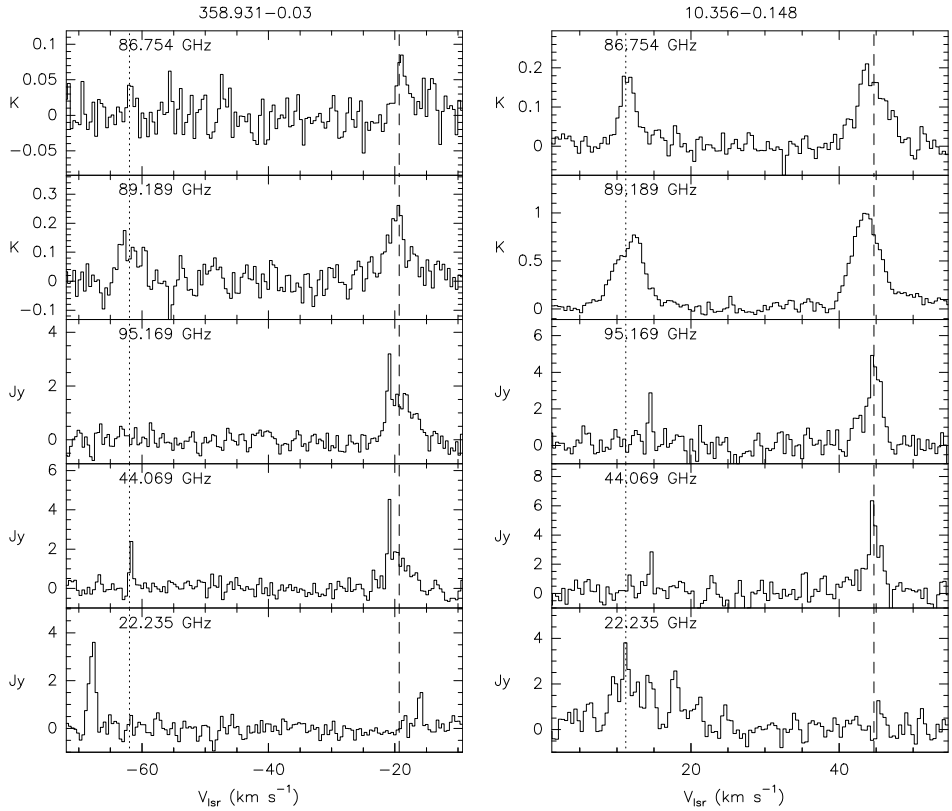

Figure 4.3: Two sources, 358.931-0.030 (left) and 10.356-0.148 (right), have two HCO^+ lines that can be different sources at a line of sight. Dashed line presents systemic velocity. On left picture, dot line shows velocity of 6.7 GHz.

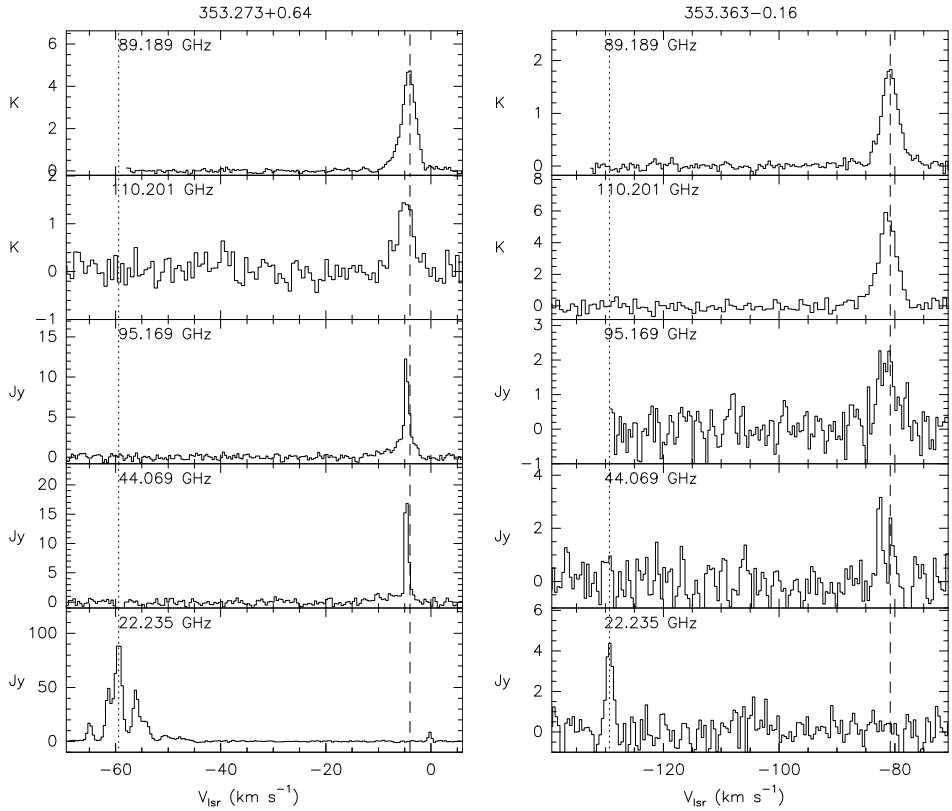

Figure 4.4: Seven sources, 353.273+0.641, 353.363-0.166, 353.378+0.438, 357.965-0.164, 12.181-0.123, 16.112-0.303, and 16.855+0.641, do not appear any other lines at high velocity feature position.

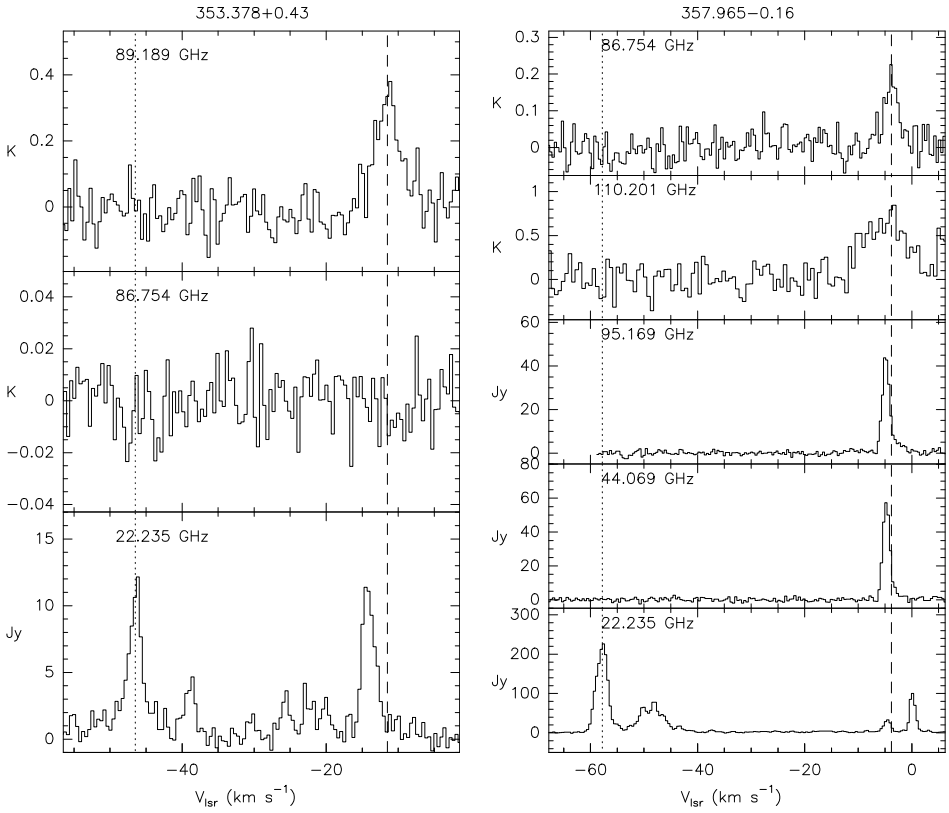

Figure 4.4: continued

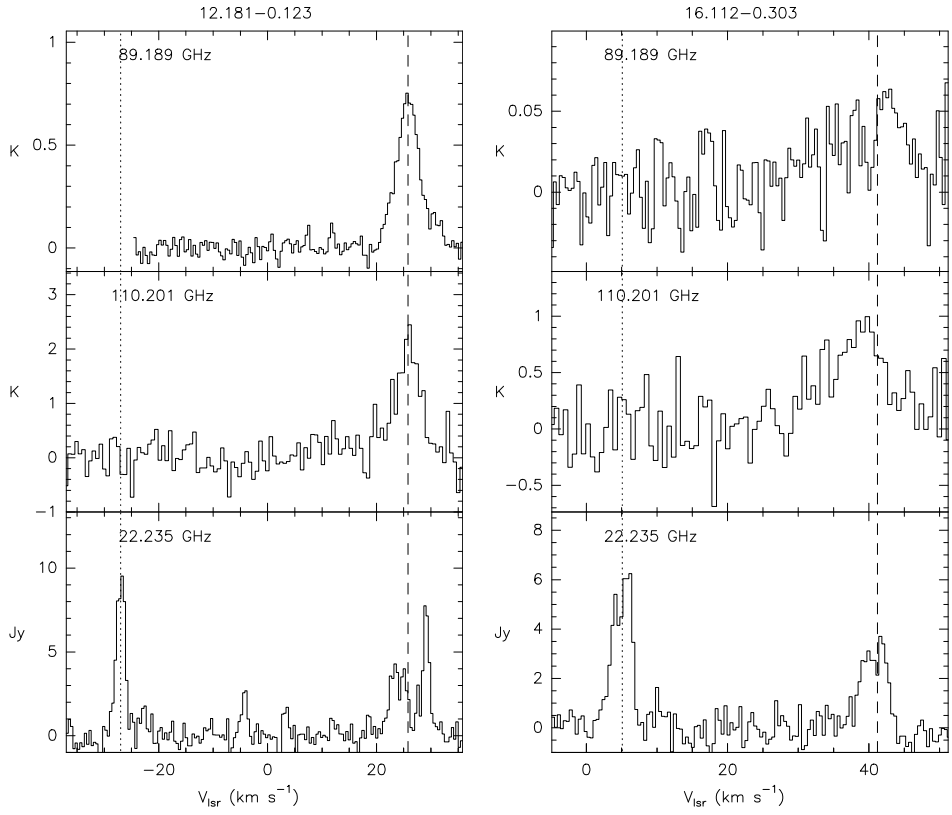

Figure 4.4: continued

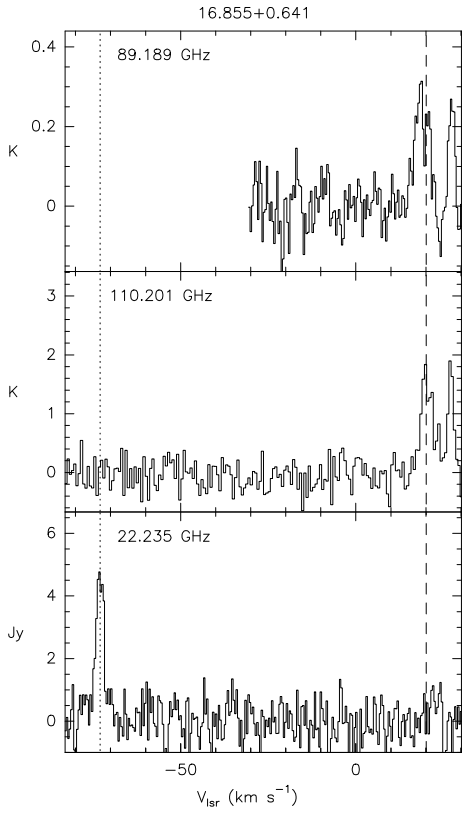

Figure 4.4: continued

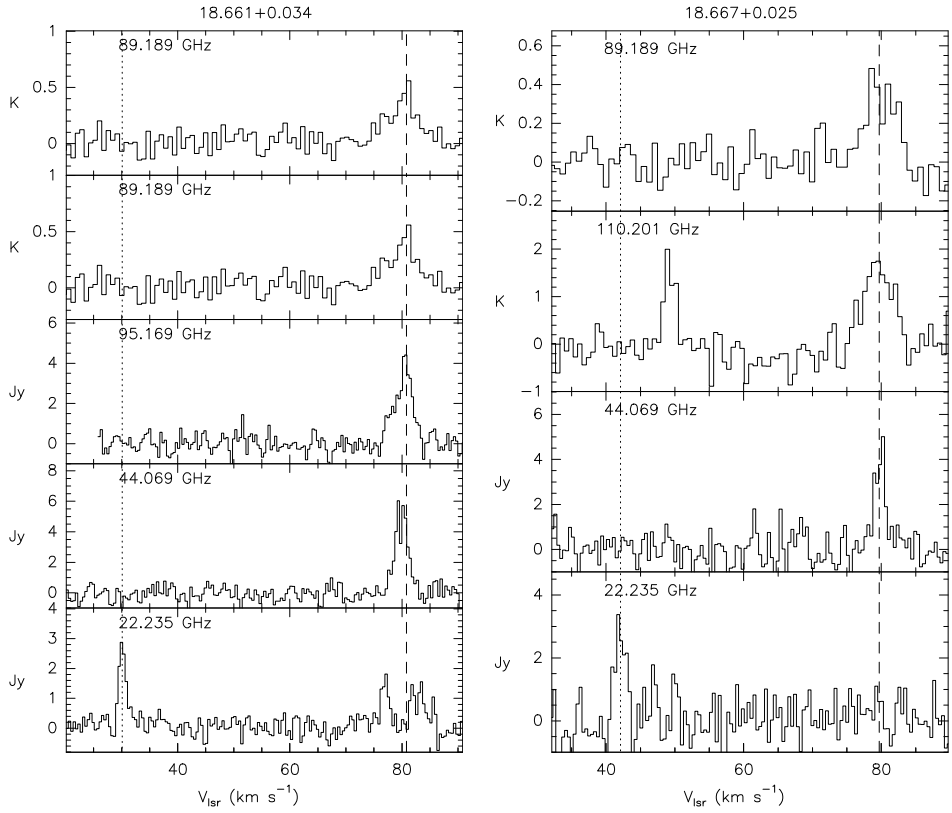

Figure 4.5: Three sources, 18.661+0.034, 18.667+0.025, and 18.999-0.239, represent weak ^{13}CO line at the high velocity position, but not appear HCO^+ line at the position.

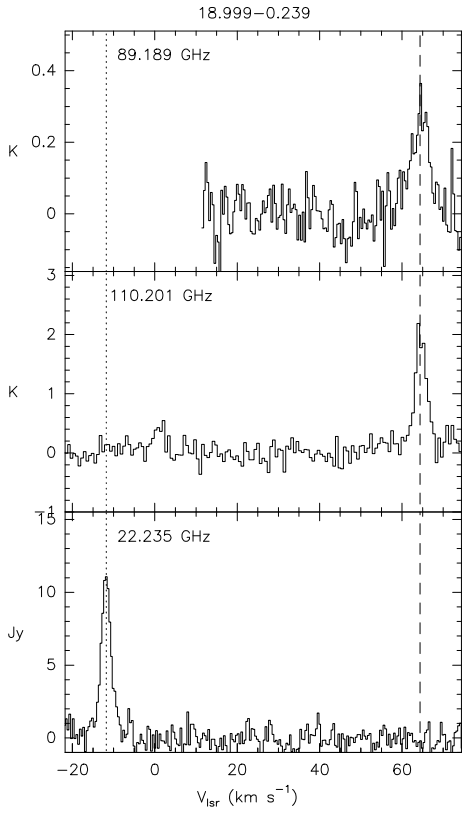

Figure 4.5: continued

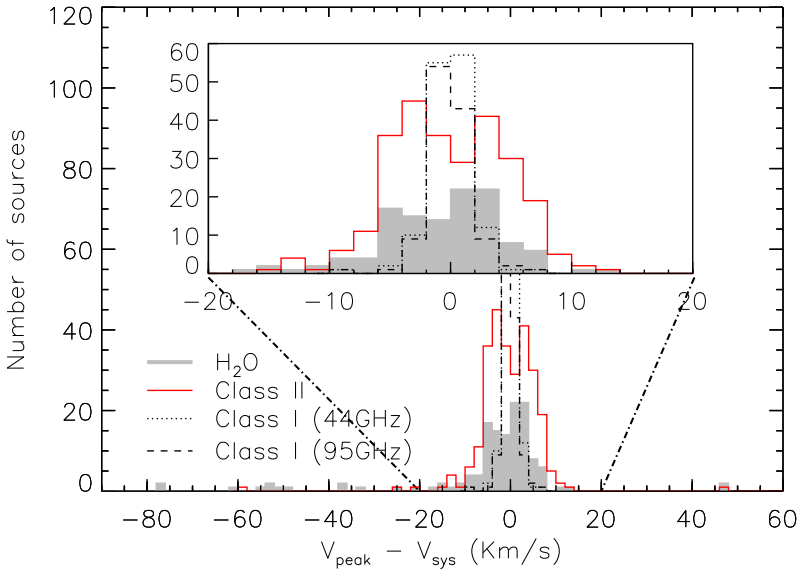

Figure 4.6: Velocity offset distributions of the four maser transitions.

tion (see also Byun et al. (2012); Kang et al. (2014)), while the other maser species show single-peaked distributions. In order to understand what causes the double-peak distribution of 6.7 GHz masers, further studies are required. The mean velocity offsets of 6.7 GHz, 22 GHz, 44 GHz, and 95 GHz masers are $-0.2\pm4.8\,\mathrm{km\,s^{-1}}$, $-0.9\pm5.1\,\mathrm{km\,s^{-1}}$, $-0.1\pm1.9\,\mathrm{km\,s^{-1}}$, and $-0.1\pm1.9\,\mathrm{km\,s^{-1}}$, respectively. The distributions of 44 GHz and 95 GHz masers are nearly overlapped. A strong correlation exists between the two parameters with a correlation coefficient of 0.9: $V_{offset,95} = 1.0\ V_{offset,44}\pm2.4$. There is no more correlation between any other pair. This is consistent with the results of Kang et al. (2014). On the contrary, Fontani et al. (2010) reported a significant correlation between the velocity offsets of 6.7 GHz and 22 GHz masers.

Slysh et al. (1994) claimed that anti-correlations exist between 44 GHz class I and 6.7 GHz class II methanol masers in velocity and flux density. However, Ellingsen

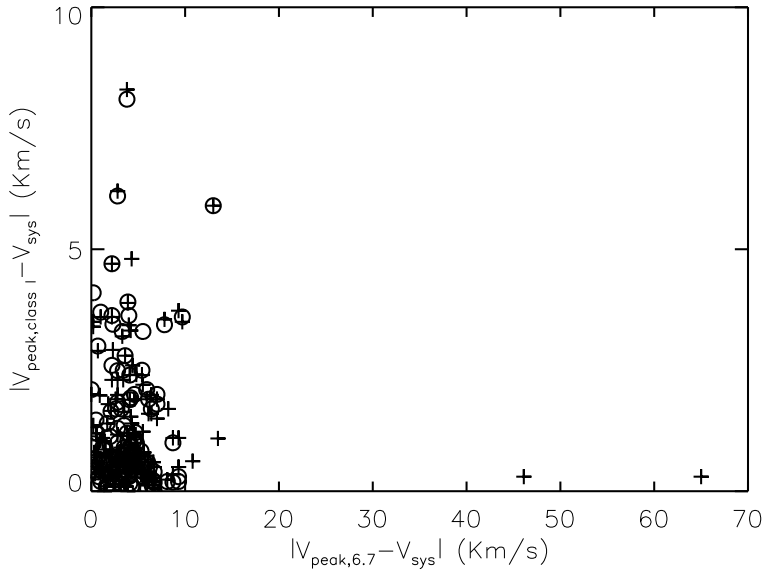

Figure 4.7: Comparison of velocity offsets between class I and class II methanol masers. Cross is related with 44 GHz, and open circle is 95 GHz.

(2005) did not find any correlation or anti-correlation between 95 GHz class I and 6.7 GHz class II methanol masers. Kang et al. (2014) cannot, either, by comparing both 44 GHz and 95 GHz masers with 6.7 GHz maser. Figure 4.7 compares the velocity offset of 6.7 GHz class II methanol maser with those of 44 GHz and 95 GHz class I methanol masers. We cannot find any significant correlation or anti-correlation. Figure 4.8 displays the distributions of velocity range overlap between class I and II methanol maser spectra. Here we adopt the definition of overlap by Ellingsen (2005). The spectra of class I masers are frequently overlapped with that of 6.7 GHz maser: 81 % of 44 GHzand 83 % of 95 GHzmaser sources.

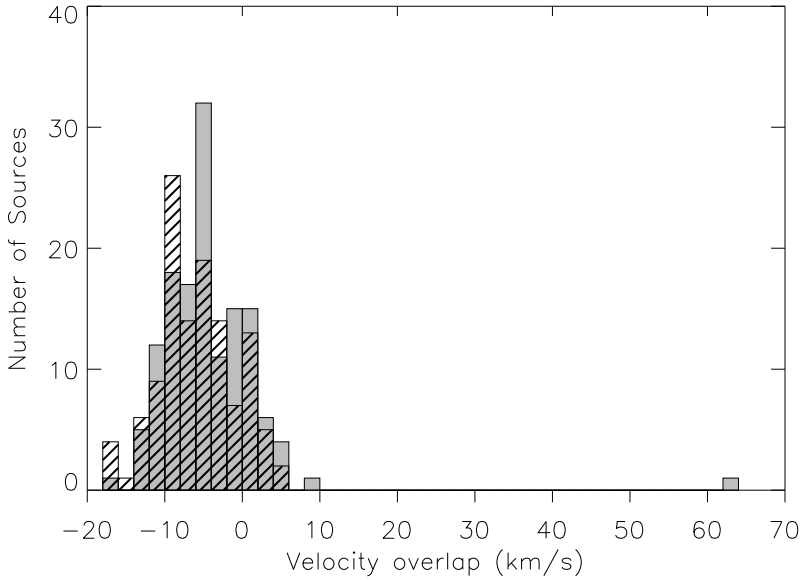

Figure 4.8: Histogram of the velocity overlap between the class I and class II methanol masers. The filled bar is for the 44 GHz, and the slant bar is for the 95 GHz. A negative value means that the velocity ranges of the two masers overlap. See the text for details.

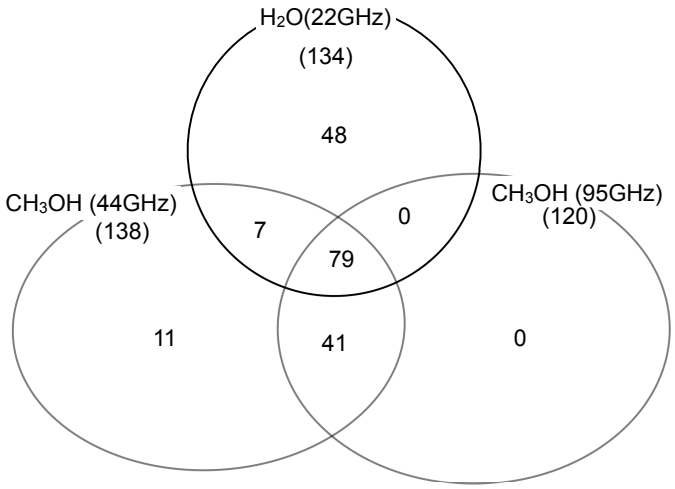

Figure 4.9: Venn diagram displaying the maser detected sources from 271 targets. Detection rates of 22 GHz, 44 GHz, and 95 GHz are 49 %, 51 %, and 44 %, respectively.

4.4.2 Analysis of detection rates

Kang et al. (2014) conducted the same survey of 77 sources in the AMGPS catalog. The AMGPS was a blind survey covering the galactic region of $35.2^\circ \lesssim l \lesssim 53.7^\circ$ and $|b| \lesssim 0.41^\circ$ with a rms noise level of 0.09 Jy. We combine the 77 AMGPS sources with our 194 MMB sources for the subsequent statistical analyses. Figure (4.9) is a Venn diagram summarizing the detection rates of three maser species toward 271 6.7 GHz maser sources. The rates are 49 %, 51 %, and 44 % for 22 GHz, 44 GHz, and 95 GHz masers, respectively. 95 GHz masers were detected only in 44 GHz maser sources, and 87 % of 44 GHz maser sources accompany 95 GHz maser emission.

Kang et al. (2014) reported that the detection rates of 22 GHz, 44 GHz, and 95 GHz masers toward the AMGPS sources are 51 %, 31 %, and 24 %, respectively. The AMGPS sources were found with rms noise level of 0.09 Jy, which is twice lower than 0.17 Jy of the MMB sources. We set the rms noise level equal to the MMB catalog sources. 65 out of 77 sources are agreed with the level, and resampled detection rates. The detection rates of 22 GHz, 44 GHz, and 95 GHz are 57 %, 35 %, and 29 %, individually. All rates are slightly increased, but do not match with our result. Because two catalog sources of MMB and AMGPS are detected from different galactic positions, the detection rates can be mismatched. The former is from 352° to 20° in galactic longitudes with ±2° galactic latitudes, and the latter is from 35.2° to 53.7° in galactic longitudes with ±0.41° galactic latitudes. We resample all sources with $|b| \lesssim 0.41°$ and 0.5 Jy of detection limit level of MMB surveys. Figure 4.10 displays detection positions of 22 GHz, 44 GHz, and 95 GHz toward 6.7 GHz sources. Figure 4.11 represents the detection rates of 22 GHz, 44 GHz, and 95 GHz at inner region (MMB catalog) and outer region (AMGPS). Water maser detection rate of outer region (58 %) is higher than inner region (43 %). But class I methanol masers in the outer region are lower than in the inner region. The differences are significantly appeared in the regions.

We investigate variations in the detection rates of three maser species with the peak flux density of 6.7 GHz maser. Figure 4.12 displays the variations. Most of the detected 22 GHz, 44 GHz, and 95 GHz maser sources are associated with 6.7 GHz maser sources with peak flux densities <50 Jy: 87 % of 22 GHz, 89 % of 44 GHz, 88 % of 95 GHz masers. We thus include all the sources with flux densities >50 Jy in one flux density range. The detection rates of water and class I methanol masers tend to increase with the peak flux density of 6.7 GHz class II methanol maser. This seems to be consistent with the fact that the isotropic luminosities of all four maser species are roughly correlated to the bolometric luminosity of the central (proto)star

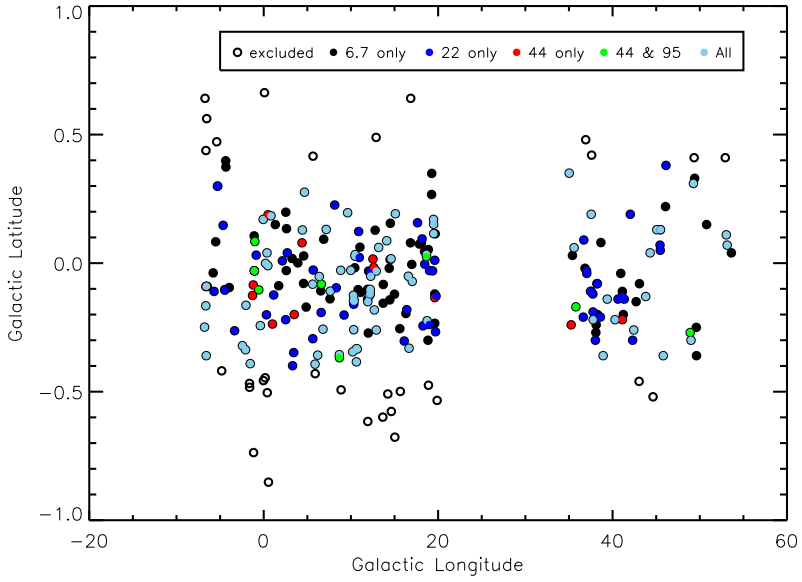

Figure 4.10: The positions in galactic coordinates of 271 sources of 6.7 GHz class II methanol maser is detected. Open circles are excluded sources over $|b| > 0.41°$ and colored circles are resampled sources. In colored circle sources, black is no other maser detected source, blue is only water maser is detected, red is only 44 GHz class I methanol maser is found, and green is class I methanol masers are searched. Sky circle is that all maser lines are detected.

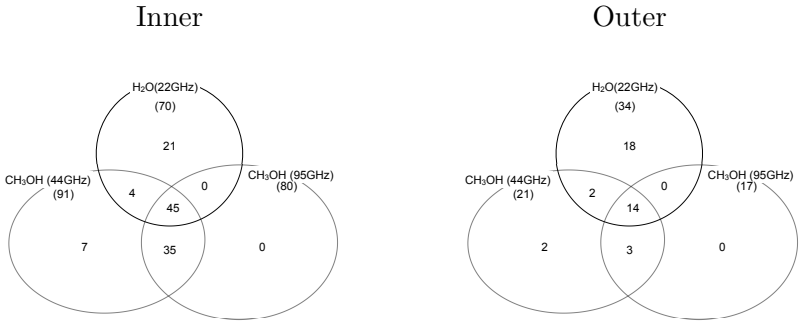

Figure 4.11: The detection rates with inner galactic region ($l < 20°$) and outer galactic region ($l > 20°$). Samples at inner and outer region are 163 and 59 sources. Detection rates of 22 GHz, 44 GHz, and 95 GHz are 43 %, 56 %, and 49 % at inner regions, respectively. Outer region detection rates of 22 GHz, 44 GHz, and 95 GHz are 58 %, 36 %, and 29 %, individually.

(e.g., Bae et al. (2011)).

4.4.3 Flux Densities

Table 4.1 lists the line parameters of the detected 104 maser sources in this study. We examine correlations among the peak flux densities of four maser species for the sample of 271 sources. A tight correlation exists between the flux densities of 44 GHz and 95 GHz class I methanol masers (Figure 4.13). There is no significant correlation between any other pair.

$$\mathrm{S_{peak}}(95) = (0.68 \pm 0.06)\ \mathrm{S_{peak}}(44) + (0.32 \pm 0.52), \quad \mathrm{r} = 0.87, \tag{4.1}$$

$$\log(\mathrm{S_{peak}}(95)) = (0.89 \pm 0.03)\ \log(\mathrm{S_{peak}}(44)) + (0.01 \pm 0.03), \quad \mathrm{r} = 0.93, \tag{4.2}$$

Val'tts et al. (2000) and Kang et al. (2014) also derived the peak flux density ratio of 95 GHz to 44 GHz masers. Our estimate is the same as that of Kang et al.

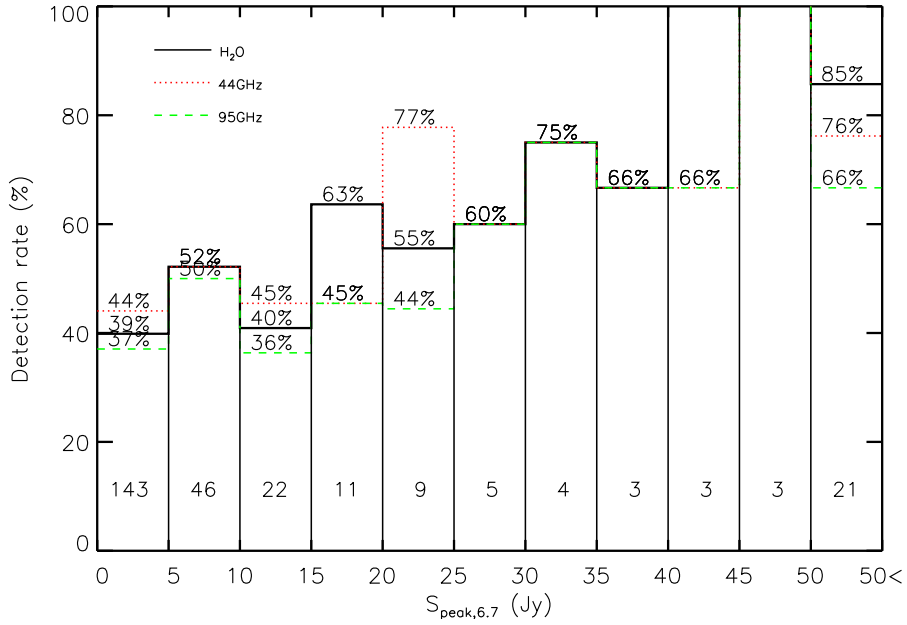

Figure 4.12: Detection rates as 6.7 GHz peak flux ranges. Solid, dotted, and dashed lines are water, 44 GHz, and 95 GHz, respectively. All maser detection rates are increased as 6.7 GHz peak flux density goes high.

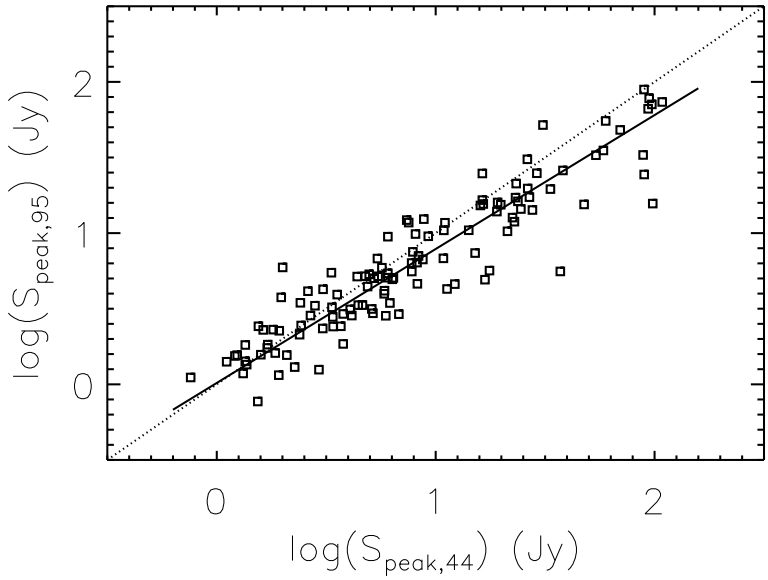

Figure 4.13: Comparison between the peak flux densities of the 44 GHz and 95 GHz class I methanol masers in log scale. A strong correlation exists between the two parameters. The solid line is the least-squares fitting result with a correlation coefficient of 0.93.

(2014) within errors, but is twice greater than that of Val'tts et al. (2000).

4.4.4 BGPS counterparts

Chen et al. (2012) proposed criteria of targeted search of 95 GHz class I methanol maser for the BGPS clumps (Rosolowsky et al. 2010): $\log(S_{\rm int}) \lesssim -38.0 + 1.72$ $\log(N_{H_2}^{\rm beam})$ and $\log(N_{H_2}^{\rm beam}) \gtrsim 22.1$. It is interesting to test the criteria with our data. We searched for BGPS clumps associated with 194 MMB sources within $16''$ radius, and identified 105 BGPS counterparts (Table 4.3). Pandian et al. (2012) also found 44 BGPS clumps associated with their AMGPS sources. We calculate the beam-averaged H_2 column densities of these 149 BGPS clumps. Here we use the same parameters as in Chen et al. (2012): kinetic temperature of 20 K, beam solid angle of 2×10^{-8} Sr, dust-to-gas mass ratio of 0.01, mass absorption coefficient of 1.14 $\rm cm^2\,g^{-1}$, and mean molecular weight of μ=2.37,

$$N_{H_2}^{\rm beam} = \frac{S_{40''}}{\Omega_{\rm beam}\mu k_d B_\nu(T_{\rm dust})R_d} \tag{4.3}$$

Figure 4.14 plots the 149 BGPS clumps on the $\log(N_{H_2}^{\rm beam})-\log(S_{\rm int})$ plane. The Chen's criteria are satisfied by 84 % (125) of 6.7 GHz, 88 % (65) of 22 GHz, 94 % (74) of 44 GHz, and 99 % (68) of 95 GHz maser sources. Chen et al. (2012) suggested ∼75 % of BGPS clumps meeting the criteria would have 95 GHz maser counterparts. However, only 54 % of the 125 BGPS clumps satisfying the criteria show 95 GHz maser emission.

4.5 Conclusions

We performed simultaneous surveys of 22 GHz water and 44 GHz and 95 GHz class I methanol masers toward 155 6.7 GHz class II methanol maser sources in the MMB catalog. Thirty nine other MMB sources observed by Kim C.-H. et al. (2014) were

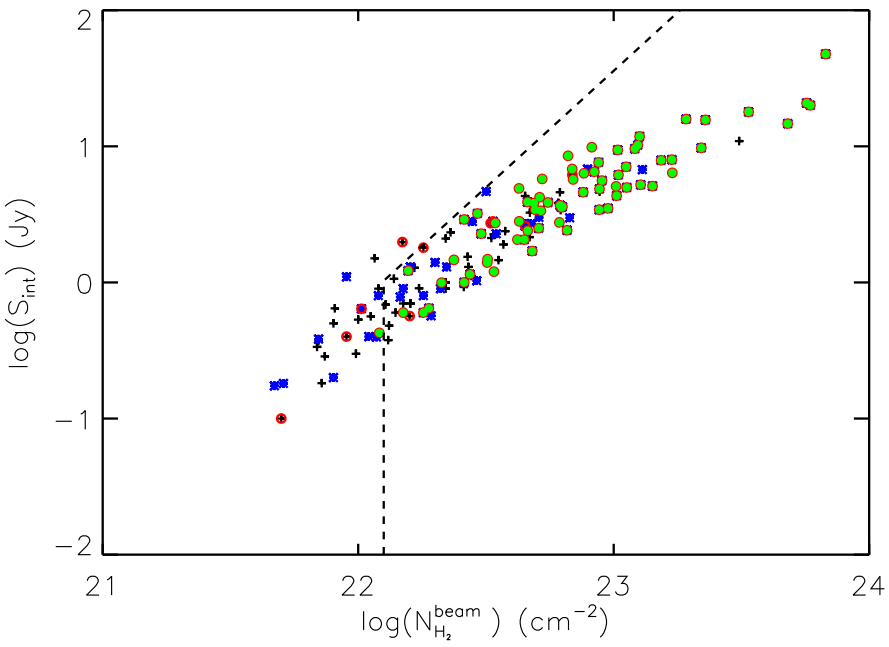

Figure 4.14: Plots of associated BGPS sources in a plane of the beam-averaged column density and integrated 1.1 mm continuum flux density. Black plus , blue cross, red open circle and green filled circles represent sources related with 6.7 GHz, 22 GHz, 44 GHz, and 95 GHz , respectively.

combined with our sample for statistical analyses. We also determined the systemic velocities of 108 MMB sources by observing the (1−0) transitions of HCO^+, $H^{13}CO^+$, ^{13}CO. The systemic velocities of the other 86 sources were adopted from Kim J.-S. et al. (2014) and the literature. The main results of this study are summarized as follows.

(1) The detection rates of 22 GHz, 44 GHz, and 95 GHz are 49 %, 51 %, and 44 % toward the 271 6.7 GHz maser sources, respectively. 95 GHz masers were detected only in 44 GHz maser sources, and 87% of 44 GHz maser sources accompany 95 GHz maser emission. The detection rates of the three maser species tend to increase with the peak flux density of 6.7 GHz maser.

(2) The MMB sample in the inner galactic plane exhibits high detection rates of class I methanol masers, while the AMGPS sample in the outer galactic plane shows a high detection rate of water maser.

(3) 44 GHz and 95 GHz class I methanol masers have strong correlations both in velocity and flux density. There is no significant correlation between any other pair. In particular, we did not find any anti-correlation between class I and II methanol masers either in velocity or flux density.

(4) We detected 10 dominant blueshifted (>30 $\mathrm{km\,s^{-1}}$) water maser sources: 7 likely and 3 possible sources.

(5) The vast majority of BGPS counterparts of the detected maser sources satisfy the criteria of Chen et al. (2012). Almost all for 95 GHz class I methanol maser sources. However, only half of the BGPS clumps meeting the criteria have 95 GHz maser emission. This value is significantly lower than the prediction of Chen et al. (2012), 75 %.

References

Bae, J.-H., Kim, K.-T., Youn, S.-Y., Kim, W.-J., Byun, D.-Y., Kang, H., & Oh, C.S. 2011, ApJS, 196, 21

Bartkiewicz, A., Szymczak, M., van Langevelde, H.J., Richards, A.M.S., & Pihlström, Y.M., 2009, A&A, 502, 155

Beuther, H., Walsh, A., Schilike, P., Sridharan, T.K., Menten, K.M., & Wyrowski, F. 2002, A&A, 390, 289

Byun, D.-Y., Kim, K.-T. & Bae, J.-H. 2012, in IAU Symp. 287, Cosmic Masers-from OH to H0 (Cambridge: Cambridge Univ. Press), 284

Caswell, J.L., & Phillips, C.J. 2008, MNRAS, 386, 1521

Caswell, J.K., Fuller, G.A., Green, J.A., et al. 2010, MNRAS, 404, 1029

Chen, X., Shen, Z.-Q., Li, J.-J., & He, J.-H. 2010, ApJ, 710, 150

Chen, X., Ellingsen, S.P., He, J.-H., et al. 2012, ApJS, 200, 5

Churchwell, E., Walmsley, C.M., & Cesaroni, R. 1990, A&AS, 83, 119

Cragg, D.M., Johns, K.P., Godfrey, P.D., & Brown, R.D. 1992, MNRAS, 259,203

Cragg, D.M., Sobolev, A.M., & Godfrey, P.D. 2005, MNRAS, 260, 533

Dodson, R., Ohja, R., & Ellingsen, S.P. 2004, MNRAS, 351, 779

Ellingsen, S.P. 2005, MNRAS, 359, 1498

Elitzur, M., Hollenbach, D.J., & McKee, C.F. 1989, ApJ, 346, 983

Fontani, F., Cesaroni, R., & Furuya, R.S. 2010, A&A, 517, A56

Furuya, R.S., Kitamura, Y., Wootten, H.A., Claussen, M.J., & Kawabe, R. 2003, ApJS, 144, 71 Genzel, R. & Downes, D. 1977, A&AS, 30, 145

Green, J.A., Caswell, J.L., Fuller, G.A., et al. 2010, MNRAS, 409, 913

Gwinn, C.R., Moran, J.M., & Reid, M.J. 1992, ApJ, 393, 149

Gwinn, C.R. 1994, ApJ, 429, 253

Han, S.-T., Lee, J.-W., Kang, J., et al. 2008, Int. J. Infrared Millim. Waves, 29, 69

Kalenskii, S.V., Johansson, L.E.B., Bergman, P., et al. 2010, MNRAS, 405, 613

Kang, H., Kim, K.-T., Byun, D.-Y., Lee, S., & Park, Y.-S., 2014, ApJS, submitted

Kim, C.-H., Kim, K.-T., & Park, Y.-S., in prep

Kim, K.-T., Byun, D.-Y., Je, D.-H., et al. 2011, J. Korean Astron. Soc., 44, 81

Kim, J.-S., Kim, K.-T., & Yonekura, Y., & Shon, J., in prep

Kurtz, S., Hofner, P., & Álvarez, C.V. 2004, ApJS, 155, 149

Lee, S.-S., Byun, D.-Y., Oh, C.S., et al. 2011, PASP, 123, 1398

Menten, K.M. 1991, in ASP Conf. Ser. 16, Atoms, Ions and Molecules: New Results in Spectral Line Astrophysics, ed. A.D. Haschick & P.T.P. Ho (San Francisco, CA: ASP), 119

Minier, V., Booth, R.S., & Conway, J.E. 2000, A&A, 362, 1093

Molinari, S., Brand, J., Cesaroni, R., & Palla, F. 1996, A&A, 308, 573

Pandian, J.D., Goldsmith, P.F., & Deshpande, A.A. 2007a, ApJ, 656, 255

Pandian, J.D., Momjian, E., Xu, Y., Menten, K.M., & Goldsmith, P.F. 2011, ApJ, 730, 55

Pandian, J.D., Wyrowski, F., & Menten, K.M. 2012, ApJ, 753, 50

Plambeck, P.L. & Wright, M.C.H. 1988, ApJ, 330, 61

Plambeck, P.L. & Menten, K.H. 1990, ApJ, 364, 555

Rosolowsky, E., et al. 2010, ApJS, 188, 123

Sanhueza, P., Jackson, J.M., Foster, J.B.,Garay, G., Silva, A., & Finn, S.C. 2012, ApJ, 756, 60

Slysh, V.I., Kalenskii, S.V., Val'tts, I.E., & Otrupcek, R. 1994, MNRAS, 268, 464

Sridharan, T.K., Beuther, H., Schilke, P., Menten, K.M., & Wyrowski, F. 2002, ApJ, 566, 931

Sugiyama, K., Fujisawa, K., Doi, A., et al. 2014, A&A, 562, A82

Val'tts, I.E., Ellingsen, S.P., Slysh, V.I., Otrupcek, R., & Larionov, G.M. 2000, MNRAS, 317, 315

Voronkov, M.A., Brooks, K.J., Sobolev, A.M., Ellingsen, S.P., Ostrovskii, A.B., & Caswell, J.L. 2006, MNRAS, 373, 411

Table 4.1. Line Parameters of Detected Masers

Source	Frequency (GHz)	Gaussian Fit				Integrated Fit					Obs. Date yyyymmdd†
		S_{int} (Jy km s^{-1})	V_{peak} (km s^{-1})	FWHM (km s^{-1})	S_{peak} (Jy)	S_{int} (Jy km s^{-1})	v_{min} (km s^{-1})	v_{max} (km s^{-1})	S_{peak} (Jy)	V_{peak} (km s^{-1})	
353.216-0.249	22	5.94 ± 0.46	-48.4 ± 0.0	0.8 ± 0.1	6.90 ± 0.60	5.74	-49.4	-47.5	7.30	-48.5	20120411TN
	22	31.26 ± 0.50	-15.4 ± 0.0	0.9 ± 0.0	32.78 ± 0.60	32.26	-16.8	-14.0	32.56	-15.4	
	22	10.09 ± 0.49	7.3 ± 0.0	0.9 ± 0.0	11.09 ± 0.60	12.24	4.8	9.4	11.10	7.3	
	44	6.27 ± 0.40	-15.7 ± 0.0	0.5 ± 0.0	12.24 ± 0.43	6.19	-16.5	-15.1	11.67	-15.7	
	95	4.10 ± 0.51	-15.8 ± 0.0	0.8 ± 0.1	4.60 ± 0.70	4.61	-16.9	-14.8	5.38	-15.6	
353.273+0.641	22	41.30 ± 2.66	-108.5 ± 0.2	2.0 ± 0.2	19.67 ± 0.94	41.56	-111.2	-106.4	20.21	-108.3	20120411TN
	22	22.22 ± 2.66	-64.9 ± 0.2	1.1 ± 0.2	18.98 ± 0.94	21.04	-66.2	-63.7	18.67	-65.1	
	22	58.89 ± 2.66	-61.4 ± 0.2	1.1 ± 0.2	51.93 ± 0.94	72.68	-63.0	-60.6	52.95	-61.3	
	22	156.80 ± 2.66	-59.4 ± 0.2	1.5 ± 0.2	96.27 ± 0.94	154.47	-60.6	-57.7	100.66	-59.4	
	22	68.20 ± 2.66	-56.2 ± 0.2	1.3 ± 0.2	50.73 ± 0.94	74.91	-57.7	-55.1	50.51	-56.2	
	22	49.53 ± 4.78	-54.6 ± 0.1	2.2 ± 0.2	20.70 ± 2.36	29.08	-55.0	-52.2	19.87	-54.5	
	22	9.58 ± 3.40	-50.6 ± 0.2	1.5 ± 0.5	5.85 ± 2.36	13.12	-52.2	-48.5	6.22	-50.5	
	22	10.51 ± 3.92	-47.8 ± 0.5	3.0 ± 1.3	3.30 ± 2.36	7.35	-48.5	-44.7	4.93	-47.8	
	22	6.48 ± 1.23	-0.2 ± 0.1	0.6 ± 0.1	10.42 ± 2.36	6.21	-1.3	0.7	10.29	-0.2	
	44	16.30 ± 0.40	-4.7 ± 0.0	0.6 ± 0.0	24.51 ± 0.63	18.88	-5.8	-3.0	29.09	-4.8	
	95	17.32 ± 0.49	-4.6 ± 0.0	1.1 ± 0.0	14.43 ± 0.59	25.41	-11.6	-1.6	18.91	-4.8	
353.363-0.166	22	6.63 ± 0.79	-129.3 ± 0.1	1.3 ± 0.2	4.76 ± 1.00	5.94	-131.7	-127.5	5.47	-129.5	20120415TN
	44	3.37 ± 0.58	-82.6 ± 0.1	0.9 ± 0.2	3.69 ± 0.93	5.55	-84.2	-79.1	3.63	-82.9	
	95	9.12 ± 1.08	-81.4 ± 0.2	3.5 ± 0.5	2.42 ± 0.83	9.29	-84.1	-77.3	3.41	-82.8	
353.370-0.091	44	2.08 ± 0.50	-53.0 ± 0.1	0.5 ± 0.2	3.87 ± 0.90	2.23	-54.2	-52.3	4.09	-53.0	20120414TN
	44	3.21 ± 0.58	-51.2 ± 0.0	0.6 ± 0.2	5.21 ± 0.90	3.70	-52.3	-50.1	5.52	-51.1	
353.378+0.438	22	1.79 ± 1.13	-66.0 ± 0.2	0.7 ± 0.4	2.38 ± 2.12	1.57	-66.8	-65.2	2.80	-65.9	20120415TN
	22	4.84 ± 1.98	-63.2 ± 0.4	1.9 ± 0.9	2.38 ± 2.12	4.53	-65.2	-60.9	3.50	-63.6	
	22	29.12 ± 2.78	-46.5 ± 0.1	2.6 ± 0.4	10.61 ± 2.12	34.00	-50.4	-42.0	12.67	-46.1	
	22	8.80 ± 2.19	-38.9 ± 0.2	1.9 ± 0.6	4.28 ± 2.12	9.16	-42.0	-37.0	5.25	-38.3	
	22	5.40 ± 1.85	-25.6 ± 0.2	1.5 ± 0.7	3.42 ± 2.04	5.87	-27.4	-24.2	4.41	-25.7	
	22	6.19 ± 2.04	-22.5 ± 0.3	1.8 ± 0.7	3.30 ± 2.04	5.87	-24.2	-21.2	4.99	-23.0	
	22	4.39 ± 2.05	-20.0 ± 0.3	1.4 ± 0.8	3.02 ± 2.04	4.45	-21.2	-18.6	3.40	-20.0	

Table 4.1 (cont'd)

Source	Frequency (GHz)	Gaussian Fit S_{int} (Jy km s^{-1})	Gaussian Fit V_{peak} (km s^{-1})	Gaussian Fit FWHM (km s^{-1})	Gaussian Fit S_{peak} (Jy)	Integrated Fit S_{int} (Jy km s^{-1})	Integrated Fit v_{min} (km s^{-1})	Integrated Fit v_{max} (km s^{-1})	Integrated Fit S_{peak} (Jy)	Integrated Fit V_{peak} (km s^{-1})	Obs. Date yyyymmdd[†]
	22	27.67 ± 2.16	-14.1 ± 0.1	2.2 ± 0.2	11.63 ± 2.04	28.14	-16.8	-11.3	13.61	-14.3	
353.410-0.360	22	6.76 ± 1.27	-31.2 ± 0.1	0.7 ± 0.2	8.89 ± 2.05	7.41	-32.6	-29.8	9.27	-31.1	20120411TN
	22	13.11 ± 1.34	-21.7 ± 0.0	0.9 ± 0.1	14.41 ± 2.05	13.80	-22.5	-21.0	14.25	-21.7	
	22	33.32 ± 1.38	-20.1 ± 0.0	0.9 ± 0.0	35.54 ± 2.05	34.57	-21.0	-18.7	34.87	-20.0	
	22	14.00 ± 1.30	-17.8 ± 0.0	0.7 ± 0.1	18.81 ± 2.05	15.71	-18.7	-16.3	18.92	-17.9	
	22	4.41 ± 1.19	-11.0 ± 0.1	0.7 ± 0.2	6.04 ± 2.05	4.70	-11.7	-10.0	6.15	-10.9	
	22	22.07 ± 2.50	-6.5 ± 0.1	1.0 ± 0.1	21.05 ± 3.61	22.81	-8.0	-4.6	20.10	-6.3	
	44	43.49 ± 3.76	-18.1 ± 0.2	4.5 ± 0.4	9.13 ± 0.77	24.13	-23.3	-17.9	9.55	-18.9	
	44	15.61 ± 0.48	-16.5 ± 0.0	0.6 ± 0.0	22.90 ± 0.77	35.06	-17.9	-13.8	28.98	-16.5	
	95	38.93 ± 2.05	-17.7 ± 0.1	4.2 ± 0.3	8.64 ± 0.55	20.23	-22.8	-18.1	7.92	-18.6	
	95	11.59 ± 1.08	-16.6 ± 0.0	0.9 ± 0.1	11.90 ± 0.55	37.50	-18.1	-10.9	18.76	-16.6	
353.429-0.090	44	11.32 ± 1.22	-57.1 ± 0.2	3.8 ± 0.5	2.81 ± 0.85	10.74	-60.9	-53.0	4.50	-57.4	20120414TN
	95	6.43 ± 1.03	-57.4 ± 0.1	1.8 ± 0.4	3.31 ± 1.11	7.02	-59.3	-54.3	5.02	-57.5	
353.464+0.562	44	97.55 ± 1.71	-46.5 ± 0.0	1.3 ± 0.0	69.66 ± 2.10	100.68	-48.6	-43.4	70.16	-46.7	20120414TN
	95	71.42 ± 2.13	-46.5 ± 0.0	1.4 ± 0.1	48.11 ± 2.44	76.73	-48.3	-43.4	52.75	-46.8	
354.308-0.110	22	6.17 ± 0.80	6.9 ± 0.1	1.2 ± 0.2	4.74 ± 0.96	6.30	5.8	8.0	5.06	7.1	20120415TN
	22	6.83 ± 0.65	9.1 ± 0.0	0.8 ± 0.1	8.13 ± 0.96	6.95	8.0	10.1	8.52	9.0	
	22	19.27 ± 0.79	15.1 ± 0.0	1.3 ± 0.1	14.39 ± 0.96	19.94	13.2	17.1	15.77	14.9	
354.615+0.472	44	5.08 ± 0.88	-21.4 ± 0.0	0.3 ± 0.1	14.50 ± 1.24	12.60	-22.0	-20.8	17.14	-21.5	20120414TN
	44	23.85 ± 2.14	-20.3 ± 0.1	2.4 ± 0.3	9.38 ± 1.24	15.79	-20.8	-18.7	11.52	-20.4	
	44	30.20 ± 0.64	-17.9 ± 0.0	0.5 ± 0.0	58.37 ± 1.24	31.65	-18.7	-17.0	59.03	-17.9	
	95	13.95 ± 1.08	-21.4 ± 0.2	0.7 ± 0.2	20.02 ± 1.51	24.10	-23.9	-20.9	22.95	-21.5	
	95	27.18 ± 1.08	-20.1 ± 0.2	1.8 ± 0.2	14.41 ± 1.51	25.44	-20.9	-18.7	14.90	-20.3	
	95	25.30 ± 1.08	-17.8 ± 0.2	0.7 ± 0.2	35.20 ± 1.51	28.92	-18.7	-15.8	36.17	-17.9	
354.701+0.299	44	9.32 ± 0.71	95.0 ± 0.1	1.4 ± 0.1	6.05 ± 0.83	9.18	93.7	96.5	8.10	94.9	20120414TN
	44	10.42 ± 0.74	98.4 ± 0.1	1.6 ± 0.1	5.98 ± 0.83	9.72	96.5	100.2	6.02	98.7	
	95	5.38 ± 0.68	94.8 ± 0.1	1.0 ± 0.2	5.07 ± 0.95	7.50	93.3	96.6	4.93	94.7	
	95	10.06 ± 1.26	98.2 ± 0.1	2.5 ± 0.4	3.76 ± 0.95	10.57	96.6	101.5	5.07	97.9	

Table 4.1 (cont'd)

Source	Frequency (GHz)	Gaussian Fit S_{int} (Jy km s^{-1})	Gaussian Fit V_{peak} (km s^{-1})	Gaussian Fit FWHM (km s^{-1})	Gaussian Fit S_{peak} (Jy)	Integrated Fit S_{int} (Jy km s^{-1})	Integrated Fit v_{min} (km s^{-1})	Integrated Fit v_{max} (km s^{-1})	Integrated Fit S_{peak} (Jy)	Integrated Fit V_{peak} (km s^{-1})	Obs. Date yyyymmdd[†]
354.724+0.300	44	18.17 ± 0.81	97.9 ± 0.0	2.0 ± 0.1	8.51 ± 0.77	17.73	95.1	99.0	10.27	98.3	20120411TN
	44	11.59 ± 0.50	100.4 ± 0.0	0.8 ± 0.0	14.16 ± 0.77	13.57	99.0	102.0	15.16	100.4	
	95	15.34 ± 1.31	98.1 ± 0.1	2.6 ± 0.3	5.47 ± 0.60	15.79	94.9	99.4	7.46	98.2	
	95	9.48 ± 0.73	100.4 ± 0.0	0.9 ± 0.1	10.44 ± 0.60	12.80	99.4	102.3	11.84	100.4	
355.184-0.419	22	20.29 ± 0.63	-2.6 ± 0.0	1.1 ± 0.0	17.60 ± 0.85	22.13	-3.7	-0.5	17.47	-2.6	20120411TN
	44	10.10 ± 0.87	-5.2 ± 0.0	1.2 ± 0.1	7.72 ± 0.94	10.08	-6.1	-4.4	8.93	-5.4	
	44	10.52 ± 0.81	-3.8 ± 0.0	0.7 ± 0.1	15.14 ± 0.94	19.63	-4.4	-3.4	35.31	-3.2	
	44	54.23 ± 1.21	-2.9 ± 0.0	0.6 ± 0.0	89.65 ± 0.94	64.32	-3.4	-2.1	85.10	-2.8	
	44	18.88 ± 1.22	-2.0 ± 0.0	1.0 ± 0.1	17.90 ± 0.94	12.08	-2.1	-0.9	18.17	-2.0	
	95	10.50 ± 1.33	-5.1 ± 0.0	1.1 ± 0.2	9.18 ± 0.78	13.33	-7.0	-4.5	9.11	-5.3	
	95	15.33 ± 2.22	-3.7 ± 0.0	1.0 ± 0.1	14.71 ± 0.78	17.19	-4.5	-3.4	17.71	-3.3	
	95	15.41 ± 2.70	-2.9 ± 0.0	0.6 ± 0.0	24.41 ± 0.78	30.31	-3.4	-2.2	31.34	-2.9	
	95	23.28 ± 1.68	-2.1 ± 0.0	1.3 ± 0.1	17.04 ± 0.78	17.25	-2.2	1.2	17.44	-1.9	
355.344+0.147	22	7.48 ± 0.38	9.0 ± 0.0	0.7 ± 0.0	10.32 ± 0.60	7.70	8.2	9.4	9.82	8.8	20120503TN
	22	11.34 ± 0.36	10.0 ± 0.1	0.6 ± 0.0	19.15 ± 0.60	12.68	9.4	11.4	18.00	9.9	
	22	1.26 ± 0.31	13.5 ± 0.1	0.7 ± 0.2	1.68 ± 0.60	1.21	12.9	14.3	2.34	13.3	
	22	5.58 ± 0.45	15.5 ± 0.1	1.2 ± 0.1	4.23 ± 0.60	5.32	14.3	16.9	4.39	15.6	
	22	1.60 ± 0.38	18.2 ± 0.1	0.8 ± 0.2	1.81 ± 0.60	1.56	17.2	19.2	1.89	18.3	
355.538-0.105	22	2.98 ± 0.56	-1.4 ± 0.1	0.7 ± 0.2	3.95 ± 0.93	3.48	-2.9	-0.1	3.99	-1.4	20120503TN
356.662-0.263	44	1.14 ± 0.34	-54.0 ± 0.1	0.7 ± 0.2	1.56 ± 0.44	0.85	-55.2	-53.1	1.49	-53.9	20130302TN
	44	1.28 ± 0.40	-52.1 ± 0.1	0.7 ± 0.3	1.70 ± 0.44	1.36	-53.1	-50.7	1.67	-52.2	
	95	4.24 ± 0.59	-53.2 ± 0.1	2.3 ± 0.4	1.74 ± 0.35	4.94	-57.3	-50.0	1.91	-53.1	
357.558-0.321	22	4.87 ± 0.42	-43.3 ± 0.2	2.2 ± 0.2	2.07 ± 0.71	4.71	-45.3	-41.1	2.58	-43.6	20120511US
	22	6.89 ± 0.42	-13.6 ± 0.2	1.2 ± 0.2	5.22 ± 0.71	6.78	-14.8	-13.2	5.95	-13.1	
	22	12.22 ± 0.42	-12.4 ± 0.2	1.0 ± 0.2	11.05 ± 0.71	14.28	-13.2	-11.4	11.48	-12.4	
	22	4.71 ± 0.42	-10.8 ± 0.2	1.2 ± 0.2	3.68 ± 0.71	6.13	-11.4	-9.7	3.92	-10.7	
	22	33.07 ± 2.76	-8.1 ± 0.2	2.3 ± 0.2	13.76 ± 0.74	42.24	-9.7	-7.5	37.41	-7.4	
	22	61.08 ± 2.76	-6.9 ± 0.2	1.5 ± 0.2	37.76 ± 0.74	64.13	-7.5	-6.2	50.86	-6.7	

Table 4.1 (cont'd)

Source	Frequency (GHz)	Gaussian Fit S_{int} (Jy km s^{-1})	Gaussian Fit V_{peak} (km s^{-1})	Gaussian Fit FWHM (km s^{-1})	Gaussian Fit S_{peak} (Jy)	Integrated Fit S_{int} (Jy km s^{-1})	Integrated Fit v_{min} (km s^{-1})	Integrated Fit v_{max} (km s^{-1})	Integrated Fit S_{peak} (Jy)	Integrated Fit V_{peak} (km s^{-1})	Obs. Date yyyymmdd[†]
	22	94.34 ± 2.76	-5.2 ± 0.2	1.6 ± 0.2	57.14 ± 0.74	107.43	-6.2	-3.8	64.64	-5.5	
	22	29.09 ± 2.76	-3.4 ± 0.2	2.6 ± 0.2	10.41 ± 0.74	24.74	-3.8	-1.9	13.21	-3.8	
	22	20.18 ± 2.76	-1.2 ± 0.2	2.1 ± 0.2	9.13 ± 0.74	19.29	-1.9	0.4	11.96	-1.3	
	22	5.69 ± 0.56	1.0 ± 0.2	1.0 ± 0.2	5.50 ± 1.19	5.43	0.4	1.4	6.05	1.1	
	22	11.77 ± 0.56	2.6 ± 0.2	1.4 ± 0.2	7.96 ± 1.19	14.36	1.4	3.5	8.55	2.7	
	22	5.37 ± 0.56	3.8 ± 0.2	1.1 ± 0.2	4.79 ± 1.19	7.16	3.5	4.6	6.41	3.8	
	22	21.59 ± 0.56	5.7 ± 0.2	1.7 ± 0.2	11.82 ± 1.19	22.14	4.6	7.4	12.43	5.5	
	22	11.48 ± 0.56	8.5 ± 0.2	1.6 ± 0.2	6.73 ± 1.19	10.83	7.4	10.1	7.02	8.4	
	22	4.02 ± 0.90	11.5 ± 0.3	2.6 ± 0.7	1.45 ± 0.72	3.59	10.1	13.8	2.31	11.4	
	22	6.07 ± 0.51	17.8 ± 0.0	1.0 ± 0.1	5.73 ± 0.72	7.34	16.5	19.4	5.88	17.9	
	22	15.14 ± 1.13	23.0 ± 0.2	4.5 ± 0.4	3.19 ± 0.72	14.45	19.4	27.8	3.98	23.8	
	44	6.95 ± 0.87	0.8 ± 0.6	8.4 ± 1.0	0.78 ± 0.46	5.90	-6.5	4.3	1.23	2.8	
	44	2.31 ± 0.26	5.1 ± 0.0	0.5 ± 0.1	4.63 ± 0.46	3.64	4.3	6.9	4.67	5.0	
	95	16.13 ± 1.64	0.0 ± 0.4	8.2 ± 1.0	1.84 ± 0.79	13.62	-6.7	4.2	3.11	-2.0	
	95	1.12 ± 0.37	5.0 ± 0.0	0.3 ± 0.1	3.34 ± 0.79	2.67	4.2	6.5	3.70	4.9	
357.922-0.337	44	3.81 ± 0.55	-0.9 ± 0.1	1.8 ± 0.3	2.00 ± 0.57	3.86	-3.2	1.0	2.35	-0.9	20120513US
	95	2.93 ± 0.50	-0.9 ± 0.0	0.5 ± 0.1	5.93 ± 1.08	3.82	-3.8	0.1	5.91	-0.9	
357.965-0.164	22	620.79 ± 12.95	-57.8 ± 0.0	2.5 ± 0.1	230.21 ± 10.74	604.93	-60.7	-55.6	233.89	-57.6	20120324YS
	22	27.30 ± 25.06	-54.1 ± 0.9	2.1 ± 0.9	12.43 ± 10.74	33.12	-55.6	-53.7	23.08	-55.3	
	22	33.08 ± 4.07	-52.5 ± 0.2	1.7 ± 0.2	18.48 ± 11.54	24.74	-53.7	-52.2	20.74	-52.7	
	22	25.82 ± 4.07	-50.7 ± 0.2	1.8 ± 0.2	13.83 ± 11.54	152.23	-52.2	-50.9	42.64	-50.8	
	22	116.69 ± 4.07	-50.0 ± 0.2	1.9 ± 0.2	58.10 ± 11.54	120.69	-50.9	-49.0	69.95	-50.2	
	22	79.24 ± 4.07	-48.2 ± 0.2	1.1 ± 0.2	65.62 ± 11.54	144.59	-49.0	-46.9	86.43	-48.1	
	22	123.78 ± 4.07	-46.6 ± 0.2	2.6 ± 0.2	45.26 ± 11.54	76.39	-46.9	-44.6	50.72	-46.4	
	22	33.95 ± 7.69	-43.4 ± 0.0	1.7 ± 0.5	18.48 ± 10.74	33.19	-44.6	-41.8	19.18	-43.5	
	22	59.70 ± 2.93	-4.6 ± 0.0	1.7 ± 0.1	33.67 ± 3.13	61.95	-6.9	-2.8	35.05	-4.7	
	22	141.43 ± 2.41	0.1 ± 0.0	1.2 ± 0.0	109.31 ± 3.13	157.98	-2.8	3.8	105.68	0.1	
	22	59.42 ± 2.38	11.2 ± 0.2	2.5 ± 0.2	21.93 ± 3.85	53.60	6.8	11.9	25.46	11.1	

Table 4.1 (cont'd)

Source	Frequency (GHz)	Gaussian Fit S_{int} (Jy km s^{-1})	Gaussian Fit V_{peak} (km s^{-1})	Gaussian Fit FWHM (km s^{-1})	Gaussian Fit S_{peak} (Jy)	Integrated Fit S_{int} (Jy km s^{-1})	Integrated Fit v_{min} (km s^{-1})	Integrated Fit v_{max} (km s^{-1})	Integrated Fit S_{peak} (Jy)	Integrated Fit V_{peak} (km s^{-1})	Obs. Date yyyymmdd[†]
	22	110.93 ± 2.38	14.0 ± 0.2	2.0 ± 0.2	51.84 ± 3.85	131.35	11.9	15.8	60.32	14.0	
	22	47.91 ± 2.38	16.9 ± 0.2	1.7 ± 0.2	25.68 ± 3.85	61.78	15.8	18.6	28.47	17.0	
	22	86.43 ± 2.38	19.6 ± 0.2	2.4 ± 0.2	33.20 ± 3.85	74.88	18.6	21.4	37.50	19.3	
	22	28.24 ± 2.38	22.9 ± 0.2	2.4 ± 0.2	11.26 ± 3.85	27.67	21.4	24.5	13.23	22.9	
	22	27.72 ± 2.98	33.3 ± 0.1	1.8 ± 0.2	109.31 ± 3.13	27.19	31.5	34.9	15.37	33.2	
	22	20.89 ± 2.96	58.3 ± 0.1	1.7 ± 0.3	14.27 ± 3.13	21.28	56.7	60.4	13.40	58.3	
	22	31.56 ± 3.30	91.3 ± 0.1	2.3 ± 0.3	11.48 ± 3.13	30.52	88.9	94.3	13.85	90.9	
	44	97.13 ± 1.31	-4.8 ± 0.0	1.5 ± 0.0	59.82 ± 1.52	65.04	-6.6	-0.9	37.41	-4.9	
	95	93.74 ± 1.47	-4.8 ± 0.0	1.6 ± 0.0	55.17 ± 1.70	103.52	-7.1	-1.1	59.94	-4.9	
358.371-0.468	22	21.71 ± 0.48	-2.1 ± 0.2	0.9 ± 0.2	22.99 ± 0.72	24.29	-4.3	-1.0	22.90	-2.2	20120512US
	22	4.05 ± 0.48	-0.5 ± 0.2	1.3 ± 0.2	2.92 ± 0.72	3.75	-1.0	0.9	3.31	-0.5	
	22	2.05 ± 0.48	1.8 ± 0.2	0.8 ± 0.2	2.28 ± 0.72	2.34	0.9	3.1	2.37	1.6	
	22	5.24 ± 0.48	5.2 ± 0.2	1.3 ± 0.2	3.68 ± 0.72	5.76	3.1	6.8	4.08	5.0	
	22	3.49 ± 0.48	9.9 ± 0.2	1.6 ± 0.2	2.09 ± 0.72	3.51	8.2	11.6	2.65	9.8	
358.386-0.483	22	97.66 ± 0.83	-2.5 ± 0.0	1.3 ± 0.0	73.29 ± 1.03	103.64	-4.5	-1.0	76.46	-2.3	20120324YS
	22	18.10 ± 0.67	-0.3 ± 0.0	0.9 ± 0.0	19.26 ± 1.03	18.10	-1.0	1.3	19.64	-0.2	
	44	21.76 ± 1.12	-3.3 ± 0.0	0.9 ± 0.1	23.17 ± 1.53	25.04	-5.0	-1.3	24.83	-3.3	
	95	26.14 ± 1.20	-3.4 ± 0.0	1.4 ± 0.1	17.16 ± 1.45	26.96	-6.0	-1.6	23.44	-3.3	
358.460-0.391	22	11.75 ± 0.64	-19.5 ± 0.0	1.2 ± 0.0	9.04 ± 1.04	12.91	-21.2	-17.7	10.57	-19.5	20120324YS
	22	29.66 ± 1.30	-16.4 ± 0.0	1.1 ± 0.0	25.21 ± 1.04	32.60	-17.7	-14.9	25.93	-16.5	
	22	7.68 ± 1.83	-14.5 ± 0.2	2.1 ± 0.6	3.45 ± 1.04	4.99	-14.9	-13.4	3.82	-14.2	
	22	11.82 ± 1.26	-12.4 ± 0.0	1.2 ± 0.1	9.58 ± 1.04	12.97	-13.4	-11.2	10.34	-12.3	
	22	6.62 ± 1.02	-10.4 ± 0.1	1.0 ± 0.2	6.15 ± 1.05	6.74	-11.2	-9.8	6.20	-10.2	
	22	16.40 ± 1.01	-8.9 ± 0.0	1.1 ± 0.1	14.03 ± 1.05	18.60	-9.8	-5.9	14.61	-8.7	
	22	4.57 ± 0.58	-4.6 ± 0.0	0.7 ± 0.1	6.55 ± 1.05	4.21	-5.9	-3.4	5.99	-4.7	
	44	82.80 ± 1.79	-3.2 ± 0.0	2.9 ± 0.1	26.82 ± 1.50	84.59	-7.4	0.5	32.86	-3.6	
	95	71.16 ± 1.98	-3.0 ± 0.1	3.9 ± 0.1	17.29 ± 1.52	68.86	-7.0	0.6	18.57	-2.7	
358.721-0.126	44	6.49 ± 0.50	10.1 ± 0.1	1.9 ± 0.2	3.25 ± 0.53	6.32	8.1	12.6	4.35	10.3	20120325YS

Table 4.1 (cont'd)

Source	Frequency (GHz)	Gaussian Fit				Integrated Fit					Obs. Date yyyymmdd†
		S_{int} (Jy km s^{-1})	V_{peak} (km s^{-1})	FWHM (km s^{-1})	S_{peak} (Jy)	S_{int} (Jy km s^{-1})	v_{min} (km s^{-1})	v_{max} (km s^{-1})	S_{peak} (Jy)	V_{peak} (km s^{-1})	
358.809-0.085	44	14.60 ± 0.61	-53.9 ± 0.0	0.7 ± 0.0	19.83 ± 1.04	15.25	-55.1	-52.2	20.21	-53.9	20120414TN
	95	14.11 ± 0.68	-54.0 ± 0.0	0.9 ± 0.1	15.40 ± 1.05	14.53	-55.8	-52.2	16.02	-54.1	
358.931-0.030a	22	1.32 ± 0.21	-16.0 ± 0.0	0.6 ± 0.1	2.09 ± 0.38	1.45	-17.0	-14.7	2.00	-16.1	20120411TN
	44	2.09 ± 0.18	-20.9 ± 0.0	0.3 ± 0.0	5.84 ± 0.37	3.26	-21.6	-20.4	6.77	-20.9	
	44	6.42 ± 0.58	-19.3 ± 0.2	3.7 ± 0.4	1.64 ± 0.37	5.19	-20.4	-15.6	2.39	-19.9	
	95	1.70 ± 0.27	-20.9 ± 0.0	0.4 ± 0.1	4.16 ± 0.57	6.85	-25.1	-20.1	5.88	-21.0	
	95	16.90 ± 1.07	-18.7 ± 0.2	6.8 ± 0.5	2.32 ± 0.57	12.01	-20.1	-12.5	2.97	-19.8	
358.931-0.030b	22	4.30 ± 0.28	-67.8 ± 0.0	1.1 ± 0.1	3.58 ± 0.38	4.20	-69.2	-66.4	3.71	-67.7	20120411TN
	44	1.86 ± 0.17	-61.7 ± 0.0	0.4 ± 0.0	4.50 ± 0.37	2.15	-62.5	-60.5	3.89	-61.8	
359.138+0.031	22	55.88 ± 64.63	-107.7 ± 1.7	3.0 ± 5.2	17.32 ± 0.42	63.74	-114.3	-104.0	21.46	-107.3	20130321TN
	22	15.41 ± 80.80	-99.4 ± 12.3	3.6 ± 61.8	2.92 ± 0.42	11.28	-102.4	-95.7	3.36	-99.8	
	22	6.65 ± 0.88	-13.6 ± 0.1	1.3 ± 0.3	3.63 ± 0.44	5.11	-14.7	-13.0	4.00	-13.8	
	22	14.60 ± 0.98	-11.7 ± 0.1	1.6 ± 0.2	6.23 ± 0.44	13.72	-13.0	-10.2	6.41	-11.7	
	22	23.67 ± 0.72	-9.1 ± 0.0	1.4 ± 0.1	12.05 ± 0.44	24.22	-10.2	-7.5	13.19	-9.2	
	22	50.16 ± 1.00	-5.9 ± 0.0	2.6 ± 0.1	13.34 ± 0.44	29.65	-7.5	-4.7	15.58	-5.8	
	22	282.21 ± 23.86	-2.7 ± 0.4	1.4 ± 0.4	138.42 ± 0.40	249.47	-4.4	-2.8	292.02	-2.4	
	22	473.32 ± 23.86	-1.9 ± 0.4	1.0 ± 0.4	319.86 ± 0.40	498.91	-2.8	-1.4	396.64	-2.0	
	22	623.92 ± 23.86	-0.6 ± 0.4	0.8 ± 0.4	515.31 ± 0.40	522.70	-1.4	0.3	472.93	-0.7	
	22	76.12 ± 23.86	1.0 ± 0.4	1.1 ± 0.4	49.76 ± 0.40	73.84	0.3	2.8	56.05	0.9	
	22	38.32 ± 1.78	4.3 ± 0.4	0.9 ± 0.4	28.14 ± 0.40	36.50	3.3	6.4	29.61	4.3	
	22	70.41 ± 1.78	10.2 ± 0.4	7.0 ± 0.4	6.96 ± 0.40	14.04	6.4	9.1	5.53	7.7	
	22	44.79 ± 1.78	12.2 ± 0.4	1.4 ± 0.4	22.86 ± 0.40	62.31	9.1	13.8	28.99	12.3	
	22	5.71 ± 1.78	15.5 ± 0.4	1.6 ± 0.4	2.46 ± 0.40	10.85	13.8	17.4	3.80	14.4	
	22	27.40 ± 1.78	19.1 ± 0.4	1.6 ± 0.4	11.92 ± 0.40	22.12	17.4	21.3	13.71	19.1	
359.938+0.170	44	8.57 ± 0.52	-1.0 ± 0.0	1.0 ± 0.1	8.22 ± 0.66	11.23	-2.7	3.0	9.30	-1.2	20120324YS
	44	2.48 ± 0.40	16.0 ± 0.0	0.6 ± 0.1	3.76 ± 0.66	2.64	13.4	17.4	4.16	16.0	
	95	13.08 ± 0.75	-0.7 ± 0.1	1.9 ± 0.1	6.38 ± 0.75	13.21	-2.5	1.3	8.24	-1.1	
	95	1.79 ± 0.47	16.1 ± 0.1	0.8 ± 0.3	2.01 ± 0.75	2.60	14.4	17.6	2.17	16.0	

Table 4.1 (cont'd)

Source	Frequency (GHz)	Gaussian Fit				Integrated Fit					Obs. Date yyyymmdd†
		S_{int} (Jy km s^{-1})	V_{peak} (km s^{-1})	FWHM (km s^{-1})	S_{peak} (Jy)	S_{int} (Jy km s^{-1})	v_{min} (km s^{-1})	v_{max} (km s^{-1})	S_{peak} (Jy)	V_{peak} (km s^{-1})	
359.970-0.457	22	23.42 ± 0.59	3.9 ± 0.0	0.9 ± 0.0	18.72 ± 0.65	17.89	2.8	5.0	18.77	3.8	20130308TN
	22	11.32 ± 0.50	10.5 ± 0.0	0.6 ± 0.0	12.99 ± 0.65	8.72	9.5	11.4	12.25	10.6	
	44	1.75 ± 0.52	19.7 ± 0.1	0.7 ± 0.4	2.39 ± 0.46	2.07	18.2	21.3	2.11	19.5	
	95	6.53 ± 0.84	19.6 ± 0.0	2.9 ± 0.5	2.13 ± 0.47	7.30	15.2	23.9	2.49	19.8	
358.980+0.084	44	1.97 ± 0.39	-2.0 ± 0.1	1.4 ± 0.4	1.35 ± 0.45	1.97	-4.3	0.0	2.01	-1.9	20120513US
	95	8.71 ± 1.11	-3.3 ± 0.3	4.5 ± 0.6	1.82 ± 0.81	8.40	-7.8	0.6	3.23	-1.9	
0.092+0.663	22	25.98 ± 0.57	15.9 ± 0.0	0.8 ± 0.0	31.79 ± 0.82	29.88	14.7	16.4	33.41	15.9	20120324YS
	22	69.28 ± 0.65	17.4 ± 0.0	1.1 ± 0.0	57.32 ± 0.82	69.57	16.4	19.0	57.76	17.4	
	44	58.41 ± 1.38	17.2 ± 0.0	2.4 ± 0.1	23.33 ± 1.08	60.84	13.1	21.4	27.48	16.9	
	95	55.50 ± 1.54	17.1 ± 0.0	2.5 ± 0.1	21.25 ± 1.11	65.44	12.7	22.2	24.86	16.7	
0.167-0.446	22	11.30 ± 0.89	11.0 ± 0.1	2.0 ± 0.2	5.24 ± 0.92	10.86	9.1	12.9	5.46	12.5	20120513US
	22	2.30 ± 0.55	15.7 ± 0.1	0.6 ± 0.2	3.69 ± 0.92	2.71	15.1	17.1	3.76	16.3	
	44	2.04 ± 0.45	16.1 ± 0.2	1.5 ± 0.4	1.27 ± 0.39	1.52	13.9	18.5	1.34	16.3	
0.376+0.040	22	6.49 ± 7.86	29.0 ± 0.4	1.1 ± 0.4	4.05 ± 0.48	4.94	27.9	29.8	4.89	29.3	20130224TN
	22	16.36 ± 7.86	33.0 ± 0.4	1.8 ± 0.4	6.12 ± 0.48	10.97	31.7	34.8	6.77	33.1	
	22	223.32 ± 7.86	39.6 ± 0.4	1.1 ± 0.4	136.89 ± 0.48	164.15	37.5	41.4	123.76	39.4	
	44	8.78 ± 0.92	40.7 ± 0.3	5.1 ± 0.5	1.63 ± 0.44	7.89	36.9	47.1	2.76	41.7	
	95	14.02 ± 0.89	39.7 ± 0.2	5.8 ± 0.5	2.29 ± 0.38	14.42	32.2	44.6	2.70	40.6	
0.475-0.010	44	28.75 ± 2.14	29.9 ± 0.5	13.7 ± 1.3	1.97 ± 0.80	28.82	18.2	44.0	3.55	30.0	20120414TN
	95	39.12 ± 1.85	29.7 ± 0.2	9.8 ± 0.6	3.76 ± 0.86	37.25	21.8	40.6	5.50	28.4	
0.546-0.852	22	40.08 ± 54.68	-56.5 ± 0.8	1.1 ± 1.7	25.64 ± 0.46	33.51	-59.3	-54.1	24.46	-56.7	20130221TN
	22	78.28 ± 121.15	1.4 ± 4.2	5.6 ± 10.9	9.73 ± 0.46	51.99	-5.7	3.0	17.12	0.2	
	22	161.09 ± 108.64	4.3 ± 0.3	1.3 ± 0.8	88.57 ± 0.46	156.32	3.0	6.4	94.09	4.4	
	22	61.13 ± 114.20	6.5 ± 1.8	3.0 ± 7.0	14.25 ± 0.46	31.34	6.4	10.3	17.74	7.0	
	22	494.96 ± 66.51	13.3 ± 0.1	1.5 ± 0.2	233.02 ± 0.46	383.70	10.3	14.6	245.19	13.3	
	22	441.10 ± 24.90	16.6 ± 0.4	2.1 ± 0.4	146.91 ± 0.46	318.64	15.1	18.1	159.66	17.1	
	22	138.34 ± 24.90	19.2 ± 0.4	1.3 ± 0.4	72.65 ± 0.46	143.33	18.1	25.0	77.96	19.2	
	22	774.33 ± 24.90	30.8 ± 0.4	0.7 ± 0.4	768.23 ± 0.46	625.15	25.0	34.1	633.34	31.0	

Table 4.1 (cont'd)

Source	Frequency (GHz)	Gaussian Fit S_{int} (Jy km s^{-1})	Gaussian Fit V_{peak} (km s^{-1})	Gaussian Fit FWHM (km s^{-1})	Gaussian Fit S_{peak} (Jy)	Integrated Fit S_{int} (Jy km s^{-1})	Integrated Fit v_{min} (km s^{-1})	Integrated Fit v_{max} (km s^{-1})	Integrated Fit S_{peak} (Jy)	Integrated Fit V_{peak} (km s^{-1})	Obs. Date yyyymmdd[†]
	22	265.34 ± 24.90	36.2 ± 0.4	17.9 ± 0.4	10.23 ± 0.46	114.66	34.1	51.4	24.56	36.0	
	22	76.83 ± 24.90	55.0 ± 0.4	1.3 ± 0.4	41.80 ± 0.46	66.14	51.4	57.9	45.78	55.0	
	22	53.37 ± 24.90	80.2 ± 0.4	1.2 ± 0.4	29.68 ± 0.46	42.55	78.4	81.0	29.69	80.3	
	22	24.19 ± 24.90	81.8 ± 0.4	1.1 ± 0.4	15.81 ± 0.46	21.30	81.0	83.0	15.83	81.5	
	22	24.70 ± 24.90	93.9 ± 0.4	1.9 ± 0.4	8.91 ± 0.46	18.83	91.6	95.8	9.37	94.2	
	22	29.77 ± 24.90	99.2 ± 0.4	4.0 ± 0.4	5.15 ± 0.46	22.82	95.8	100.9	8.49	101.3	
	22	23.23 ± 24.90	101.9 ± 0.4	1.0 ± 0.4	15.84 ± 0.46	19.05	100.9	103.0	15.75	101.8	
	44	55.26 ± 2.53	16.6 ± 0.2	6.9 ± 0.4	7.53 ± 0.52	48.54	9.4	26.0	8.22	17.2	
	95	87.51 ± 2.07	17.1 ± 0.1	7.0 ± 0.2	11.73 ± 0.45	82.62	0.0	25.3	13.28	16.1	
1.008-0.237	44	4.09 ± 0.41	-0.7 ± 0.1	2.5 ± 0.3	1.56 ± 0.36	4.10	-2.8	2.8	1.80	-0.6	20120609TN
2.143+0.009	22	19.50 ± 1.06	58.2 ± 0.1	2.1 ± 0.1	65.05 ± 0.37	12.48	56.4	58.7	5.93	57.8	20130222TN
	22	15.59 ± 0.89	60.0 ± 0.0	0.9 ± 0.0	12.22 ± 0.37	15.02	58.7	61.3	12.60	59.9	
2.521-0.220	22	1.02 ± 0.34	1.5 ± 0.1	0.3 ± 0.2	2.93 ± 0.59	1.46	0.7	2.2	2.34	1.6	20120610TN
2.703+0.040	44	3.64 ± 0.55	96.1 ± 0.2	1.8 ± 0.3	1.85 ± 0.44	2.84	92.1	99.1	2.15	96.4	20130222TN
	95	2.42 ± 0.38	96.2 ± 0.1	1.4 ± 0.3	1.61 ± 0.33	2.78	93.5	98.4	1.61	96.2	
3.312-0.399	44	14.10 ± 1.22	5.5 ± 0.2	4.3 ± 0.6	3.05 ± 0.65	15.78	-1.7	12.2	5.07	6.1	20120504TN
	95	8.65 ± 0.87	5.5 ± 0.2	3.5 ± 0.4	2.34 ± 0.65	8.65	1.6	11.0	2.97	5.7	
3.442-0.348	44	5.16 ± 0.58	-28.0 ± 0.0	0.5 ± 0.1	9.25 ± 1.13	6.82	-29.5	-26.8	8.56	-27.9	20120325YS
	44	18.01 ± 1.28	-25.3 ± 0.1	1.9 ± 0.2	9.03 ± 1.13	16.83	-26.8	-24.0	9.03	-25.6	
	44	3.98 ± 1.05	-23.1 ± 0.1	1.2 ± 0.3	3.16 ± 1.13	4.55	-24.0	-21.6	4.84	-23.5	
	95	7.56 ± 0.77	-28.0 ± 0.0	0.7 ± 0.1	9.53 ± 1.19	9.19	-29.5	-27.1	9.22	-28.0	
	95	17.07 ± 1.23	-25.5 ± 0.1	2.1 ± 0.2	7.73 ± 1.19	16.31	-27.1	-23.9	8.26	-25.5	
	95	2.04 ± 0.57	-23.3 ± 0.1	0.5 ± 0.1	3.61 ± 1.19	2.69	-23.9	-22.3	3.63	-23.5	
3.502-0.200	44	2.87 ± 0.23	-21.4 ± 0.0	0.5 ± 0.1	4.97 ± 0.46	2.89	-22.5	-20.1	4.94	-21.5	20120411TN
4.393+0.079	44	2.62 ± 0.47	4.8 ± 0.2	1.8 ± 0.3	1.35 ± 0.39	2.27	1.2	8.1	1.36	5.6	20130224TN
	95	2.12 ± 0.38	5.6 ± 0.1	1.4 ± 0.3	1.42 ± 0.32	1.89	3.9	8.0	1.47	5.4	
4.434+0.129	22	2.49 ± 0.31	4.2 ± 0.1	1.3 ± 0.2	1.83 ± 0.38	3.84	0.2	5.7	1.83	4.2	20120325YS
	44	8.81 ± 0.99	3.5 ± 0.4	6.9 ± 0.8	1.21 ± 0.58	8.26	-1.7	8.5	1.88	5.5	

Table 4.1 (cont'd)

Source	Frequency (GHz)	Gaussian Fit S_{int} (Jy km s^{-1})	Gaussian Fit V_{peak} (km s^{-1})	Gaussian Fit FWHM (km s^{-1})	Gaussian Fit S_{peak} (Jy)	Integrated Fit S_{int} (Jy km s^{-1})	Integrated Fit v_{min} (km s^{-1})	Integrated Fit v_{max} (km s^{-1})	Integrated Fit S_{peak} (Jy)	Integrated Fit V_{peak} (km s^{-1})	Obs. Date yyyymmdd†
	95	11.20 ± 1.00	3.8 ± 0.3	6.8 ± 0.7	1.54 ± 0.59	10.53	-2.6	8.3	2.52	4.3	
4.676+0.276	44	19.11 ± 0.70	7.0 ± 0.0	0.9 ± 0.0	19.19 ± 1.06	19.17	5.5	8.0	18.42	7.2	20120411TN
	95	14.77 ± 0.56	7.0 ± 0.0	0.9 ± 0.0	15.94 ± 0.88	16.26	0.8	9.8	15.56	7.0	
5.618-0.082	44	8.79 ± 1.10	-24.9 ± 0.2	3.2 ± 0.5	2.61 ± 0.84	8.90	-28.8	-21.4	3.40	-25.2	20120414TN
	95	12.40 ± 0.96	-24.8 ± 0.1	2.8 ± 0.3	4.13 ± 0.85	12.26	-28.5	-21.4	4.53	-25.4	
5.630-0.294	22	3.61 ± 0.73	17.9 ± 0.1	1.3 ± 0.3	1.91 ± 0.47	2.75	16.9	19.8	1.80	17.9	20130223TN
5.657+0.416	22	2.16 ± 0.35	13.5 ± 0.0	0.5 ± 0.1	4.07 ± 0.74	2.27	12.2	14.3	3.69	13.4	20120502TN
	22	4.88 ± 0.84	19.0 ± 0.1	1.8 ± 0.5	2.59 ± 0.74	5.35	16.7	21.4	3.62	19.3	
	22	1.09 ± 0.29	29.9 ± 0.1	0.3 ± 0.1	3.05 ± 0.74	0.32	29.0	30.9	2.48	29.8	
5.677-0.027	22	5.53 ± 0.58	-2.1 ± 0.1	1.2 ± 0.1	4.32 ± 0.79	5.27	-3.8	-0.9	4.25	-2.5	20120512US
06.189-0.358	22	1.82 ± 0.34	-46.3 ± 0.1	0.6 ± 0.2	2.65 ± 0.59	3.47	-48.9	-45.5	2.73	-46.2	20120325YS
	22	14.72 ± 0.35	-29.6 ± 0.0	0.7 ± 0.0	19.58 ± 0.59	16.56	-30.7	-27.4	19.27	-29.6	
	44	2.16 ± 0.79	-34.6 ± 0.1	0.6 ± 0.2	3.52 ± 0.80	2.89	-35.3	-34.2	3.93	-34.6	
	44	4.77 ± 0.97	-33.6 ± 0.1	1.0 ± 0.3	4.59 ± 0.80	4.97	-34.2	-32.9	5.09	-33.7	
	44	4.95 ± 0.52	-32.0 ± 0.0	0.7 ± 0.1	6.41 ± 0.80	5.00	-32.9	-31.1	7.61	-31.8	
	95	2.06 ± 0.51	-35.0 ± 0.1	0.6 ± 0.1	3.28 ± 0.75	2.84	-35.6	-34.4	3.69	-34.8	
	95	6.28 ± 0.77	-33.8 ± 0.1	1.2 ± 0.2	5.06 ± 0.75	6.01	-34.4	-32.9	5.56	-33.8	
	95	4.74 ± 0.59	-32.0 ± 0.1	1.0 ± 0.2	4.55 ± 0.75	5.41	-32.9	-30.4	4.28	-31.8	
06.368-0.052	44	20.45 ± 0.89	141.4 ± 0.1	3.1 ± 0.2	6.18 ± 0.49	20.73	137.1	146.0	7.33	140.9	20130224TN
	95	14.35 ± 0.89	141.7 ± 0.1	3.9 ± 0.3	3.45 ± 0.47	14.66	136.9	145.6	4.29	141.0	
06.588-0.192	22	3.43 ± 0.66	-1.7 ± 0.1	1.0 ± 0.2	2.39 ± 0.48	2.83	-3.2	0.0	2.37	-1.8	20130223TN
06.610-0.082	22	5.28 ± 0.75	-38.7 ± 0.1	1.1 ± 0.2	3.45 ± 0.50	4.88	-41.3	-36.6	3.48	-38.8	20130223TN
	22	7.65 ± 0.66	2.4 ± 0.0	1.0 ± 0.1	5.20 ± 0.50	8.14	-2.9	4.4	5.13	2.5	
	44	2.11 ± 0.53	4.7 ± 0.1	0.8 ± 0.3	2.43 ± 0.50	3.40	2.1	6.6	2.51	4.8	
07.166+0.131	22	4.96 ± 0.68	77.0 ± 0.1	1.1 ± 0.2	4.28 ± 0.96	5.83	74.3	78.1	5.13	77.1	20120414TN
	44	6.91 ± 0.64	82.7 ± 0.1	1.4 ± 0.2	4.77 ± 0.76	6.94	81.0	84.7	6.57	83.0	
	95	5.92 ± 0.79	82.8 ± 0.1	1.1 ± 0.2	5.19 ± 0.86	8.92	78.9	87.1	6.16	82.9	
07.632-0.109	44	32.93 ± 0.98	153.8 ± 0.0	2.8 ± 0.1	11.03 ± 0.84	33.28	150.0	157.0	12.58	153.5	20120325YS

Table 4.1 (cont'd)

Source	Frequency (GHz)	Gaussian Fit S_{int} (Jy km s^{-1})	Gaussian Fit V_{peak} (km s^{-1})	Gaussian Fit FWHM (km s^{-1})	Gaussian Fit S_{peak} (Jy)	Integrated Fit S_{int} (Jy km s^{-1})	Integrated Fit v_{min} (km s^{-1})	Integrated Fit v_{max} (km s^{-1})	Integrated Fit S_{peak} (Jy)	Integrated Fit V_{peak} (km s^{-1})	Obs. Date yyyymmdd[†]
	95	38.26 ± 1.09	153.7 ± 0.0	3.1 ± 0.1	11.70 ± 0.91	38.68	150.4	157.3	12.66	153.6	
08.317-0.096	44	4.61 ± 0.34	45.8 ± 0.0	0.7 ± 0.1	5.92 ± 0.56	5.80	44.4	48.5	5.91	45.6	20120415TN
	95	2.56 ± 0.46	45.8 ± 0.1	0.8 ± 0.2	2.84 ± 0.61	3.39	44.1	48.9	3.09	45.9	
08.832-0.028	22	26.55 ± 1.95	-13.0 ± 0.0	0.8 ± 0.0	23.55 ± 0.68	25.80	-14.8	-11.0	24.40	-13.0	20130220TN
	22	18.92 ± 3.66	-10.5 ± 0.4	4.5 ± 1.1	2.90 ± 0.68	7.81	-11.0	-7.8	5.25	-9.2	
	22	64.05 ± 0.89	-3.9 ± 0.0	1.0 ± 0.0	44.05 ± 0.68	48.59	-5.8	-2.0	40.30	-3.7	
	22	25.60 ± 1.29	-0.4 ± 0.0	1.5 ± 0.1	11.77 ± 0.68	21.19	-2.0	1.5	11.78	-0.3	
	22	12.90 ± 1.53	2.8 ± 0.1	2.3 ± 0.3	3.93 ± 0.68	8.02	1.5	4.7	4.36	3.1	
	44	18.31 ± 0.76	-0.0 ± 0.0	1.0 ± 0.1	17.62 ± 0.75	22.67	-2.9	4.6	17.75	-0.2	
	95	12.80 ± 1.01	-0.0 ± 0.1	2.1 ± 0.2	5.65 ± 0.65	13.79	-3.4	3.0	6.80	-0.1	
08.872-0.493	22	11.34 ± 0.73	18.6 ± 0.0	1.3 ± 0.1	6.20 ± 0.49	8.16	16.6	20.2	6.05	18.9	20130224TN
09.215-0.202	22	6.22 ± 0.38	36.1 ± 0.0	0.8 ± 0.1	7.71 ± 0.60	7.99	34.3	39.1	8.16	36.1	20120513US
09.986-0.028	22	3.98 ± 0.59	40.6 ± 0.1	1.7 ± 0.3	1.67 ± 0.34	3.02	38.7	42.2	1.68	40.8	20130224TN
	22	2.76 ± 0.87	46.5 ± 0.2	1.5 ± 0.5	1.28 ± 0.34	1.75	45.1	47.1	1.35	46.7	
	22	7.14 ± 1.10	49.0 ± 0.1	1.9 ± 0.4	2.66 ± 0.34	6.00	47.1	50.6	3.10	49.2	
	22	2.37 ± 0.40	57.8 ± 0.1	0.7 ± 0.2	2.25 ± 0.34	2.33	56.4	59.0	1.93	57.7	
	44	2.62 ± 0.44	50.2 ± 0.2	1.8 ± 0.3	1.37 ± 0.34	2.44	46.8	52.5	1.59	50.3	
	95	4.31 ± 0.56	50.3 ± 0.2	3.0 ± 0.5	1.35 ± 0.31	4.81	45.2	54.6	1.53	50.8	
10.205-0.345	44	3.28 ± 0.38	13.2 ± 0.0	0.6 ± 0.1	5.17 ± 0.64	4.42	11.4	14.3	5.49	13.2	20120326YS
	95	2.56 ± 0.84	13.2 ± 0.1	0.8 ± 0.5	2.95 ± 0.69	3.20	10.9	14.1	4.22	13.3	
10.287-0.125	22	3.66 ± 1.09	-85.9 ± 0.2	1.3 ± 0.6	2.70 ± 0.79	4.26	-88.2	-84.2	2.70	-85.9	20130418TN
	22	5.91 ± 0.74	16.7 ± 0.0	0.8 ± 0.1	6.79 ± 0.79	8.48	14.0	19.1	6.24	16.9	
	44	21.08 ± 1.04	14.4 ± 0.1	2.4 ± 0.2	8.25 ± 0.64	24.59	9.4	18.8	8.80	14.6	
	95	13.69 ± 1.47	14.3 ± 0.1	2.8 ± 0.4	4.62 ± 0.79	15.47	9.8	17.2	5.25	14.8	
10.323-0.160	22	2.30 ± 0.59	-2.4 ± 0.2	1.3 ± 0.4	1.24 ± 0.35	2.31	-4.9	1.2	1.28	-2.5	20130224TN
	22	3.72 ± 0.82	5.0 ± 0.2	2.4 ± 0.7	1.06 ± 0.35	3.08	1.2	7.8	1.38	4.6	
	22	8.24 ± 1.15	12.0 ± 0.3	4.0 ± 0.7	1.41 ± 0.35	6.06	7.8	16.0	2.07	12.6	
	22	7.72 ± 0.68	18.6 ± 0.1	1.9 ± 0.2	2.84 ± 0.35	6.20	16.0	22.7	2.77	19.0	

Table 4.1 (cont'd)

Source	Frequency (GHz)	Gaussian Fit S_{int} (Jy km s^{-1})	Gaussian Fit V_{peak} (km s^{-1})	Gaussian Fit FWHM (km s^{-1})	Gaussian Fit S_{peak} (Jy)	Integrated Fit S_{int} (Jy km s^{-1})	Integrated Fit v_{min} (km s^{-1})	Integrated Fit v_{max} (km s^{-1})	Integrated Fit S_{peak} (Jy)	Integrated Fit V_{peak} (km s^{-1})	Obs. Date yyyymmdd[†]
10.342-0.142	22	51.81 ± 5.74	9.2 ± 0.5	8.5 ± 1.1	5.75 ± 1.99	48.20	1.3	15.0	7.47	13.0	20130418TN
	22	26.48 ± 2.78	18.3 ± 0.1	1.7 ± 0.2	14.48 ± 1.99	35.93	15.0	22.4	16.30	18.4	
	44	47.28 ± 2.42	11.8 ± 0.0	2.0 ± 0.1	21.86 ± 1.54	47.23	10.2	13.7	27.96	11.4	
	44	64.17 ± 1.31	14.6 ± 0.0	0.6 ± 0.0	94.49 ± 1.54	65.77	13.7	16.0	76.71	14.8	
	95	73.33 ± 4.57	11.9 ± 0.2	5.4 ± 0.4	12.70 ± 1.76	56.42	5.6	13.0	18.43	11.5	
	95	47.48 ± 1.56	14.6 ± 0.0	0.6 ± 0.0	77.83 ± 1.76	69.51	13.0	16.4	84.11	14.6	
10.356-0.148	22	3.34 ± 0.48	9.5 ± 0.1	1.3 ± 0.2	2.51 ± 0.55	3.28	8.2	10.3	2.74	9.7	20120324YS
	22	4.11 ± 0.44	11.2 ± 0.0	0.9 ± 0.1	4.23 ± 0.55	7.03	10.3	13.5	4.36	11.4	
	22	3.78 ± 0.46	14.4 ± 0.1	1.4 ± 0.2	2.47 ± 0.55	3.53	13.5	16.4	2.85	14.1	
	22	3.92 ± 0.49	17.9 ± 0.1	1.4 ± 0.2	2.65 ± 0.55	4.08	16.4	19.5	2.96	17.9	
	44	1.74 ± 0.43	14.6 ± 0.1	0.4 ± 0.1	3.92 ± 0.85	2.55	13.0	15.8	4.08	14.7	
	44	10.73 ± 0.90	44.7 ± 0.1	2.0 ± 0.2	4.97 ± 0.85	11.30	41.5	47.7	8.70	44.7	
	95	2.37 ± 0.43	14.6 ± 0.1	0.5 ± 0.1	4.53 ± 0.88	2.16	12.8	15.3	4.73	14.7	
	95	13.20 ± 0.99	44.8 ± 0.1	2.3 ± 0.2	5.34 ± 0.88	14.18	40.6	47.2	7.38	44.7	
10.480+0.033	22	6.16 ± 0.60	38.3 ± 0.2	0.8 ± 0.2	6.91 ± 0.52	6.54	37.5	39.6	7.62	38.4	20120324YS
	22	6.91 ± 0.60	47.1 ± 0.2	2.3 ± 0.2	2.88 ± 0.52	5.34	45.7	48.0	3.56	47.0	
	22	9.90 ± 0.60	49.3 ± 0.2	1.4 ± 0.2	6.66 ± 0.52	12.56	48.0	50.6	7.62	49.3	
	22	10.02 ± 0.60	51.8 ± 0.2	1.4 ± 0.2	6.66 ± 0.52	10.43	50.6	52.5	7.64	51.8	
	22	21.77 ± 0.60	53.8 ± 0.2	1.5 ± 0.2	13.33 ± 0.52	22.81	52.5	55.1	13.64	53.9	
	22	31.09 ± 3.57	56.5 ± 0.2	1.6 ± 0.2	18.79 ± 0.53	32.49	55.1	57.4	19.65	56.5	
	22	21.17 ± 3.57	58.3 ± 0.2	1.1 ± 0.2	18.01 ± 0.52	26.20	57.4	59.1	18.46	58.4	
	22	15.01 ± 3.57	59.6 ± 0.2	1.0 ± 0.2	14.24 ± 0.52	14.44	59.1	60.1	16.96	59.6	
	22	179.47 ± 3.57	62.1 ± 0.2	1.9 ± 0.2	89.27 ± 0.52	184.47	60.1	64.9	96.82	62.0	
	22	56.91 ± 3.57	66.8 ± 0.2	1.8 ± 0.2	30.07 ± 0.52	55.39	64.9	68.4	32.32	67.0	
	22	7.20 ± 0.98	69.2 ± 0.2	1.3 ± 0.2	5.20 ± 0.52	8.13	68.4	69.7	7.08	69.3	
	22	46.72 ± 0.98	71.2 ± 0.2	1.6 ± 0.2	26.62 ± 0.52	46.14	69.7	72.9	31.93	71.2	
	22	5.65 ± 0.98	75.7 ± 0.2	2.0 ± 0.2	2.71 ± 0.52	5.51	73.6	76.7	3.74	75.6	
	22	2.94 ± 0.98	77.5 ± 0.2	0.6 ± 0.2	4.42 ± 0.52	4.62	76.7	78.0	5.53	77.5	

Table 4.1 (cont'd)

Source	Frequency (GHz)	Gaussian Fit S_{int} (Jy km s^{-1})	Gaussian Fit V_{peak} (km s^{-1})	Gaussian Fit FWHM (km s^{-1})	Gaussian Fit S_{peak} (Jy)	Integrated Fit S_{int} (Jy km s^{-1})	Integrated Fit v_{min} (km s^{-1})	Integrated Fit v_{max} (km s^{-1})	Integrated Fit S_{peak} (Jy)	Integrated Fit V_{peak} (km s^{-1})	Obs. Date yyyymmdd[†]
	22	7.03 ± 0.98	79.0 ± 0.2	1.6 ± 0.2	4.04 ± 0.52	6.86	78.0	80.9	4.34	78.8	
	22	45.93 ± 0.40	83.6 ± 0.0	2.1 ± 0.0	20.99 ± 0.53	47.76	80.9	85.9	23.81	83.4	
	22	15.88 ± 0.71	87.5 ± 0.0	0.8 ± 0.0	17.70 ± 0.53	37.09	85.9	88.2	28.00	87.7	
	22	110.74 ± 0.89	89.3 ± 0.0	2.3 ± 0.0	45.26 ± 0.53	97.48	88.2	92.4	46.58	89.1	
	44	24.09 ± 1.43	65.7 ± 0.2	6.0 ± 0.4	3.74 ± 0.74	20.01	58.9	67.5	5.27	66.7	
	44	1.86 ± 0.35	68.0 ± 0.0	0.3 ± 0.1	5.11 ± 0.74	6.47	67.5	70.9	7.39	68.0	
	95	15.45 ± 1.87	64.5 ± 0.2	4.6 ± 0.8	3.15 ± 0.84	13.77	59.1	66.7	4.13	64.1	
	95	2.69 ± 1.21	68.0 ± 0.1	1.0 ± 0.5	2.42 ± 0.84	4.63	66.7	70.1	4.59	68.0	
10.629-0.333	44	7.25 ± 0.55	-5.3 ± 0.1	3.5 ± 0.3	1.92 ± 0.42	6.87	-10.2	-1.8	3.49	-4.8	
	95	4.86 ± 0.65	-4.3 ± 0.3	4.0 ± 0.5	1.15 ± 0.52	4.57	-8.2	-0.6	2.36	-3.9	
10.724-0.334	22	4.38 ± 0.50	0.8 ± 0.1	2.3 ± 0.3	1.78 ± 0.51	3.91	-1.6	3.3	2.35	-0.1	20120411TN
	22	2.39 ± 0.42	13.6 ± 0.1	1.5 ± 0.3	1.49 ± 0.51	2.25	11.9	15.8	1.86	14.0	
	44	34.36 ± 0.43	-2.1 ± 0.0	1.5 ± 0.0	21.28 ± 0.52	34.81	-4.5	1.9	21.40	-2.6	
	95	20.72 ± 0.73	-2.0 ± 0.0	1.9 ± 0.1	10.28 ± 0.78	21.05	-4.3	0.2	11.11	-2.1	
10.886+0.123	22	4.09 ± 0.42	13.4 ± 0.0	0.5 ± 0.1	7.19 ± 0.74	3.71	12.2	14.3	6.75	13.3	20120502TN
	22	3.02 ± 0.95	15.2 ± 0.2	1.5 ± 0.6	1.92 ± 0.74	2.89	14.3	16.1	2.15	15.4	
	22	3.74 ± 0.91	17.1 ± 0.1	1.1 ± 0.3	3.28 ± 0.74	3.93	16.1	17.7	3.37	17.1	
	22	2.61 ± 0.40	18.4 ± 0.0	0.5 ± 0.1	5.09 ± 0.74	3.62	17.7	19.6	4.53	18.5	
	22	4.32 ± 0.69	21.1 ± 0.1	1.0 ± 0.3	3.92 ± 0.74	4.87	19.6	22.3	4.12	21.1	
	22	7.69 ± 0.50	23.5 ± 0.0	0.9 ± 0.1	8.13 ± 0.74	8.02	22.3	25.0	8.20	23.6	
10.958+0.022	22	5.65 ± 0.52	24.0 ± 0.0	0.6 ± 0.1	6.41 ± 0.50	4.85	22.6	25.9	6.40	24.1	20130225TN
11.497-1.485	22	2.53 ± 0.53	13.8 ± 0.1	0.8 ± 0.2	3.06 ± 0.58	3.19	11.7	15.4	3.08	13.9	20130418TN
11.936-0.150	22	77.21 ± 1.41	41.4 ± 0.0	4.3 ± 0.1	16.76 ± 0.69	52.99	36.3	42.0	17.99	41.0	20120324YS
	22	26.25 ± 0.81	43.0 ± 0.0	0.9 ± 0.0	26.94 ± 0.69	53.32	42.0	46.2	38.19	42.9	
	22	8.54 ± 0.66	48.6 ± 0.0	1.3 ± 0.1	6.42 ± 0.69	10.22	46.2	51.1	7.50	48.4	
	44	17.17 ± 1.15	42.5 ± 0.1	2.7 ± 0.2	6.05 ± 1.01	17.27	39.4	45.5	7.71	41.9	
	95	14.23 ± 1.25	42.0 ± 0.1	2.5 ± 0.3	5.42 ± 1.02	15.14	39.2	45.9	8.35	42.0	
12.112-0.126	22	1.05 ± 0.30	23.7 ± 0.0	0.4 ± 0.2	2.57 ± 0.56	1.59	22.6	24.5	2.40	23.8	20120325YS

Table 4.1 (cont'd)

Source	Frequency (GHz)	Gaussian Fit S_{int} (Jy km s^{-1})	Gaussian Fit V_{peak} (km s^{-1})	Gaussian Fit FWHM (km s^{-1})	Gaussian Fit S_{peak} (Jy)	Integrated Fit S_{int} (Jy km s^{-1})	Integrated Fit v_{min} (km s^{-1})	Integrated Fit v_{max} (km s^{-1})	Integrated Fit S_{peak} (Jy)	Integrated Fit V_{peak} (km s^{-1})	Obs. Date yyyymmdd[†]
	22	3.64 ± 0.48	28.9 ± 0.1	1.5 ± 0.2	2.22 ± 0.56	3.75	27.3	30.7	2.54	29.0	
	44	9.89 ± 1.03	44.9 ± 0.1	2.5 ± 0.3	3.78 ± 0.93	10.09	41.9	47.6	5.48	44.3	
	95	7.75 ± 0.89	45.0 ± 0.1	2.5 ± 0.3	2.92 ± 0.84	7.22	43.1	47.2	4.26	44.3	
12.181-0.123	22	2.02 ± 0.80	-27.0 ± 0.0	1.9 ± 0.1	10.00 ± 0.84	20.53	-30.1	-24.0	10.55	-26.5	20120511US
	22	3.66 ± 0.64	-4.2 ± 0.1	1.2 ± 0.2	2.91 ± 0.84	3.34	-6.4	-2.3	3.39	-4.0	
	22	9.22 ± 1.30	23.2 ± 0.1	2.1 ± 0.3	4.22 ± 0.84	9.29	20.9	24.3	5.54	23.6	
	22	5.16 ± 1.11	25.2 ± 0.1	1.3 ± 0.3	3.61 ± 0.84	6.26	24.3	27.2	4.61	25.1	
	22	11.81 ± 0.76	29.1 ± 0.0	1.4 ± 0.1	8.14 ± 0.84	13.33	27.2	31.4	8.27	28.9	
12.199-0.033	44	12.14 ± 1.75	50.8 ± 0.3	4.7 ± 0.8	2.43 ± 0.82	11.23	42.3	56.8	2.95	52.3	20130421TN
	95	13.85 ± 1.41	50.3 ± 0.3	5.3 ± 0.7	2.45 ± 0.63	14.18	45.5	57.5	3.57	49.3	
12.202-0.120	22	9.57 ± 0.60	-26.5 ± 0.1	2.7 ± 0.2	3.32 ± 0.53	9.54	-29.4	-22.9	4.29	-26.4	20120322YS
	22	2.69 ± 0.43	-11.7 ± 0.1	0.9 ± 0.2	2.76 ± 0.53	3.05	-12.7	-10.8	3.17	-11.8	
	22	3.95 ± 0.46	-9.8 ± 0.1	1.3 ± 0.2	2.93 ± 0.53	4.56	-10.8	-8.6	3.27	-10.1	
	22	10.72 ± 0.63	-7.3 ± 0.0	1.9 ± 0.2	5.34 ± 0.53	9.99	-8.6	-5.9	6.07	-7.4	
	22	21.03 ± 0.42	-4.1 ± 0.0	1.1 ± 0.0	17.38 ± 0.53	23.31	-5.9	-2.7	18.25	-4.2	
	22	13.76 ± 1.37	-0.9 ± 0.1	3.3 ± 0.4	3.98 ± 0.49	11.34	-2.7	0.7	4.60	-0.6	
	22	10.00 ± 0.90	2.4 ± 0.1	1.6 ± 0.1	5.78 ± 0.49	14.72	0.7	3.9	6.62	2.5	
	22	23.79 ± 0.96	5.5 ± 0.0	3.0 ± 0.2	7.47 ± 0.49	20.24	3.9	7.2	8.33	5.2	
	22	15.33 ± 0.56	8.7 ± 0.0	1.3 ± 0.1	11.51 ± 0.49	15.77	7.2	9.2	12.83	8.6	
	22	14.22 ± 0.84	13.9 ± 0.1	2.4 ± 0.2	5.54 ± 0.49	11.11	12.2	15.1	5.85	13.5	
	22	14.74 ± 3.84	16.0 ± 0.2	3.1 ± 0.9	4.40 ± 0.63	8.42	15.1	16.9	5.25	16.2	
	22	26.50 ± 2.96	19.6 ± 0.1	2.6 ± 0.3	9.66 ± 0.63	27.02	16.9	20.6	10.08	19.4	
	22	23.24 ± 1.32	21.5 ± 0.0	1.1 ± 0.0	20.67 ± 0.63	28.50	20.6	22.0	22.02	21.5	
	22	21.55 ± 0.69	22.5 ± 0.0	0.6 ± 0.0	33.98 ± 0.63	43.80	22.0	23.1	43.61	23.2	
	22	127.85 ± 0.62	23.8 ± 0.0	1.3 ± 0.1	96.16 ± 0.63	124.95	23.1	25.3	103.01	23.8	
	22	17.96 ± 2.52	25.9 ± 0.0	1.0 ± 0.2	16.76 ± 0.89	17.15	25.3	26.5	17.34	25.9	
	22	302.41 ± 0.89	29.2 ± 0.0	2.0 ± 0.0	142.20 ± 0.89	316.26	26.5	33.5	143.12	29.5	
	44	8.87 ± 0.58	23.8 ± 0.0	1.1 ± 0.1	7.78 ± 0.71	10.18	21.9	25.2	7.98	23.6	

Table 4.1 (cont'd)

Source	Frequency (GHz)	Gaussian Fit S_{int} (Jy km s^{-1})	Gaussian Fit V_{peak} (km s^{-1})	Gaussian Fit FWHM (km s^{-1})	Gaussian Fit S_{peak} (Jy)	Integrated Fit S_{int} (Jy km s^{-1})	Integrated Fit v_{min} (km s^{-1})	Integrated Fit v_{max} (km s^{-1})	Integrated Fit S_{peak} (Jy)	Integrated Fit V_{peak} (km s^{-1})	Obs. Date yyyymmdd[†]
	44	13.38 ± 1.10	28.3 ± 0.2	4.4 ± 0.4	2.86 ± 0.71	11.93	25.2	31.1	4.42	28.1	
	95	4.78 ± 0.60	23.7 ± 0.0	0.8 ± 0.1	5.57 ± 0.81	5.55	22.1	24.8	6.25	23.6	
	95	11.54 ± 1.28	28.1 ± 0.3	5.3 ± 0.7	2.03 ± 0.81	10.50	24.8	32.8	2.97	29.7	
12.203-0.107	22	42.58 ± 4.39	-7.3 ± 0.4	5.0 ± 0.4	5.84 ± 0.50	27.70	-10.5	-4.5	7.80	-7.6	20130302TN
	22	53.57 ± 4.39	-1.7 ± 0.4	2.3 ± 0.4	15.80 ± 0.50	65.59	-4.5	-1.2	56.45	-0.9	
	22	141.22 ± 4.39	-0.4 ± 0.4	1.3 ± 0.4	73.91 ± 0.50	113.50	-1.2	1.0	82.84	-0.4	
	22	37.39 ± 4.39	1.6 ± 0.4	1.1 ± 0.4	23.96 ± 0.50	31.72	1.0	2.9	24.08	1.7	
	22	22.34 ± 4.39	3.4 ± 0.4	2.4 ± 0.4	6.37 ± 0.50	13.99	2.9	5.6	6.12	2.9	
	22	45.30 ± 1.81	10.6 ± 0.1	5.3 ± 0.3	5.93 ± 0.53	28.55	5.6	12.4	7.56	10.5	
	22	31.55 ± 2.70	14.6 ± 0.0	1.7 ± 0.1	13.00 ± 0.53	40.33	12.4	16.0	15.89	14.3	
	22	56.15 ± 3.83	18.0 ± 0.1	5.0 ± 0.4	7.78 ± 0.53	24.95	16.0	19.3	8.86	18.1	
	22	268.60 ± 3.76	23.1 ± 0.0	3.4 ± 0.0	54.40 ± 0.53	236.27	19.3	26.1	79.47	22.7	
	22	165.74 ± 2.84	27.9 ± 0.0	3.7 ± 0.1	30.60 ± 0.53	124.03	26.1	33.0	38.11	27.8	
	44	13.90 ± 1.11	24.6 ± 0.2	4.5 ± 0.5	2.93 ± 0.50	15.55	19.6	31.5	4.79	23.7	
	95	3.74 ± 0.77	25.4 ± 0.3	2.8 ± 0.9	1.25 ± 0.42	5.37	19.3	27.8	2.06	25.5	
12.265-0.051	44	4.59 ± 0.82	64.9 ± 0.3	2.8 ± 0.6	1.54 ± 0.51	4.37	61.8	68.3	1.99	66.0	20130302TN
	95	4.11 ± 1.08	63.9 ± 0.7	5.0 ± 2.0	0.77 ± 0.42	3.32	60.6	67.4	1.46	63.1	
12.526+0.016	44	3.46 ± 0.55	46.2 ± 0.1	1.2 ± 0.2	2.68 ± 0.51	3.38	44.6	47.5	2.55	46.3	20130302TN
12.625-0.017	44	7.97 ± 0.66	19.6 ± 0.0	1.0 ± 0.1	7.77 ± 0.53	12.00	18.5	20.7	7.74	19.8	20130302TN
	44	17.83 ± 1.00	22.1 ± 0.1	2.5 ± 0.2	6.61 ± 0.53	16.06	20.7	25.4	7.64	22.4	
	95	8.73 ± 1.06	19.5 ± 0.0	1.3 ± 0.1	6.34 ± 0.50	12.37	17.2	20.7	7.33	19.6	
	95	18.27 ± 1.36	22.1 ± 0.1	3.1 ± 0.3	5.57 ± 0.50	18.05	20.7	30.1	5.81	21.9	
12.904-0.031	22	47.68 ± 4.63	62.3 ± 0.1	1.1 ± 0.1	40.47 ± 4.71	44.05	61.0	63.4	36.99	62.3	20130513TN
	22	395.62 ± 5.31	66.9 ± 0.0	1.3 ± 0.0	278.80 ± 4.71	393.16	64.7	68.2	266.95	67.0	
	44	17.56 ± 1.66	55.1 ± 0.1	1.4 ± 0.2	11.44 ± 1.02	20.66	52.7	56.0	13.23	55.3	
	44	35.48 ± 1.66	57.2 ± 0.0	1.5 ± 0.1	22.45 ± 1.02	39.36	56.0	60.9	21.93	57.4	
	95	7.49 ± 1.97	55.1 ± 0.1	1.3 ± 0.4	5.61 ± 0.87	14.71	52.5	55.8	9.02	55.4	
	95	30.39 ± 2.02	57.2 ± 0.1	2.3 ± 0.2	12.66 ± 0.87	28.42	55.8	60.4	13.96	57.3	

Table 4.1 (cont'd)

Source	Frequency (GHz)	Gaussian Fit				Integrated Fit					Obs. Date yyyymmdd†
		S_{int} (Jy km s^{-1})	V_{peak} (km s^{-1})	FWHM (km s^{-1})	S_{peak} (Jy)	S_{int} (Jy km s^{-1})	v_{min} (km s^{-1})	v_{max} (km s^{-1})	S_{peak} (Jy)	V_{peak} (km s^{-1})	
13.179+0.061	22	3.89 ± 0.70	-1.7 ± 0.1	1.3 ± 0.2	2.14 ± 0.52	2.72	-2.6	-0.4	2.29	-1.4	20130302TN
	22	3.36 ± 1.08	37.7 ± 0.3	1.8 ± 0.6	1.29 ± 0.54	2.40	36.1	38.6	1.48	37.0	
	22	5.21 ± 1.13	39.7 ± 0.1	1.1 ± 0.3	3.32 ± 0.54	4.12	38.6	40.3	3.44	39.5	
	22	7.65 ± 0.73	41.3 ± 0.0	0.7 ± 0.1	7.39 ± 0.54	9.22	40.3	42.0	7.26	41.2	
	22	46.89 ± 1.13	43.4 ± 0.0	2.2 ± 0.1	14.67 ± 0.54	31.93	42.0	47.4	16.59	42.9	
	22	4.47 ± 0.70	51.7 ± 0.1	1.0 ± 0.2	2.96 ± 0.54	3.36	50.7	53.1	2.73	51.7	
	44	67.62 ± 0.77	49.4 ± 0.0	1.9 ± 0.0	33.44 ± 0.52	72.46	45.2	53.0	36.57	49.3	
	95	54.27 ± 0.77	49.3 ± 0.0	2.6 ± 0.0	19.54 ± 0.48	57.76	45.4	54.2	22.53	49.5	
14.101+0.087	22	7.14 ± 0.24	8.3 ± 0.0	0.7 ± 0.0	9.03 ± 0.36	8.20	6.7	9.7	9.56	8.3	20120512US
	22	2.26 ± 0.32	10.2 ± 0.1	1.5 ± 0.3	1.38 ± 0.36	1.72	9.7	11.9	1.71	10.4	
	44	3.64 ± 0.34	9.5 ± 0.1	2.6 ± 0.3	1.32 ± 0.29	3.38	7.4	11.8	2.33	9.0	
	95	5.90 ± 0.48	9.5 ± 0.2	4.7 ± 0.4	1.18 ± 0.34	5.15	6.2	13.1	2.09	8.9	
14.230-0.509	22	4.51 ± 0.40	4.8 ± 0.0	0.9 ± 0.1	4.68 ± 0.60	5.20	3.7	6.4	4.68	4.7	20120320YS
	22	15.83 ± 0.55	8.6 ± 0.0	1.6 ± 0.1	9.47 ± 0.60	16.73	6.4	11.0	9.84	8.9	
	44	16.98 ± 0.83	20.2 ± 0.0	1.0 ± 0.1	16.34 ± 0.95	20.53	18.2	21.9	20.19	20.1	
	95	33.61 ± 0.90	20.1 ± 0.0	1.3 ± 0.0	24.79 ± 1.02	47.62	13.0	26.4	30.18	20.0	
14.631-0.577	22	3.57 ± 0.69	13.7 ± 0.1	1.0 ± 0.2	3.50 ± 0.72	3.60	12.4	14.5	3.10	13.6	20130421TN
	22	2.16 ± 0.67	16.5 ± 0.1	0.8 ± 0.3	2.54 ± 0.72	2.14	15.7	17.0	2.59	16.5	
	22	2.22 ± 0.56	19.6 ± 0.1	0.6 ± 0.2	3.37 ± 0.72	1.88	18.9	20.7	3.11	19.5	
	22	4.95 ± 0.72	22.9 ± 0.1	0.9 ± 0.2	5.14 ± 0.72	5.38	21.7	23.7	5.13	22.8	
	44	30.74 ± 0.83	18.7 ± 0.0	1.1 ± 0.0	26.34 ± 0.75	35.04	12.2	23.8	28.35	18.7	
	95	26.18 ± 0.81	18.5 ± 0.0	1.2 ± 0.1	19.72 ± 0.69	30.12	15.8	21.2	21.45	18.7	
15.094+0.192	22	3.60 ± 2.07	-9.1 ± 0.4	1.3 ± 0.8	2.55 ± 1.83	4.86	-10.6	-8.1	3.23	-7.9	20120504TN
	22	6.46 ± 2.47	-7.3 ± 0.3	1.5 ± 0.7	3.93 ± 1.83	5.67	-8.1	-6.4	4.20	-7.1	
	22	3.80 ± 1.33	-5.4 ± 0.1	0.8 ± 0.3	4.26 ± 1.83	4.37	-6.4	-4.2	4.49	-5.4	
	22	3.46 ± 0.47	22.2 ± 0.0	0.6 ± 0.1	5.80 ± 0.93	3.38	21.6	22.9	5.83	22.2	
	22	15.60 ± 0.55	28.0 ± 0.0	0.7 ± 0.0	20.19 ± 0.93	15.58	26.9	28.7	20.16	28.1	
	22	1.85 ± 0.43	29.1 ± 0.1	0.4 ± 0.1	3.88 ± 0.93	2.04	28.7	29.7	3.71	29.1	

Table 4.1 (cont'd)

Source	Frequency (GHz)	Gaussian Fit S_{int} (Jy km s^{-1})	Gaussian Fit V_{peak} (km s^{-1})	Gaussian Fit FWHM (km s^{-1})	Gaussian Fit S_{peak} (Jy)	Integrated Fit S_{int} (Jy km s^{-1})	Integrated Fit v_{min} (km s^{-1})	Integrated Fit v_{max} (km s^{-1})	Integrated Fit S_{peak} (Jy)	Integrated Fit V_{peak} (km s^{-1})	Obs. Date yyyymmdd[†]
	22	2.57 ± 0.49	30.3 ± 0.1	0.6 ± 0.1	4.31 ± 0.93	2.37	29.7	31.1	4.21	30.2	
	44	1.80 ± 0.33	30.6 ± 0.1	0.9 ± 0.2	1.93 ± 0.50	1.80	29.0	32.3	2.39	30.7	
	95	2.38 ± 0.47	30.7 ± 0.1	1.0 ± 0.2	2.26 ± 0.69	2.43	29.3	31.7	3.07	30.7	
15.665-0.499	22	3.23 ± 0.41	-11.9 ± 0.1	1.3 ± 0.2	2.33 ± 0.51	3.33	-13.7	-10.2	2.55	-11.6	20120321YS
	22	4.13 ± 0.56	-9.0 ± 0.1	1.1 ± 0.2	3.45 ± 0.51	4.75	-10.2	-8.2	3.70	-9.3	
	22	8.79 ± 0.79	-7.0 ± 0.1	1.7 ± 0.2	5.00 ± 0.51	8.37	-8.2	-6.0	5.28	-6.8	
	22	5.56 ± 0.44	-5.4 ± 0.0	0.7 ± 0.1	7.33 ± 0.51	6.64	-6.0	-4.1	7.56	-5.3	
	22	3.52 ± 0.31	-3.2 ± 0.0	0.7 ± 0.1	4.76 ± 0.51	3.74	-4.1	-1.2	5.13	-3.2	
	44	3.37 ± 0.42	-7.2 ± 0.0	0.7 ± 0.1	4.62 ± 0.71	3.68	-8.3	-6.7	4.24	-7.4	
	44	11.09 ± 0.59	-5.3 ± 0.0	1.3 ± 0.1	8.09 ± 0.71	11.91	-6.7	-3.0	7.95	-5.7	
	95	6.16 ± 0.55	-7.2 ± 0.0	0.9 ± 0.1	6.10 ± 0.74	9.54	-11.0	-6.4	6.09	-7.2	
	95	14.22 ± 0.68	-5.3 ± 0.0	1.4 ± 0.1	9.86 ± 0.74	14.77	-6.4	-2.6	10.49	-5.4	
16.112-0.303	22	1.20 ± 1.20	5.1 ± 0.1	3.2 ± 0.2	6.13 ± 0.53	20.23	0.4	8.6	6.38	6.2	20130303TN
	22	0.85 ± 0.85	40.7 ± 0.1	4.1 ± 0.3	3.39 ± 0.53	14.14	36.3	44.2	3.79	41.6	
16.403-0.181	44	7.09 ± 0.78	45.4 ± 0.1	1.2 ± 0.2	5.68 ± 0.92	8.39	43.0	47.0	6.16	45.4	20120326YS
	95	7.53 ± 0.70	45.3 ± 0.1	1.2 ± 0.1	5.90 ± 0.93	7.25	43.1	47.6	6.82	45.2	
16.662-0.331	44	1.86 ± 0.48	38.5 ± 0.2	1.1 ± 0.4	1.59 ± 0.37	2.17	36.5	39.8	1.68	38.6	20130302TN
	95	0.93 ± 0.28	38.7 ± 0.1	0.6 ± 0.3	1.57 ± 0.33	1.32	37.1	40.9	1.31	38.5	
16.855+0.641	22	14.13 ± 1.11	-73.0 ± 0.1	2.7 ± 0.3	4.97 ± 0.95	13.77	-75.1	-70.3	6.59	-73.4	20120415TN
17.021-2.403	22	6.12 ± 0.34	2.9 ± 0.0	1.1 ± 0.1	5.40 ± 0.49	6.46	0.9	4.2	5.12	3.0	20120321YS
	22	0.91 ± 0.28	5.5 ± 0.1	0.6 ± 0.2	1.42 ± 0.49	1.16	4.2	6.5	1.45	5.5	
	22	3.51 ± 0.24	18.6 ± 0.0	0.5 ± 0.0	6.36 ± 0.49	3.66	17.5	20.0	6.48	18.6	
	22	2.54 ± 0.33	21.7 ± 0.1	0.8 ± 0.1	2.82 ± 0.49	3.36	20.0	23.3	2.92	21.7	
	44	7.26 ± 0.46	18.5 ± 0.2	1.1 ± 0.2	6.05 ± 0.81	9.99	14.9	19.0	7.47	18.4	
	44	15.70 ± 0.46	20.2 ± 0.2	0.8 ± 0.2	19.04 ± 0.81	20.58	19.0	22.2	25.65	19.9	
	44	4.42 ± 0.46	25.7 ± 0.2	1.3 ± 0.2	3.21 ± 0.81	4.30	24.6	26.8	3.44	25.7	
	44	7.71 ± 0.46	27.7 ± 0.2	0.7 ± 0.2	9.66 ± 0.81	7.63	26.8	28.3	9.82	27.8	
	95	10.36 ± 0.99	18.6 ± 0.0	1.4 ± 0.2	6.79 ± 0.77	14.49	14.0	19.4	7.68	18.6	

Table 4.1 (cont'd)

Source	Frequency (GHz)	Gaussian Fit S_{int} (Jy km s^{-1})	Gaussian Fit V_{peak} (km s^{-1})	Gaussian Fit FWHM (km s^{-1})	Gaussian Fit S_{peak} (Jy)	Integrated Fit S_{int} (Jy km s^{-1})	Integrated Fit v_{min} (km s^{-1})	Integrated Fit v_{max} (km s^{-1})	Integrated Fit S_{peak} (Jy)	Integrated Fit V_{peak} (km s^{-1})	Obs. Date yyyymmdd[†]
	95	10.43 ± 0.73	20.0 ± 0.0	0.7 ± 0.1	13.88 ± 0.77	14.57	19.4	23.2	16.46	19.9	
	95	1.61 ± 0.47	26.1 ± 0.1	0.8 ± 0.3	1.81 ± 0.77	1.78	24.8	27.2	2.77	26.2	
	95	2.91 ± 0.73	28.6 ± 0.3	2.2 ± 0.6	1.24 ± 0.77	2.49	27.2	31.1	2.19	28.0	
17.029-0.071	44	4.89 ± 0.85	91.7 ± 0.1	0.9 ± 0.2	4.89 ± 0.81	8.05	89.5	95.2	5.01	91.6	20130224TN
	95	4.31 ± 0.66	91.7 ± 0.1	0.9 ± 0.2	4.43 ± 0.69	5.21	90.2	93.5	4.48	91.5	
17.638+0.157	22	2.86 ± 0.34	16.5 ± 0.0	0.6 ± 0.1	4.23 ± 0.62	3.14	15.4	17.5	3.77	16.5	20120617US
	22	4.24 ± 0.52	23.1 ± 0.1	1.2 ± 0.2	3.38 ± 0.62	4.70	21.2	23.9	3.91	23.1	
	22	7.66 ± 0.42	26.0 ± 0.0	1.0 ± 0.1	7.45 ± 0.62	7.67	24.8	27.1	7.39	26.0	
18.159+0.094	44	3.19 ± 0.47	56.4 ± 0.2	2.4 ± 0.4	1.24 ± 0.31	2.81	54.9	58.6	1.56	56.0	20130302TN
	95	2.46 ± 0.59	56.6 ± 0.2	1.5 ± 0.5	1.56 ± 0.43	2.43	55.0	58.3	1.68	56.7	
18.262-0.244	44	4.36 ± 0.64	69.8 ± 0.1	1.2 ± 0.2	3.36 ± 0.82	3.88	69.0	70.8	3.48	69.4	20120326YS
	95	2.17 ± 0.46	70.1 ± 0.1	0.6 ± 0.2	3.23 ± 0.79	2.73	69.1	70.8	3.63	70.0	
18.460-0.004	44	6.78 ± 1.08	52.7 ± 0.2	3.0 ± 0.5	2.09 ± 0.65	6.77	48.8	56.0	2.81	52.1	20130421TN
	95	4.19 ± 0.75	53.3 ± 0.2	2.5 ± 0.4	1.56 ± 0.54	3.73	51.3	56.4	2.05	53.7	
18.661+0.034	22	4.69 ± 0.36	30.1 ± 0.1	1.5 ± 0.1	3.04 ± 0.43	4.96	28.6	32.4	3.28	30.0	20120325YS
	22	3.01 ± 0.40	77.0 ± 0.1	1.6 ± 0.3	1.77 ± 0.43	2.81	75.5	78.4	2.05	76.9	
	22	1.53 ± 0.31	81.8 ± 0.1	0.9 ± 0.2	1.68 ± 0.43	1.78	80.7	82.7	1.96	81.6	
	22	2.04 ± 0.43	83.5 ± 0.1	1.3 ± 0.4	1.51 ± 0.43	2.12	82.7	85.2	1.96	83.5	
	44	4.68 ± 0.94	79.1 ± 0.1	0.9 ± 0.1	5.05 ± 0.67	7.41	76.9	79.7	7.27	79.3	
	44	9.02 ± 1.21	80.5 ± 0.1	1.6 ± 0.3	5.24 ± 0.67	8.64	79.7	83.3	6.52	80.4	
	95	3.72 ± 0.97	77.9 ± 0.3	1.9 ± 0.4	1.87 ± 0.66	6.86	76.0	79.8	3.30	79.3	
	95	13.87 ± 1.18	80.7 ± 0.1	2.6 ± 0.3	5.03 ± 0.66	11.30	79.8	83.5	5.85	80.7	
18.667+0.025	22	7.91 ± 1.13	42.1 ± 0.1	1.8 ± 0.2	4.24 ± 0.91	6.13	39.8	44.2	4.63	41.8	20130418TN
	44	11.28 ± 1.08	79.8 ± 0.1	2.0 ± 0.2	5.43 ± 0.75	13.24	76.0	84.7	6.49	80.2	
18.888-0.475	44	92.72 ± 1.17	65.3 ± 0.0	2.3 ± 0.0	38.15 ± 0.81	93.48	61.6	71.0	38.70	64.8	20130418TN
	95	73.46 ± 1.28	65.5 ± 0.0	2.7 ± 0.1	25.96 ± 1.24	72.86	62.7	69.4	43.71	65.9	
18.999-0.239	22	33.13 ± 1.23	-11.8 ± 0.0	2.8 ± 0.1	11.06 ± 1.03	35.83	-17.1	-7.2	11.83	-12.2	20120414TN
19.009-0.029	44	70.14 ± 1.17	59.5 ± 0.0	1.4 ± 0.0	47.65 ± 0.94	94.57	52.8	63.4	46.83	59.7	20130418TN

Table 4.1 (cont'd)

Source	Frequency (GHz)	Gaussian Fit S_{int} (Jy km s^{-1})	Gaussian Fit V_{peak} (km s^{-1})	Gaussian Fit FWHM (km s^{-1})	Gaussian Fit S_{peak} (Jy)	Integrated Fit S_{int} (Jy km s^{-1})	Integrated Fit v_{min} (km s^{-1})	Integrated Fit v_{max} (km s^{-1})	Integrated Fit S_{peak} (Jy)	Integrated Fit V_{peak} (km s^{-1})	Obs. Date yyyymmdd[†]
	95	31.27 ± 1.53	59.4 ± 0.0	1.9 ± 0.1	15.47 ± 0.89	40.42	53.3	63.0	18.17	59.6	
19.472+0.170	22	2.97 ± 0.64	-79.3 ± 0.1	1.5 ± 0.4	1.83 ± 0.52	5.34	-84.5	-78.4	2.03	-79.3	20120320YS
	22	3.92 ± 0.64	-77.5 ± 0.1	1.1 ± 0.2	3.49 ± 0.52	4.57	-78.4	-76.7	3.61	-77.6	
	22	4.19 ± 0.62	-75.4 ± 0.1	1.8 ± 0.3	2.15 ± 0.52	4.00	-76.7	-73.8	2.47	-75.7	
	22	4.36 ± 0.32	2.8 ± 0.0	0.8 ± 0.1	5.43 ± 0.50	5.00	1.4	5.1	5.30	2.9	
	22	2.93 ± 0.47	7.5 ± 0.0	0.7 ± 0.1	3.71 ± 0.50	3.79	6.5	8.1	4.39	7.7	
	22	5.94 ± 0.63	9.1 ± 0.1	1.9 ± 0.2	2.99 ± 0.50	5.39	8.1	11.0	3.66	9.0	
	22	6.33 ± 0.51	13.1 ± 0.0	0.8 ± 0.1	7.74 ± 0.50	7.95	11.9	13.9	7.79	13.2	
	22	3.33 ± 0.54	14.2 ± 0.1	1.0 ± 0.2	3.18 ± 0.50	2.40	13.9	15.1	3.36	14.3	
	22	3.28 ± 0.93	16.3 ± 0.1	1.7 ± 0.6	1.86 ± 0.47	3.67	15.1	18.1	2.26	16.2	
	22	4.69 ± 1.39	20.1 ± 0.5	3.7 ± 1.2	1.20 ± 0.47	2.62	18.1	20.6	1.98	20.2	
	22	1.36 ± 0.56	21.5 ± 0.1	0.7 ± 0.2	1.79 ± 0.47	3.24	20.6	22.6	2.72	21.4	
	22	0.63 ± 0.37	23.4 ± 0.1	0.6 ± 0.3	1.02 ± 0.47	0.99	22.6	24.3	1.28	23.5	
	22	2.88 ± 0.51	25.9 ± 0.2	2.1 ± 0.5	1.30 ± 0.47	2.78	24.3	28.2	1.84	25.9	
	44	6.57 ± 0.80	17.1 ± 0.0	1.1 ± 0.2	5.82 ± 0.80	8.43	15.1	19.1	6.51	17.1	
	44	11.66 ± 2.52	21.6 ± 0.4	4.2 ± 1.1	2.62 ± 0.80	8.01	19.1	22.7	4.00	22.0	
	44	3.33 ± 1.73	24.1 ± 0.2	1.5 ± 0.4	2.11 ± 0.80	6.18	22.7	26.4	4.05	23.9	
	95	3.77 ± 1.02	17.0 ± 0.2	1.4 ± 0.4	2.45 ± 0.75	4.63	15.4	18.2	2.58	16.8	
	95	4.20 ± 1.65	19.1 ± 0.2	1.8 ± 0.7	2.19 ± 0.75	5.07	18.2	20.3	3.21	19.4	
	95	16.36 ± 1.46	22.6 ± 0.2	3.9 ± 0.4	3.97 ± 0.75	15.16	20.3	26.5	5.01	22.1	
19.496+0.115	22	0.13 ± 0.18	107.5 ± 0.1	1.3 ± 0.3	1.65 ± 0.36	2.35	105.9	109.4	1.69	107.6	20130302TN
	22	0.12 ± 0.18	116.5 ± 0.2	1.4 ± 0.5	1.45 ± 0.36	2.67	114.1	118.2	1.47	116.4	
	44	0.15 ± 0.15	119.9 ± 0.1	1.3 ± 0.3	1.81 ± 0.37	2.24	117.4	122.0	2.09	119.9	
	95	2.30 ± 0.33	120.0 ± 0.1	0.9 ± 0.2	2.30 ± 0.34	2.74	118.4	122.3	2.29	120.0	
19.614+0.011	22	2.24 ± 0.34	35.1 ± 0.1	0.7 ± 0.1	2.85 ± 0.55	2.02	33.5	36.0	3.43	35.1	20120325YS
19.701-0.267	44	9.14 ± 1.27	41.7 ± 0.4	5.6 ± 0.8	1.55 ± 0.58	8.63	36.5	46.5	2.61	43.1	20130418TN
	95	12.24 ± 1.16	41.6 ± 0.2	4.8 ± 0.5	2.42 ± 0.59	11.34	38.1	45.8	3.86	43.0	
19.884-0.534	22	4.75 ± 1.25	-1.2 ± 0.2	1.6 ± 0.5	2.88 ± 1.00	4.93	-3.3	0.0	3.25	-1.4	20130418TN

Table 4.1 (cont'd)

Source	Frequency (GHz)	Gaussian Fit				Integrated Fit					Obs. Date yyyymmdd†
		S_{int} (Jy km s^{-1})	V_{peak} (km s^{-1})	FWHM (km s^{-1})	S_{peak} (Jy)	S_{int} (Jy km s^{-1})	v_{min} (km s^{-1})	v_{max} (km s^{-1})	S_{peak} (Jy)	V_{peak} (km s^{-1})	
	22	9.18 ± 1.34	2.1 ± 0.1	1.7 ± 0.3	5.18 ± 1.00	9.26	0.0	5.0	6.01	2.0	
	22	21.97 ± 1.83	27.2 ± 0.1	2.8 ± 0.3	7.38 ± 1.00	20.95	24.7	29.7	9.06	26.8	
	22	8.58 ± 1.23	31.4 ± 0.1	1.8 ± 0.2	4.37 ± 1.00	11.52	29.7	33.1	4.98	32.3	
	22	50.71 ± 1.46	34.7 ± 0.0	2.3 ± 0.1	20.84 ± 1.00	50.74	33.1	37.1	22.72	34.4	
	22	30.06 ± 1.27	38.6 ± 0.0	1.5 ± 0.1	18.25 ± 1.00	30.46	37.1	40.4	19.36	38.6	
	22	38.45 ± 1.04	42.3 ± 0.0	1.2 ± 0.0	31.35 ± 1.00	45.56	40.4	44.1	31.25	42.4	
	22	17.20 ± 0.83	44.8 ± 0.0	0.8 ± 0.0	21.42 ± 1.00	18.18	44.1	47.1	19.85	44.9	
	44	52.69 ± 0.94	43.6 ± 0.0	1.6 ± 0.0	30.92 ± 0.75	57.09	40.1	47.3	30.38	43.3	
	95	102.04 ± 1.19	43.6 0.0	1.8 0.0	51.84 0.89	115.75	39.6	48.3	53.87	43.2	

†The observation sites : YS - yonsei, US - Ulsan, and TN - Tamna

Table 4.2. Observation lists and results

Source	V_{sys}	22 GHz detection	44 GHz detection	95 GHz detection	V_{sys} determined line	Comments
353.216-0.249	-16.2	O	O	O	Other	
353.273+0.641	-4.0	O	O	O	Other	HV at -59.4 km s^{-1}
353.363-0.166	-80.8	O	O	O	Other	HV at -129.3 km s^{-1}
353.370-0.091	-52.9		O		Other	
353.378+0.438	-11.5	O			Other	HV at -46.5 km s^{-1}
353.410-0.360	-16.6	O	O	O	Other	
353.429-0.090	-57.5		O	O	Other	
353.464+0.562	-45.7		O	O	Other	
353.537-0.091	-56.2				HCO^+	
354.206-0.038	-30.7				HCO^+	
354.308-0.110	17.8	O			Other	
354.496+0.083	19.6				HCO^+	
354.615+0.472	-21.1		O	O	Other	
354.701+0.299	96.9		O	O	Other	
354.724+0.300	98.0		O	O	Other	
355.184-0.419	-3.0	O	O	O	Other	
355.344+0.147	14.0	O			Other	
355.538-0.105	1.3	O			$H^{13}CO^+$	
355.545-0.103	-29.7				HCO^+	
355.642+0.398	-4.4				$H^{13}CO^+$	
355.666+0.374	-2.7				HCO^+	
356.054-0.095	15.8				HCO^+	
356.662-0.263	-52.6		O	O	$H^{13}CO^+$	
357.558-0.321	-1.1	O	O	O	Other	
357.922-0.337	-0.6		O	O	Other	
357.965-0.164	-3.8	O	O	O	$H^{13}CO^+$	HV at -57.8 km s^{-1}
358.263-2.061	3.9				HCO^+	
358.371-0.468	6.2	O			Other	
358.386-0.483	-1.4	O	O	O	Other	
358.460-0.391	-1.3	O	O	O	Other	

Table 4.2 (cont'd)

Source	V_{sys}	22 GHz detection	44 GHz detection	95 GHz detection	V_{sys} determined line	Comments
358.721-0.126	14.9		O		Other	
358.809-0.085	-54.6		O	O	$H^{13}CO^+$	
358.841-0.737	-20.0				HCO^+	
358.906+0.106	-21.8				$H^{13}CO^+$	
358.931-0.030	-19.7	O	O	O	HCO^+	other component at -67.8 $km\,s^{-1}$
358.980+0.084	-3.1		O	O	Other	
359.138+0.031	-2.6	O			$H^{13}CO^+$	
359.436-0.104	-52.0	O	O		$H^{13}CO^+$	Kim C.-H. et al. (2014)
359.615-0.243	18.9	O	O	O	$H^{13}CO^+$	Kim C.-H. et al. (2014)
359.938+0.170	-0.2		O	O	Other	
359.970-0.457	19.0	O	O	O	HCO^+	
0.092+0.663	17.6	O	O	O	Other	
0.167-0.446	16.4	O	O		Other	
0.212-0.001	45.3		O	O	HCO^+	Kim C.-H. et al. (2014)
0.315-0.201	18.6	O			HCO^+	Kim C.-H. et al. (2014)
0.376+0.040	40.6	O	O	O	HCO^+	
0.409-0.504	20.7				HCO^+	
0.475-0.010	32.2		O	O	Other	
0.496+0.188	-5.5		O		$H^{13}CO^+$	Kim C.-H. et al. (2014)
0.546-0.852	17.4	O	O	O	$H^{13}CO^+$	
0.836+0.184	7.0	O	O	O	HCO^+	Kim C.-H. et al. (2014)
1.008-0.237	0.4		O		^{13}CO	
1.147-0.124	-16.6	O			HCO^+	Kim C.-H. et al. (2014)
1.329+0.150	-16.9				Molinari et al.(2006)	Kim C.-H. et al. (2014)
1.719-0.088	50.6				HCO^+	
2.143+0.009	60.5	O			HCO^+	
2.521-0.220	-2.1	O			Other	
2.536+0.198	9.5				$H^{13}CO^+$	Kim C.-H. et al. (2014)
2.591-0.029	-5.8				^{13}CO	
2.615+0.134	96.6				$H^{13}CO^+$	

Table 4.2 (cont'd)

Source	V_{sys}	22 GHz detection	44 GHz detection	95 GHz detection	V_{sys} determined line	Comments
2.703+0.040	96.5		O	O	HCO^+	
3.253+0.018	6.8				^{13}CO	
3.312-0.399	6.1		O	O	Other	
3.442-0.348	-22.1		O	O	Other	
3.502-0.200	-21.1		O		Other	
3.910+0.001	14.8				HCO^+	
4.393+0.079	6.2		O	O	$H^{13}CO^+$	
4.434+0.129	1.2	O	O	O	Other	
4.569-0.079	15.6				HCO^+	
4.586+0.028	15.5				HCO^+	
4.676+0.276	2.3		O	O	Other	
4.866-0.171	9.6				HCO^+	
5.618-0.082	-25.7		O	O	Other	
5.630-0.294	15.6	O			HCO^+	
5.657+0.416	18.6	O			Other	
5.677-0.027	14.0	O			$H^{13}CO^+$	
5.885-0.393	8.9	O	O	O	Churhwell et al.(1990)	Kim C.-H. et al. (2014)
5.900-0.430	6.2	O	O	O	HCO^+	Kim C.-H. et al. (2014)
6.189-0.358	-34.6	O	O	O	Other	
06.368-0.052	141.7		O	O	$H^{13}CO^+$	
06.539-0.108	12.9				HCO^+	
06.588-0.192	-0.2	O			HCO^+	
06.610-0.082	4.7	O	O		$H^{13}CO^+$	
06.795-0.257	21.0	O	O	O	$H^{13}CO^+$	Kim C.-H. et al. (2014)
06.881+0.093	-3.2				HCO^+	
7.166+0.131	80.3	O	O	O	Other	
07.601-0.139	154.4				HCO^+	
7.632-0.109	153.2		O	O	Other	
08.139+0.226	19.7	O			Churhwell et al.(1990)	Kim C.-H. et al. (2014)
8.317-0.096	47.0		O	O	Other	

Table 4.2 (cont'd)

Source	V_{sys}	22 GHz detection	44 GHz detection	95 GHz detection	V_{sys} determined line	Comments
08.669-0.356	35.3	O	O	O	Churhwell et al.(1990)	Kim C.-H. et al. (2014)
08.683-0.368	33.9	O	O	O	HCO^+	Kim C.-H. et al. (2014)
08.832-0.028	0.7	O	O	O	$H^{13}CO^+$	
08.872-0.493	17.0	O			HCO^+	
9.215-0.202	41.9	O			Other	
09.621+0.196	4.2	O	O	O	$H^{13}CO^+$	Kim C.-H. et al. (2014)
09.986-0.028	48.6	O	O	O	HCO^+	
10.205-0.345	12.6		O	O	Other	
10.287-0.125	13.3	O	O	O	Chen et al.(2010)	
10.299-0.146	13.8	O	O	O	Churhwell et al.(1990)	Kim C.-H. et al. (2014)
10.320-0.259	32.3		O	O	HCO^+	Kim C.-H. et al. (2014)
10.323-0.160	12.6	O			HCO^+	
10.342-0.142	11.8	O	O	O	Chen et al.(2010)	
10.356-0.148	44.3	O	O	O	HCO^+	HV at $11.2\,km\,s^{-1}$
10.444-0.018	73.5				HCO^+	
10.472+0.027	66.9	O	O	O	$H^{13}CO^+$	Kim C.-H. et al. (2014)
10.480+0.033	66.5	O	O	O	Other	
10.627-0.384	-3.2	O	O	O	$H^{13}CO^+$	Kim C.-H. et al. (2014)
10.629-0.333	-3.0		O	O	Other	
10.724-0.334	-1.6	O	O	O	Other	
10.822-0.103	68.2				HCO^+	
10.886+0.123	20.9	O			Other	
10.958+0.022	21.3	O			HCO^+	
11.034+0.062	17.8				HCO^+	
11.109-0.114	29.9				Chen et al.(2010)	
11.497-1.485	10.5	O			Molinari et al.(2006)	
11.903-0.102	36.4				HCO^+	
11.904-0.141	35.7				HCO^+	
11.936-0.150	41.9	O	O	O	Other	
11.936-0.616	38.9	O	O	O	Churhwell et al.(1990)	Kim C.-H. et al. (2014)

Table 4.2 (cont'd)

Source	V_{sys}	22 GHz detection	44 GHz detection	95 GHz detection	V_{sys} determined line	Comments
11.992-0.272	59.9				$H^{13}CO^+$	
12.025-0.031	109.8				Sridharan et al.(2002)	Kim C.-H. et al. (2014)
12.112-0.126	45.3	O	O	O	Other	
12.181-0.123	25.8	O			Other	HV at -27.0 km s^{-1}
12.199-0.033	50.9		O	O	Chen et al.(2010)	
12.202-0.120	27.4	O	O	O	Other	
12.203-0.107	23.7	O	O	O	$H^{13}CO^+$	
12.209-0.102	22.6	O	O	O	HCO^+	Kim C.-H. et al. (2014)
12.265-0.051	64.7		O	O	^{13}CO	
12.526+0.016	42.8		O		HCO^+	
12.625-0.017	21.6		O	O	$H^{13}CO^+$	
12.681-0.182	56.0	O	O	O	$H^{13}CO^+$	Kim C.-H. et al. (2014)
12.776+0.128	35.0				HCO^+	
12.889+0.489	35.4	O	O	O	HCO^+	Kim C.-H. et al. (2014)
12.904-0.031	56.5	O	O	O	Chen et al.(2010)	
12.909-0.260	35.4	O	O	O	HCO^+	Kim C.-H. et al. (2014)
13.179+0.061	48.7	O	O	O	HCO^+	
13.657-0.599	47.3	O	O	O	Molinari et al.(2006)	Kim C.-H. et al. (2014)
13.696-0.156	103.0				HCO^+	
13.713-0.083	47.6				HCO^+	
14.101+0.087	9.9	O	O	O	Other	
14.230-0.509	18.3	O	O	O	Other	
14.390-0.020	40.0				HCO^+	
14.457-0.143	43.3				HCO^+	
14.490+0.014	22.5				$H^{13}CO^+$	
14.521+0.155	-3.3				HCO^+	
14.604+0.017	28.6	O	O	O	HCO^+	Kim C.-H. et al. (2014)
14.631-0.577	18.5	O	O	O	Chen et al.(2010)	
14.991-0.121	50.1				HCO^+	
15.034-0.677	19.3	O	O	O	$H^{13}CO^+$	Kim C.-H. et al. (2014)

Table 4.2 (cont'd)

Source	V_{sys}	22 GHz detection	44 GHz detection	95 GHz detection	V_{sys} determined line	Comments
15.094+0.192	30.1	O	O	O	Other	
15.607-0.255	58.0				HCO^+	
15.665-0.499	-4.9	O	O	O	Other	
16.112-0.303	41.2	O			HCO^+	HV at 5.1 km s^{-1}
16.302-0.196	48.8				HCO^+	
16.403-0.181	48.9		O	O	Other	
16.585-0.051	59.3	O	O	O	$H^{13}CO^+$	Kim C.-H. et al. (2014)
16.662-0.331	46.8		O	O	HCO^+	
16.831+0.079	62.7				Other	
16.855+0.641	20.1	O			Other	HV at -73.0 km s^{-1}
16.864-2.159	17.5	O	O	O	$H^{13}CO^+$	Kim C.-H. et al. (2014)
16.976-0.005	21.5				HCO^+	
17.021-2.403	19.5	O	O	O	Other	
17.029-0.071	93.1		O	O	HCO^+	
17.638+0.157	22.1	O			Other	
17.862+0.074	113.2				HCO^+	
18.073+0.077	51.4				HCO^+	
18.159+0.094	55.6		O	O	HCO^+	
18.262-0.244	68.2		O	O	Other	
18.341+1.768	32.8	O	O	O	Sridharan et al.(2002)	Kim C.-H. et al. (2014)
18.440+0.045	61.4				HCO^+	
18.460-0.004	49.2		O	O	HCO^+	
18.661+0.034	80.8	O	O	O	Other	HV at 30.1 km s^{-1}
18.667+0.025	79.7	O	O		Chen et al.(2010)	HV at 42.1 km s^{-1}
18.733-0.224	41.7	O	O	O	Sanhueza et al.(2012)	Kim C.-H. et al. (2014)
18.834-0.300	63.1				Sanhueza et al.(2012)	Kim C.-H. et al. (2014)
18.874+0.053	50.0				HCO^+	
18.888-0.475	65.8		O	O	Chen et al.(2010)	
18.999-0.239	64.4	O			Other	HV at -11.8 km s^{-1}
19.009-0.029	60.0		O	O	Chen et al.(2010)	

Table 4.2 (cont'd)

Source	V_{sys}	22 GHz detection	44 GHz detection	95 GHz detection	V_{sys} determined line	Comments
19.249+0.267	13.5				HCO^+	
19.267+0.349	20.6				HCO^+	
19.365-0.030	25.1		O	O	HCO^+	Kim C.-H. et al. (2014)
19.472+0.170	19.3	O	O	O	Other	
19.486+0.151	22.6	O	O	O	HCO^+	Kim C.-H. et al. (2014)
19.496+0.115	120.2	O	O	O	$H^{13}CO^+$	
19.609-0.234	40.5	O	O	O	HCO^+	Kim C.-H. et al. (2014)
19.612-0.120	57.6				Chen et al.(2010)	
19.612-0.134	57.4		O		HCO^+	Kim C.-H. et al. (2014)
19.614+0.011	28.3	O			Other	
19.667+0.114	22.6				Other	
19.701-0.267	44.6		O	O	HCO^+	
19.755-0.128	121.7		O	O	Sridharan et al.(2002)	Kim C.-H. et al. (2014)
19.884-0.534	44.1	O	O	O	Chen et al.(2010)	

Note. — At the V_{sys} determined lines, 'Other' means that the observation of HCO^+ toward the source is done by others of a local group of star-forming-region in the KASI using the KVN. The information is given to us but they do not decide a publication related with the information.

Table 4.3. BGPS counterparts list

Source	distance† ($''$)	BGPS name	radius ($''$)	$S_{40''}$ (Jy)	S_{int} (Jy)	$N_{H_2}^{beam}$ (cm^{-2})
353.216-0.249	9.94	G353.216-00.246	46.93	0.738	2.062	4.47
353.363-0.166	11.09	G353.365-00.166	29.34	1.086	2.415	6.57
353.370-0.091	15.50	G353.374-00.092	52.45	0.545	2.726	3.30
353.410-0.360	8.77	G353.412-00.360	70.35	11.158	47.618	67.55
353.429-0.090	12.20	G353.432-00.088	96.60	0.867	5.758	5.25
354.206-0.038	12.16	G354.208-00.036	62.71	0.728	2.748	4.41
354.308-0.110	7.01	G354.307-00.108	12.38	0.319	0.568	1.93
354.615+0.472	12.07	G354.617+00.472	32.71	2.802	6.385	16.96
354.724+0.300	9.57	G354.725+00.302	46.50	1.689	5.077	10.22
355.184-0.419	10.04	G355.186-00.418	42.43	1.859	4.982	11.25
355.344+0.147	9.57	G355.346+00.148	51.78	1.112	2.981	6.73
355.538-0.105	7.66	G355.540-00.106	41.59	0.366	1.299	2.22
355.642+0.398	11.11	G355.644+00.400	-	0.162	0.299	0.98
355.666+0.374	1.48	G355.663+00.376	28.10	0.166	0.533	1.00
356.662-0.263	3.84	G356.662-00.264	38.11	1.012	2.760	6.13
357.558-0.321	2.20	G357.557-00.322	44.42	1.697	4.335	10.27
357.922-0.337	4.52	G357.922-00.336	38.78	0.531	1.481	3.21
357.965-0.164	10.18	G357.968-00.164	29.85	2.344	5.099	14.19
358.371-0.468	4.01	G358.372-00.468	47.60	0.573	2.276	3.47
358.386-0.483	12.47	G358.389-00.484	44.66	1.453	4.861	8.80
358.460-0.391	6.94	G358.461-00.392	60.77	1.725	6.165	10.44
358.809-0.085	15.68	G358.812-00.088	51.28	0.392	1.465	2.37
358.906+0.106	12.91	G358.908+00.106	32.25	0.114	0.336	0.69
359.615-0.243	13.27	G359.617-00.243	63.30	3.776	15.635	22.86
359.970-0.457	13.85	G359.971-00.459	88.42	1.442	7.617	8.73
0.167-0.446	5.01	G000.166-00.447	66.79	0.557	2.808	3.37
0.376+0.040	10.72	G000.378+00.041	56.02	1.849	7.068	11.19
0.409-0.504	15.94	G000.412-00.503	42.31	0.774	2.154	4.69
1.008-0.237	14.61	G001.010-00.240	89.20	1.138	6.168	6.89
2.143+0.009	12.79	G002.144+00.006	26.46	0.480	1.029	2.91
2.536+0.198	6.16	G002.534+00.198	56.78	0.777	3.257	4.70
2.615+0.134	10.01	G002.616+00.132	83.96	0.743	4.316	4.50
3.253+0.018	15.04	G003.254+00.018	93.45	0.191	1.504	1.16
3.312-0.399	13.40	G003.310-00.402	71.84	0.847	4.224	5.13
3.502-0.200	9.94	G003.500-00.202	18.80	0.262	0.566	1.59
4.434+0.129	9.92	G004.434+00.126	56.14	1.020	3.685	6.17
4.569-0.079	4.08	G004.569-00.079	59.35	0.134	0.645	0.81
4.586+0.028	5.90	G004.587+00.027	38.49	0.116	0.374	0.70
5.618-0.082	10.69	G005.621-00.081	69.67	0.705	2.811	4.27
5.630-0.294	15.41	G005.633-00.293	53.16	0.241	0.781	1.46
5.657+0.416	8.08	G005.659+00.415	9.57	0.077	0.174	0.47
5.885-0.393	10.20	G005.887-00.391	21.32	7.927	14.677	47.99

Table 4.3 (cont'd)

Source	distance[†] ($''$)	BGPS name	radius ($''$)	$S_{40''}$ (Jy)	S_{int} (Jy)	$N_{H_2}^{beam}$ (cm^{-2})
6.189-0.358	7.52	G006.191-00.359	48.27	1.455	4.638	8.81
06.588-0.192	9.99	G006.589-00.189	-	0.085	0.181	0.51
06.610-0.082	11.95	G006.613-00.083	45.91	0.170	0.640	1.03
7.166+0.131	7.22	G007.167+00.133	41.06	0.457	1.114	2.77
7.632-0.109	3.70	G007.632-00.110	33.25	0.585	1.459	3.54
08.669-0.356	15.45	G008.670-00.356	58.34	5.573	17.907	33.74
08.832-0.028	9.98	G008.832-00.028	70.29	0.913	3.865	5.53
08.872-0.493	12.14	G008.874-00.494	99.87	0.523	4.651	3.17
9.215-0.202	10.05	G009.212-00.202	64.29	1.018	4.599	6.16
09.621+0.196	14.65	G009.620+00.194	46.92	3.638	9.744	22.02
09.986-0.028	10.97	G009.986-00.030	-	0.452	1.147	2.74
10.205-0.345	10.76	G010.204-00.348	40.93	0.814	3.424	4.93
10.287-0.125	13.75	G010.286-00.120	68.12	1.713	9.409	10.37
10.299-0.146	15.10	G010.300-00.148	46.85	2.790	7.981	16.89
10.320-0.259	2.57	G010.320-00.258	62.32	0.857	3.361	5.19
10.472+0.027	8.41	G010.472+00.026	37.59	9.398	20.789	56.89
10.627-0.384	2.89	G010.625-00.384	31.39	9.722	20.020	58.86
10.724-0.334	14.78	G010.727-00.332	66.59	0.501	2.281	3.03
10.822-0.103	14.17	G010.825-00.102	-	0.119	0.182	0.72
10.886+0.123	4.46	G010.885+00.124	11.31	0.195	0.397	1.18
10.958+0.022	13.49	G010.959+00.020	49.81	0.783	2.702	4.74
11.034+0.062	14.06	G011.035+00.062	58.57	0.548	2.121	3.32
11.109-0.114	11.55	G011.107-00.116	56.71	0.560	2.258	3.39
11.903-0.102	9.41	G011.903-00.102	-	0.218	0.481	1.32
11.904-0.141	7.53	G011.904-00.140	57.07	1.003	3.836	6.07
11.992-0.272	4.96	G011.991-00.270	60.14	0.275	1.281	1.66
12.025-0.031	13.81	G012.025-00.032	43.89	0.285	0.906	1.73
12.112-0.126	8.62	G012.113-00.128	22.39	0.312	0.645	1.89
12.199-0.033	12.83	G012.201-00.034	52.77	0.694	2.064	4.20
12.526+0.016	14.23	G012.529+00.018	93.29	0.246	1.979	1.49
12.625-0.017	11.21	G012.627-00.016	78.87	1.146	5.708	6.94
12.681-0.182	11.20	G012.681-00.182	86.15	2.086	11.822	12.63
12.889+0.489	5.74	G012.889+00.490	53.31	2.534	7.895	15.34
12.904-0.031	4.96	G012.905-00.030	65.04	1.032	3.558	6.25
12.909-0.260	8.21	G012.909-00.260	79.15	3.174	15.852	19.21
14.101+0.087	2.60	G014.102+00.087	46.82	0.841	2.502	5.09
14.390-0.020	11.03	G014.388-00.021	64.21	0.228	1.062	1.38
14.490+0.014	5.77	G014.488+00.015	50.49	0.621	2.381	3.76
14.631-0.577	10.01	G014.633-00.574	72.46	2.053	10.197	12.43
14.991-0.121	9.25	G014.988-00.122	91.29	0.380	2.334	2.30
15.665-0.499	2.89	G015.665-00.499	66.26	0.804	3.829	4.87
16.112-0.303	12.50	G016.114-00.301	38.80	0.116	0.383	0.70

Table 4.3 (cont'd)

Source	distance[†] ($''$)	BGPS name	radius ($''$)	$S_{40''}$ (Jy)	S_{int} (Jy)	$N_{H_2}^{beam}$ (cm^{-2})
16.403-0.181	5.93	G016.402-00.183	24.87	0.200	0.426	1.21
16.585-0.051	4.33	G016.586-00.051	31.69	1.451	3.424	8.78
16.831+0.079	4.89	G016.832+00.080	24.03	0.428	0.926	2.59
17.029-0.071	4.52	G017.030-00.070	35.82	0.351	0.996	2.12
17.638+0.157	9.79	G017.638+00.154	49.78	2.139	6.742	12.95
17.862+0.074	13.51	G017.864+00.072	29.35	0.212	0.687	1.28
18.262-0.244	9.40	G018.260-00.246	85.23	1.095	8.511	6.63
18.460-0.004	9.54	G018.462-00.002	79.26	1.263	6.336	7.65
18.834-0.300	8.00	G018.834-00.299	56.78	0.442	1.542	2.68
18.888-0.475	15.04	G018.888-00.475	100.92	1.356	9.848	8.21
19.009-0.029	14.74	G019.010-00.029	44.10	0.761	2.401	4.61
19.249+0.267	10.30	G019.251+00.267	-	0.217	0.377	1.31
19.267+0.349	7.40	G019.268+00.349	37.70	0.185	0.563	1.12
19.365-0.030	14.64	G019.364-00.031	95.65	1.136	6.818	6.88
19.486+0.151	15.25	G019.488+00.149	73.37	0.484	3.210	2.93
19.496+0.115	13.33	G019.498+00.119	65.73	0.260	1.220	1.57
19.609-0.234	13.92	G019.609-00.233	38.07	5.116	10.927	30.97
19.667+0.114	6.56	G019.667+00.113	-	0.123	0.286	0.74
19.701-0.267	10.94	G019.702-00.263	94.98	0.703	4.907	4.26
19.755-0.128	14.15	G019.756-00.129	73.67	0.569	2.739	3.44
19.884-0.534	10.10	G019.884-00.535	40.73	2.106	5.221	12.75

[†]A distance between center position of BGPS point source and 6.7 GHz class I methanol maser position

Chapter 5

Conclusions

TRAO has imported the 15 beam receiver, QUARRY and bought autocorrelation spectrometers to support the receiver in order to drastically improve observation efficiency. Since these systems produce large amount of data and need complicated control of devices, we developed several control programs, used various communication means among devices, and installed a few new devices such as data acquisition storage (DAS).

In Chapter 2, first we introduced the revised systems and new PCs. Performance improvement of softwares was the most important task. Using asynchronous timer and non-blocking programming techniques, we succeeded in controlling the QUARRY with untested pre-existing instruments. A front-end / platform PC (PPC) especially, could manage all peripherals together by the non-blocking programming. Tuning process could work without bottleneck, infinite loops, or errors. The asynchronous timer is also used in the back-end system to control 15 correlators and a time generator (TG). The correlators had low speed and unstable transfer rates with USB 1.1. Finally the back-end system is optimized spending only 7 ms to take data with 50 ms exposure. DAS was newly installed in the TRAO system. It plays not only a data storage and but also a bridge for users to operate the TRAO system. A

DMA with cyclic redundancy check (CRC) is adopted to carry data among the BPC, DAS, and Modcomp. To minimize error of the DMA method, a new DIO board was fabricated.

The TRAO has started observation in 2009 with the multi-beam receiver. Fig 5.1 shows a first light of the QUARRY toward Orion in ^{12}CO line. The observation with the QUARRY started with 13 beams since the 5th and 15th mixers were out of order. Typical system temperatures at ^{12}CO (115.271204 GHz) and ^{13}CO (110.201353 GHz) are ∼900 K and ∼500 K at 45° elevation, individually. Grid spacing is $\sim 50.47'' \pm 5.2$, and pointing errors in azimuth and elevation are $5.34''$ and $5.69''$, respectively. Beam efficiency is ∼50% at 86 GHz (Figure 5.2).

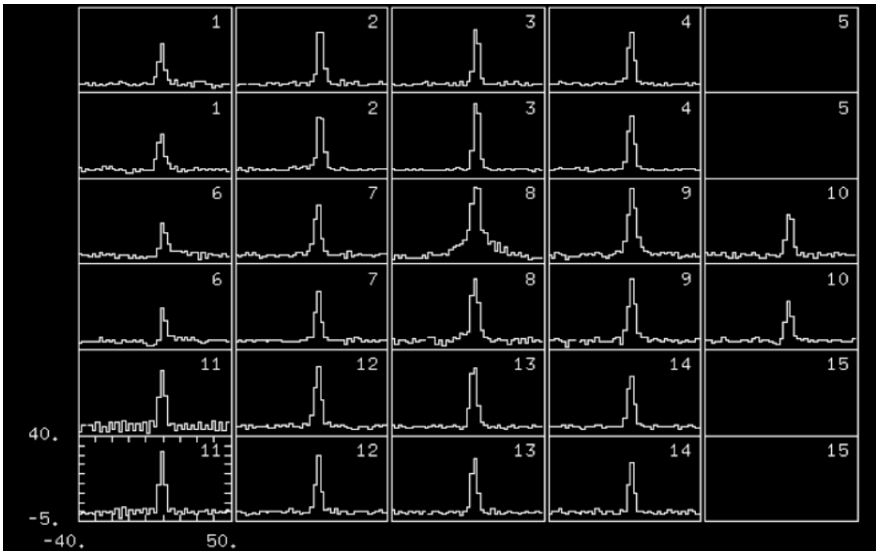

Figure 5.1: A first light by the QUARRY toward Orion at ^{12}CO line.

In Chapter 3, we presented a result of simultaneous observation of 22 GHz water and 44 GHz and 95 GHz class I methanol masers toward 77 6.7 GHz class II methanol maser detected source from AMGPS catalog that may be related with massive star

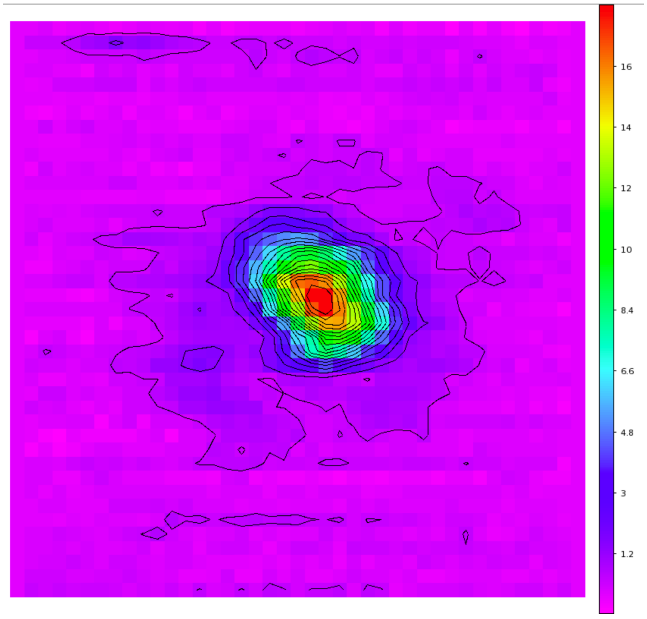

Figure 5.2: A continuum observation result of the Jupiter at 86 GHz. Beam efficiency is ∼50%.

forming regions. The KVN telescope as a single dish instrument was utilized to observe the three maser lines, and the TRAO telescope was used to confirm high velocity features at 22 GHz water maser. There are 15, 21, and 13 new detections at 22 GHz , 44 GHz, and 95 GHz, respectively. It is found that class I methanol masers of 44 GHz and 95 GHz show strong correlations in velocity and peak flux density. We could not find any anti-correlations between class I and class II methanol masers claimed by previous observations. 6.7 GHz maser exhibits a distribution of velocity offset slightly different from those of other masers. The isotropic luminosities of the class I methanol maser are correlated with the BGPS clump mass. With these relations of the class I methanol masers, we calculated the methanol abundances using LVG model. The estimated abundances are between 4.2×10^{-8} to 2.3×10^{-6}, which are comparable to the typical value in the interface region of outflow with the

surrounding molecular cloud.

We observed more 6.7 GHz sources using the KVN and the TRAO, which is described in chapter 4. The 155 sources are selected from the MMB catalog and observed in the same maser transitions with the KVN telescopes. The TRAO and the KVN were used to confirm systemic velocities of the sources and high velocity features found in 22 GHz water maser line with ^{13}CO and HCO^+ molecular lines. With more samples of 271 sources from MMB and AMGPS catalogues, we got detection rates of 22 GHz, 44 GHz, and 95 GHz masers are 49 %, 51 %, and 44 %, respectively. The tendencies found in chapter 3 for AMGPS sources was confirmed that class I methanol masers have strong correlations with each other, and the class I methanol masers are not related with others. The distribution of the velocity offset of class II methanol masers with a significant central dip is different from the those of other masers. Inner galactic region ($l < 20^\circ$) seems to exhibit higher detection rates of class I methanol maser and lower detection rates of water maser than outer region ($l > 20^\circ$). 44 GHz maser is frequently found with 95 GHz (87 %). Interestingly, as 6.7 GHz peak flux density goes high, water and class I methanol masers detection rates also increase. The BGPS counterpart of our 95 GHz detected source is well agreed with the criteria of Chen et al.(2010), but the expected detection rates of Chen is somewhat higher than ours.

요 약

다중빔 수신기는 짧은 시간에 넓은 영역을 관측할 수 있어서 관측 효율을 비약적으로 증가시킨다. 전세계적으로 단일경 전파망원경들은 이러한 다중빔 수신기를 도입하기 위한 노력을 기울이고 있다. 대덕전파천문대 또한 국제적인 추세에 빠르게 맞추기 위해 미국 FCRAO로부터 QUARRY라고 불리는 15개의 피드-혼을 갖춘 다중빔 수신기를 도입하였다. 우리는 이 수신기를 대덕전파천문대에서 사용하기 위한 시스템을 개발하였다. 그러기 위해 백엔드 시스템의 프로그램과 인터페이스를 새로 제작하였다. 프론트엔드 시스템의 경우 수신기를 원활히 제어하도록 구현하였으며, 모드컴의 데이터를 저장하기 위하 새로운 저장 시스템을 개발하였다. 이를 위해 소프트웨어 측면에서 비동기 시간 함수와 논블로킹 방식의 프로그램을 백엔드 시스템에서 구현하였다. 각 시스템 간의 명령 및 데이터 전송을 위해 여러 통신 프로그래밍을 구현하였다. 프론트엔드 시스템의 경우는 논블로킹 방식의 프로그램 수정을 통해 수신기의 제어가 안정적으로 이루어지도록 하였다. 하드웨어 측면에서, 이전의 노후된 디지털 입출력 보드를 교체하였다. 시스템 간의 명령 전송을 위한 디지털 입출력 및 시리얼 입출력 라인을 구성하였다. 또한 DMA 전송 방식을 각 시스템 간에 구현하였다.

우리는 다중빔 수신기를 설치한 대덕전파천문대와 KVN 단일경을 이용하여 고질량성 영역에 대한 22 GHz 물메이저원, 44 GHz 와 95 GHz 클래스 1 메탄올 메이저원, 그리고 HCO^+ (1-0), $H^{13}CO$ (1-0), and ^{13}CO (1-0) 분자선 관측을 수행하였다. 관측 대상은 6.7 GHz 클래스 2 메탄올 메이저원 카탈로그인 AMGPS와 MMB 카탈로그로부터 선택하였다. 총 271개의 천체에 대해 22 GHz, 44 GHz, 95 GHz 메이저원의 검출율은 각각 49 %, 51 %, 44 %를 얻었다. 물메이저원은 대부분 다른 메이저원들과 같이 검출되었으나 최대선속밀도나 속도영역에서 특별한 상관관계를 보이지는 않았다. 66개 중 12개의 천체에 대해 22 GHz에서 중심속도로부터 멀리 떨어진 위치에 최대선속밀도가 나타나는 것을 발견하였다. 대덕전파천문대의 ^{13}CO 관측 결과를 보면 이 중에 7개만이 확실한 고속도 성분을 보인 것을 확인할 수 있었다. 95 GHz 메이저원은 44 GHz 메이저원과 속도, 최대선속밀도 등에서 높은 상관관계를 보인다. 또한 44 GHz의 87 %가

95 GHz와 같이 검출되었다. 6.7 GHz의 경우 중심분자운 속도에 대한 최대선속밀도의 분포가 독특한 형태를 띄는데, 중심속도 위치에 대해 양쪽으로 봉우리를 갖는 형태를 보인다.

주요어: 전파망원경, 제어시스템, 메이저, 별탄생

학 번: 2004-30138